MICROCOPY RESOLUTION TEST CHART
NATIONAL BUREAU OF STANDARDS

$\textcircled{10}$

Multiplex Holography for Space-Variant Optical Processing

by

Mike I. Jones
E. Lee Kral

LEVEL III A05-0973

SEAL OF TEXAS TECH UNIVERSITY

D D C
RECEIVED
OCT 12 1979
E
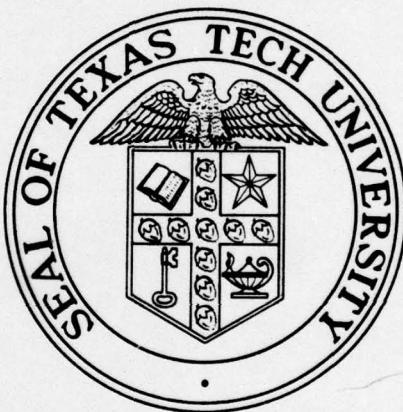
September 1, 1979

410 597

Optical Systems Laboratory
DEPARTMENT OF ELECTRICAL ENGINEERING

406 820

TEXAS TECH UNIVERSITY

Lubbock, Texas 79409

AD A074987

79 10 12 101

⑥ MULTIPLEX HOLOGRAPHY FOR SPACE-VARIANT OPTICAL PROCESSING.

Part I and II

⑪ 1 Sep 79

⑩ Mike I. /Jones
E. Lee/Kral

September 1, 1979

⑱ AFOSR

⑲ TR-79-Ø99Y

Scientific Report No. 2 on

⑤ AFOSR-75-2855

⑬ 329

"Space-Variant Optical Systems"

Principal Investigator: Dr. John F. Walkup, Assoc. Prof.

⑭ SCIENTIFIC-2

Optical Systems Laboratory

Department of Electrical Engineering

Texas Tech University

Lubbock, Texas 79409

The views and conclusions contained in this document are those of the authors, and should not be interpreted as necessarily representing the official policies or endorsements, either expressed or implied, of the Air Force Office of Scientific Research or the U. S. Government.

PREFACE

A major goal of the research effort has been the implementation of two-dimensional representations of space-variant optical systems. In a sampling theorem-based approach this requires sampling the system's input plane and multiplexing the system's transfer functions for the various imput plane samples. Our technique utilizes diffusers in the individual reference beams to encode the sequentially-recorded holograms so as to minimize hologram-to-hologram crosstalk on playback. Part I of this report presents the results of a detailed examination of the use of ground glass diffusers with up to 100 holograms being multiplexed. Experimental results include the representation of a strongly space-variant magnifier, and a demonstration that indeed the individually multiplexed holograms are adding coherently on playback. Part II contains analytical work describing the autocorrelation and crosscorrelation properties of various models of pure phase, pure amplitude, and combined amplitude and phase diffusers. A spatial random telegraph wave description is employed for the diffusers, with either evenly spaced transition points or Poisson distributed transitions assumed. The correlation properties of these "model" diffusers, and the signal-to-noise ratios expected when such multiplexed holograms are played back, are presented. This analytical work, based on rather idealized models of real world diffusers, helps explain many of the experimental results described in Part I.

PART I

MULTIPLEX HOLOGRAPHY FOR TWO-DIMENSIONAL
SPACE-VARIANT OPTICAL PROCESSING

by

Mike I. Jones

PART II

CORRELATION PROPERTIES OF DIFFUSERS
FOR MULTIPLEX HOLOGRAPHY

by

E. Lee Kral

<u>PART I</u>

MULTIPLEX HOLOGRAPHY FOR TWO-DIMENSIONAL
SPACE-VARIANT OPTICAL PROCESSING

by

Mike I. Jones

ABSTRACT -- PART I

This report describes extensive experimental implementations of multiplex holography for use in representing two-dimensional space-variant optical systems. Diffusers are used to encode the reference beams for effective crosstalk suppression. The problem of hologram-to-hologram crosstalk is both analytically and experimentally examined, and various methods for its suppression are discussed. The merits of using ground glass diffusers for crosstalk suppression are experimentally investigated, and the superiority of chirped-wave diffuser illumination over plane-wave illumination in crosstalk suppression is demonstrated. The first implementations of binary-coded diffuser masks for crosstalk suppression in multiplex holography are shown. The experimental proof of coherent addition in overlapping holographic outputs is presented, and the first holographic representation of an extremely space-variant optical system is shown. The holographic representation of an optical system using a large (10 x 10) array of input sampling points is also shown. With a working 2-D space-variant holographic processor thus available, a variety of space-variant processing operations for future investigations are suggested.

TABLE OF CONTENTS -- PART I

Page

LIST OF FIGURES

iii

iv

v

CHAPTER 1
INTRODUCTION

The concept of two-dimensional space-variant optical information

processing has been the subject of extensive recent theoretical work

[1-12]. Previous experimental verifications of this theoretical work

have, on the other hand, been limited [1, 2, 7, 11, 12]. The purpose

of this thesis is to present the results of the first large-scale in-

vestigation into the use of multiplex holography for two-dimensional

space-variant optical system representation and processing. Several

problems associated with multiplex holography, including hologram-

to-hologram crosstalk and hologram exposure problems are discussed.

Solutions to some of these problems, such as the use of binary or

random diffusers for crosstalk suppression, are described in detail.

In general, this thesis describes a variety of achievements, includ-

ing the following:

(1) The use of diffuserless hologram outputs, to show
the location of hologram-to-hologram crosstalk, and
the presentation of a new analytical method whereby
the number, location and relative strengths of this
crosstalk may be predicted;

(2) The use of ground glass as a diffuser material for
attenuating these unwanted cross-terms, for a
variety of array sizes, magnifications and illumi-
nating wavefront curvatures;

(3) The use of computer-generated binary diffuser masks
for crosstalk attenuation for a similar variety of
system parameters;

1

(4) The first experimental implementations of actual
2-D space-variant processing with a multiplex
hologram, using an extremely space-variant
system as an example;

(5) The experimental verification of coherent addition
in multiplex holography;

and (6) The implementation of large (10 x 10) arrays of
sampling points for optical system representation.

At this point the author wishes to take the liberty of coining a
new word, holoplex, for brevity and for the sake of coining a new
word. Used as a noun, it will mean a completely processed multiplexed
hologram, as distinct from a simple, single hologram. Used as a verb,
holoplex will mean the act of making a multiplexed hologram.

1.1. Historical Background

Several methods of holographically representing 2-D space-variant
optical systems have been investigated previously [1-4]. The methods
can be categorized, in approximately the chronological order of their
investigation, as follows:

(1) Volume Hologram Representation
(2) Piecewise Isoplanatic Approximation (PIA)
(3) Discrete Orthonormal Basis Set Response (DBₖ)
(4) Computer-Multiplexing Representation
(5) Encoded Reference Beam Approach

Common to all of these approaches is the goal of faithfully re-
presenting the characteristics of a 2-D space-variant optical system
holographically, so that accurate coherent optical processing (some-
times referred to as optical computing) may be realized, while at

the same time maintaining a high signal-to-noise ratio through the reduction of any offending crosstalk (i.e., noise) present.

A thorough theoretical investigation of the PIA, DBR, and volume hologram methods was given by Marks [3]. Deen [1, 2] presented additional theoretical and experimental work on volume hologram representations. Theoretical work on the PIA and DBR methods has yet to be supported by experimental work. Experimental work by Deen [1, 2] showed that the volume hologram method, although capable of accurate 2-D space-variant system representation, provided effective crosstalk attenuation along only one spatial axis. This outcome was obviously detrimental to the overall signal-to-noise ratio of the volume holoplex.

The computer-generated transmittance mask approach to 2-D space-variant system representation is presently under investigation by Irby et al. [10]. A primary goal of this method is to reduce the total number of hologram exposures necessary to represent a space-variant optical system, a goal which clearly has practical significance when large sampling arrays are contemplated. The reduction of hologram exposures is accomplished by numerically "premultiplexing" groups of holograms together in the computer. A composite holographic transmittance mask of these premultiplexed holograms is then generated, plotted, and photoreduced. A single hologram of this transmittance mask is then recorded, which then ideally contains the full amount of sampled information about an optical system, but requires only one exposure. Theoretically, a large total number of holograms

may thus be stored without causing plate overexposure problems. Experimental results from this method are rudimentary but encouraging at the time of this writing.

1.2. The Encoded Reference Beam Approach

The remaining (fifth) method listed, that of the encoded reference beam approach, is the one upon which the experimental work presented in this thesis is based. This scheme has proved to be the most promising to date, as was predicted by Marks [3, p. 194]. The basic idea of this method is to spatially sample the input plane of a space-variant optical system at a rate determined by the space-variant sampling theorem [6]. The respective transfer functions of the space-variant system are then sequentially holoplexed together on a thin recording medium. A crucial problem inherent in this method is the generation of hologram-to-hologram crosstalk interference when the holoplex is played back. It has been shown in several recent papers [4-9] that if the respective reference beams are encoded with random or psuedo-random diffusers, the crosstalk may be attenuated significantly. Recent work has shown that crosstalk suppression may be achieved by using binary phase-encoding masks in the reference beams [8] and even better suppression may be attained by illuminating these masks with spherical ("chirped") wavefronts [9]. The experimental data presented in the following chapters verifies the theoretical work well, and in addition contains some previously unpredicted results which, however, agree well with the mathematical theory.

1.3. Experimental Setups for Recording and Playback

The schematic diagram of the recording process used in the encoded reference beam method is shown in Fig. 1-1. The object-reference point-source pairs are denoted by δ_1 through δ_n, and the optical system's point spread functions are denoted by h_1 through h_n, where n is the total number of holograms recorded. The respective diffuser masks are denoted as $M_1(x)$ through $M_n(x)$, and are all located a distance d from the plane of the reference point sources. These point sources illuminate their respective diffusers with expanding spherical wavefronts whose degree of curvature may be expressed by the parameter α, where $\alpha = \pi/\lambda d$ [10]. The effective mask function for the jth mask may then be written as [9]

$$M_j(x) = M_j(x)\exp(-j\alpha x^2). \qquad (1-1)$$

Lenses L_1 and L_2 then perform 2-D Fourier transforms on the incident light field amplitudes, and the resultant complex transfer functions are sequentially holoplexed together at the recording plate P. Lenses L_1 and L_2 are schematically depicted here as simple biconvex thin lenses; in reality, two well-corrected multi-element lenses were used to minimize aberrations. A main goal in this thesis was to have as nearly a diffraction-limited recording and playback system as possible, so that the transfer functions holoplexed together at P would be those produced by the space-variant optical system alone, free of optical degradations from other components. Methods by which a nearly perfect recording/playback system was achieved are covered in detail in Appendix A.

REFERENCE
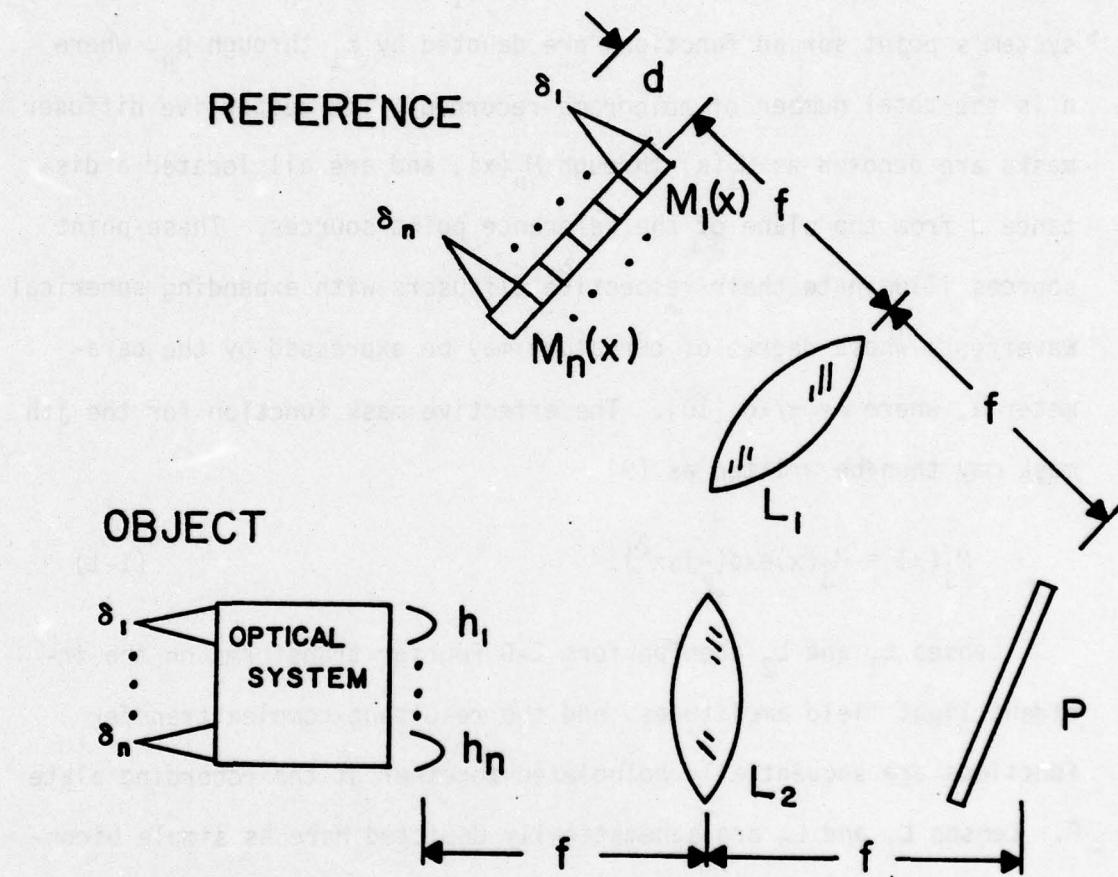
OBJECT

Figure 1-1. Schematic diagram of recording process.

Once all n holograms have been recorded, the plate is processed and reinserted, and the system shown in Fig. 1-2 is used to play back the holoplex. The object beam is blocked and L_2 is positioned behind the holoplex as shown. Then an input plane object is simultaneously sampled with the reference point array $\delta_1 \ldots \delta_n$, yielding input point sources $S_1\delta_1$ through $S_n\delta_n$. The holoplex ideally processes the light field incident on it exactly as the 2-D space-variant optical system it is intended to represent, and the processed, Fourier-transformed result appears in the output plane as shown. Lens L_2 is reused as shown if identical output scaling is desired; otherwise any well-corrected photographic lens may be used at this point for transforming and recording the output on regular film. Lens L_2 is usually placed a distance f behind the holoplex. If its aperture is too small to collect and focus all the diffracted light emanating from the holoplex (i.e., vignetting), however, it may be necessary to position L_2 directly behind the holoplex. This has no effect on the appearance of the photo-graphed outputs, and L_2 was placed directly behind all holoplexes in this project.

Figure 1-3 shows the experimental recording and playback equipment used throughout the project. The collimated laser light has already been divided by a beamsplitter, and both beams enter the system from the left. The reference beam components are arranged diagonally across the center of the photo. The object beam travels horizontally across the top of the photo, intercepts a flat folding mirror, then travels vertically down the right side of the photo. The angle
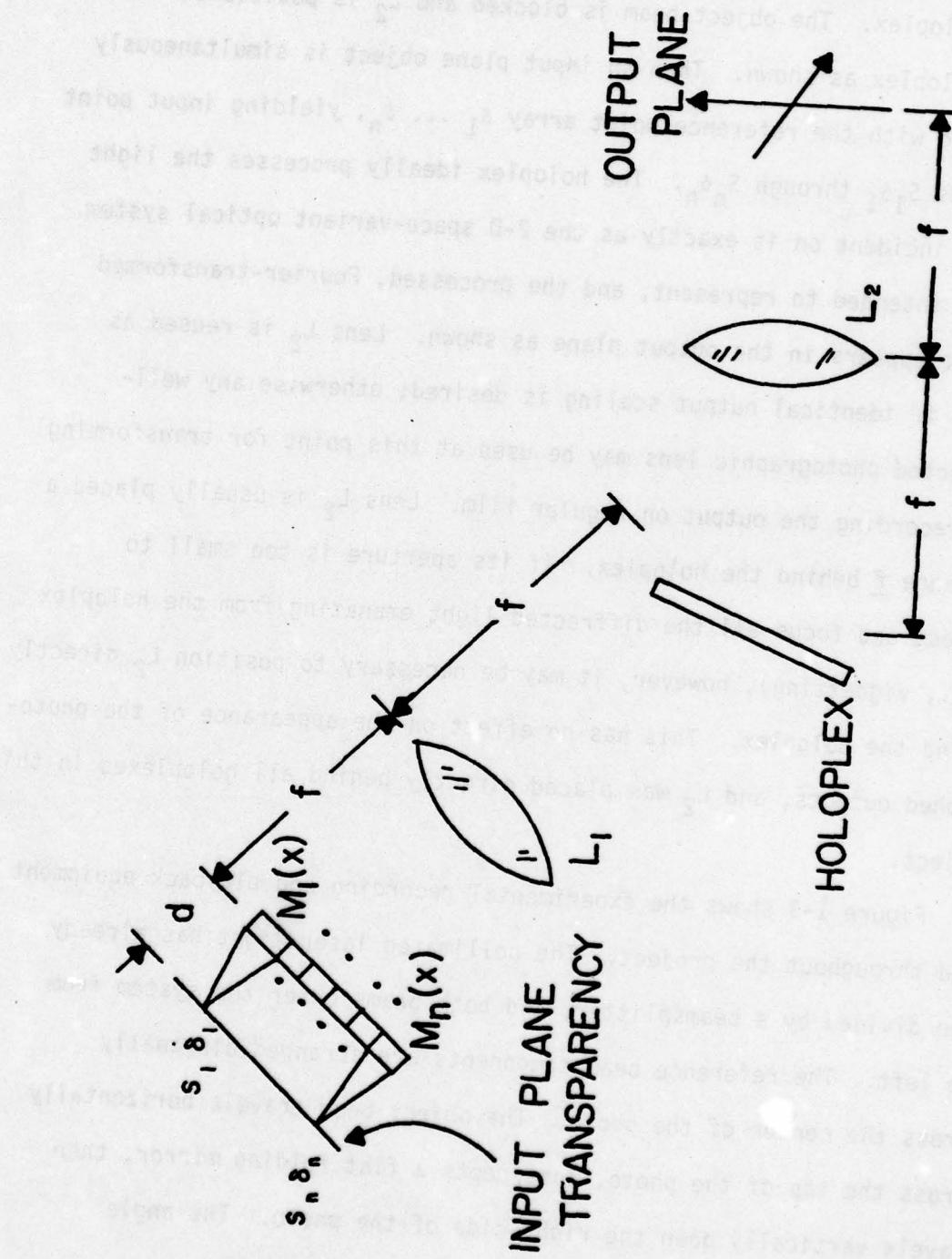
Figure 1-2. Schematic diagram of playback process.
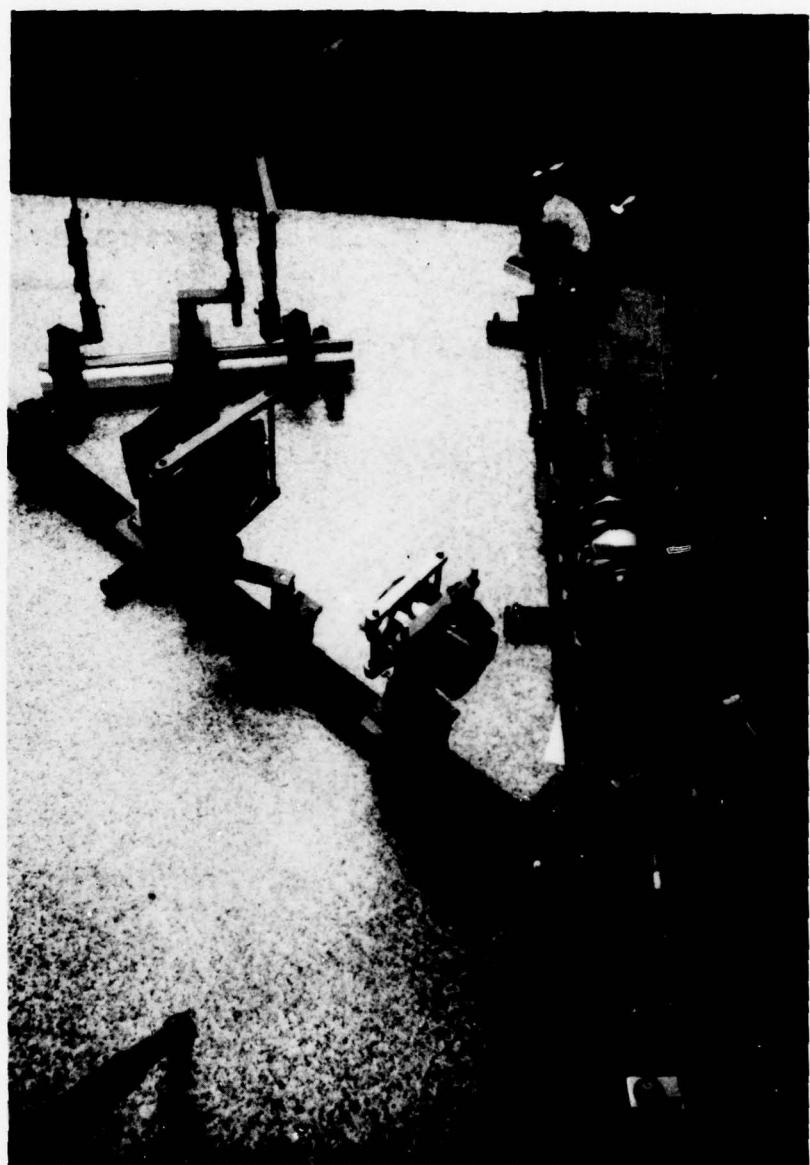
Figure 1-3. Photograph of experimental recording and playback equipment.

between object and reference beams was 45° for all holoplexes recorded in
the project. The two fly's eye arrays used to generate the sample point
sources are located at upper left, with the reference array partially fac-
ing the camera. The reference beam Fourier transforming lens is at exact
center, and the object beam transforming lens is to its right. The object
beam folding mirror and the simple imaging system to be holographically
represented are visible above the object beam transforming lens. A better
picture of these two components is shown in Fig. 5-6. Below the object
beam transforming lens, at the intersection of the object and reference
beam axes, is the micropositioning plateholder. Immediately below it
are the camera and zoom lens used to record the holoplex outputs.

1.4. Mathematical Analysis and Discussion

The amplitude transmittance of the holoplex may be expressed as
[5, 7, 8]

$$t = \sum_{j=1}^{n} |H_j + R_j|^2 \tag{1-2}$$

So

$$t = \sum_{j=1}^{n} (H_j + R_j)(H_j^* + R_j^*)$$

and

$$t = \sum_{j=1}^{n} (|H_j|^2 + |R_j|^2 + H_j^* R_j + H_j R_j^*) \tag{1-3}$$

where n is the total number of holograms multiplexed together. Of
the four terms in Eq. (1-3), only the last term is of interest, as

it is the one that appears in the output plane. Therefore, for our purposes,

$$t_0 = \sum_{j=1}^{n} H_j R_j^* \quad . \tag{1-4}$$

When we play back the holoplex, the sampled-input light field incident on it is

$$U_i = \sum_{j=1}^{n} S_j R_j \tag{1-5}$$

and the field immediately to the right of the holoplex in Fig. 1-2 is

$$U_0 = U_i t_0$$

$$= \sum_{j=1}^{n} S_j R_j \left(\sum_{i=1}^{n} H_i R_i^* \right)$$

$$= \sum_{i=1}^{n} S_i H_i |R_i|^2 + \sum_{i \neq j}^{n} \sum (S_i H_j R_i R_j^*) \tag{1-6}$$

This output is then Fourier transformed either by L_2 or the photographic lens, yielding at the output plane

$$0 = \sum_{i=1}^{n} S_i F\{H_i |R_i|^2\} + \sum_{i \neq j}^{n} \sum S_i F\{H_j R_i R_j^*\}$$

$$0 = \sum_{i=1}^{n} S_i h_i \ast F\{|R_i|^2\} + \sum_{i \neq j}^{n} \sum S_i h_j \ast F\{R_i R_j^*\} \tag{1-7}$$

$$0 = \sum_{i=1}^{n} S_i h_i \ast (r_i \circledast r_i) + \sum_{i \neq j}^{n} \sum S_i h_j \ast (r_i \circledast r_j) \tag{1-8}$$

where * as usual denotes convolution and ⊛ denotes correlation. The step from Eq. (1-7) to Eq. (1-8) employs the autocorrelation property of Fourier analysis [13, 14, 15].

Equation (1-8) is an important result; from it we shall soon see the value of using diffusers in the reference beams for cross-talk attenuation. Remember that the desired space-variant processor output is [8]

$$O' = \sum_{i=1}^{n} S_i h_i .$$ (1-9)

In Eq. (1-8) the first summation term is nearly the desired result, except for its convolution with an autocorrelation function. The second term is the undesired output, previously referred to as hologram-to-hologram crosstalk. We see that it is the summation of the $S_i h_j$ cross-term products convolved with corresponding crosscorrelation functions. Obviously we wish to preserve the first term and ideally eliminate the second term. The solution we have used is to insert a hypothetical family of diffuser masks into the reference beams that have the following properties:

$$r_i(x, y) \otimes r_i(x, y) = \delta(x, y) \; \forall_i$$

$$r_i(x, y) \otimes r_j(x, y) = 0 \; \forall_{i \neq j}$$ (1-10)

Rewriting Eq. (1-8) using these properties,

$$0 = \sum_{i=1}^{n} S_i h_i * \delta(x, y) + \sum_{i \neq j}^{n} \sum^{n} S_i h_j * (0)$$

$$\overset{\circ}{\underset{\circ}{\circ}} \qquad 0 = \sum_{i=1}^{n} S_i h_i,$$

exactly the desired result given in Eq. (1-9).

A family of diffusers with the properties of Eq. (1-10), however, exists only in the mathematician's mind. Strictly speaking, any family of physically realizable diffusers will have finite-width auto-correlation functions and non-zero crosscorrelation functions. This is just as well, for a holoplex recorded using the "perfect" diffuser of Eq. (1-10) would have to be repositioned _perfectly_ for playback after processing, which is of course equally impossible. It is im-portant to realize that the width of the autocorrelation function of the diffuser is a direct measure of the repositioning accuracy necessary to achieve playback.

Because of our inability to satisfy exactly the condition stated in Eq. (1-10), we must settle for some output degradation. Referr-ing to Eq. (1-8), we see that a non-delta autocorrelation degrades the desired $S_i h_i$ output terms by spreading them out, the usual effect of convolution. However, with non-infinite diffuser apertures we cannot realize δ-functions optically, anyway, and are instead limited by diffraction. If the individual apertures illuminating the dif-fusers are circular, each produces the well-known Airy pattern at $\delta_1 \ldots \delta_n$ in Fig. 1-1. In other words, we are unavoidably degraded at the outset, as we are sampling the optical system with Airy patterns

instead of delta functions. Therefore, it is only necessary that the individual diffuser autocorrelation functions have smaller spatial dimensions than the Airy patterns produced by the illuminating apertures. If this condition is satisfied the desired output terms will suffer little degradation other than that produced by diffraction.

Unfortunately we do not have a similar tolerance when considering crosstalk. The presence of non-zero crosscorrelation, even at low amplitudes, can seriously degrade the overall signal-to-noise ratio of the holoplex. Since it is impossible to fabricate a family of diffusers with perfectly zero diffuser-to-diffuser correlation values, it is this problem that ultimately limits the overall effectiveness of the encoded reference beam approach.

Of the various diffusers investigated to date, the diffuser that most closely matches the characterizations dictated in Eq. (1-10) is ground glass. The properties of ground glass as a diffuser will be discussed in greater detail in Chapter 3, and methods by which the diffusers used in this thesis were fabricated are covered in Appendix B. Suffice it to say here that the autocorrelation width of finely ground glass approaches the dimensions of the Airy patterns produced by the reference point source array, and the crosscorrelation is very diffuse and faint. The computer-generated binary amplitude diffusers discussed in detail in Chapter 4 are inferior to ground glass in their crosstalk dispersion performance at present. However, theory predicts that if the individual cell size in each diffuser is made sufficiently small, they should provide better crosstalk suppression than was obtained experimentally in the present work.

In addition to the use of diffusers, the use of chirped (expand-
ing spherical) wavefronts for diffuser illumination has proved to be
a very powerful method for crosstalk attenuation in the 2-D space-
variant holographic processor. Chirping the reference beam wavefronts
can make even a mediocre diffuser look good, and in general, the
greater the degree of chirp (i.e., the more strongly the illuminat-
ing wavefront is curved), the better the attenuation. The power of
chirping lies in the fact that a given plane diffuser is automatic-
ally phase-encoded, by receiving illumination having an increasingly
delayed phase with increasing distance from its center. The phase
delay is zero at the diffuser's center and can amount to tens or
even hundreds of wavelengths at the extreme edge of the diffuser.
This method of automatic phase coding in free space is well-analyzed
by Krile et al. [9], Redus [4], and Kral [5]. In the chapters that
follow, we will see the striking differences in performance that chirp-
ing can make.

Possibly the most important contribution of this thesis is the
experimental verification that the use of chirped illuminating wave-
fronts in conjunction with finely ground glass as a diffuser is the
most powerful method for crosstalk attenuation presently known. Us-
ing this combination, the crosstalk terms are suppressed and dis-
persed to the extent that they may safely be neglected, so that other
aspects of the use of holoplexes in representing 2-D space-variant
optical systems may be more carefully examined.

CHAPTER 2

THE CROSSTALK PROBLEM

The suppression of hologram-to-hologram crosstalk in the representation of space-variant optical systems by multiplex holography is of paramount importance. Crosstalk constitutes undesired noise, and, depending on its spatial distribution, can severely interfere with the desired holographic signal output. Except for the case of simple space-variant imaging systems, this crosstalk distribution can be exceedingly complex, and consequently very difficult to analyze. For the sake of simplicity, in this chapter we will examine only the crosstalk distribution for simple space-variant imaging systems having an arbitrary magnification β. First, some preliminary analytical work will be presented, and then a simple graphical method for predicting the distribution and relative amplitude of the crosstalk terms for simple magnifiers will be demonstrated. Then, actual holoplex outputs substantiating the analytical predictions will be presented, covering a wide range of array sizes and system magnifications. No diffusers were used in recording the holoplexes in this chapter, thus enabling us to see the crosstalk at its undiminished amplitude, as well as its spatial distribution around the desired signal terms. The mode of recording affects the crosstalk distribution significantly, and the remarkably different outputs for sequentially and simultaneously recorded holoplexes will be contrasted. Based on the outputs presented in this chapter we will see the necessity of attenuating crosstalk

16

before attempting to perform any holographic 2-D space-variant process-
ing operations. These diffuserless outputs are also of additional im-
portance; the outputs presented in all following chapters may be com-
pared to those presented here in order to evaluate the relative effi-
ciency of the various types of diffusers in suppressing crosstalk.

2.1. Preliminary Analytical Work

The equations that show how crosstalk is produced were presented
in Chapter 1. The expression for the amplitude of the 2-D space-
variant holographic processor output was given in Eq. (1-8) as

$$0 = \sum_{i=1}^{n} S_i h_i * (r_i \odot r_i) + \sum_{i \neq j}^{n} \sum_{j}^{n} S_i h_j * (r_i \odot r_j).$$

The first term is the summation of the desired signal terms convolved
with their respective diffuser autocorrelation functions, and the
second term is the summation of the undesired crosstalk terms convolved
with their respective diffuser crosscorrelation functions. This equa-
tion is informative in that:

(1) It is valid for any type of 2-D space-variant processing
operation;

(2) It explains the existence of the crosstalk;

(3) It predicts the total number of crosstalk terms ex-
pected when a simple magnifier is holographically repre-
sented, namely n(n-1) terms, where n is the total number
of individual holograms in the holoplex, and

(4) It describes the properties the diffusers must have
in order to obtain the desired output.

By itself, however, Eq. (1-8) gives no information about the spatial
distribution and relative amplitude of the signal and crosstalk terms.

As mentioned, in this chapter we are concerned only with the cross-talk distribution for simple imaging systems. The following derivation by Kral [5] directly gives the distribution of both the signal terms and crosstalk terms, for any imaging system having magnification β, with the assumption that β is constant over the system's entire output plane (i.e., the system has zero distortion). In this derivation we let the inputs to the system be $\delta(x-x_i)$, a row of point sources ($S_i = 1$) equally spaced along the x-axis. Neglecting diffraction effects, the n system impulse responses h_i to this input are ideally $h_i = \delta(x-\beta x_i)$, a row of n points whose separations are scaled by β. Substituting these $S_i h_i$ terms into Eq. (1-8) gives

$$0 = \sum_{i=1}^{n} \delta(x-\beta x_i)*(r_i \circledast r_i) + \sum_{i\neq j}^{n}\sum^{n} \delta(x-\beta x_j)*(r_i \circledast r_j). \qquad (2-1)$$

Equation (2-1) is the expression for the holoplex output when all n holograms are played back simultaneously. To see the distribution of crosstalk when any one hologram is played back, let us select one arbitrary k^{th} hologram from Eq. (2-1). The output is then

$$0_k = \delta(x-\beta x_k)*(r_k \circledast r_k) + \sum_{j\neq k}^{n} \delta(x-\beta x_j)*(r_k \circledast r_j). \qquad (2-2)$$

The first term is the kth signal term, which is convolved with the corresponding k^{th} autocorrelation function. When no diffuser is present, $r_k \circledast r_k$ is simply the unnormalized optical transfer function (OTF) [14, 15] of the circular aperture of the Fourier transform lens. Convolution with $\delta(x-\beta x_k)$ replicates this OTF and centers it at $x = \beta x_k$.

Likewise, the second term in Eq. (2-2) gives the n-1 crosstalk terms given by $\delta(x-\beta x_j)$, which are convolved with crosscorrelations $r_k \circledast r_j$. With no diffuser present, these crosscorrelations also have the form of OTF's characteristic of circular apertures. When convolved with the n-1 delta functions $\delta(x-\beta x_j)$, these OTF's are replicated, each being centered at $\beta x_j + (x_k-x_j)$. Because the coordinates are separable for simple imaging systems, we may utilize Eq. (2-2) to determine output terms along the y-axis as well, and for all off-axis terms in general. Thus Eq. (2-2) may be used to determine the spatial distribution of both signal and crosstalk terms for holographic imaging systems having any given magnification β.

2.2. A Graphical Method for Simple Magnifiers

The preceding analytical method can become laborious, even for simple magnifiers, when it is desired to determine the distribution of crosstalk for large arrays of sampling points. The method presented here enables us to predict the crosstalk distribution and its relative amplitude graphically, for sampling arrays of any size, and for any system magnification, with equal simplicity. The method, derived by the author, is an extension of the previous derivation by Kral, and bears a significant resemblance to that used to graphically compute optical transfer functions for arbitrary optical apertures.

The graphical method is accurate only if a particular numbering convention on the input and output arrays is followed. To illustrate this convention suppose, for simplicity, that our sampling array consists of a 2 x 2 array of points located at the corners of a square having sides of length d, as shown in Fig. 2-1(a). We will label

(a) Input sampling array

(b) Output array for β = +1/3

(c) Output array for β = -1/3
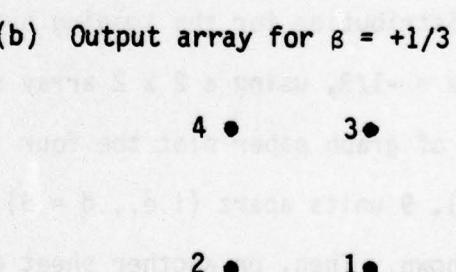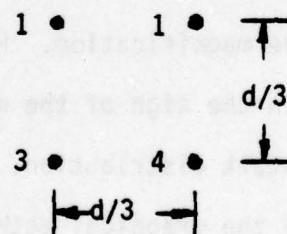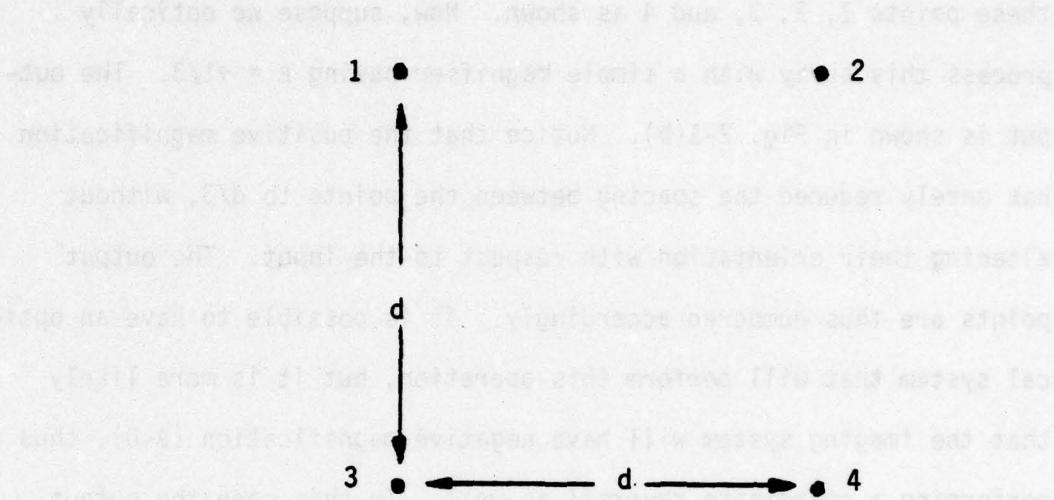
Figure 2-1. Numbering convention for graphical method.

these points 1, 2, 3, and 4 as shown. Now, suppose we optically process this array with a simple magnifier having $\beta = +1/3$. The output is shown in Fig. 2-1(b). Notice that the positive magnification has merely reduced the spacing between the points to $d/3$, without altering their orientation with respect to the input. The output points are thus numbered accordingly. It is possible to have an optical system that will perform this operation, but it is more likely that the imaging system will have negative magnification ($\beta < 0$), thus performing a coordinate reversal as well. In this case the output for $\beta = -1/3$ would appear as in Fig. 2-1(c), with the output points numbered by convention as shown. The graphical method to be described will accurately predict the crosstalk distribution for either positive or negative magnification. However, as we will see, this simple difference in the sign of the magnification has a drastic effect on the crosstalk distribution.

To demonstrate the graphical method, let us determine the holographic crosstalk distribution for the imaging system just described, a magnifier having $\beta = -1/3$, using a 2 x 2 array of input sampling points. On a sheet of graph paper plot the four input points as shown in Fig. 2-2(a), 9 units apart (i.e., $d = 9$). Label the points 1, 2, 3, and 4 as shown. Then, on another sheet of graph paper, plot the four output points as shown in Fig. 2-2(b), 3 units apart (i.e., $d = 3$). Label these points 4, 3, 2, and 1 as shown, to take coordinate reversal into account.

To plot the crosstalk, place the output sheet over the input sheet and, holding over a light, superimpose output point 1 over input

1 ●   2 ●

3 ●   4 ●

(a) Input

4 ●   3 ●

2 ●   1 ●
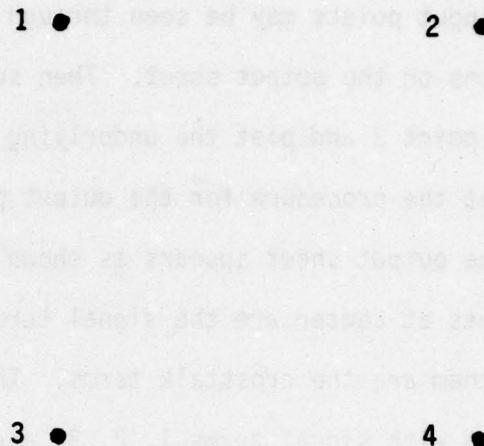
(b) Output

Figure 2-2. Proper preparation of 2 x 2 input and output arrays ($\beta = -1/3$) for graphical method.

point 1. Be sure to accurately align the two sheets in x and y. The three other input points may be seen through the output sheet. Plot their positions on the output sheet. Then superimpose output point 2 over input point 2 and plot the underlying points on the output sheet. Repeat the procedure for the output points 3 and 4. When completed, the output sheet appears as shown in Fig. 2-3. The four numbered points at center are the signal terms, and the 12 points surrounding them are the crosstalk terms. The crosstalk terms that are associated with signal terms 1, 2, 3, and 4 are labeled 1C, 2C, 3C, and 4C, respectively, in Fig. 2-3. Note that three crosstalk terms appear for each signal term, thus following the n(n-1) rule predicted by Eq. 2-2. Here, n = 4 holograms, therefore we can expect 4(4-1) = 12 crosstalk terms. The experimental verification of this distribution appears in Fig. 2-12, which shows the output of 2 x 2 holoplex representing an imaging system having magnification $\beta = -1/3$.

A small array, such as shown here for illustration, is so simple graphically that Eqs. (2-1) and (2-2) might just as well have been used. However, when considering larger arrays, the graphical method immediately becomes the preferred method. For example, let us plot the crosstalk for a 3 x 3 array, using the same magnifier having $\beta = -1/3$. The input and output arrays are shown in Fig. 2-4(a) and 2-4(b), respectively, with the proper point numbering shown. As in the 2 x 2 case, we place output over input, superimpose matching point numbers, and plot the remaining input points visible through the output

Figure 2-3. Signal and crosstalk locations for β = -1/3.

1 ●   2●   3●

                             9● 8● 7●

4 ●   5●   6●   6● 5● 4●

                             3● 2● 1●

7 ●   8●   9●   (b) Output

   (a) Input

Figure 2-4. Preparation of 3 x 3 input and output arrays
$(\beta = -1/3)$ for graphical method.

sheet. When completed, the output sheet appears as shown in Fig. 2-5.
We see at once how intricate the crosstalk distribution has become, with
the addition of only five extra holograms. The 9 signal terms are at
center in Fig. 2-5, with $9(9-1) = 72$ crosstalk terms surrounding them.
Experimental verification of this output may be seen in Fig. 2-18.
Interestingly, this holoplex was recorded only after the distribution
in Fig. 2-5 was predicted graphically, with the obviously pleasing re-
sult.

It was stated that the graphical method will work for positive β
as well. As we will see, a positive value of β generally produces a
very unfavorable distribution of crosstalk. To illustrate, let us use
the same 3 x 3 array as in the previous example. Now, however, let
the system have $\beta = +1/3$. To plot crosstalk for positive β the out-
put points are numbered so that their orientation is identical to that
of the input array, as in Fig. 2-1(b). Then, the steps of the graphical
method are performed, and when completed, the output sheet appears as
shown in Fig. 2-6. The nine signal terms are at center as usual
(numbers omitted), with 72 crosstalk terms surrounding them. Notice,
however, how the crosstalk has been drawn inward, in comparison with
Fig. 2-5. This is a highly undesirable effect, as it can only mean
poorer signal-to-noise ratios when diffusers are used to disperse the
crosstalk. Experimental verification of this predicted output may
be seen in Fig. 2-19.

Another deleterious effect on signal-to-noise ratios occurs
when crosstalk terms overlap each other in the output plane. In
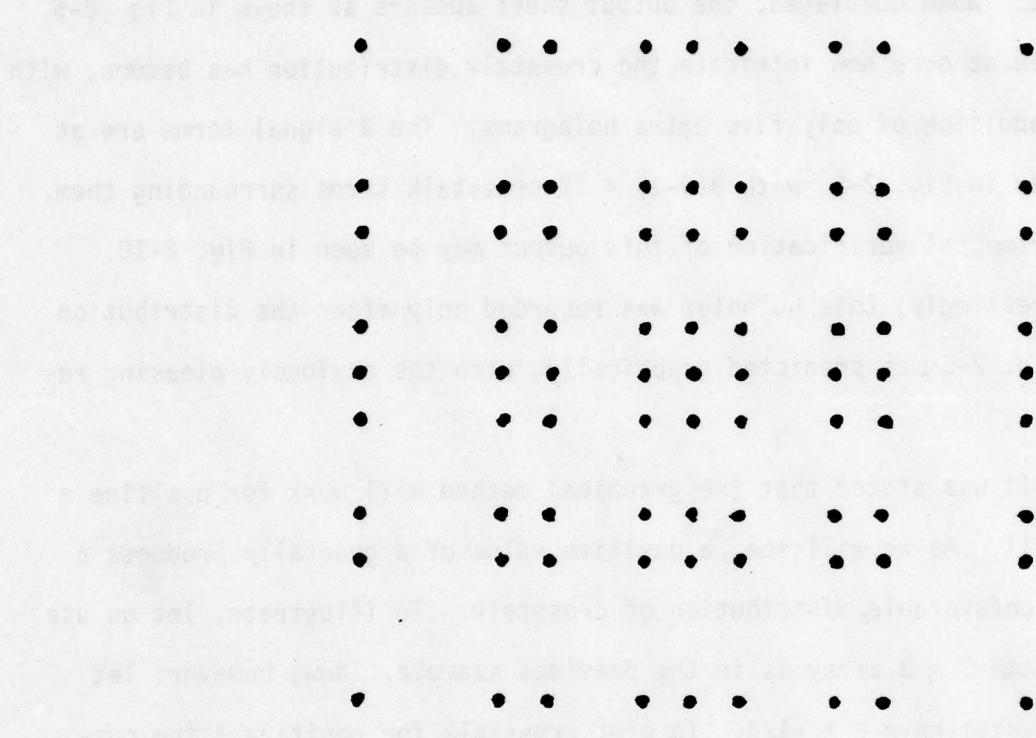
Figure 2-5. Graphical output of 3 x 3 holoplex with β = -1/3.
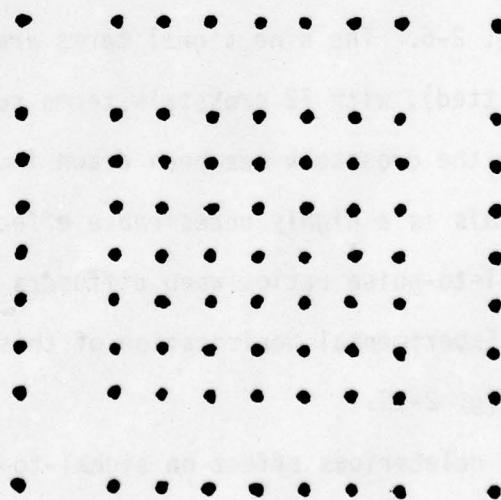
Figure 2-6. Graphical output of 3 x 3 holoplex with β = +1/3.

this case their amplitudes add, thus creating a significant noise problem when using large sampling arrays. We have not seen examples of overlapping in the pr vious figures. In the following examples, though, we will see overlapping in a 5 x 5 holoplex for both positive and negative β. If desired, the relative amplitudes of the overlapping crosstalk terms may be computed by using superposition.

To illustrate overlapping, let us first plot the expected crosstalk for a 5 x 5 array of points and β = +1/3. The graphical output appears in Fig. 2-7, and the experimental verification may be seen in Fig. 2-20. In Fig. 2-7 the 25 signal terms are circled at center. Normally we expect to see 25(25-1) = 600 crosstalk terms. However, the total number of output terms appearing in Fig. 2-7 is only 19 x 19 = 361. Twenty-five of these are the signal terms, which leaves 361-25 = 336 undesired crosstalk terms, 264 short of the expected 600. Unfortunately the missing 264 terms are not gone, but instead are symmetrically distributed throughout the innermost regions of Fig. 2-7, overlapping each other in space and adding their amplitudes to other terms having the same coordinates. When performing the graphical method with this example, one actually sees several crosstalk terms overlapping the signal terms. This is clearly detrimental to the signal-to-noise ratio when diffusers are used, since the non-zero crosscorrelation functions add their amplitudes to the autocorrelation functions they overlap, thus lowering the composite signal-to-noise ratios.

In Fig. 2-5 and 2-6 we saw that using a negative magnification instead of positive has the desirable effect of shifting the crosstalk
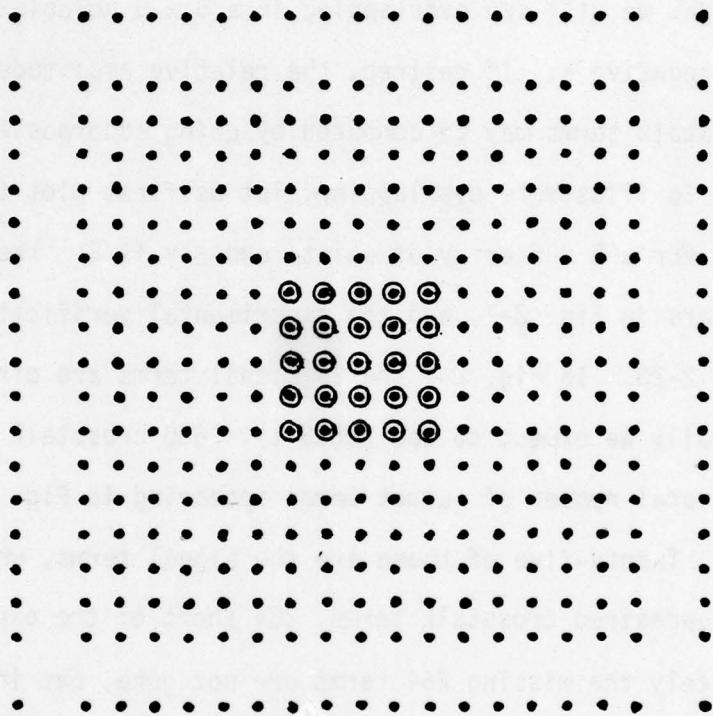
Figure 2-7. Graphical output for 5 x 5 holoplex with
β = +1/3.

outward. Let us then plot the crosstalk for the same 5 x 5 array as in Fig. 2-7, but now for β = -1/3. The remarkably different output is shown in Fig. 2-8, and the experimental verification is shown in Fig. 2-21. The 25 signal terms are circled in Fig. 2-8, as in Fig. 2-7. Now, however, the total output is 23 x 23, giving 529 total terms and 529-25 = 504 visible crosstalk terms. Thus, there are 168 more crosstalk terms visible in Fig. 2-8 than in Fig. 2-7, meaning that a significant amount of noise energy has been displaced outward and away from the signal term array at center. Roughly speaking, if diffusers were used in recording the two 5 x 5 holoplexes described, the holoplex of the system with β = -1/3 would have about a 50% better overall signal-to-noise ratio than the holoplex representing a system with β = +1/3. For simple imaging systems, then, we obviously desire negative rather than positive magnification for optimum cross-talk scattering, if we have the liberty of choosing β.

Negative magnification minimizes overlap but cannot by itself eliminate it. In Fig. 2-8 there are 504 crosstalk terms visible, but by the n(n-1) rule we expect 600. This indicates that there are still 96 undesired terms distributed inside the output pattern, which repre-sents a significant amount of noise energy. If the magnification of the optical system represented holographically is fixed, then this represents the minimum number of overlapping terms achievable for this particular array size and value of β. An effect we shall see shortly, however, is that by reducing $|\beta|$, we can "zoom" the cross-talk outward and away from the center. The requisite for this is that
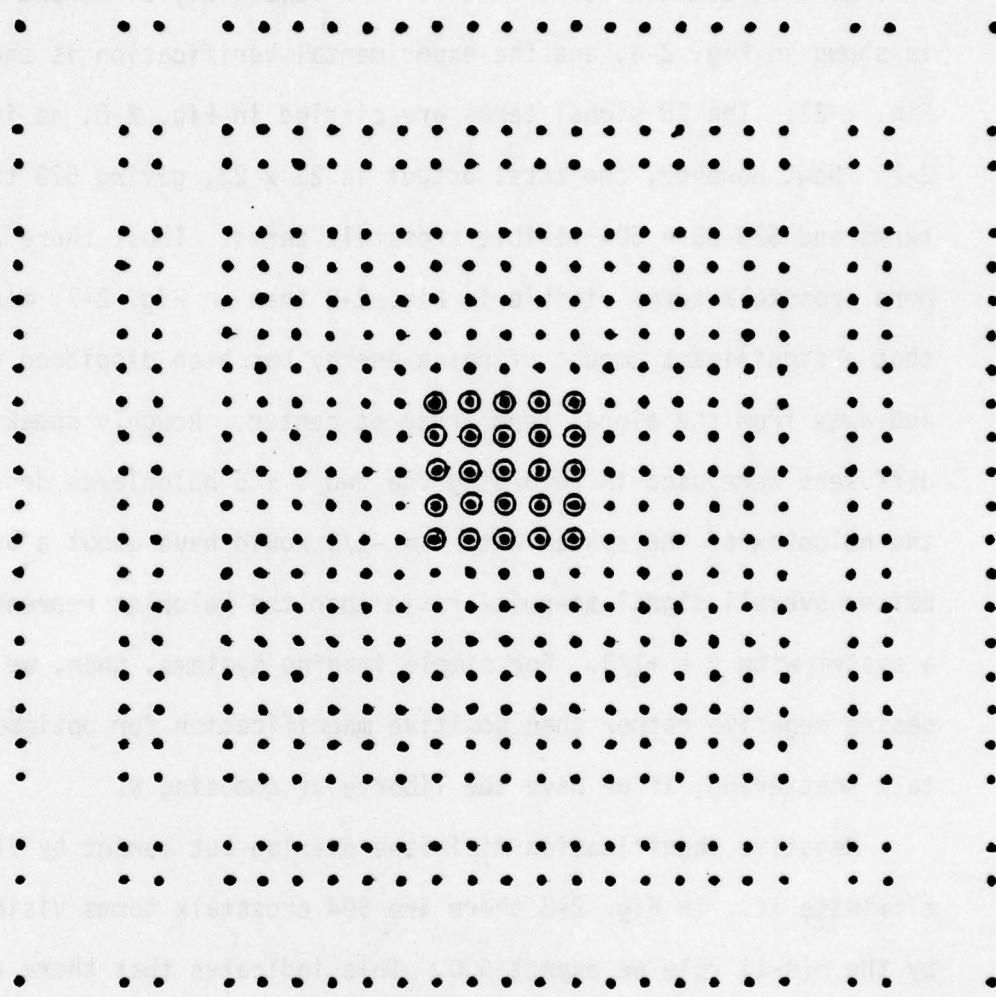
Figure 2-8. Graphical output for 5 x 5 holoplex with β = -1/3.

β is free to vary in the optical system being holographically repre-
sented, which is not often possible. In Fig. 2-8 we can reduce β to,
say, -1/4 or -1/5, and shift the 96 terms out and away from the signal
array, thus improving the signal-to-noise ratio considerably.

In summary we have demonstrated two methods (i.e., analytical
and graphical) by which the distribution and relative amplitudes of
crosstalk terms in holoplexes representing simple magnifiers may be
determined. The use of negative magnification, which produces co-
ordinate reversal at the output, has been shown to be very effective
in improving the signal-to-noise ratios in magnifier holoplexes, by
providing the maximum crosstalk scatter possible for a given β. In
the next section we will explore diffuserless holoplex outputs for
a variety of array sizes and system magnifications.

2.3. Diffuserless Holoplex Outputs

2.3.1. Standardization of Parameters

The holoplexes in this thesis vary widely in such parameters
as emulsion types, total number of multiplexed holograms, intensity
of plate illumination, and reference-to-object intensity ratios.
With so many parameters free to vary, it was necessary at the beginn-
ing of the project to standardize several parameters, in order to
reduce plate waste.

Two parameters standardized from the beginning were the output
power and the wavelength of the laser used for recording. The out-
put power was fixed at 400 mw., and the recording and playback wave-

length was 514.5 nm. for all the holoplexes. The darkroom processing
procedure was also standardized and rigidly adhered to without ex-
ception. The steps for processing all plates in this thesis are given
as follows:

>Develop 5 min. in D-19 at 75° F.
>Stop 30 sec. in Kodak Indicator Stop Bath
>Fix 2 min. in Kodak Rapid Fixer
>Wash 30 sec. in tap water
>Bathe 2 min. in Hypo-Clearing Agent
>Wash 5 min. in slowly running tap water

The plates were developed in open 5" x 7" trays and agitated
every 30 seconds in all chemicals by gently rocking the trays. Dry-
ing time was approximately 20 to 40 minutes, depending on room humidity.

An effort was made to try to standardize the emulsions used, and
several types were tried in the course of the project. Of the several
emulsions used, the Kodak 125-02 and 131-02 emulsions are unhesitatingly
recommended for multiplex holography in general. Their resolution
is only slightly less than Kodak 649-F emulsion, but the gain in speed
is substantial, on the order of 10 to 20 times. The 649-F emulsion is
agonizingly slow, and exposure times for large arrays can easily run
into hours.

2.3.2. Specific Diffuserless Holoplex Outputs

Figures 2-9, 2-10, 2-11, and 2-12 demonstrate the effect of
"zooming" the magnification β for a simple imaging system. For sim-
plicity, a 2 x 2 square array of points was recorded so that the be-
havior of the crosstalk could be more clearly seen. The four signal

terms are located at the center of each figure, and the 12 crosstalk terms are distributed around the periphery. Figure 2-9 shows the holoplex output for β = -1.5, and is of particular importance, as it serves as the standard of comparison for several outputs in the chapters that follow. The value of β was chosen to draw the crosstalk terms inward somewhat, so that when they were dispersed by the various diffuser types, the maximum printing scale would be afforded. Smaller values of β would shift the crosstalk terms outward so far that in order to fit all the terms in the output plane into one small photograph, the fine structure in each of the output functions would be invisible. The emulsion used for this holoplex was Kodak 131-02, with each individual hologram receiving 5-second exposures.

Figure 2-10 shows the holoplex output for β = -1. This is simply a unity magnifier with coordinate reversal. Notice that the crosstalk has spread outward slightly, so that the terms are evenly spaced with the signal terms at center. Kodak 131-02 emulsion was used for this holoplex, with individual hologram exposure times of 3 seconds.

Figure 2-11 is the output for β = -2/3. The crosstalk terms have shifted out even farther than in Fig. 2-10. The central 2 x 2 arrays of Figs. 2-10 and 2-11 are printed at the same scale, for comparison. Kodak 131-02 emulsion was used, with individual exposures of 5 seconds.

Figure 2-12 is the last in this series, recorded at β = -1/3. The crosstalk terms are clearly continuing their outward migration,
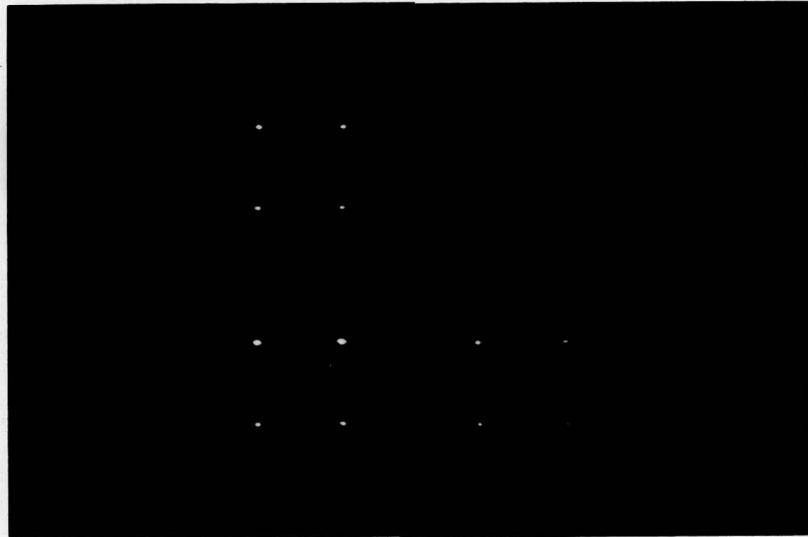
Figure 2-9. Diffuserless 2 x 2 holoplex output for β = -1.5.

Figure 2-10. Diffuserless 2 x 2 holoplex output for β = -1.
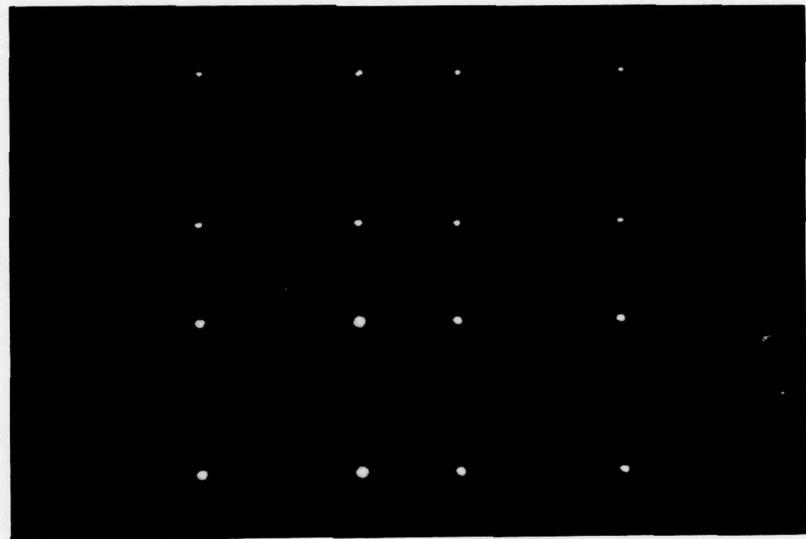
Figure 2-11. Diffuserless 2 x 2 holoplex output for β = -2/3.
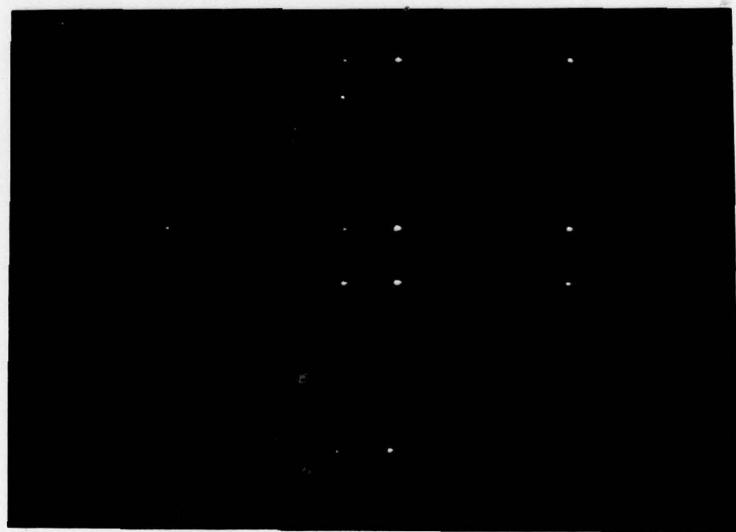
Figure 2.12. Diffuserless 2 x 2 holoplex output for β = -1/3.

leaving the four signal terms at center farther behind. It may be safely extrapolated that this outward migration would continue as we further reduce the magnification. Measurement of Fig. 2-12 shows that the central square of signal terms is about 1/3" on a side, while the crosstalk terms are about 1", or 3 times farther out, thus verifying the graphical output predicted in Fig. 2-3. Kodak 131-02 emulsion was used, with individual exposures of 8 seconds.

Thus it is seen that β can control the position of the crosstalk in holoplexes representing imaging systems. As the value of $|\beta|$ is reduced, the crosstalk shifts outward and away from the signal term array. As mentioned, β is not usually a variable when representing a given system, but it is important to know its effect on the crosstalk distribution shown here.

The effect of positive or negative magnification for a given $|\beta|$ is shown in Figs. 2-13, 2-14, and 2-15. In all three, the optical system magnification was $|2/3|$. The difference in crosstalk distribution is due to the changing of the sign of the magnification, simulated by changing the recording sequence.

Figure 2-13 at top is merely a duplication of Figure 2-11, where $\beta = -2/3$. It is reproduced here to simplify comparison with Figs. 2-14 and 2-15. Figure 2-14 is the holoplex output using the same 2 x 2 input array as in Fig. 2-13, but here $\beta = +2/3$. The same 2/3x optical system was used; the change in sign of β was accomplished by reversing the order the holograms were recorded in. The crosstalk terms have drawn inward, as predicted by the graphical method, and

except for the scale, Fig. 2-14 resembles exactly Fig. 2-9, where β = -1.5. Thus we see the desirability of using negative magnification, if we have the liberty of controlling this parameter available. Kodak 131-02 emulsion was used for recording, with individual exposure times of 5 seconds.

Figure 2-15 is the curious hybrid between the two preceding figures. It occurred by accident when first recording Fig. 2-13, for β = -2/3. A large, flat mirror was used to fold the 2/3x magnifying system around a corner, due to space limitations on the optical slab. When the processed, dried holoplex was played back, the peculiar, asymmetric crosstalk distribution was observed. Why would a symmetric array of signal terms produce an asymmetric distribution of crosstalk? The question was answered when it was realized that the previously neglected mirror was to blame. The simple but subtle reason for the asymmetry is that the -2/3x magnifier was performing a coordinate reversal as well as a 2/3 scaling. The mirror, however, was restoring the output along the x-axis but not along the y-axis. The mirror, therefore, belonged inside the optical system "black box" as well, as it was effectively performing a 1-D processing operation, that of x-coordinate negation. Expressed differently, the mirror was performing a matrix column interchange on the input array. Figure 2-15, therefore, is the correct holoplex output for this system, as the "black box" represented holographically consisted of a -2/3X magnifier and the mirror, and performed a 2/3 scaling operation, coordinate negation, and a matrix column interchange. However, due to space limitations,
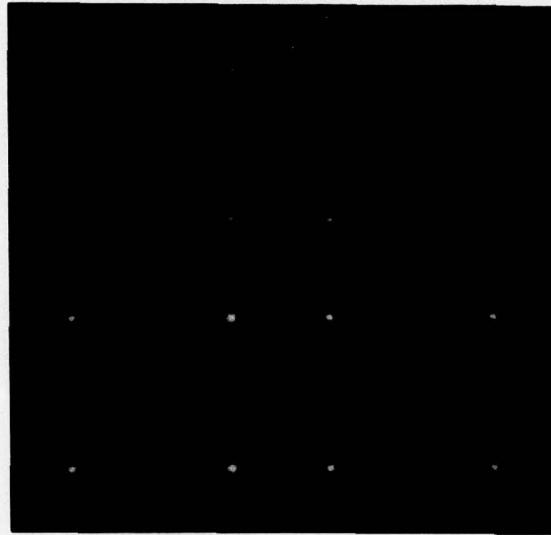
Figure 2-13. Output for $|\beta| = 2/3$ with x, y coordinate reversal.
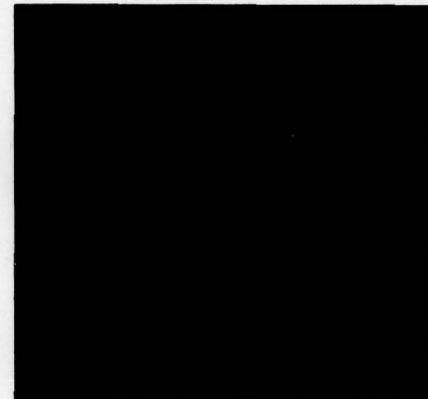
Figure 2-14. Output for $|\beta| = 2/3$, no x, y co-ordinate reversal.
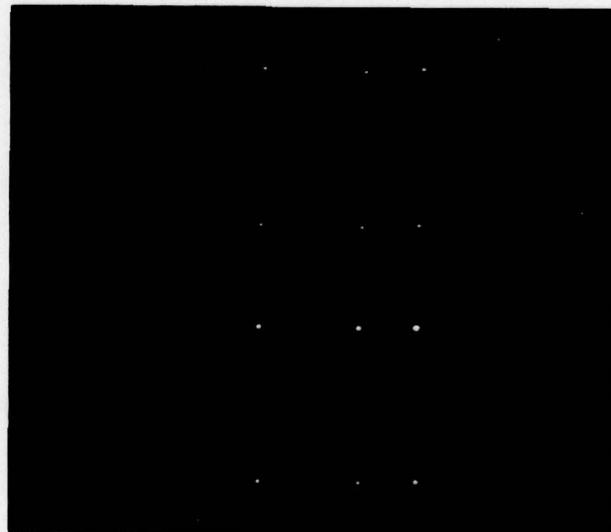
Figure 2-15. Output for $|\beta| = 2/3$, with y - axis reversal, no x - axis reversal.

the mirror could not be removed from the overall optical system, and thus the column interchange would be present in all the holoplexes recorded. Therefore it was desired to remove the effect of the mirror. This was easily accomplished by pre-interchanging the columns on the input array during recording, so that after reflection from the mirror, the x and y axes had the same polarity. The emulsion used for recording this holoplex was Kodak 131-02, with individual hologram exposure times of 8 seconds.

Figures 2-16 and 2-17 contrast the striking difference between sequential and simultaneous recording in multiplex holography. When recording holoplexes for large arrays, involving possibly dozens of individual hologram exposures, it would be much quicker to expose all the holograms at once, instead of sequentially exposing them, one at a time. The difference this makes may be explained by recalling Eq. (1-2) from Chapter 1,

$$t = \sum_{j=1}^{n} |H_j + R_j|^2$$

which gives the amplitude transmittance for a sequentially recorded holoplex. If we instead expose all the holograms at once, the amplitude transmittance is then given by

$$t = |\sum_{j=1}^{n} (H_j + R_j)|^2 .$$

This equation has the effect, when expanded, of generating $n(n^2-1)$ crosstalk terms, which is $n^2(n-1)$ more than the $n(n-1)$ terms given by Eq. (1-2) for the case of sequential recording. Outputs

for simultaneous recording, both with and without diffusers, are shown here merely as reference, as simultaneously recorded holoplexes are of no value in 2-D space-variant system representations. They are, however, capable of some surprising outputs, and in the chapters that follow we will see some of those surprises.

Figure 2-16 is merely a duplication of Fig. 2-12, a 2 x 2 array sequentially recorded at $\beta = -1/3$. It is seen that there are 4(4-1) = 12 crosstalk terms surrounding the central 2 x 2 array of desired signal terms.

Figure 2-17 was recorded using exactly the same magnifier as in Fig. 2-16, except that here the four holograms were exposed simultaneously. We can see at once the dozens of crosstalk terms generated when this holoplex was played back, with terms extending even beyond the border of the photograph. One property of simultaneous holoplexes not shown here, but vividly shown in Chapter 3, is even more serious than the abundance of crosstalk terms observed. When we select and play back the kth hologram from a sequential holoplex, we observe that hologram alone at the output. When we play back any k^{th} hologram from a simultaneous holoplex, all of the holograms stored play back together, even if a diffuser is used! This effect, well documented in Chapter 3, clearly makes the simultaneously recorded holoplex useless for representing optical systems, although its properties may be of use in other applications. Kodak 131-02 emulsion was used for recording this simultaneous holoplex, with a single exposure time of 1 second.
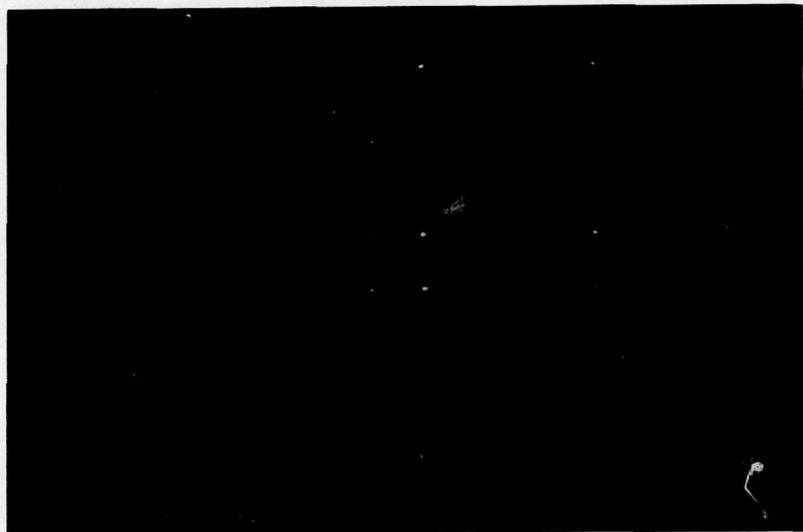
Figure 2-16. Diffuserless, output for β = -1/3, sequential recording.
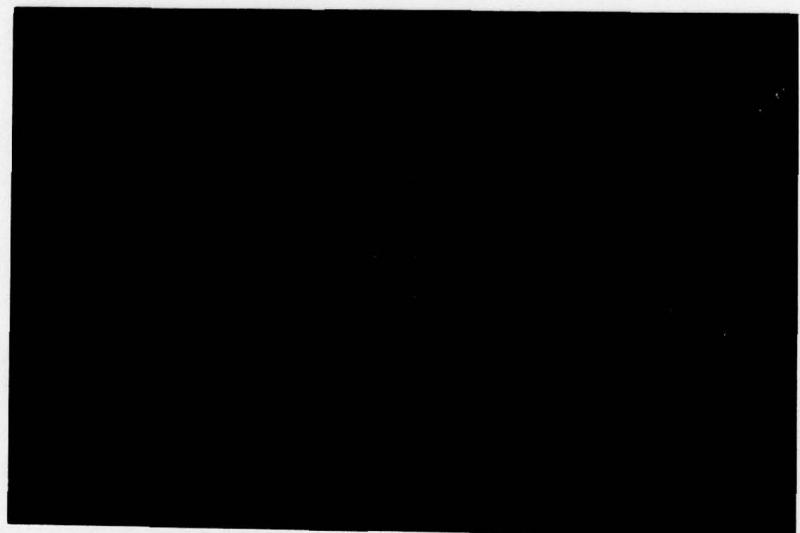
Figure 2-17. Diffuserless output for |β| = -1/3, simultaneous recording.

Figures 2-18 and 2-19 vividly show the effect of changing the polarity of the magnification β, for a simple imaging system, on the distribution of the crosstalk terms. The two photos also verify the outputs predicted by the graphical method described earlier in this chapter. Figure 2-18 is the 3 x 3 holoplex output for β = -1/3. It should be compared to the output correctly predicted by the graphical method, seen in Fig. 2-5. The 3 x 3 array of desired signal terms is located at center, with 9(9-1), or 72 crosstalk terms surrounding it. An important feature of this output is the gap that separates the central array from the neighboring crosstalk. Kodak 649-F emulsion was used for recording this holoplex, with 90-second individual exposure times.

Figure 2-19 is the 3 x 3 holoplex output for β = +1/3. Its graphical counterpart is shown in Fig. 2-6. Again, this change in the polarity of β was simulated by merely reversing the recording sequence. We immediately see that the crosstalk has drawn inward, filling the gap around the desired signal array present in Fig. 2-18. When diffusers are used to disperse crosstalk, this holoplex would have a lower overall signal-to-noise ratio than that of Fig. 2-18, where β = -1/3. Kodak 649-F emulsion was used, with 90-second individual exposure times.

Figures 2-20 and 2-21 exhibit a problem characteristic of the majority of the holoplexes in this project, that of vignetting at the output plane. Vignetting, discussed in Chapter 1, was reduced by placing the recording lens directly behind the holoplexes. In
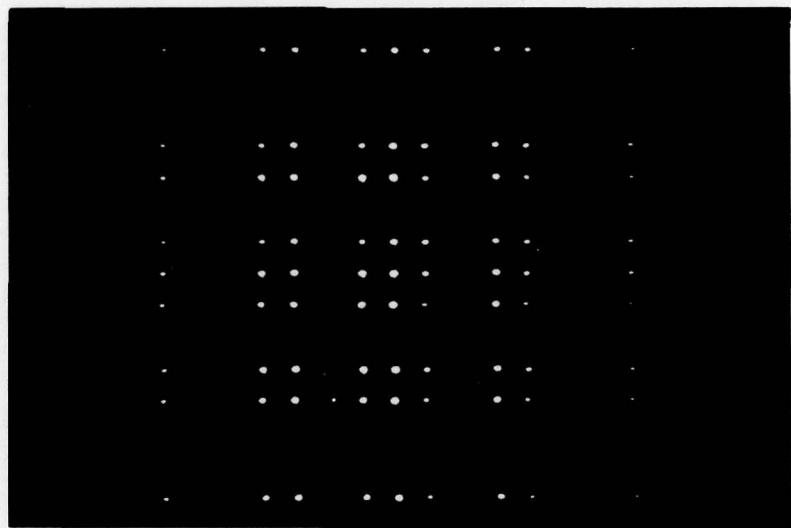
Figure 2-18.   Diffuserless 3 x 3 holoplex output for β = -1/3.
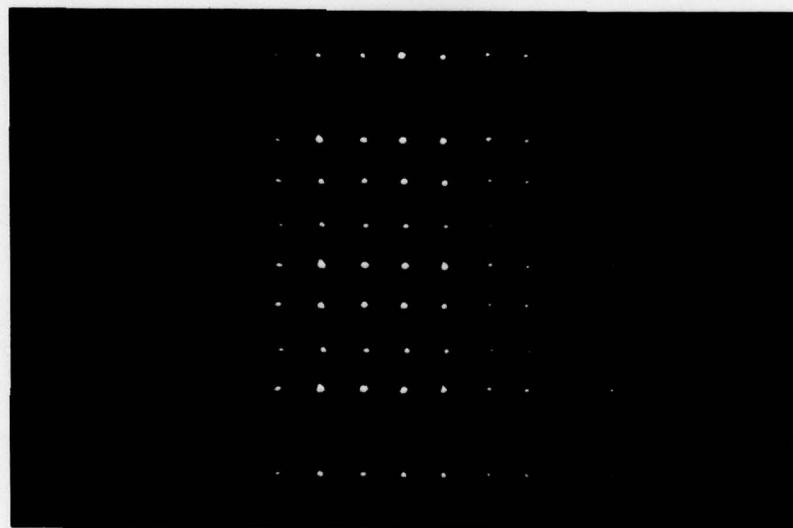
Figure 2-19.   Diffuserless 3 x 3 holoplex output for β = +1/3.

Figure 2-20.   Diffuserless 5 x 5 holoplex output for β = +1/3.
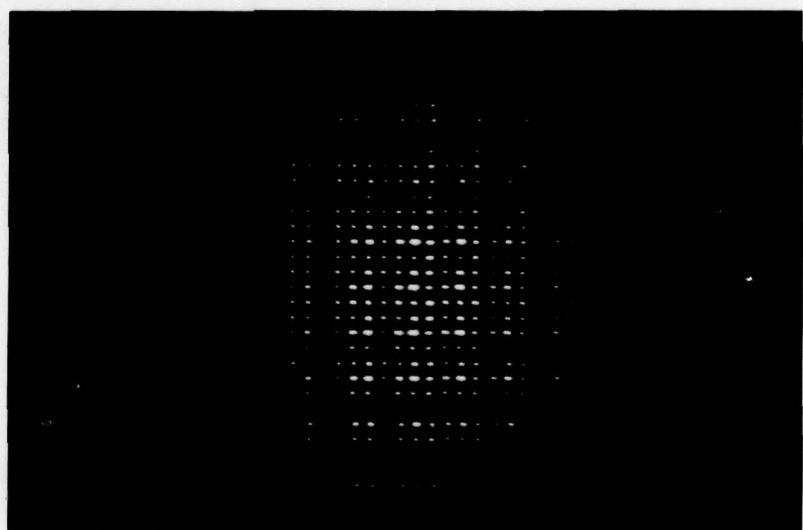
Figure 2-21. Diffuserless 5 x 5 holoplex output for β = -1/3.

large-array holoplexes such as these, however, some of the crosstalk is so distant from the center that it is still not possible to collect their light and bring it to focus. Crosstalk vignetting is not important, though, as long as the signal term array is not vignetted.

Figure 2-20 is the holoplex output for a 5 x 5 array, representing a magnifier having β = +1/3. This holoplex was recorded on Kodak 649-F emulsion, with individual hologram exposure times of 2 minutes. The 5 x 5 signal term array is located at the center. The amount of vignetting in this photograph may be appreciated when compared with its predicted graphical output seen in Fig. 2-7.

Figure 2-21 is the holoplex output for the same array, but with β = -1/3. Kodak 649-F emulsion was used for recording, with 2-minute individual exposure times. The graphical plot of this output shown in Fig. 2-8 tells us that a considerable amount of undesired energy has been redistributed out and away from the central 5 x 5 array of signal terms. Used with a diffuser, this holoplex would have a better overall signal-to-noise ratio than the holoplex in the previous figure. Vignetting was reduced in Fig. 2-21 by using a recording lens of shorter focal length, yielding a smaller image on film and thus bringing more of the crosstalk to focus.

of the fabrication of ground-glass diffuser plates is given in Appendix B.

In order to show the diffusion effects of ground glass on crosstalk more clearly, the holoplex outputs in this chapter will be those representing simple imaging systems only. The more complex space-variant processing operations using ground glass as a diffuser are deferred to Chapter 5.

All holoplexes in this chapter, with the exception of Fig. 3-6, were recorded using a diffuser plate ground with #80 grit, a relatively coarse grit (avg. particle size 180 μ). The autocorrelation of this plate is quite sharp, however, having a total width of only 20-30 μ [12, 16]. This width was estimated by the following simple procedure: the processed, repositioned holoplex was laterally displaced in the micropositioning plateholder until the output points extinguished. The micrometer reading at the exact point of extinction was recorded. Then, the holoplex was displaced in the opposite direction, past the position of maximum output point intensity, to the point where the output points extinguished again. The micrometer reading was recorded at this position, and the difference calculated. This difference gave a fair approximation to the width of the central autocorrelation peak for the #80 grit diffuser plate.

The degree of chirping was the same for all chirped holoplexes in this chapter. Recalling that $\alpha = \pi/\lambda d$, the wavelength for all the holoplexes was 514.5 nm., and the distance d from the reference point source array to the diffuser was 11 mm. Therefore, $\alpha = 5.55 \times 10^8$ m^{-2}.

Figure 3-1. 2 x 2 Ground-glass holoplex output, β = -1.5, #80 grit diffuser, chirped illumination.
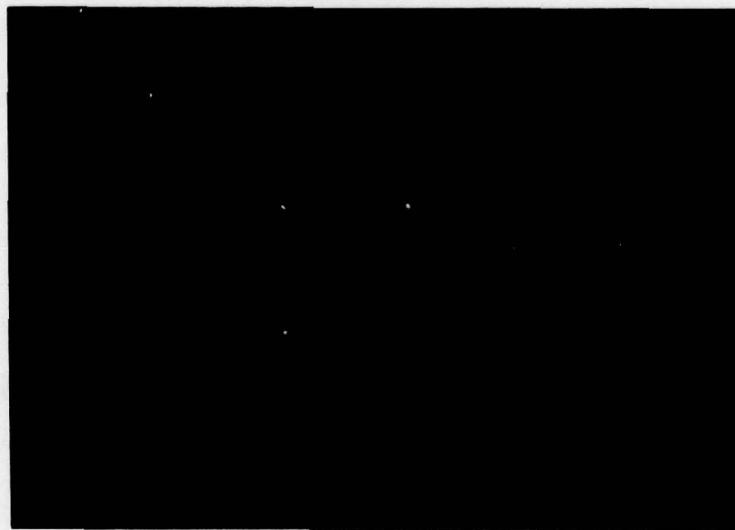
Figure 3-2. 2 x 2 ground-glass holoplex output, β = -1, #80 grit diffuser, chirped illumination.

achieved at 514.5 nm. However, when the playback wavelength was shortened to 488.0 nm. by readjusting the laser, the four signal terms vanished, with only the diffuse background noise remaining.

Figure 3-2 is the holoplex output for a magnifier having $\beta = -1$. Chirped-wavefront diffuser illumination and Kodak 649-F emulsion was used in recording this holoplex, with 60-second individual hologram exposure times. This output should be compared to the corresponding diffuserless output seen in Fig. 2-10. We see from Fig. 3-2 that the crosstalk points in Fig. 2-10 have been spread into faint, nebulous patches by the ground glass. The four signal terms are clearly visible, each surrounded by a similar fuzzy halo of light, this being part of the autocorrelation pattern of ground glass.

Figure 3-3 is the holoplex output for $\beta = -1/3$, and its corresponding diffuserless output is shown in Fig. 2-12. Chirped-wavefront diffuser illumination and Kodak 649-F emulsion were used for this holoplex, with individual hologram exposure times of 2 minutes. As in the preceding outputs, the crosstalk has been smeared out into the nebulous patches above, below, and to either side of the central array. The four signal terms are clearly visible, each being surrounded by its respective autocorrelation haze. The positions of the crosstalk patches are seen to coincide with those in Fig. 2-12, and when Fig. 3-3 is compared with Figs. 3-1 and 3-2, we see that the crosstalk patches are being displaced out and away from the signal term array with diminishing β, an effect well described in Chapter 2.

Figure 3-3.   2 x 2 ground-glass holoplex output β = -1/3, #80
grit diffuser, chirped illumination.
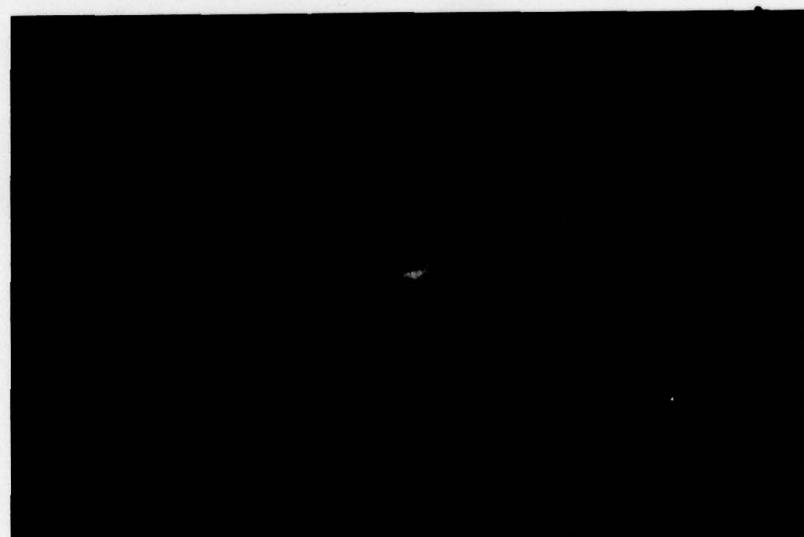
Figure 3-4.   100x enlargement of one single term in Fig. 3-1.

Figure 3-4 is presented to give an idea of the degree of optical quality attained in the recording and playback systems used in this project. This shows a roughly 100X magnification of one of the signal terms in Fig. 3-1. The ideal output point would be an Airy pattern whose first dark ring is 7.6 μ in diameter. The V-shape of the image seen here is due primarily to holographic coma and minor repositioning errors. The majority of the diffracted energy is concentrated inside a circle of roughly 15 μ in diameter; only twice the size of the ideal Airy pattern diameter. Figure 3-4 was recorded by projecting the image formed by the Fourier transforming lens with a 20x microscope objective, through a blackened tube and onto the film plane. The extremely faint image required a 15 minute exposure on Plus-X to record well. The optical quality achieved in this system may be appreciated by the fact that if simple "thin" lenses had been used for recording and playback, instead of the well-corrected lenses actually employed, the image blur spot, printed at the scale of Fig. 3-4, would not fit completely on the print. The on-axis spherical aberration, and astigmatism and coma off axis would produce an immense blur spot, in comparison to Fig. 3-4, with dimensions exceeding 500 μ or more. The use of high-quality, corrected lens systems, properly aligned, is strongly advised if the very finest performance is desired. As mentioned, Appendix A contains detailed information on how the recording/playback system performances were optimized.

Figure 3-5 shows the single-point playback of Fig. 3-1. Notice that when holoplexes are sequentially recorded, playing back any one
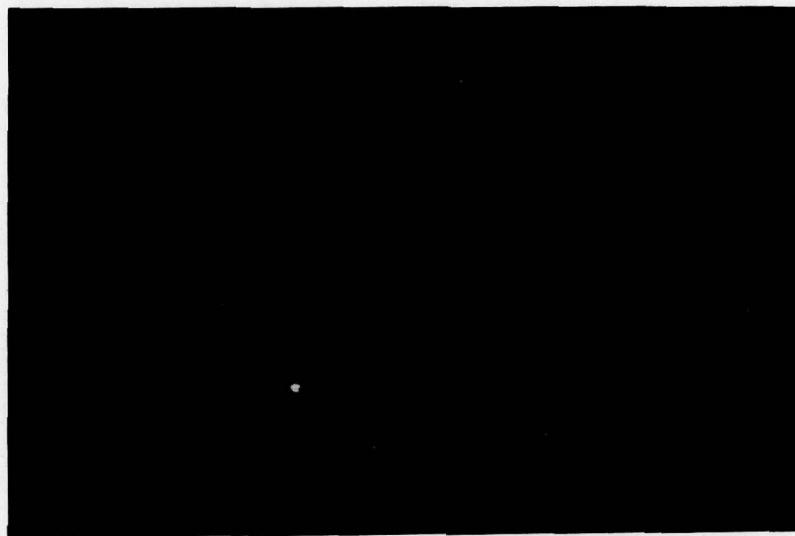
Figure 3-5. Single-point playback of Fig. 3-1.

Figure 3-6. 2 x 2 ground-glass holoplex output, β = -1.5,
#320 grit diffuser, chirped illumination.

reference point source accesses only one hologram, and only the single corresponding point appears, with its associated crosstalk, in the output plane. We will see an entirely different playback phenomenon in multiplex holography shortly.

Figure 3-6 is the output of a holoplex in which a diffuser plate ground with #320 grit was used, instead of the coarser #80 grit used in all other holoplexes in this chapter. The average particle size of #320 grit is 36 μ, and a glass plate ground with this grit has a total central autocorrelation peak width of only 10-12 μ, roughly half that produced by the #80 diffuser [12]. Repositioning of this holoplex was far more critical, and would certainly be impossible without some form of micropositioning plateholder. The system holoplexed was the -1.5x simple magnifier, using chirped-wavefront diffuser illumination and Kodak 649-F emulsion, with 2-minute individual exposure times. A comparison of this output with the output in Fig. 3-1 shows that the crosstalk diffusion with the #320 diffuser is much better, being fainter and more uniform than that produced by the #80 diffuser. Densitometer scans of the two outputs would be necessary to determine just what improvements in signal-to-noise ratios have been made by using the finer diffuser. From an experimental standpoint, however, the #80 diffuser is preferred, primarily due to its greater repositioning insensitivity.

Figure 3-7 shows one of the many surprises encountered in this project. It is the output of the 2 x 2 holoplex representing the standard -1.5x magnifier, with the #80 diffuser in place, using Kodak
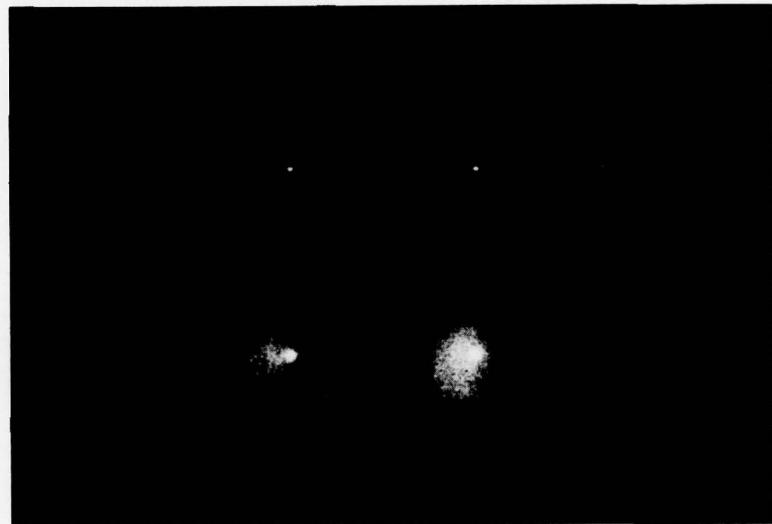
Figure 3-7. 2 x 2 ground-glass holoplex output, $\beta = -1.5$,
#80 grit diffuser, plane-wave illumination.

649-F emulsion and 2-minute individual exposures. The difference is
that plane-wavefront diffuser illumination was used when recording.
This was accomplished by simply removing the fly's eye array from the
reference beam path and using a cardboard mask with appropriately-
spaced holes to expose the individual holograms. The collimated
reference beam was simply incident directly on the diffuser. The
surprise in this output is the remarkable difference in the appear-
ance of the crosscorrelation, when compared to Fig. 3-1. Instead of
the smooth, nearly-uniform haze seen in Fig. 3-1, the crosscorrelation
has condensed into circular, non-uniform patches, each being centered
on the crosstalk locations seen in the diffuserless -1.5x magnifier
output shown in Fig. 2-9 [12]. The significance of this holoplex
is that the signal-to-noise ratio has deteriorated by using plane-
wave diffuser illumination even for as finely structured and random
a diffuser as ground glass. Again, densitometer scans would be
necessary to determine closely the degree of signal-to-noise degrada-
tion. Qualitatively, though, we see from Fig. 3-7 that both the auto-
correlation and crosscorrelation functions have shrunk somewhat and
become much brighter near their centers, with the increase in bright-
ness especially noticeable near the signal terms. Lens vignetting
is again to blame for the asymmetry; the two bottom groups are those
most accurately photographed.

Figure 3-8 through 3-11 present yet another unexpected phenomenon
in multiplex holography. These outputs contrast the striking differ-
ence in sequential and simultaneous recording. Both holoplexes were

Figure 3-8. 2 x 2 holoplex, β = -1/3, #80 grit diffuser, chirped-wave illumination, sequential recording simultaneous playback.

Figure 3-9. Single-point playback of upper left point in Fig. 3-8.

recorded with the same parameters: they both represent a -1/3x simple magnifier, they were both recorded using chirped-wavefront diffuser illumination and Kodak 649-F emulsion, and the #80 diffuser was used for both. The only difference is the recording technique. Figure 3-8 is a duplication of Fig. 3-3, which shows the simultaneous playback of this sequentially recorded holoplex. Figure 3-9 is the single-point playback of the upper left-hand signal term. We see but one signal term embedded in its autocorrelation noise, and the three fainter crosscorrelation patches associated with it.

Figure 3-10 is the output of the holoplex recorded simultaneously, with all four signal terms played back simultaneously. The single exposure given the plate was only 20 seconds. We see the four signal terms at center, surrounded by a very bright autocorrelation haze. The diffuserless, simultaneously-recorded, 2 x 2 holoplex output shown in Fig. 2-17 should be referred to for comparison. The 12 spurious points of light that surround the 4 signal terms are unique, and appear only in simultaneously recorded holoplexes. The four corner points are very faint and may not be clearly visible in the halftone reproduction. The other 8 are brighter and of the same magnitude, and are equally spaced around the four signal terms. Simultaneous, as opposed to sequential, recording has permitted all 12 spurious points to elude suppression by the ground glass diffuser.

Figure 3-11 shows the most unexpected property of simultaneously recorded holoplexes observed in this project. This is the single-point playback of the upper left-hand signal term, as in Fig. 3-9.
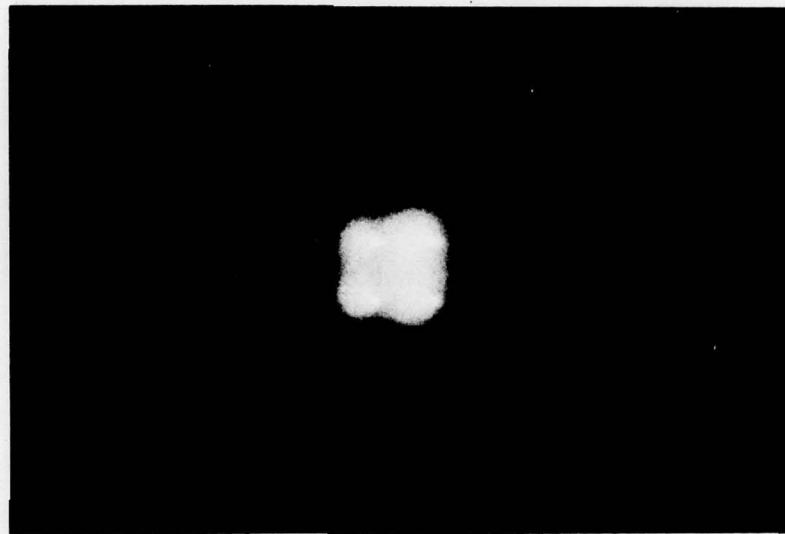
Figure 3-10. 2 x 2 holoplex $|\beta|$ = 1/3, #80 grit diffuser, chirped-wave illumination, simultaneous recording, simultaneous playback.

Figure 3-11. Single-point playback of upper left point in Fig. 3-10.

But instead of the single signal term playing back, we see all four!
In addition, all 12 spurious points play back as well. The explanation
is simple: in playing back simultaneously recorded holoplexes, any
one term acts as a reference beam for all the other terms. However,
in Fig. 3-11 the crosstalk failed to play back in its entirety, as
in Fig. 3-10, with only the upper left-hand patches being visible.
It is apparent that the crosstalk, at least, is associated with in-
dividual holograms in a simultaneously recorded holoplex. Figure 3-11
dramatically substantiates the fact mentioned in Chapter 2, that
simultaneously recorded holoplexes are useless for 2-D space-variant
optical system representation. The sequential recording method takes
much more time, comparatively, but at least yields the desired form
of representation.

At this point we move on from the 2 x 2 array to larger arrays.
Two were exposed, to gain necessary information for proceeding on to
large arrays representing space-variant processing operations more
complex than the simple magnifiers.

Figures 3-12 and 3-13 show the simultaneous and single-point
playback, respectively, of the 3 x 3 sequentially recorded holoplex
representing a simple magnifier having $\beta = +1/3$. The #80 grit dif-
fuser was used, illuminated by a chirped wavefront. Kodak 649-F
emulsion was used, with 2-minute individual exposures. This output
should be compared to that of Fig. 2-19, in which no diffuser was
used. As usual, the 9 desired signal terms are clearly visible in
Fig. 3-12, with the crosscorrelation haze surrounding them. Fig.
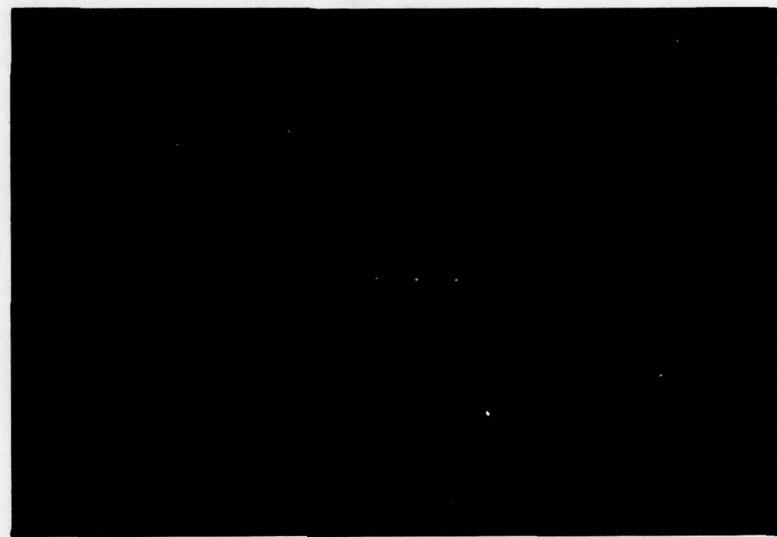
Figure 3-12. 3 x 3 ground-glass holoplex output, β = +1/3,
#80 grit diffuser, chirped illumination, sequential
recording, simultaneous playback.
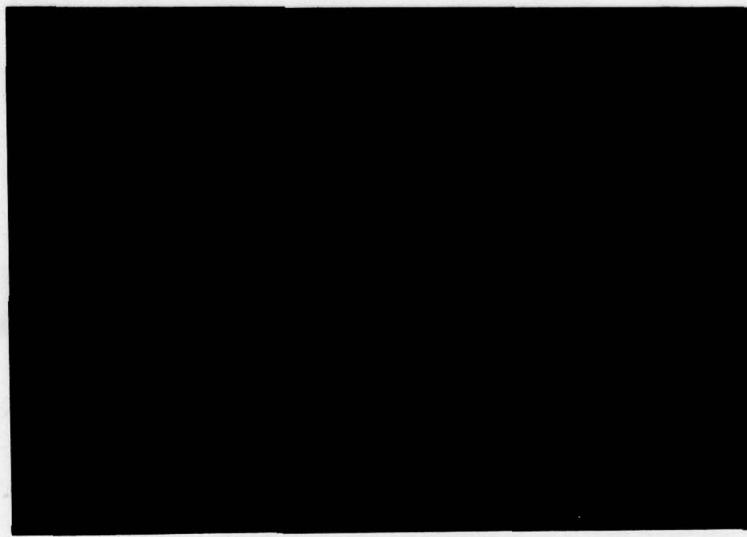
Figure 3-13. Single-input playback of middle right-hand term in
Fig. 3-12.

3-13 shows the single-point playback of the middle right-hand term. The associated crosscorrelation may be seen above, below, and to the right of the signal term. It should be mentioned that the sum of the nine individual exposures darkened the plate only to the extent of about an ND 0.2 or ND 0.3 filter, yet the holoplex played back brightly.

Figures 3-14 and 3-15 are the simultaneous and single-point playbacks, respectively, of a sequentially recorded 5 x 5 holoplex representing the simple unity magnifier, where $\beta = 1$. A problem first encountered with this holoplex was that of reference beam non-uniformity. In Fig. 3-14 we see only 17 out of 25 signal terms playing back. This time lens vignetting was not to blame. The collimated laser beam had roughly a Gaussian profile, and previously all smaller arrays had been exposed in the relatively uniform central portion of this beam. The 5 x 5 array, however, had large enough dimensions that nearly the entire 2" beam diameter was necessary to illuminate it. Intensity fall-off at the outer portions of the beam was estimated, after examining this holoplex, at greater than 2 photographic stops. Exposure time compensation was in order, but to conserve plates it was decided to delay shooting another 5 x 5 until a more complex 2-D space-variant processing operation could be devised. This output appears in Chapter 5, along with data about exposure compensation.

The 10-minute overall exposure time for the holoplex in Fig. 3-14, made on Kodak 131-02 emulsion, gave a density of approximately ND 0.7, somewhat darker than desired for only 25 exposures. A reduced overall

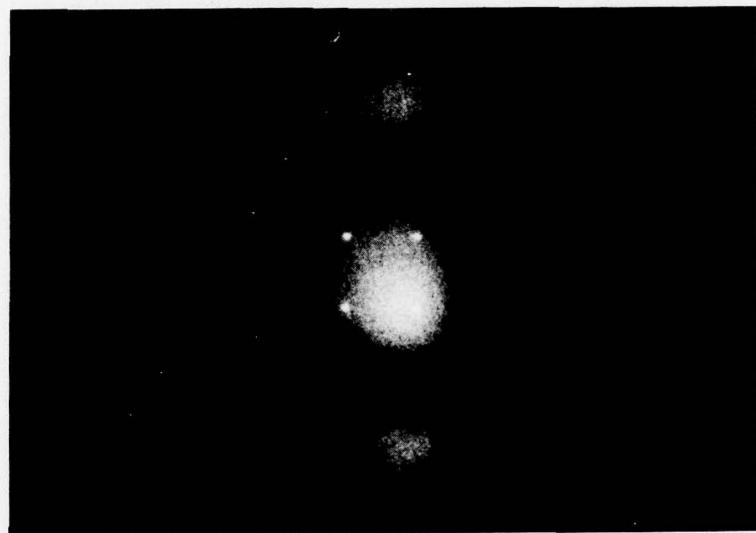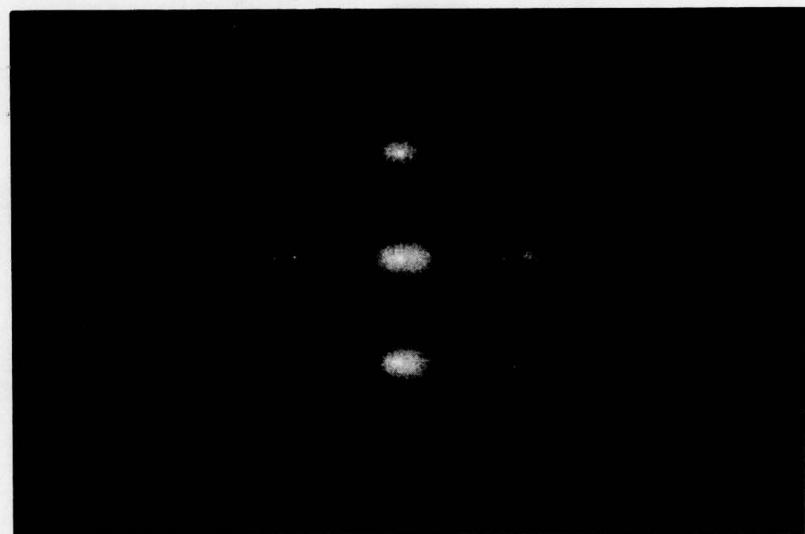Figure 3-14.   5 x 5 ground-glass holoplex output, β = 1.0, #80 grit diffuser, chirped illumination, sequential recording, simultaneous playback.
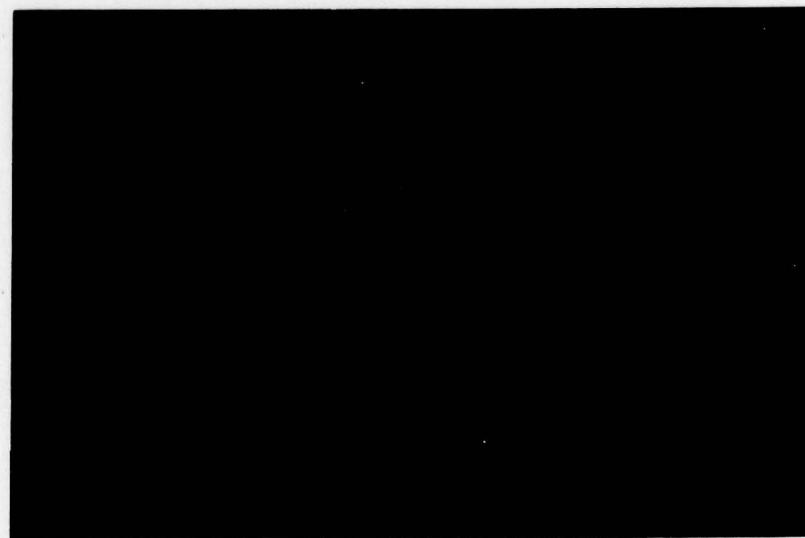
Figure 3-15.   Single-point playback of signal term 14 in Fig. 3-14.

exposure was necessary if the anticipated 10 x 10 holoplex was to be successful. A density of as much as 1.2 could be tolerated, but for any greater density the holoplex would have to be bleached in order to see the playback. From experience, bleaching multiplexed holograms typically reduces their sharpness and lowers the signal-to-noise ratio, due to increased scattering. It is preferable to tailor the individual exposure times so that each hologram is recorded well, without over-exposure, and the sum of all the exposures does not produce a density greater than about 1.0 or 1.2, so that bleaching is unnecessary.

Figure 3-15 is the single-point playback of signal term 14, if we number the array by rows. As this is the unity magnifier, the crosstalk is nearly superimposed on the signal term and thus no additional patches are observed. This is obviously not the ideal signal-to-noise situation, but for this holoplex the crosstalk distribution was of no concern. It was merely desired to determine at least a rough estimate of the proper exposures necessary for these larger array sizes. As may be seen, no other signal terms are playing back in this photo.

In this chapter we have explored a wide variety of recording and playback situations in multiplex holography using ground glass diffusers, and observed the merits and faults of each. The differences in using plane and chirped wavefronts for diffuser illumination were presented and discussed, and the superiority of chirped wavefront illumination, even for ground glass diffusers, was demonstrated. The improved crosstalk suppression and increased repositioning difficulties involved when using a ground glass diffuser

having an extremely fine grind were discussed. Sequential and simultaneous recording using a ground glass diffuser was contrasted, and first efforts at large-array holoplexes using ground glass diffusers were presented. In the next chapter many of the same recording and playback situations will be applied to binary-coded diffusers, in order to evaluate their relative usefulness in crosstalk suppression.

CHAPTER 4

HOLOPLEX OUTPUTS USING BINARY-CODED DIFFUSERS

4.1. Discussion of Binary Diffuser Masks in General

The computer-generated binary diffuser mask has received a con-
siderable amount of analytical attention in recent work [4, 5, 7-10].
Experimental implementation [11, 12] of these binary masks for use
in 2-D space-variant optical system representation has been limited,
however, primarily because only relatively crude binary diffusers
have been fabricated so far. The outputs presented in this chapter
show the results obtained with these initial masks.

A typical mask used in this project is shown in Fig. 4-1. The
masks are 128 x 128 cell, and the technique by which they are gener-
ated is described in detail by Redus [4]. These masks have the de-
sirable property of being perfectly deterministic; the binary psuedo-
random sequences from which they are generated (Gold Codes [9] in this
instance) may be stored in their entirety in any large computer
memory for analysis. The masks are characterized by sharp, narrow,
bounded autocorrelation functions and broad, relatively flat, low-
level crosscorrelations, at least in theory. They have the major
drawback that they are extremely time-consuming to prepare and fabri-
cate for use as diffusers. A large amount of computer time is neces-
sary to numerically generate them, and each mask must then be plotted,
typically requiring over an hour per mask. Then, the individual masks
must be spaced and oriented properly, and photoreduced to the proper

67
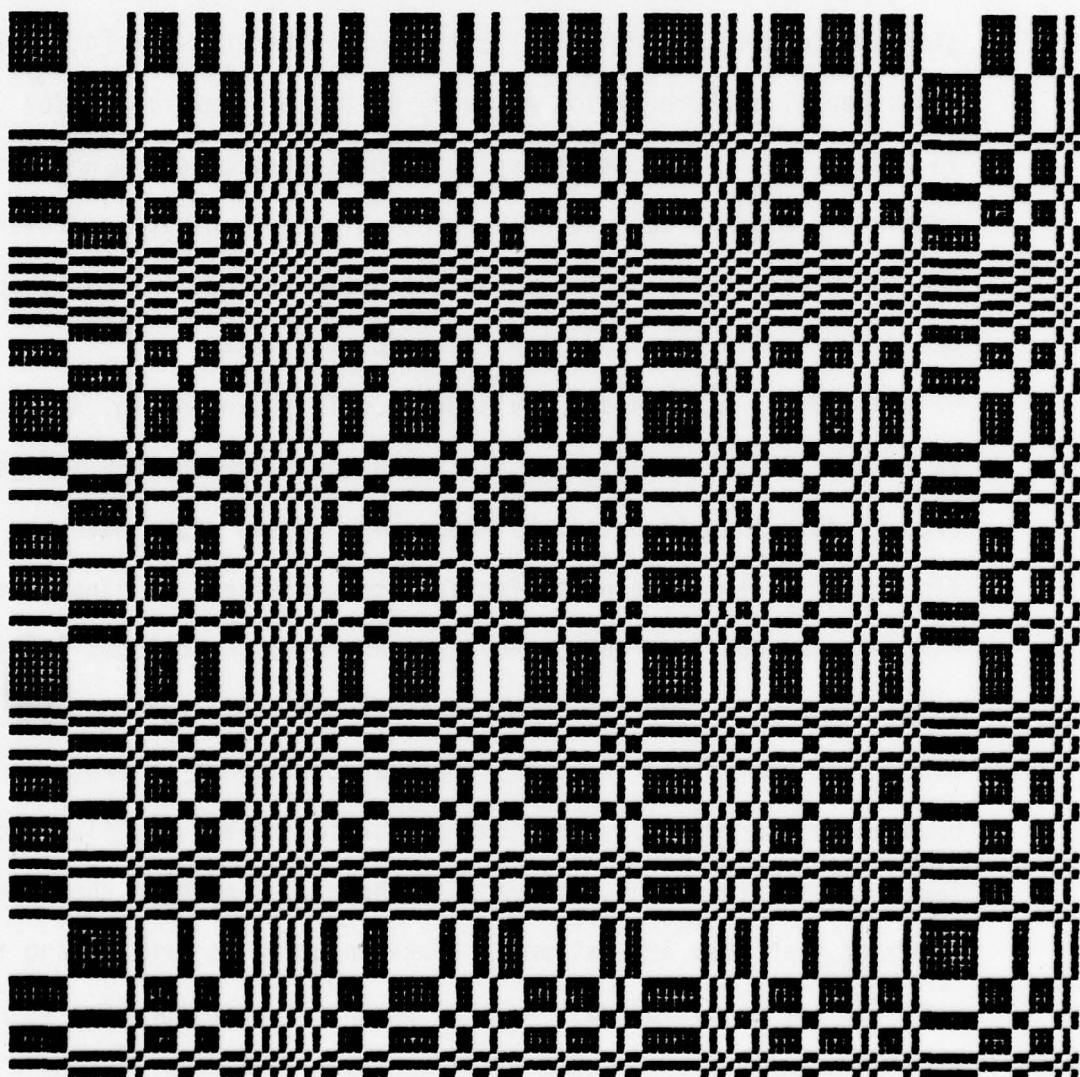
Figure 4-1. Typical 128 x 128 computer-generated binary-coded
diffuser mask, plotted and ready for photoreduction.

dimensions. This produces an amplitude master, which in itself is not a bad diffuser. Several outputs in this chapter are those in which the amplitude master was used as the diffuser. However, to improve light efficiency and correlation properties [8], a binary phase diffuser ideally having a phase shift of 0 or π must in some manner be contact-printed from this amplitude master.

The technique used to produce the one marginally satisfactory phase diffuser used in this thesis is described by Redus [4]. Briefly, the method consisted of coating a spinning disk of clean glass with a thin layer of liquid photoresist, hoping that the spinning would produce a resist film of uniform thickness. Using an exposure pre-viously determined to produce a π phase shift (at λ = 514.5 nm.) in the resist's surface, the amplitude master was contact-printed onto the resist, which is then developed. Major problems of this method were (1) non-uniformity of the basic resist film, and (2) unsharp boundaries between the regions of 0 and π thicknesses. Although the overall shift in the one binary phase diffuser fabricated was roughly π, its boundaries were jagged and had finite width, easily visible under a 70x microscope.

The masks were photoreduced to squares 0.140" on a side, with centers 0.300" apart, thus using every other fly's eye lenslet. In-ternal reflection within the fly's eye array made this necessary; when one lenslet was illuminated, the four adjacent lenslets would "turn on" as well, with obvious adverse effects. Skipping over one lenslet eliminated this problem. Reducing the squares to 0.140" made them

the same size as the individual fly's eye lenslets. Each diffuser had 128 x 128 cells, therefore each cell was 0.14/128 = .00109", or 27.7 μ on a side. It was thought that this degree of reduction would be sufficient for good crosstalk suppression. However, as we shall see in the outputs that follow, further reduction would be desirable. The minimum individual mask dimensions, though, are ultimately limited by diffraction (provided the film resolution is sufficient), due to the finite clear aperture of the photo-reduction lens. The camera lens used for photoreduction in this project gave its sharpest imaging at an aperture of f/5.6 to f/8. If we set the photoreduction lens at f/5.6, and photoreduce the masks using incoherent light (i.e. daylight or tungsten illumination) having its peak intensity at, say, 550 nm., the lens' incoherent cutoff frequency f_I may be calculated as follows [14, 15]:

$$f_I = \frac{1}{\lambda(f/\#)} = 0.3247 \text{ cycles/micron}$$

and

$$S_I = 1/f_I = 3.08 \text{ μ},$$

where S_I is the spatial period at cutoff. However, f_I is the maximum spatial frequency passed by the lens; to sharply image a diffuser cell the lens must pass a fundamental sinusoidal spatial frequency 3-5 times lower than f_I. If we desire a very crisp, sharp set of masks the mask should have a fundamental frequency of no more than $f_I/5$. Therefore the minimum cell size would be $5S_I$, or 15.4 μ, giving an overall individual mask dimension of 128(15.4 μ) = 1.971 MM., or

0.0776". This is roughly half the size of the masks used in this thesis. Crosstalk dispersion using these smaller masks would there-fore be about twice that obtained with the masks in this thesis. An added benefit from using these smaller masks is that a greater degree of chirp could be given to the illuminating wavefronts, as the masks could be placed much closer to the focal plane of the fly's eye array. As we have seen, the greater the amount of chirp, the better the crosstalk suppression. Even smaller masks would be desirable, but to maintain individual cell sharpness we must increase the aper-ture of the photoreducing lens (i.e., lower the f/#). Unfortunately, this is usually accompanied by an increase in optical aberrations, and unless the lens is particularly well-corrected it may be necessary to revert to a smaller aperture. Ultimately, diffraction and aberrations may prohibit the reduction of the cell scale in binary diffusers to that of ground glass, if the cells are to remain sharply defined. To achieve the scale of ground glass and simultaneously preserve cell sharpness it may be necessary to use an entirely different form of mask fabrication, such as the electron-beam techniques used in inte-grated circuit technology, and dispense with optical recording methods altogether. The importance of sharp edges and boundaries in binary diffuser cell structures is not clearly understood at this time, but it is suspected that the sharper the cell structure, the better the dispersion and suppression properties will be. The amplitude master masks used in this thesis were very sharp, despite their coarse structure, and in the outputs that follow we shall see several

examples of their diffusing properties.

4.2. Holoplex Outputs Using Binary Diffuser Masks

Figures 4-2 and 4-3 are the simultaneous and single-point play-backs of a sequentially-recorded holoplex representing the simple -1.5x magnifier. The binary phase diffuser described was illuminated with a chirped wavefront having the same curvature as that used in Chapter 3. The emulsion used was Kodak 649-F, with each hologram receiving a 90 sec. exposure. The location of the crosstalk is obvious in Fig. 4-2. Because the crosstalk has not been dispersed as much as with ground glass, lens vignetting is not as noticeable here. In Fig. 4-3 the brightest patch is the signal term, embedded in diffuser auto-correlation noise, and the three fainter terms are crosscorrelation terms. Again, an array of smaller diffusers, having a 15 μ cell size instead of the 28 μ size used for this holoplex, would provide sub-stantially better dispersion.

Figure 4-4 is the output of a 2 x 2 holoplex in which the ampli-tude master was used for the diffuser, instead of the phase mask copy. All other conditions are the same as for Fig. 4-2. We see that the degree of spreading in all the output terms is greater than in Fig. 4-2. As mentioned earlier, this was a particularly sharp amplitude master; all individual cells in each of the four diffuser masks were sharp and distinct when examined at 100x. The exposure was good, as the cells that were supposed to be clear were quite transparent, and the cells that were supposed to be black were virtually opaque. Cross-talk diffusion is poor here, a condition that again could be improved

Figure 4-2. 2 x 2 binary-coded holoplex output, β = -1.5, 128 x 128 binary phase diffuser masks, chirped illumination, simultaneous playback.

Figure 4-3. Single-point playback of the lower right-hand term in Fig. 4-2.

Figure 4-4. 2 x 2 binary-coded holoplex output, β = -1.5, 128 . 128 binary amplitude diffuser masks, chirped illumination, simultaneous playback.
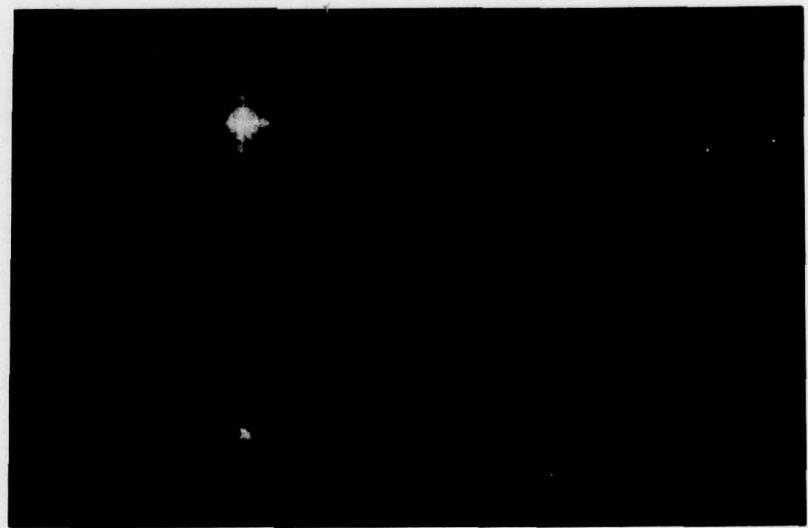
Figure 4-5. Enlargement of lower right-hand term and crosstalk in Figure 4-4.

by a greater photoreduction of the masks. A small angular rotation of the holoplex, unnoticed while recording the output, has caused some of the columns in Fig. 4-4 to playback with asymmetric brightness.

The angular rotation was corrected in Fig. 4-5, which shows an enlargement of the lower right-hand signal term in Fig. 4-4, plus its associated crosstalk. The signal term is at upper left, embedded in the autocorrelation noise of the diffuser. The crosstalk terms at right and below are fainter, and have the same general structure as the autocorrelation. No bright signal term appears at their centers, however. Repositioning accuracy was not critical for this or any of the other holoplexes in the chapter (with the exception of the next holoplex to be described). Lateral displacement of as much as 250 μ from nominal could be tolerated before the signal term extinguished. Again, with finer diffusers, this repositioning tolerance would drop drastically, accompanied by an overall improvement in crosstalk suppression.

Figure 4-6 shows the remarkable difference that plane-wave diffuser illumination can make. This holoplex was recorded under exactly the same conditions as Fig. 4-4, except that each individual hologram was given a much shorter exposure. The fly's-eye array was removed from the reference beam path, and a movable cardboard mask was used for individual hologram exposures. The 2 x 2 binary amplitude master was used as the diffuser, as in Fig. 4-4. The 2 x 2 array of signal terms is located at the intersections of the "tic-tac-toe" lines,
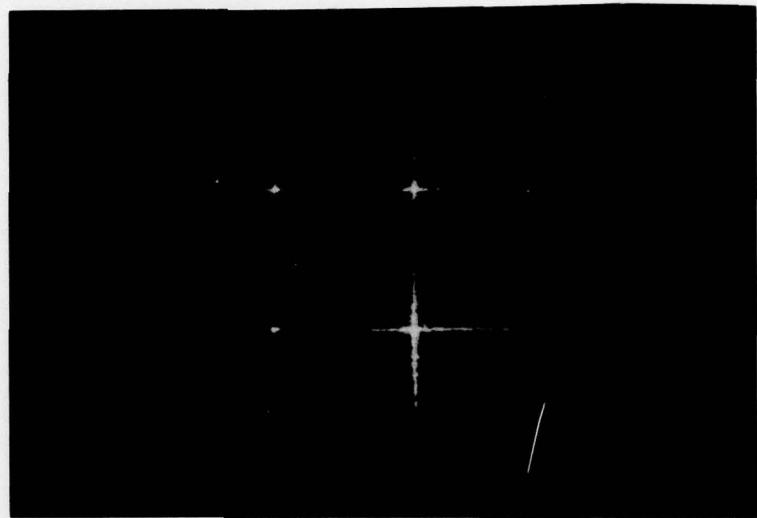
Figure 4-6. 2 x 2 binary-coded holoplex output, $\beta = -1.5$, 128 x 128 binary amplitude diffuser masks, plane-wave illumination, simultaneous playback.
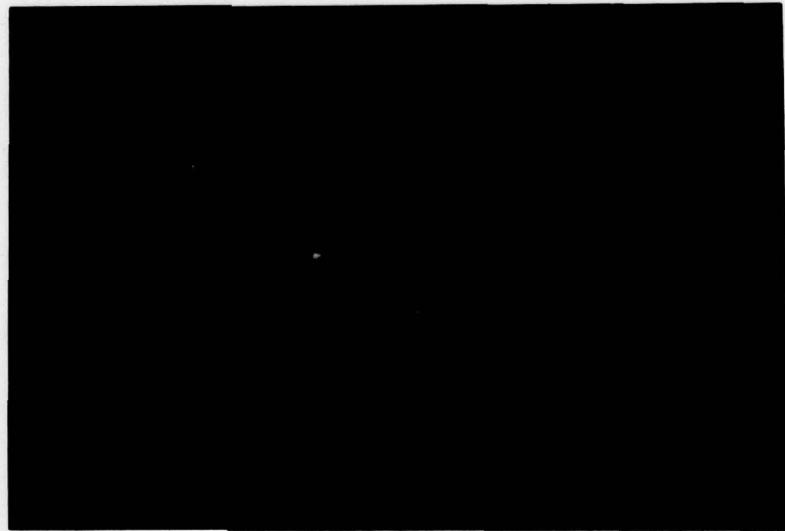
Figure 4-7. Enlargement of lower right-hand term and crosstalk in Fig. 4-6.

and the crosscorrelation manifests itself in the striated haze visible
to the right. Lens vignetting is again to blame for the output
asymmetry, and the recording lens was positioned to intercept as
much of the crosscorrelation haze as possible [12]. We see that the
signal-to-noise ratio has significantly deteriorated along the hori-
zontal and vertical lines, in contrast with Fig. 4-4, but improves
somewhat away from these lines. The output in Fig. 4-6 clearly veri-
fies previous theoretical work by Redus [4] and Krile [9], in which
it was shown that plane-wave illumination is inferior to chirped-
wave illumination for crosstalk suppression in multiplex holography.

It is interesting to note in passing that the repositioning tol-
erance for this plane-wave holoplex was extremely small. The output
points extinguished with only 10 μ of lateral displacement, which im-
plies that this holoplex had the equivalent autocorrelation width of
ground glass. Evidently chirping increases the scale in the Fourier
plane, and as LaMacchia and White pointed out [16], if the Fourier
spectrum of the diffuser is coarse the replacement tolerance is re-
laxed. Chirping therefore not only improves the crosstalk suppression,
but makes it much easier to reinsert the processed holoplex and achieve
full playback.

Figure 4-7 is an enlargement of the lower right-hand signal term
in Fig. 4-6. A slightly shorter exposure was used so that the signal
term could be more clearly seen. Remembering that for the -1.5x magni-
fier the signal term is merely a minute Airy pattern not resolvable
at this printing scale, the term is located at the intersection of

the horizontal and vertical lines. The striated crosscorrelation
haze is seen to the right of the vertical lines. The paradox of this
output is that no distinct crosstalk is visible in Fig. 4-7, in con-
trast with Fig. 4-5, and yet the signal-to-noise ratio is worse. A
considerable amount of energy is contained in the horizontal and verti-
cal lines, which leads to the poorer signal-to-noise ratio. The
emulsion used for this holoplex was Kodak 649-F, and the individual
hologram exposure times were 10 seconds, much shorter than for Figs.
4-2 or 4-4, due to a smaller, more intense concentration of reference
beam illumination.

Figure 4-8 shows the output for a 3 x 3 holoplex representing
the simple magnifier for $\beta = +1/3$, using a 3 x 3 array of binary-
amplitude computer-generated masks as diffusers, and chirped-wave-
front diffuser illumination. The emulsion used for recording was Kodak
649-F, with individual exposure times of 2 minutes. The amplitude
master mask used for the diffuser was of poor quality; the individual
cells were sharp and distinct at 100x, but some of the masks were
underexposed, due to uneven lighting during photoreduction. Cells
in the binary masks that were intended to be opaque simply were not.
The output is included here primarily to show the initial effort
in making holoplexes using larger arrays of binary diffusers. Al-
most no dispersion of crosstalk is visible in Fig. 4-8, and at the
scale shown, this output is virtually identical in appearance with
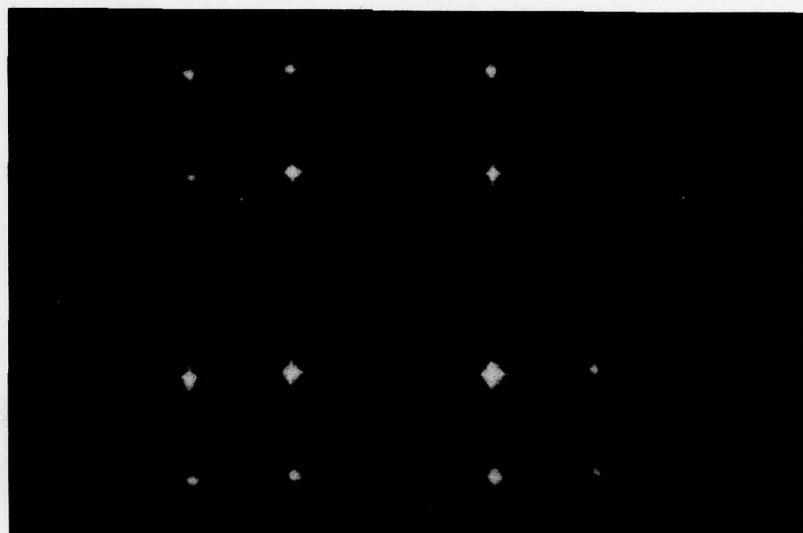Fig. 2-19, in which no diffuser was used.
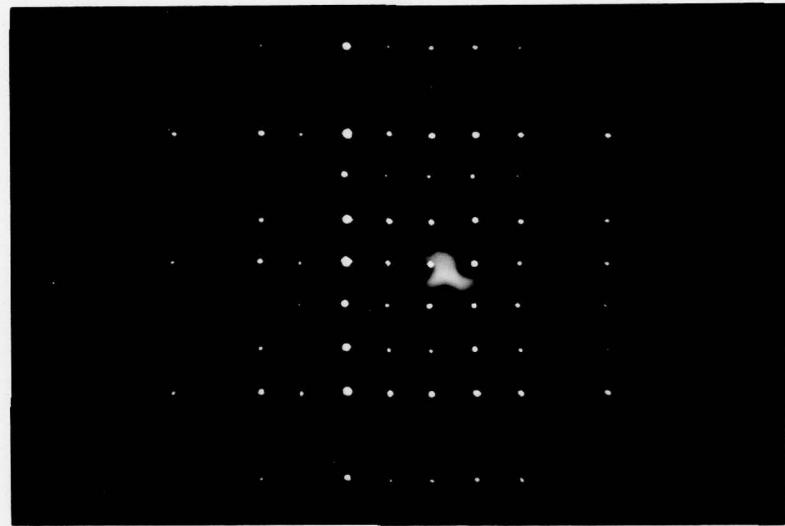
Figure 4-8.   3 x 3 binary-coded holoplex output, β = +1/3,
128 x 128 binary amplitude diffuser masks,
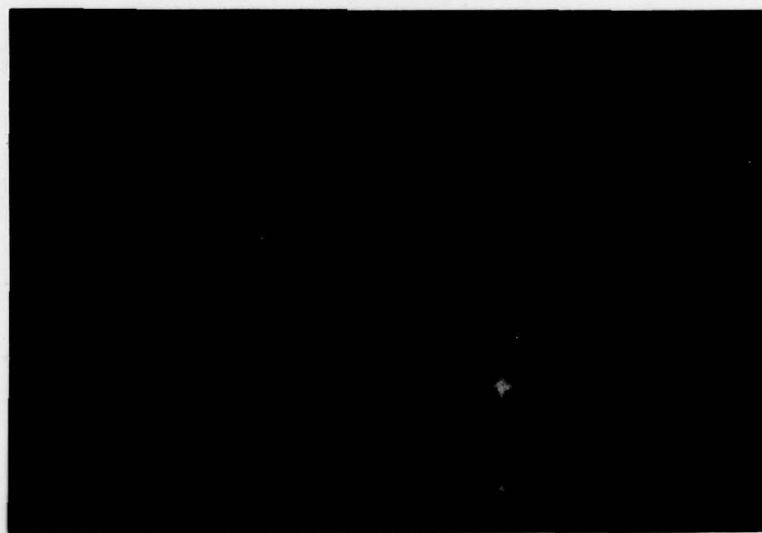chirped illumination, simultaneous playback.

Figure 4-9 shows a 7.3x enlargement of a portion of Fig. 4-8. The signal terms are indicated by arrows, and correspond to elements 1 and 4 in the 3 x 3 signal term array at center in Fig. 4-8. Some spreading is now visible in both the signal terms and in the crosstalk to their left. It may be seen that the general structure and degree of spreading is similar to the enlargement in Fig. 4-5.

Figure 4-10 shows something not previously seen in this thesis, that of the single-point playback of a 3 x 3 holoplex. The signal term played back was element 4 in Fig. 4-8, and is designated by the arrow. The other 8 patches are the crosstalk terms associated with that particular signal term.

Since this holoplex was recorded using chirped-wave diffuser illumination, the repositioning tolerance was loose, comparable to that of the 2 x 2 holoplexes in Figs. 4-2 and 4-4. Again, an array of smaller, properly-exposed masks would provide substantially better dispersal and suppression of crosstalk than was experimentally obtained in this project. The importance of a sharp, properly-exposed set of amplitude master masks cannot be overemphasized.

The anomalies shown in Figs. 4-11 and 4-12 are presented here for historical reference. In a previous paper by Krile et al. [8], before our experiments using ground glass or binary diffusers, shower stall glass, the kind having ornate floral designs on one side and a smooth, translucent surface on the other, was used as a diffuser. This "shower glass," as it is generally known, provided almost totally a phase encoding of incident light fields, with very little amplitude
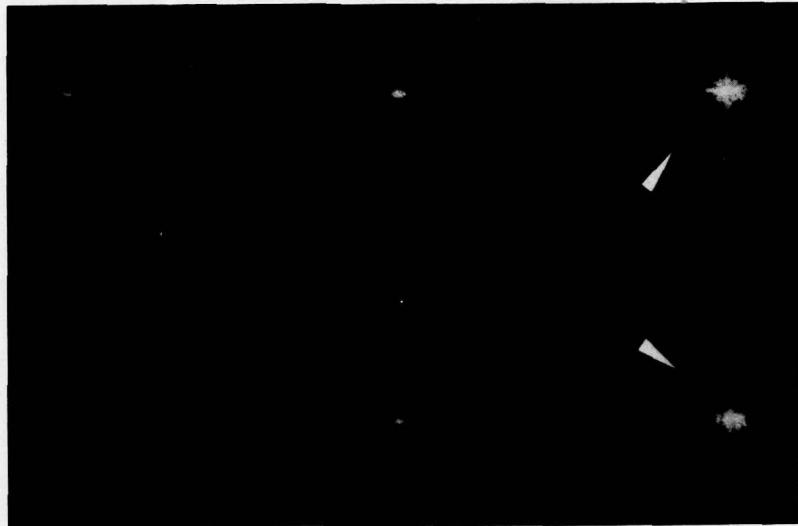
Figure 4-9. 7.3x enlargement of elements 1 and 4 in central single term array of Fig. 4-8. Single terms are indicated by arrows.
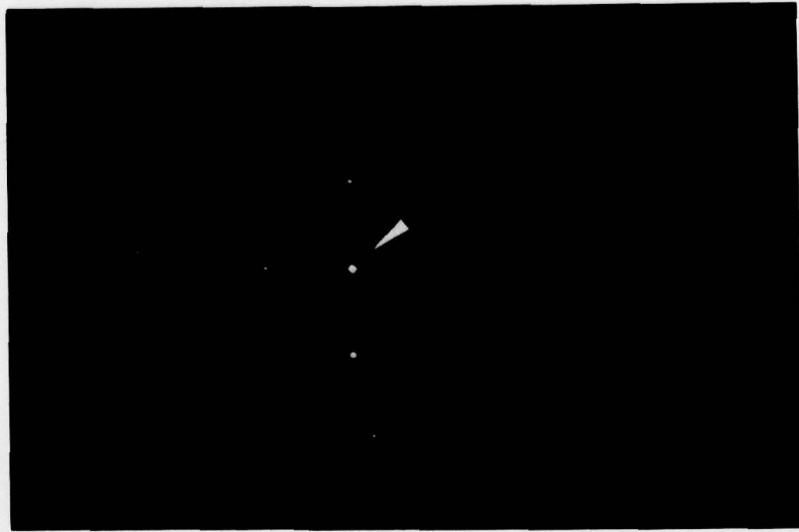
Figure 4-10. Single-point playback of element 4 (indicated by arrow) in Fig. 4-8. The other 8 terms are the crosstalk terms associated with that signal term.

encoding. Shower glass was characterized by very broad, floral-like autocorrelations, and crosscorrelations nearly as attractive. It could, though, provide some limited crosstalk suppression if a suitably rippled area was used for diffusion, as demonstrated by Krile et al. [8]. However, if used as a generalized diffuser in a larger array, with no attention being paid to its particular placement in the reference beam, the shower glass provides very poor crosstalk dispersion, as shown in Figs. 4-11 and 4-12.

Figure 4-11 is the output of a 2 x 2 holoplex representing the standard -1.5x magnifier used for comparison throughout this thesis. The shower glass diffuser was illuminated with chirped wavefronts, and as mentioned, no particular attention was given to the placement of the diffuser in the reference beam. It is impossible to discern the signal terms in this rather confusing output, so the negative was reprinted with arrows, shown in Fig. 4-12, which point to the signal terms. The motivation for exposing this holoplex was simply curiosity; it was desired to see how the shower glass diffuser, used in previous experimentation, fared in comparison to the newer binary and ground glass diffusers.

In summary, the ground glass diffuser is still by far the best form of diffuser implemented to date, but the binary diffusers are promising. If solutions to the fabrication and reduction problems mentioned earlier in this chapter are found, it should be possible to reduce the scale of the binary diffuser to that of ground glass, and maintain the individual cell sharpness as well. The performance
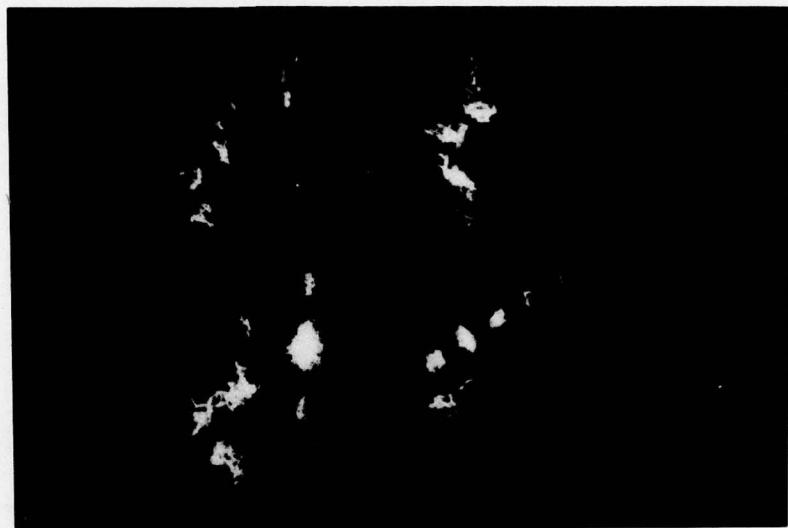
Figure 4-11.   2 x 2 shower-glass holoplex, β = -1.5, shower-glass diffuser, chirped illumination, simultaneous playback.

Figure 4-12.   Duplication of Fig. 4-11, including arrows indicating location of signal terms.

of the binary diffuser would then equal or even surpass the ground
glass diffuser, and allow the binary diffuser to reach its full
potential.

CHAPTER 5

ADDITIONAL EXPERIMENTAL RESULTS

5.1. Preliminaries

In the previous chapters we have explored a wide variety of re-
cording and playback situations in multiplex holography. The optical
systems holographically represented have been simple and the array
sizes have been small so that the differences in each of the holo-
plexes, when certain parameters were varied, would be easily discernable.
The variable parameters included wavefront curvature, diffuser type,
and form of optical system represented. From the many holoplexes
recorded it was determined that the combination of ground glass and
a chirped-wave diffuser illumination provided the optimum method of
crosstalk suppression. The next logical step in the project was to
use this diffuser-wavefront combination in the actual holographic
representation of a non-trivial 2-D space-variant optical system, and
to represent a simpler optical system with a very large array of
sampling points. In this chapter we will see these two outputs,
along with pictures and descriptions of the equipment used to record
them. First, however, we will examine a necessary requirement in
this particular application of multiplex holography, and prove that
it has indeed been satisfied.

5.2. Coherent Addition in Multiplex Holography

When representing space-variant optical systems using multiplex
holography, a necessary requirement is that all of the holographic

outputs that overlap each other add coherently, in phase. If this requirement is met, the expression

$$t = \sum_{i=1}^{n} |H_i + R_i|^2$$

is valid, where t is the amplitude transmittance of the region of total overlap on the finished holoplex, and n, as usual, is the total number of holograms. Up to this point the question of coherent addition was ignored, because imaging systems, such as the magnifiers represented in previous chapters, basically carry input plane sample points into point-like outputs that usually do not overlap. Coherent addition is therefore not usually required to represent imaging systems. Coherent addition is required, however, to represent general space-variant systems.

To demonstrate coherent addition, a simple interferometric experiment was performed. The simplicity of this method lies in the fact that only two overlapping holograms need be made. The recording setup is schematically shown in Fig. 5-1. The basic idea is to sequentially record with two reference beams, shown as 1 and 2 in the figure, the same, stationary object beam. Two overlapping holograms are thus multiplexed together on the plate P. Their crosstalk is suppressed by the #80 grit ground-glass diffuser, D, illuminated by chirped-wave illumination having the standard (previously used) curvature $\alpha = 5.55 \times 10^8 \ M^{-2}$. The single object point source is denoted as δ_0 in the figure, and the two reference point sources are denoted as δ_1 and δ_2. As usual, lenses L_1 and L_2 perform Fourier transforms.

1.0

1.1

1.25 1.4 1.6

4.5
5.0
5.6

2.8 2.5
3.2
3.6 2.2
4.0 2.0

1.8

MICROCOPY RESOLUTION TEST CHART
NATIONAL BUREAU

87 at top right
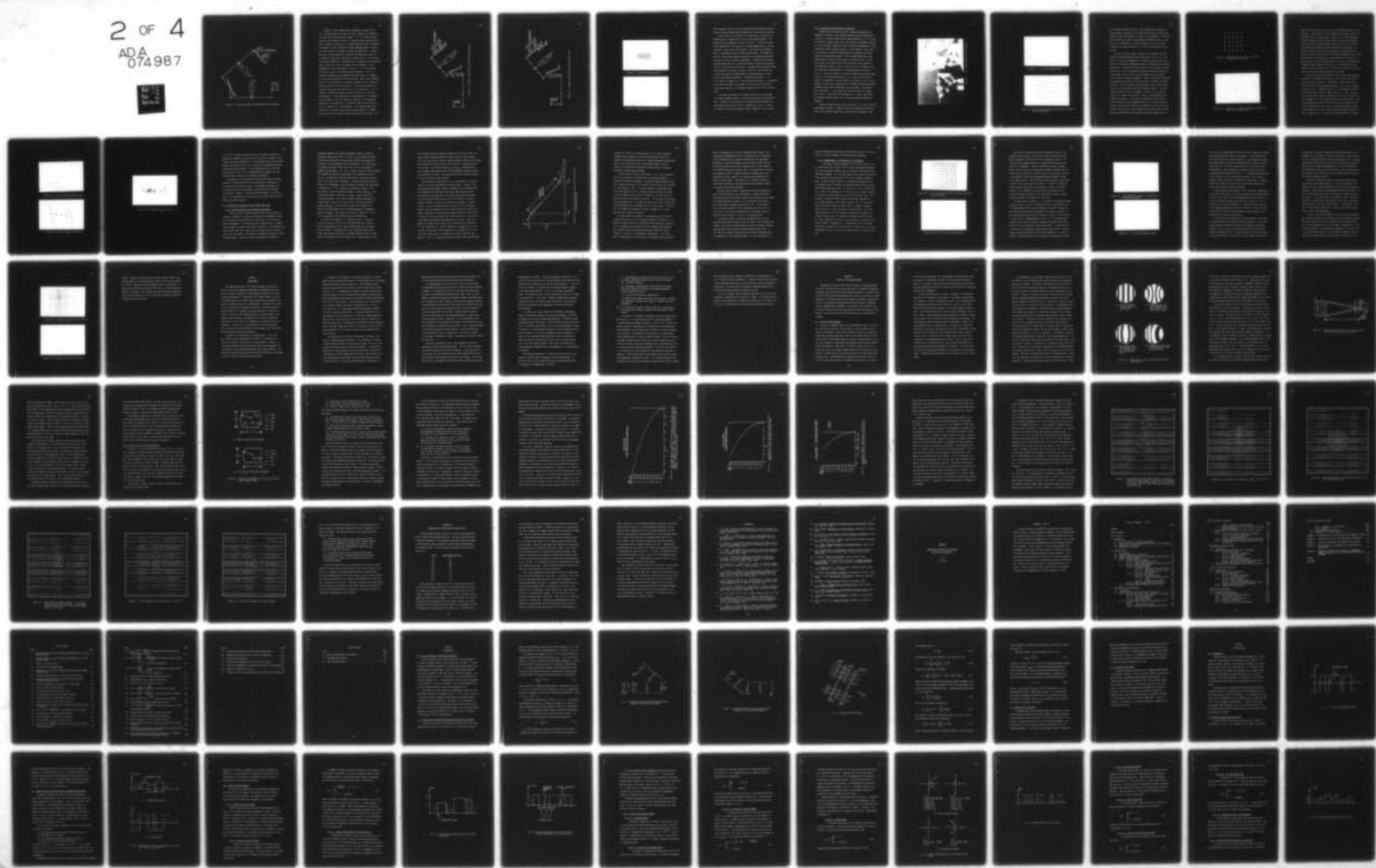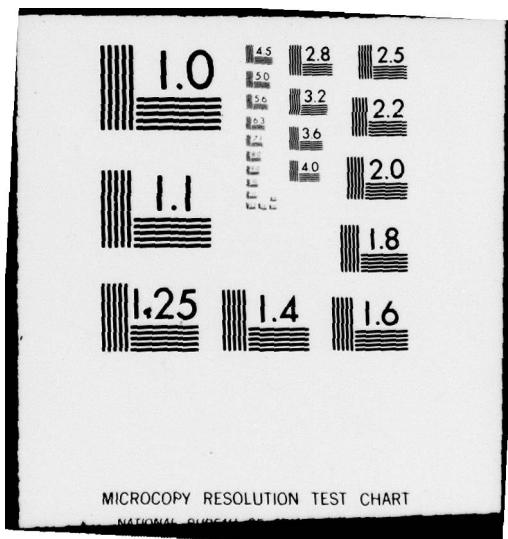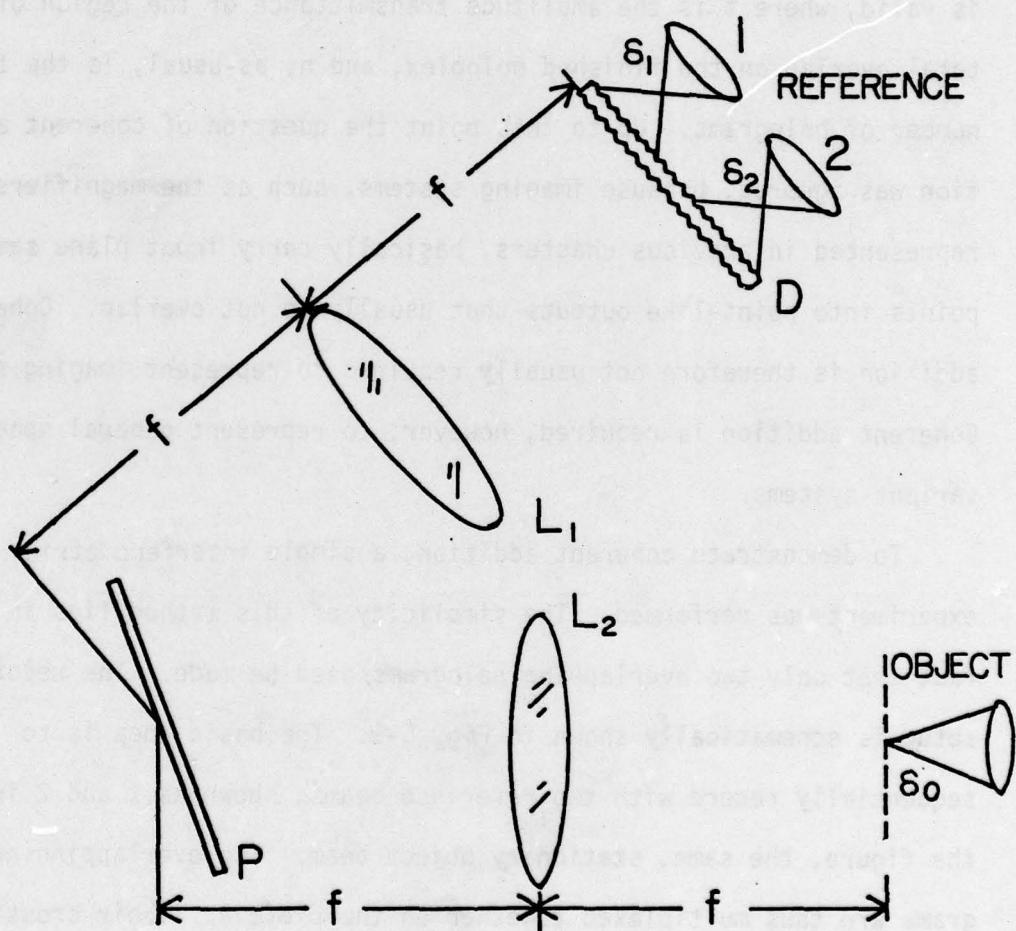
Figure 5-1. Recording scheme for coherent addition experiment.

Playback is then accomplished as schematically shown in Fig. 5-2. The object beam is blocked, and lens L, having focal length f_L, is placed directly behind the holoplex P. As in all other holoplex outputs in this thesis, the lens L is placed directly behind the holoplex, instead of a distance f_L, to reduce light loss due to vignetting. The holoplex is then illuminated by both reference beams, and the object point source δ_0 is imaged a distance f_L behind lens L. Before coming to a focus, however, we intercept the converging light cone a distance b inside focus, where the recording film, F, is positioned. The intercept distance b is chosen to give a reasonably large defocused image on the film, in this case about 6 mm. in diameter. The 8x enlargement of this image appears in Fig. 5-4. It is noticed that the circle of light is of nearly uniform brightness. This is an extremely important fact, considering that this image is a composite of two wavefronts emanating from the holoplex. When either reference beam 1 or 2 was played back, a perfectly uniform circle of defocused light was observed at the film plane F. Yet, when both beams were allowed to play back, the output in Fig. 5-4 was observed. This experiment is therefore based on the exact principle of a Michelson interferometer. From experience with interferometry it is estimated that the output in Fig. 5-4 indicates a mismatch in the emanating wavefronts of less than $\lambda/10$. The slight residual non-uniformity is due to a minute error in repositioning. This extremely good interferometric fit is proof that in-phase coherent addition is indeed taking place in this (and all other) holoplexes in this thesis. The
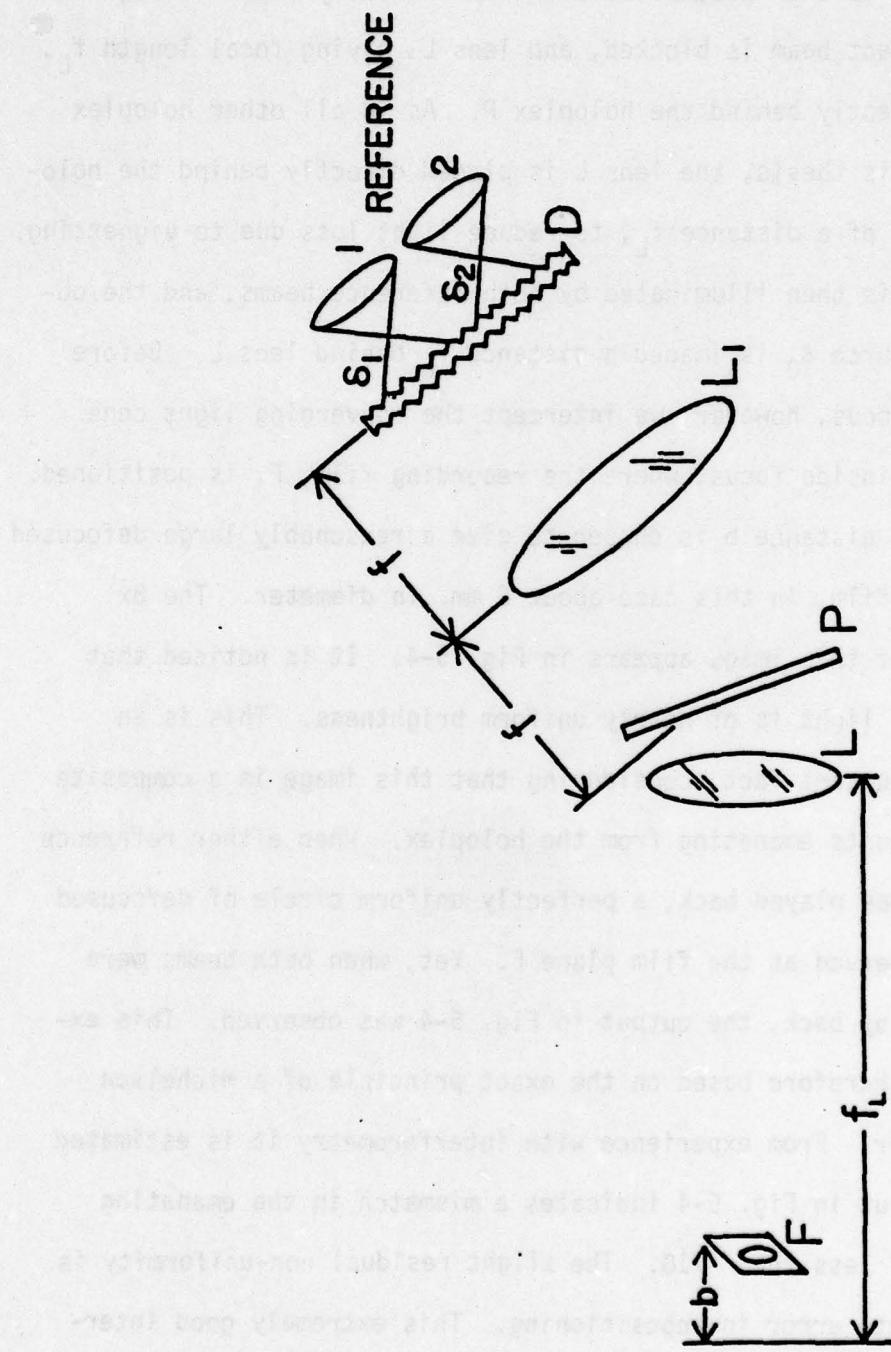
Figure 5-2. Playback scheme with no introduced phase shift.
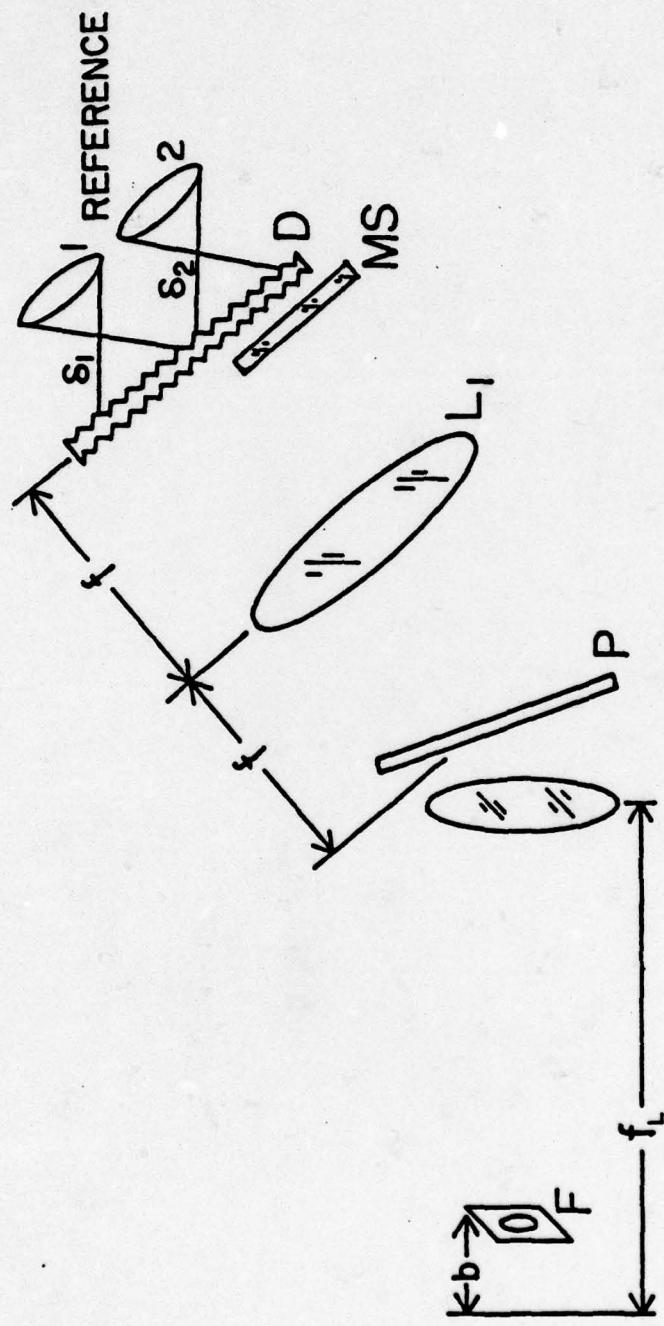
Figure 5-3. Playback scheme with introduced phase shift.
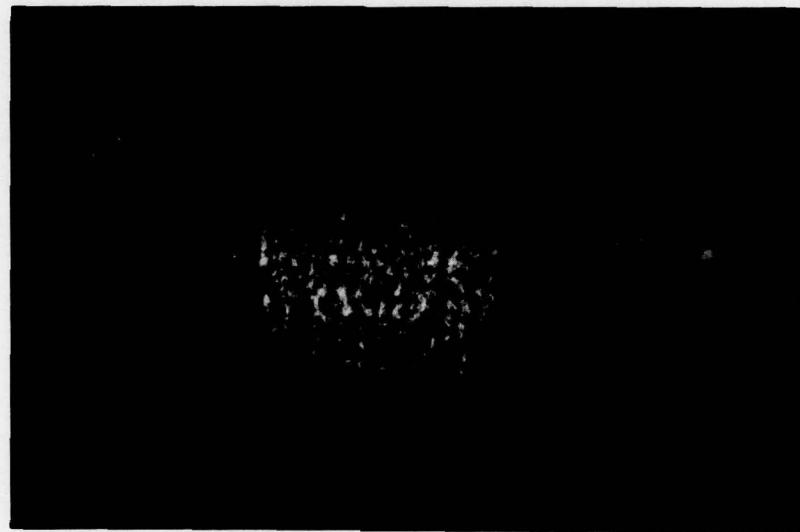
Figure 5-4. Output with no phase shift.
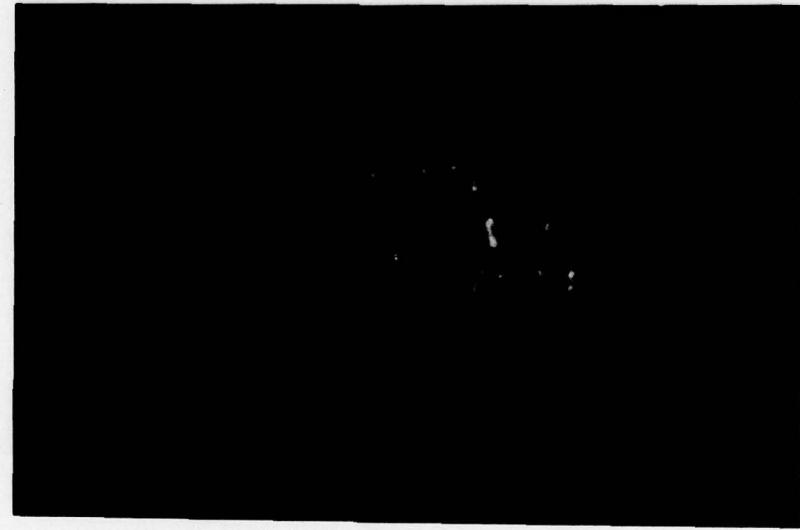
Figure 5-5. Output with introduced phase shift.

amazing aspect is that a $\lambda/10$ (or better) wavefront matching is occurr-
ing even after both beams were scrambled with a ground glass diffuser.

It was desired at this point to see the effect of wavefront mis-
matching, due to a phase shift in one of the reference beams. This
phase shift was introduced as shown in Fig. 5-3. A clean microscope
slide, denoted MS in the figure, was inserted between lens L_1 and the
diffuser D, very close to the diffuser. The slide was positioned so
that it intercepted only one of the reference beams. The presence of
this thin glass plate retards the phase of the transmitted wavefront
but does not alter its contour appreciably. Therefore, both encoded
reference beams will still cause the holoplex to play back the object
point δ_0, but now with a phase shift. We expect this to produce fringes
in the output, and it does, as shown in Fig. 5-5. The fringes are
circular because we are mismatching two converging cones of light,
each having spherical wavefronts. The wavefront mismatch in Fig.
5-5 is about 6 fringes, or 3λ. The slide was positioned to approximately
center the "bulls-eye." The outputs in Fig. 5-4 and 5-5 were very
faint, both requiring a full minute's exposure on Tri-X film to record
well.

With these experiments it has been proven that the requirement
for in-phase coherent addition in multiplex holography has been satis-
fied. Therefore, the expression for the amplitude transmittance of
the overlap region given earlier is indeed valid. Now, it is time
to proceed to the two most complex outputs attempted in this project.

5.3. 2-D Space-Variant Holographic Processing

As mentioned, all preceding optical systems represented holographically have been simple imaging systems, each having some magnification β. Non-unity magnification imaging systems (i.e., β ≠ 1) are, by definition, space-variant, but do not produce very dramatic outputs, as the only optical "computing" operation they are performing is coordinate scaling and/or polarity reversal. It was desired at this point in the project to design and holographically represent a much more complex 2-D space-variant system. Such a system would have a truly unique impulse response at each point in its output plane. It was desired that this system would distort and warp an input object in two dimensions as well as invert it and scale it to a different size. One design which accomplishes all of these operations is shown in Fig. 5-6. The lens at center is a well-corrected copy lens positioned to give an initial magnification of -1/3x. Alone it would yield a simple 1/3x reduction of an input object, and invert it. To its left, however, is the optical component that introduces the highly aberrated, asymmetric space-variant properties into the system. A cylindrical lens of 200 mm. f.l. was placed just inside the copy lens' output focal plane. The cylinder was displaced in x, y, and z, and tilted and rotated in three angles, until a suitably distorted output was observed.

Figure 5-7 shows the input to this system, a 5 x 5 array of equally spaced sampling points. Figure 5-8 shows the appearance of the input array at the system's output plane, after optical processing. Each
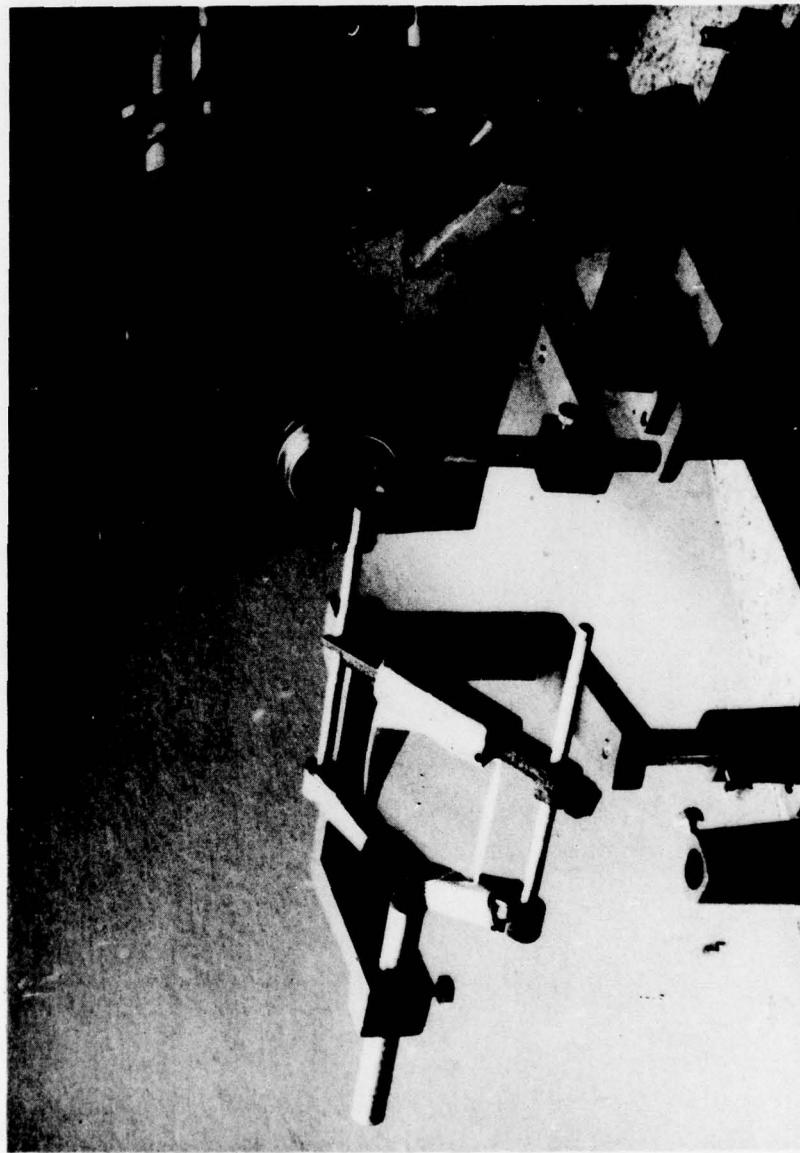
Figure 5-6. -1/3x tilted-cylinder optical system.
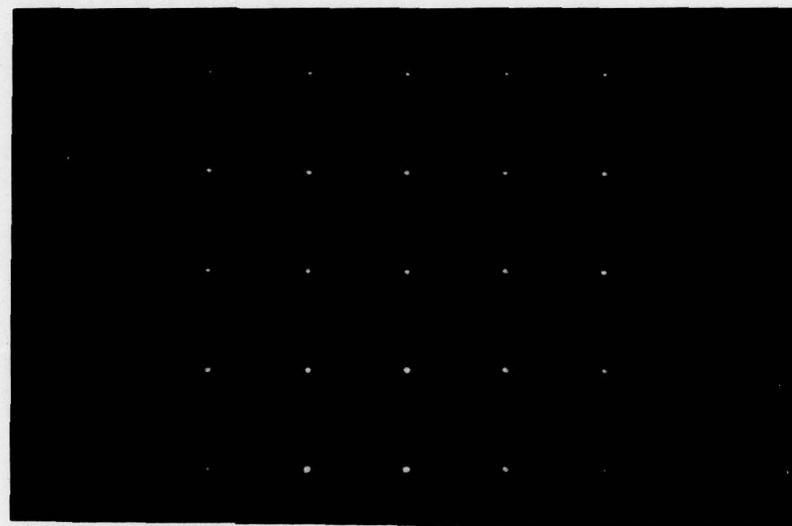
Figure 5-7. 5 x 5 input sampling array.

Figure 5-8. Input array after processing by optical system of
Fig. 5-6 (enlarged).

of the curved, slanted slivers of light represents the impulse response (modulus squared) of the tilted-cylinder system at that point. As may be seen, each response is unique in its appearance. The entire shape of the input array has been warped and distorted, and its general size at the output is roughly 1/3 that of its size at input, although it has been enlarged in Fig. 5-8 so that fine details may be seen.

The next step was to make a holoplex of the system, using the standard recording equipment setup shown earlier in Fig. 1-1. The entire 5 x 5 array was sequentially recorded, row by row, using the #80 grit diffuser and chirped-wave diffuser illumination for crosstalk suppression. The spatial non-uniformity of the collimated laser beam proved to be a real problem when considering individual hologram exposure times, and as a result three holoplexes had to be exposed, with only the third being acceptable. Figure 5-9 shows the individual hologram exposure times (in seconds) on the third and best holoplex obtained. The total exposure was 364 seconds, made on Kodak 125-02 emulsion, with the laser output set at 400 mw as usual. The simultaneous playback of all 25 holograms is shown in Fig. 5-10 below. Three of the corner terms are not visible in this photograph, and needed more exposure. The remaining 22 output slivers are easily visible, however, and when compared with Fig. 5-8, we see that the holoplex has faithfully replicated the behavior of the space-variant system. The slivers of light produced by the holoplex have the same shape and orientation as the output of the actual system, and the

35 15 15 15 15
15 15 15 15 15
15 15 10 12 10
15 15 10 10 10
20 15 12 10 15

Figure 5-9. Individual exposure times (in seconds)
for holoplex in Fig. 5-10.
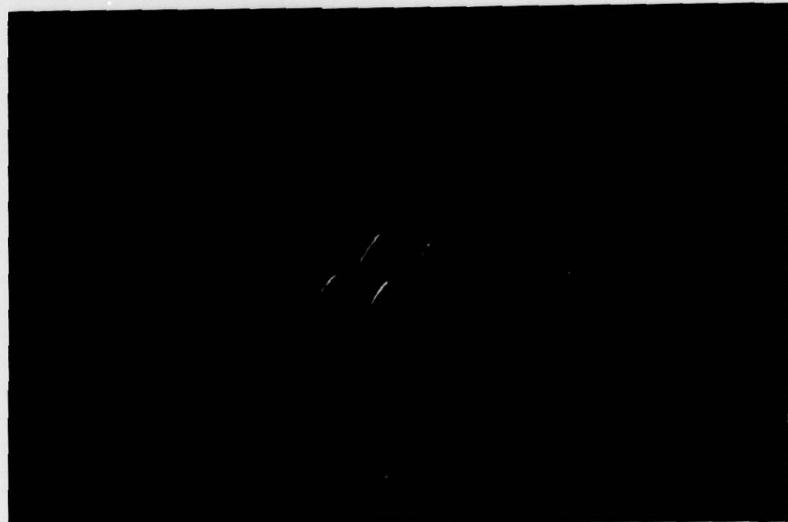
Figure 5-10. Complete 5 x 5 playback of holoplex representing
-1/3x tilted-cylinder system.

overall angle, distortion, and size of the holographic output is also identical. The crosstalk is well-suppressed, having been spread into the numerous faint, fuzzy patches of haze visible in the background. The total exposure of 364 seconds yielded an average optical density of about 0.6 in the region of total overlap, and in all likelihood a satisfactory holoplex would result with even less exposure. The exposures given the bright central holograms could probably be reduced by as much as half, and the faint corner holograms could be given more exposure, thus resulting in a redistribution of individual exposures to give a more uniform overall output, while at the same time reducing the total exposure to the plate. It was decided at this point to use this experience for the large 10 x 10 arrays that follow, rather than try for a better output for this system.

With the reasonably good holoplex of the tilted-cylinder system available, it was decided to perform an actual space-variant holographic processing operation. Accordingly, a mask of the letter "H" was cut out of black construction paper. First, it was inserted in front of the 5 x 5 object beam array. The corresponding input to the tilted-cylinder system is shown in Fig. 5-11. Then, the space-variant system was allowed to process the input, and its optical output is shown in Fig. 5-12, again enlarged to show fine details. Next, the object beam was blocked and the "H" mask was inserted in front of the reference beam array. The tilted-cylinder system's holoplex was then replaced in the micropositioner and allowed to process the input incident upon it. Its output, enlarged even further, appears
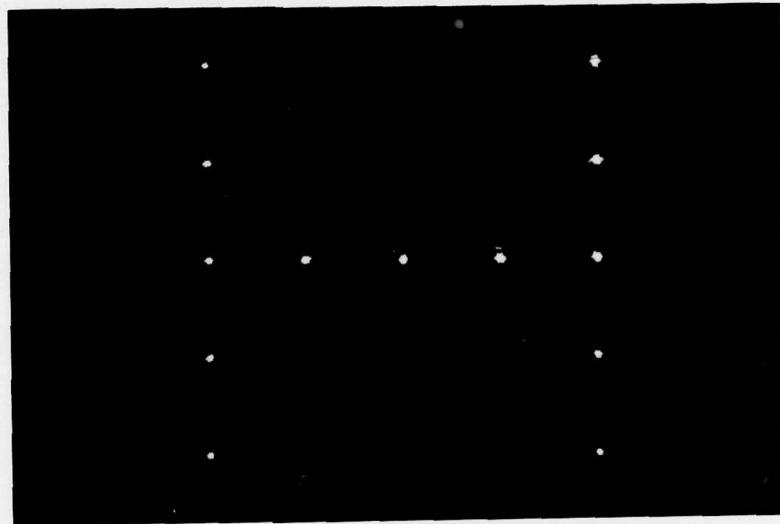
Figure 5-11. Input to tilted-cylinder system.

Figure 5-12. Optical output of letter "H".

Figure 5-13. Holographic output of letter "H".

in Fig. 5-13. We see that the optical and holographic outputs are
essentially identical, except for the non-uniformity problems in the
holoplex output discussed earlier. The horizontal bar of nebulous haze
through the center of Fig. 5-13 is the residual autocorrelation noise
of the ground glass diffuser. The crosstalk here was of even less
intensity than in Fig. 5-10, as fewer terms were present, thus con-
tributing less to the overall crosstalk distribution.

The outputs of this experiment therefore prove that a multiplex
hologram can indeed accurately store and reproduce the behavior of
a 2-D space-variant optical system of considerable complexity, and
can therefore be used to represent space-variant optical systems
in the overall scheme of a coherent optical processor. All that re-
mains is to demonstrate the feasibility of using even larger arrays of
input plane sampling points.

5.4. Holographic Processing Using a Larger Input Array

5.4.1. General Problems with Large-Array Holoplexes

The 5 x 5 array of sampling points used in the previous ex-
periment is adequate for space-variant optical or holographic process-
ing on relatively crude inputs such as the letter "H" or other geo-
metric arrangements. If processing of more complex inputs is contem-
plated, however, we must provide spatial sampling at a much higher rate,
which implies that a much larger (and thus denser) array of sampling
points must be recorded. This leads to a fundamental question in multi-
plex holography: how many individual holograms may ultimately be

superposed together on a single photographic plate? Is there any reasonable upper bound, and if so, what? A basic problem related to the upper bound problem is the amplitude transmittance-exposure relationship of the holographic recording emulsion. This relationship is commonly expressed in the form of the t-E curve, discussed by Goodman [14] and shown in Fig. 5-14. Ideally, we wish a linear relationship between the amplitude transmittance of an emulsion and the exposure it receives, but as may be seen from Fig. 5-14, the relationship is not linear for all exposures. The upper section of the curve, labeled "A", corresponds to the toe region on the H&D curve, described in Goodman [14]. In this region the transmittance changes little with exposure. When the exposure reaches a certain value E_{min}, the transmittance begins to decrease in a nearly linear fashion with increasing exposure. This linear decrease continues throughout the "Linear Region" section of the curve, until the exposure reaches another value E_{max}. At this point the emulsion is beginning to saturate, and the change in the transmittance begins to decrease as exposure increases. This section of the curve, labeled "C" in Fig. 5-14, corresponds to the shoulder region of the H&D curve.

In multiplex holography it is essential that all n exposures be made in the linear region of the recording emulsion, so that an accurate representation of a linear, space-variant optical system may be achieved. The problems are first to know the range of the linear region for the particular holographic emulsion used, and then secondly to partition the linear region into n sub-exposures, so that

each hologram receives an adequate exposure, and the sum of the n exposures does not extend beyond the linear region into the shoulder. In Fig. 5-14 we see how a typical holoplex exposure might be partitioned, when the data on the t-E curve (or H&D curve) for a proposed emulsion is available. The interval between E_{min} and E_{max} is therefore the total exposure range through which the transmittance-exposure behavior of the emulsion is linear. We must plan the overall holoplex exposure so that it fits within this interval.

Partitioning the linear region into n sub-exposures is basically simple, as all the n sub-exposures should be equal. As seen in the tilted-cylinder experiment, however, problems such as reference beam non-uniformity and vignetting require that some holograms receive more exposure time than others, thus complicating the partitioning. A further problem develops when a very large holoplex, containing possibly hundreds or thousands of individual holograms, is contemplated. A certain minimum exposure is required for any individual hologram, usually expressed in units of millijoules per square centimeters. When the n sub-exposures are added it may not be possible to fit them all into the linear region. One solution is to use an emulsion/developer/development-time combination that gives a lower film gamma, thus reducing the slope of the linear region and lengthening it. The problem here is that the lower the film gamma, the less the contrast, and we reach the point where all n holograms may fit into the linear region, but are so washed out that they play back very weakly, if at all. A promising solution currently under investigation
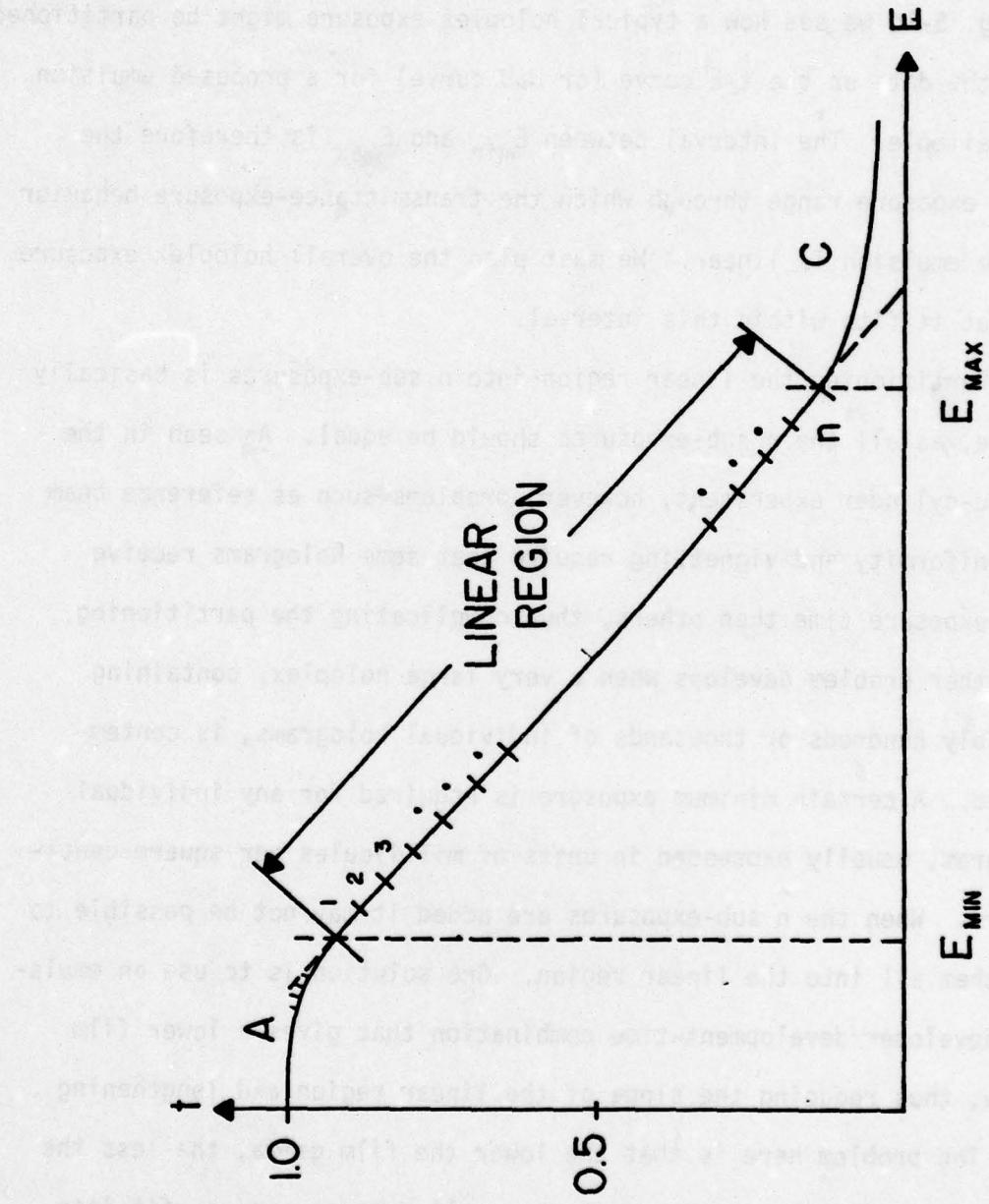
Figure 5-14. Partitioning the linear region of the t-E curve for an n-exposure holoplex.

by Irby et al. [10] is to gang portions or all of the n holograms together before exposure, by pre-multiplexing them together in a computer and representing them with a computer-generated transmittance mask. This allows the use of a higher-gamma (higher contrast) emulsion, by (hopefully) reducing the required dynamic range when making the single-exposure hologram.

The "A" region of the t-E curve shown in Fig. 5-14, corresponding to the toe region of the H&D curve, may present problems in large-array multiplex holography. Individual hologram exposure times for a large-array holoplex will typically be quite short, on the order of a few seconds or less. If we begin exposing a fresh plate, the first few holograms may fail to record, because the plate has simply failed to respond to this initial illumination, the first few holograms being lost in the plate's gross fog. If this occurs the solution is to hypersensitize, or "pre-fog" the plate with uniform illumination, to bias the plate into the beginning of the linear region. The plate will then immediately respond to further illumination in a linear fashion, and is ready for recording.

The upper bound to the numbers of holograms that may be superimposed on each other is still apparently subject to conjecture. La-Macchia and White [16] have indicated that they successfully recorded a 32 x 32 holoplex, using ground glass for reference beam encoding, but no details were given regarding the actual recording of their holoplex, or how well it simultaneously played back. In the same paper it was predicted that as many as 10^5 holograms could be superim-

posed if the object was an array of separated point sources. The experimental implementation of such a holoplex would be formidable; if the holograms were not somehow premultiplexed into aggregates beforehand, it would be necessary to partition the linear region of the recording medium into 10^5 sub-exposures, with a total exposure time possibly amounting to several days! A successful 316 x 316 holo-plex (containing 316^2 or 99,856 individual holograms) would be ex-traordinarily useful, however, for space-variant processing, and digital storage as well. The modest 10 x 10 holoplex recorded in this project effectively illustrates many of the problems inherent in large-array multiplex holography.

The other major problem in large-array multiplex holography is that of signal-to-noise ratio deterioration. LaMacchia and White have shown [14] that the signal-to-noise ratio decreases as the number of hologram exposures increases. This relationship has recently been investigated in greater detail by Kral [5]. The successful 10 x 10 holoplex recorded in this project seems to verify this re-lation well, as the overall background haze is brighter than that observed with the smaller 3 x 3 or 5 x 5 holoplexes made.

An important aspect of multiplex holography when very large sampling-point arrays are used is the fact that if the reference point sources in the array are sufficiently far apart, the Bragg extinction angle property of the recording medium becomes operative [8]. In this case the crosstalk associated with the widely separated points is suppressed by volume hologram effects. In this experiment, the

emulsion thickness of the Kodak 125-02 plates was only .15 μ, and for the 10 x 10 array recorded, volume effects were negligible.

5.4.2. Description of a Successful 10 x 10 Holoplex

The largest holoplex attempted in this project was for a 10 x 10 input point array, implying 100 individual overlapping holograms. This size was chosen primarily due to the physical limitations of the recording equipment. This was the largest array (using the available fly's eye lens array) that would fit in the 2" diameter reference beam. A beam of larger diameter could have been arranged, but the corresponding drop in intensity per hologram would have made the exposure times undesirably long. In order to fit a 10 x 10 array into the 2" beam it was necessary to use every fly's eye lenslet, instead of skipping over every other one, as with the smaller arrays. The problem of lenslet-to-lenslet internal reflections remained, but was reduced somewhat by redrilling a new pair of 10 x 10 stop-down masks with smaller apertures, namely 3/32", or .09375", compared with the 7/64", or .1094", apertures of the old masks. This gave a 26% reduction in the light intensity available per hologram, but yielded a beneficial gain in darkness of adjacent lenslets as well as further reducing each lenslet's on-axis spherical aberration (discussed in detail in Appendix A). A photograph of one of the stop-down masks, attached to a fly's eye array, is shown in Fig. 5-15, and a photograph of the 10 x 10 array of sampling points is shown in Fig. 5-16.
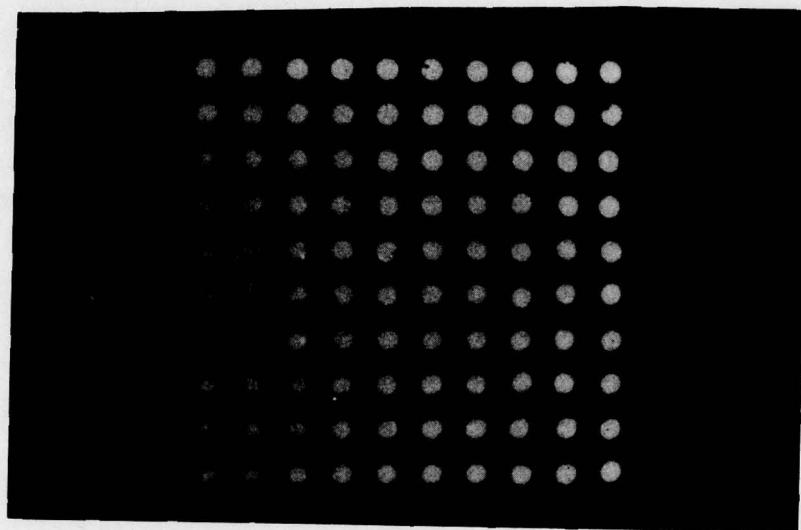
Figure 5-15. 10 x 10 stop-down mask used to improve fly's-eye
array performance.
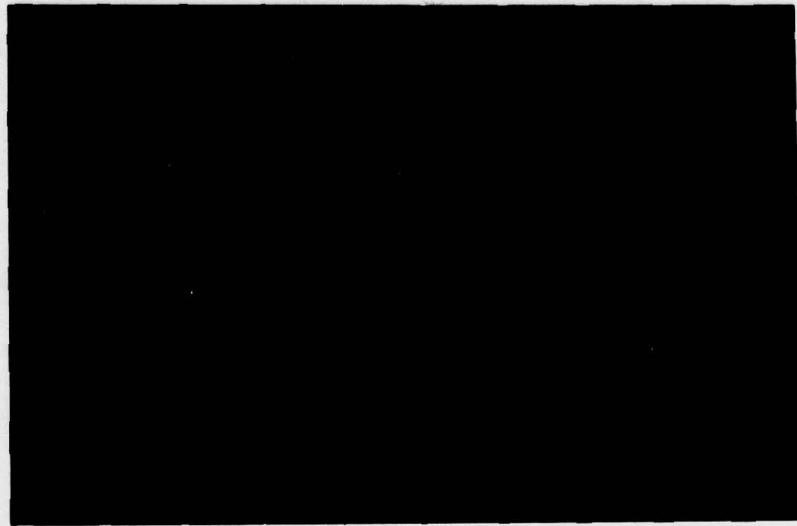
Figure 5-16. 10 x 10 array of sampling points.

The choice of optical system to be represented by the 10 x 10 holoplex posed a problem. The simple non-unity imaging system was easy to implement, but did not give very interesting outputs. The tilted cylinder systems produced very complex outputs but were more difficult to implement. The more interesting and useful systems, those in which some form of superposition integral operation was performed, had not been tried on smaller arrays first and were ruled out. It was decided to keep things uncomplicated and represent a simple -1/2x imaging system. This system would simply reduce an input object to half of its original size, and invert it. Figure 5-17 shows the input to either the optical or holographic processor, an inverted "double-T", the "double-T" being the Texas Tech University logo. Figure 5-18 shows the output of the -1/2x optical processor, which erects the double-T and shrinks it to half-size.

The next step was to make a 10 x 10 holoplex of the optical system. The data on the t-E curve for the emulsion used in recording the 10 x 10, namely Kodak 125-02, was not immediately avaliable. However, in the previous tilted-cylinder experiment, 364 seconds of exposure on this same emulsion gave an optical density of about 0.6 in the region of total overlap. Remembering that the new 10 x 10 stop-down masks allow 26% less light per hologram, we expect that about 460 seconds would yield the same density, using the new masks. Dividing by 100, an exposure of 4.6 seconds per hologram would seem correct. However, we must again boost exposure to the corner holograms, by a factor of about 2. It was decided to use an exposure of 8 seconds per hologram
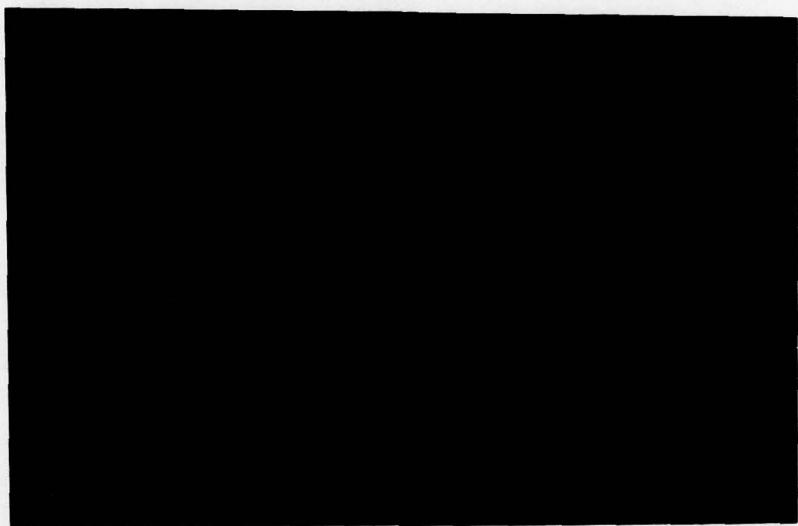
Figure 5-17. Inverted double-T input to -1/2x optical or holographic processor.
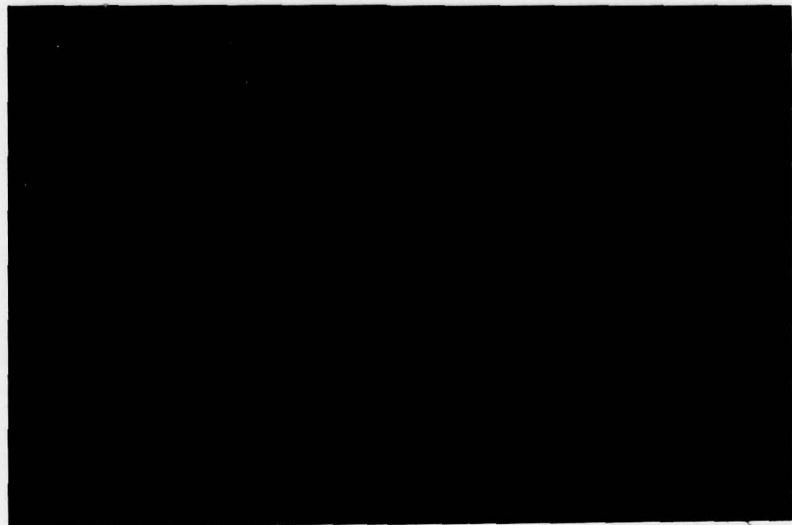
Figure 5-18. -1/2x optical processor output.

on the first holoplex attempted, with the corners receiving 16 seconds, thus giving about 900 seconds total exposure. It was thought that 4.6 seconds might not be enough exposure for the individual holograms. The standard #80 grit diffuser/chirped-wavefront illumination combination was used for crosstalk suppression on all the 10 x 10 holoplexes exposed. When processed, this holoplex was very dark, with an average measured density of about 1.3. It played back the majority of the holograms, but its output was quite faint. The plate was bleached, washed, dried and re-inserted into the system. A few more points were visible, but now all were fuzzy, thus reinforcing the lesson learned about bleaching in Chapter 3.

A second holoplex was recorded, using 6 seconds per hologram and 12 seconds for the corners, for a total exposure of about 650 seconds. It was still too dark, with an average measured density of about 1.0. It played back more holograms than the first, but the full 10 x 10 array was still not coming through. The double-T mask was inserted in the reference beam and for the first time the inverted, half-size double-T could faintly be seen through the viewing eyepiece, even though many of the points were missing.

The third and last holoplex was the best obtained in the project. Each hologram received 4 seconds of exposure except for the corners, which were given 10 seconds, giving a total exposure of about 430 seconds. This is close to the predicted value of 4.6 seconds per hologram mentioned earlier. The average optical density in the overlap region was about 0.7, and 97 out of 100 holograms could be seen

playing back. Figure 5-19 shows the holoplex output when all 100 holograms were illuminated. Several of the points failed to record on film even though they were visible to the naked eye; in this photograph one can actually see the non-uniform profile of the reference beam intensity. Some of the asymmetry is due to the same probl that plagued the outputs in earlier chapters, that of vignetting by the recording lens, which had a smaller diameter than the lens used to observe the output visually.

The double-T mask was inserted in the reference beam array, upside down, and the output shown in Fig. 5-20 was observed. The double-T has been erected and reduced to half-size by the holoplex, although it appears here enlarged somewhat to show fine details. All but 5 of the points are visible, and the double-T shape is easily discernable. If the points were more clearly visible, it would be possible to lowpass filter the holoplex at this point, and smooth the image into a continuous double-T image. The crosstalk in Fig. 5-20 is quite diffuse and faint, its soft, quilted texture barely being visible in the background.

It seems likely that if another 10 x 10 holoplex were exposed the individual exposure times could be even less, perhaps 3 seconds. The corners need more exposure to achieve a more uniform output, and the total exposure time could be reduced to 300 seconds or less. This would result in an average optical density of 0.5 or less, giving a much brighter output. Or, from another viewpoint, more holograms could be packed onto the plate before the density of 0.7 is
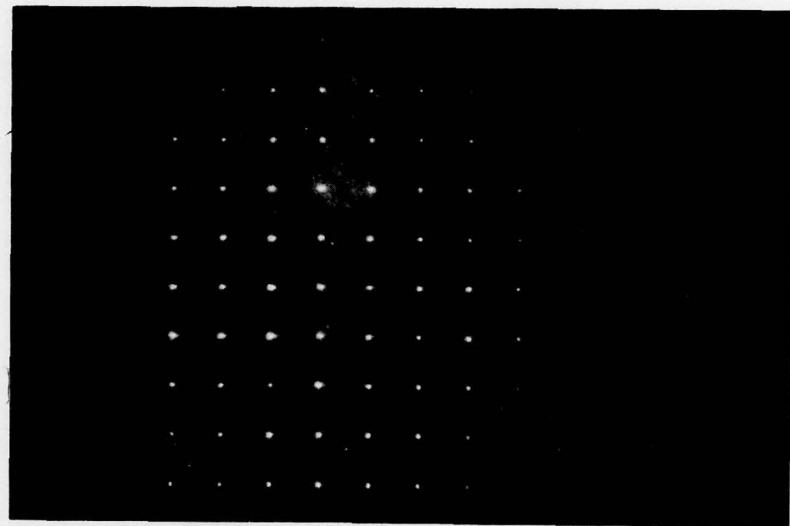
Figure 5-19. Complete playback of 10 x 10 holoplex.
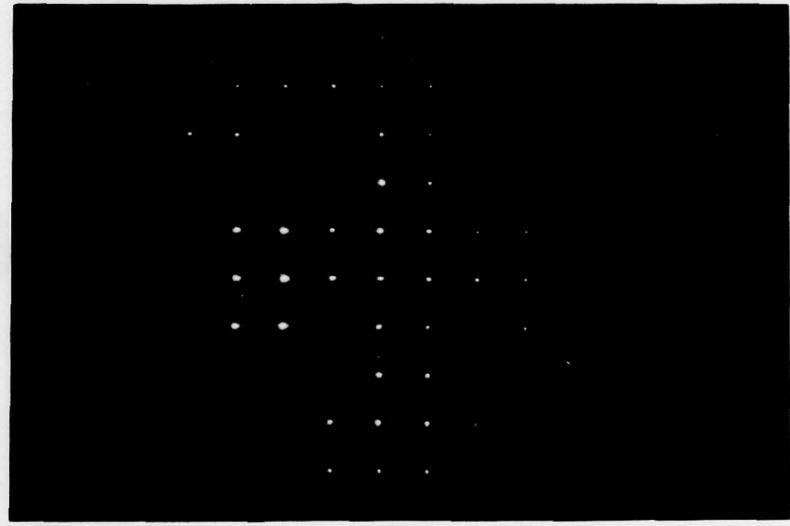
Figure 5-20. Playback of Texas Tech "Double-T".

reached. However, with decreasing individual exposure times it may become necessary to prefog the plate so that the first few holograms will record. Based on experience gathered from this experiment it seems quite likely that a successful 200-, 300-, or even 500-exposure holoplex is possible. With careful planning and advanced laboratory experience the gigantic 32 x 32 point holoplex reported by LaMacchia and White seems within reach.

CHAPTER 6

CONCLUSIONS

The primary objective of this thesis has been to present the results of the first extensive experimental investigations into the use of multiplex holography for two-dimensional space-variant optical system representations. Essentially, this thesis serves as an atlas of holoplex outputs for a broad range of recording and playback situations, including some that are unprecedented. The thesis also serves as a sort of multiplex holography "cookbook"; the emulsion type and exposure times (for a standard recording intensity) for every holoplex are indicated, thus allowing the same or similar results to be repeated without wasteful and expensive plate exposure bracketing. These results are of particular importance in recording large-array holoplexes, in which the lab time necessary for the recording process is typically 3-5 times the total plate exposure time, thus making exposure bracketing very time-consuming.

In Chapter 1 the objectives and accomplishments of the thesis were listed, and the convenient word "holoplex," a contraction of "multiplex hologram," was defined and used throughout. General recording and playback techniques were described, and the mathematical descriptions of the multiplex holography process were presented. The problems of hologram-to-hologram crosstalk were introduced, and methods by which it might be suppressed were discussed.

In Chapter 2, the problem of crosstalk was examined in greater depth, with the analysis restricted to crosstalk generated in holoplexes representing simple imaging systems only. These imaging systems basically carried point source inputs to point outputs with a magnification $\beta \neq 1$. A simple graphical method for predicting the crosstalk distribution for non-unity magnifying systems was demonstrated, and the dependence of the crosstalk distribution on both the magnitude and sign of β was discussed. It was shown that for a given value of $|\beta|$, crosstalk scatter would be at its maximum for $\beta < 0$, and at its minimum for $\beta > 0$, thus making negative magnification superior in terms of signal-to-noise ratios. It was also shown that if $|\beta|$ was decreased, the distribution of the crosstalk shifted outward and away from the signal term array, which also served to improve the signal-to-noise ratio. Experimental verifications of these predicted results followed, showing the outputs of holoplexes in which no diffusers were used, for a variety of array sizes and imaging system magnifications.

The ground glass diffuser was investigated in Chapter 3, with several interesting results presented. The differences in plane vs. chirped wavefront diffuser illumination were shown, with the chirped wavefront providing superior crosstalk suppression. The diffusing properties of coarsely-ground and finely-ground glass plates were contrasted; the finely-ground plate gave better, more uniform crosstalk suppression but made repositioning of the processed holoplex far more difficult. The interesting differences in sequential vs.

simultaneous recording using ground glass diffusers were shown, and the first problems with beam non-uniformity were encountered.

The implementations of the first 128 x 128 cell binary-coded reference-beam diffuser masks fabricated at Texas Tech were presented in Chapter 4. Difficulties involved in fabricating the masks were discussed, and photoreduction problems were noted. Only a limited number of masks were available, and holoplex outputs using these masks were presented for a small number of recording and playback parameters. The performances of the phase and amplitude binary diffusers were compared, but the results were inconclusive due to the poor quality of the binary phase diffuser available. Perhaps the most important results of the chapter are the differences observed in plane versus chirped wavefront diffuser illumination, for the amplitude diffuser. The experimental results agreed very closely with the theoretical computer simulations by Redus [5] and Krile [8]. Thus in both experimental and theoretical work with binary diffusers it has been shown that chirped-wavefront diffuser illumination is significantly superior to plane-wave illumination in terms of the degree of crosstalk suppression observed.

Additional experimental results were presented in Chapter 5, covering basically three separate topics. The first topic discussed was coherent addition in multiplex holography. A very important result obtained was the experimental proof that coherent addition was taking place in the holoplexes recorded in this project. Then in the next section, an extremely space-variant optical system was accurately

represented by a holoplex. The optical system was sampled by a 5 x 5 array of point sources, and the recorded holoplex duplicated the wildly space-variant properties of the optical system perfectly. In the last section of Chapter 5, the output of the largest holoplex attempted in the thesis was presented. This 10 x 10 holoplex represented a modest -1/2x magnifier, and correctly processed the Texas Tech "Double-T" positioned at its input plane. General problems with large-array holoplexes, such as the dynamic range limitations of the recording emulsions and exposure time compensation for beam non-uniformity, were discussed.

In closing, this thesis research has produced a considerable number of experimental results in multiplex holography, as used for 2-D space-variant optical system representations. Probably the main contribution made in the thesis is the verification that the combination of the ground glass diffuser plate and chirped-wavefront diffuser illumination is the most powerful method of crosstalk suppression presently available. The initial experimental results presented in Chapter 4 show the binary coded diffusers to be very promising, if their fabrication difficulties discussed can be overcome and their scale can be sufficiently reduced. Until then, the ground glass/chirped wavefront combination will serve admirably in the suppression of crosstalk.

The effective suppression of crosstalk paves the way for more complex 2-D space-variant holographic processing operations. An exciting vista of untried operations awaits future experimentation in holographic representations, including

(1) Two-dimensional superposition integral operations, such as integral transforms (Laplace, Abel, Z, Mellin, Hilbert, etc.) and their inverses;

(2) Holographic representation of physically non-existent operations that may be achieved using computer-generated binary transmittance masks;

(3) Space-variant aberration compensation;

(4) Space-variant image restoration and processing, including such operations as deblurring, removal of defocus, and image enhancement;

and (5) Space-variant optical testing, especially in the case of non-rotationally symmetric aspheres and other complex surface contours.

To the best of the author's knowledge, the use of coherent color multiplexing for 2-D space-variant optical system representation is a totally unexplored subject at present. Collier et al. [18] has produced three-color reconstructions of conventional color photographs from holoplexes in which ground glass diffusers were used to suppress color crosstalk. No extension of this technique to space-variant system representation is known at present, however. Collier found that a hologram recorded using a ground glass diffuser played back only a uniform noise when playback was attempted using a wavelength only 12.8 NM. shorter than the recording wavelength. This effect was observed in this thesis during the ground-glass experimentation performed in Chapter 3. Thus, ground glass diffusers have a useful form of "play-back bandwidth" associated with them. It is possible that multicolor holoplexes could be used to represent 2-D space-variant optical systems.

Such a holoplex would be capable of spectacularly colored outputs as well as being functional, especially if several different forms of space-variant processing operations, one for each color, were simultaneously represented. This application of multiplex holography would be a particularly fascinating avenue of research to pursue.

The list of space-variant processing operations that could be holographically represented could continue for pages. It is hoped that the analytical and experimental investigations presented in this thesis will be of use in implementing the various processor operations discussed.

APPENDIX A

OPTICAL SYSTEM CONSIDERATIONS

Throughout the course of this research project it was desired that
the optical systems used to record, play back, and document the numerous
holoplexes be as nearly diffraction-limited as possible. Satisfying this
criterion insured that each holoplex would give as true and exact a repre-
sentation of the space-variant optical system as possible, and would be
devoid of any additional degradations that inferior optical components
or poor alignment might introduce. The purpose of this appendix is to
describe the various analytical and practical techniques employed in the
project to achieve the best possible optical quality in each holoplex
recorded.

A.1. Optical Testing Methods

The optical components used in the experimental setups in this pro-
ject included flat mirrors, beam splitters, a well-corrected spatial
filter and collimator, several neutral density filters (for object-ref-
erence beam intensity balancing), the fly's eye lenslet arrays, two cor-
rected Fourier transforming lenses, and several corrected lenses of vari-
ous focal lengths for photographically documenting the holoplex outputs.
A well-corrected f/4.5 copy lens (f = 165 MM.), shown in Fig. 5-6 at
center, was used as the simple imaging system for all holoplexes in the
project, the magnification being set by appropriately changing the lens'
conjugate foci. Each component was optically tested before insertion
into the system, and basically two different optical tests were used to

evaluate their performance. The simple Newton interferometer was used to check all flat surfaces, and Ronchi's test was used to check all lenses in the system. Both are well-described by Malacara [19] and in many other excellent sources [17, 20-24], but will briefly be discussed here for quick reference.

As in any quality-control situation, a standard of reference was required for all testing in this project. The standard used here was a 4" diameter, 1" thick aluminized Pyrex optical flat, personally hand-corrected by the author to $\lambda/20$ at 546.1 NM. The flat mirrors were checked directly with this reference flat, using the Newton interfero-meter. A full description of this test is given by Malacara [19, pp. 1-18]. Briefly, the reference flat and the surface to be tested are thor-oughly cleaned, and all traces of dust are brushed or blown away. The two surfaces are gently contacted under a monochromatic light source. Interference fringes are observed through the upper part, either the reference or test piece (provided the rear surface is polished), and the patterns of the fringes are used to interpret the surface contour of the test piece. A deviation of two fringes implies an error of one wavelength, at the wavelength used for viewing. None of the three 5" diameter flats (unaluminized at the time of testing) deviated from a plane surface by more than a quarter of a fringe, or $\lambda/8$ at 546.1 NM.; their quality was therefore adequate for the purposes of these experi-ments. They were then packaged and sent to a coating firm to be alumi-nized.

In the meantime, the aluminized reference flat was used to check the quality of the collimating lens, using the Ronchi test (pronounced ron-key, not raunchy). This test is described from a practical view-point in many of the excellent treatises on telescope making [17, 20, 21, 22] and treated in greater theoretical detail by Malacara [19, pp. 283-317]. Basically, the Ronchi test uses a relatively coarse grating, having a square-wave amplitude transmittance along one axis, with a spatial frequency of 50-250 lines/inch. The grating is placed very near the focal point of the optical system under test. An unaberrated (perfectly spherical) converging or diverging wavefront replicates exactly the straight-line pattern of the grating on a screen a short distance behind the grating, while an aberrated wavefront forms curved fringes on the screen. The distortion of the fringes indirectly displays the contour of the transmitted wavefront, with proper interpretation. A full description of the interpretation of Ronchi fringes is beyond the scope of this appendix; however, the four most important typical fringe patterns are shown in Fig. A-1 for reference. By convention, these are the patterns observed when the grating is positioned inside focus. Figure A-1(a) shows the fringe pattern projected on the screen when no wavefront error is present. The bands are as straight as those of the grating. Figure A-1(b) is the typical fringe pattern for undercorrected on-axis spherical aberration, a defect typical of nearly all positive lens systems. Note that the bands flare outward for undercorrection. Figure A-1(c) is the typical fringe pattern for overcorrected on-axis spherical aberration. Note that the bands bow inward for overcorrection. Figure
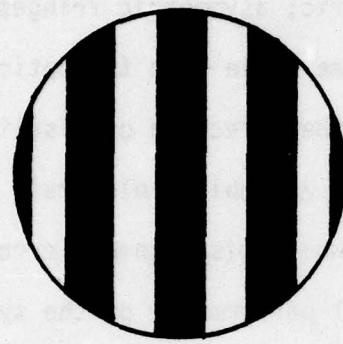
(a) Perfect wavefront, all rays focus to a common point.
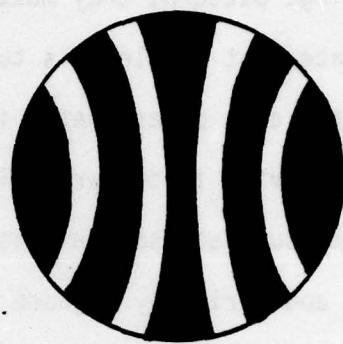
(b) Undercorrected wavefront (marginal rays focus closer to lens than paraxial rays).
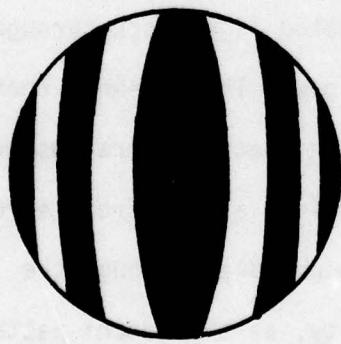
(c) Overcorrected wavefront (marginal rays focus farther from lens than paraxial rays).
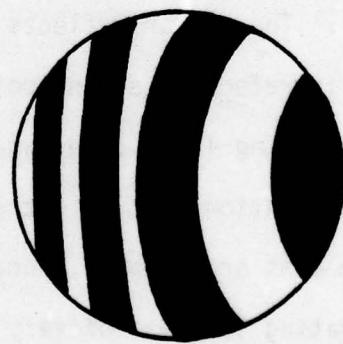
(d) Asymmetric fringes caused by misalignment of lens with optical axis.

Figure A-1. Typical on-axis Ronchi test patterns (grating inside focus).

A-1(d) shows a typical fringe pattern that might be observed when a lens is not properly aligned with the optical axis. Regardless of the type of fringe pattern, they must be symmetric; asymmetric fringes generally indicate that the lens is turned at some angle with the optical axis, with the axis of asymmetry indicating the direction of misalignment. This behavior is of particular use when assembling elaborate optical systems such as used in this project, where misalignment errors can compound and seriously degrade the overall performance of the system.

To check the quality of the collimating lens, the autocollimation test shown in Fig. A-2 was arranged. A point source of laser light is formed by a microscope objective, and is positioned a distance f_L from the lens as shown. The Ronchi grating is located at G, the collimating lens at L, and the aluminized reference flat at M. Laser light leaves the point source, passes through the grating G, and is collimated by the lens L. The mirror reflects the collimated light back through the lens, which is refocused at the point P as shown. The screen S then intercepts the diverging light cone, where the Ronchi patterns are observed. The autocollimation test is extremely sensitive, as wavefront errors produced by the lens are doubled, because of two passages through the lens. The collimating lens was of very good quality, as the Ronchi patterns observed were those of Fig. A-1(a). This was important, as it was now known that the collimated light used in the experiments would have wavefronts plane to a very small fraction of a wavelength.

This reference-quality collimated light was used to Ronchi test several lenses, from which two very well-corrected lenses having almost
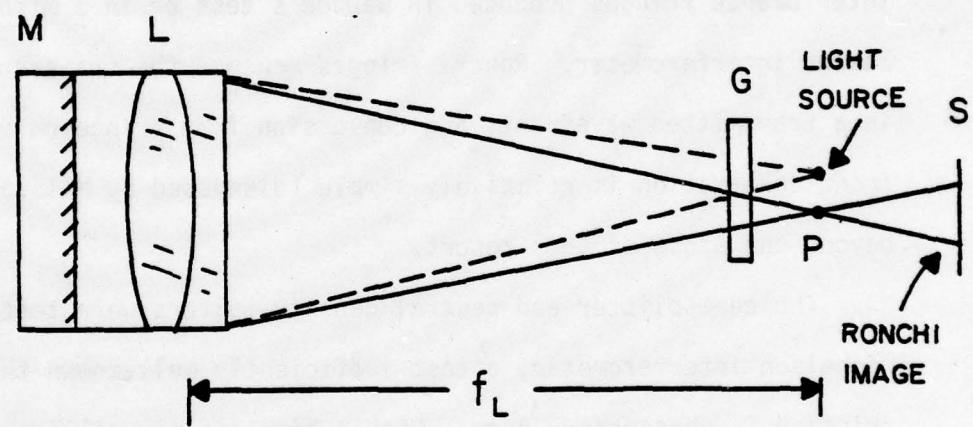
Figure A-2. Autocollimation test of lens L using an optically flat mirror M and a Ronchi grating at G.

exactly the same focal length, 300 MM., were selected, to serve as the Fourier transforming lenses L_1 and L_2 in Fig. 1-1. They were only single-pass tested, as the extreme sensitivity of the double-pass autocollimation test was unnecessary. Both were only very slightly undercorrected, the fringe curvature barely discernable but nevertheless present. An important note of caution: Ronchi fringes should not be interpreted like the interference fringes produced in Newton's test or in a Michelson or Mach-Zender interferometer. Ronchi fringes measure the transverse aberration in a transmitted wavefront, and conversion from fringe curvature to wave-front deformation is relatively simple (discussed by Malacara [19]), but beyond the scope of this report.

The beamsplitter and neutral density filters were tested using a Michelson interferometer, a test sufficiently well-known that its description is unnecessary here. With a high-quality collimated light beam and equally high-quality mirrors, any resulting wavefront deformation would be due to the beamsplitter alone. The only beamsplitters readily available were of the solid glass cube type. Several were tried in the Michelson, and even the best did its share of damage to the wavefront. The use of the membrane, or pellicle, beamsplitters is urged, if they are available in the required aperture. The neutral density filters were checked by singly inserting them in one leg of the Michelson and comparing the fringe patterns. The filters were well-made and did not appreciably alter the contour of the transmitted wavefront.

The lenses used for documenting the holoplex outputs were usually high-quality camera lenses, whose optical qualities were beyond reproach,

and who were Ronchi-tested anyway. The copy lens that serves as the imaging system holographically represented throughout the project was chosen from several lenses, and produced reasonably straight Ronchi fringes, although a slight trace of undercorrection was visible.

The discussion concerning the testing of the fly's-eye arrays has intentionally been delayed until now, as the entire next section of this appendix is devoted to their analysis. The fly's-eye arrays comprise a very important part of the 2-D space-variant holographic processor, as they are used to generate the array of n sampling points. Since these points were intended to represent true Dirac delta functions, special effort has been spent in analyzing and testing the fly's eye arrays in order to optimize their optical performance.

A.2. Analysis of Fly's Eye Lenslet Arrays

Two types of fly's eye arrays were available for use in this project, those with biconvex lenslets and those with plano-convex lenslets. The construction parameters for each are given in Fig. A-3. Both types were injection-molded, using a special optical acrylic plastic having an index of refraction of 1.491 at 590 NM. For both types, the clear aperture (C.A.) of each lenslet was .140", and the axial thickness was .200". Both radii of curvature for the biconvex array were .292", while for the plano-convex array, the convex radius was .292" and the other radius was, of course, infinite. The distance between lenslet centers was .150" for both arrays.

The two types of arrays could be oriented in three ways with respect to the collimated light:

$R_1 = +.292"$

$R_2 = -.292"$

$t = .200"$

$N_d = 1.491$

C.A. $= .140"$

(a) Biconvex construction parameters.

$R_1 = +.292"$

$R_2 = $ infinite

$t = .200"$

$N_d = 1.491$

C.A. $= .140"$
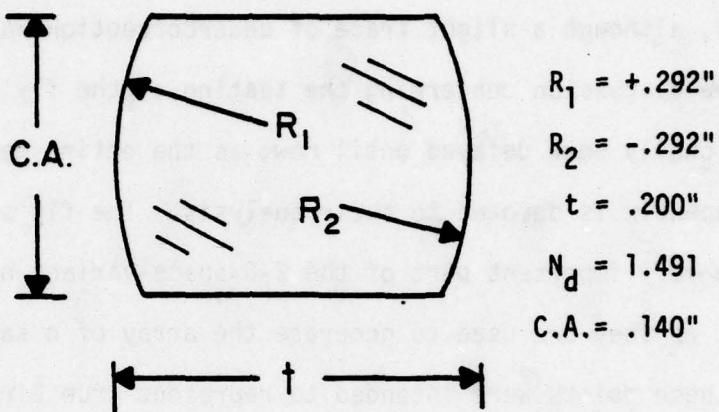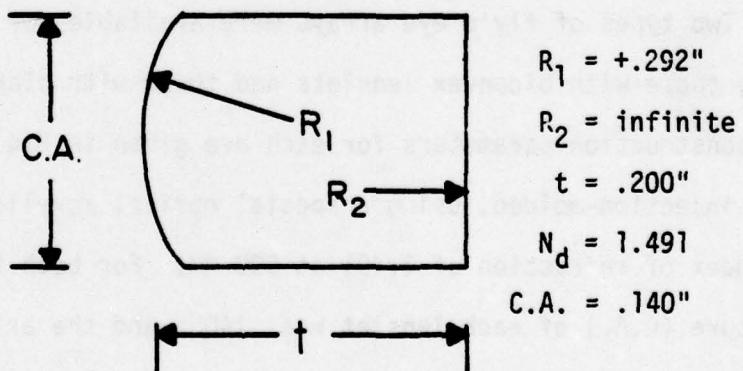
(b) Plano-convex construction parameters.

Figure A-3. Construction parameters for biconvex and plano-convex lenslet arrays.

(1) Plano-convex, convex toward parallel light.
(2) Plano-convex, plane side toward parallel light.
(3) Biconvex, either radius toward parallel light.

The arrays were Ronchi tested in all three orientations, with the following results:

(1) The plano-convex lenslet, plane side toward parallel light, gave the most strongly curved Ronchi fringes, those of undercorrection. This was the worst orientation, giving the poorest imagery.

(2) The biconvex lenslet gave only slightly curved Ronchi fringes, although undercorrection was still clearly visible.

(3) The plane-convex lenslet, with its convex surface toward parallel light, gave superb imagery, with no visible fringe curvature except for the extreme marginal rays, where a touch of undercorrected fringe "hooking" was visible.

Based on the Ronchi tests it was clear that the plano-convex array, with its convex side toward the parallel light, was the optimum orientation. The residual undercorrected fringe hooking could be removed by drilling an array of stop-down masks for both the object and reference beam arrays. These masks would serve an additional vital purpose; because the lenslets were immediately adjacent to each other, lenslet-to-lenslet internal reflections were fairly intense. This would cause obvious problems when trying to use them for sampling optical systems. Illuminating any one lenslet would "turn on" several neighboring lenslets. The stop-down masks would aid in reducing this internal reflection, and if they were drilled so that only every other lenslet was exposed, internal reflection problems would be virtually absent. In actual implementation this worked very well.

It was not known at this point exactly what aperture the stop-down masks should be drilled to. The approximate aperture could be estimated from the Ronchi test, but it was important not to drill them too small, as they ultimately limited the total amount of light available for exposing the holographic plate and for documentation. It was desired to drill them just small enough to clean up the image. The method used to determine the best apertures was raytracing. Three separate sets of raytracing equations were used, which included

(1) Paraxial trace equations, used to precisely determine such parameters as the paraxial back focal length (BFL) and effective focal length (EFL) at a given wavelength;

(2) Meridional trace equations, useful for determining, among other things, the amount of on-axis spherical aberration present at a given wavelength;

and (3) The general skew trace equations, which are an order of magnitude more lengthly to compute, but can accurately trace a general skew ray through a system, thus making them useful for spot diagram generation.

Raytracing is the cornerstone of optical design and optical system analysis. By the iterative application of appropriate raytracing equations, the precise path of an incoming ray of light may be computed, surface by surface, as it passes through an optical system and finally intersects a focal surface. Raytracing is inherently numerically tedious and repetitive; it is this repetitiveness, however, that makes raytracing particularly suitable for the computer and programmable calculator. Recent modifications to the various sets of raytracing equations [23, 24] have streamlined them for the computer for maximum speed. Mathematically,

the equations are exact; numerically, they are only as precise as the machine executing them. The ten-digit accuracy of programmable calculators was more than sufficient for the analysis of the fly's-eye arrays, however.

The paraxial equations used for the first-order tracing of the lenslet arrays were those given by Smith [23, pp. 248-250]. The equations themselves are not lengthly but the description of the sign convention for their use is, and consequently no raytracing equations will appear in this appendix. From paraxial tracing using an HP-97, it was determined that the plano-convex lenslets had an effective focal length (EFL) of .594704", or 15.105 MM., and the biconvex lenslets had an EFL of .335149", or 8.513 MM. Any deviation from these values in subsequent raytracing would constitute aberration.

The on-axis longitudinal spherical aberration was determined by using the meridional trace equations given by Conrady [25, pp. 1-10]. Longitudinal spherical aberration is defined as a variation of focal length with aperture. It was desired to obtain longitudinal spherical aberration graphs for the lenslet arrays for all three configurations; therefore, a large number of rays were traced through the lenslets at several apertures for each configuration. Figures A-4, A-5, and A-6 show the spherical aberration plots for the three configurations, drawn at the same scale. Figure A-4 is the plot for the plano-convex lenslet, with its plane surface toward the parallel light. Figure A-5 is the plot for the biconvex lenslet, and Fig. A-6 is the plot for the plane-convex lenslet with its convex surface facing the parallel light. As
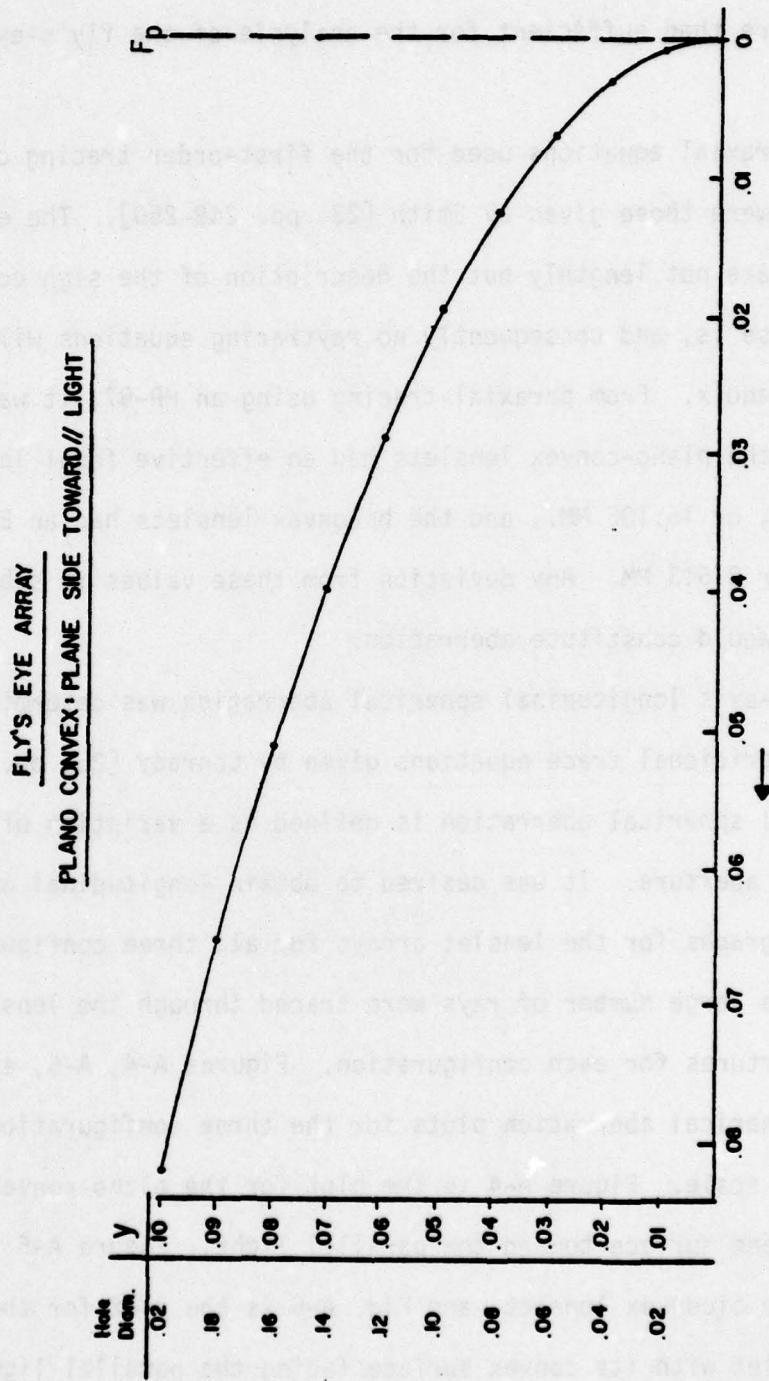
Figure A-4. Longitudinal spherical aberration at 514.5 NM. for plano-convex lenslet, plane side toward parallel light. The corresponding stop-down mask hole diameter is shown at left, and the paraxial focal plane is at right, denoted F_p. All dimensions are in inches.
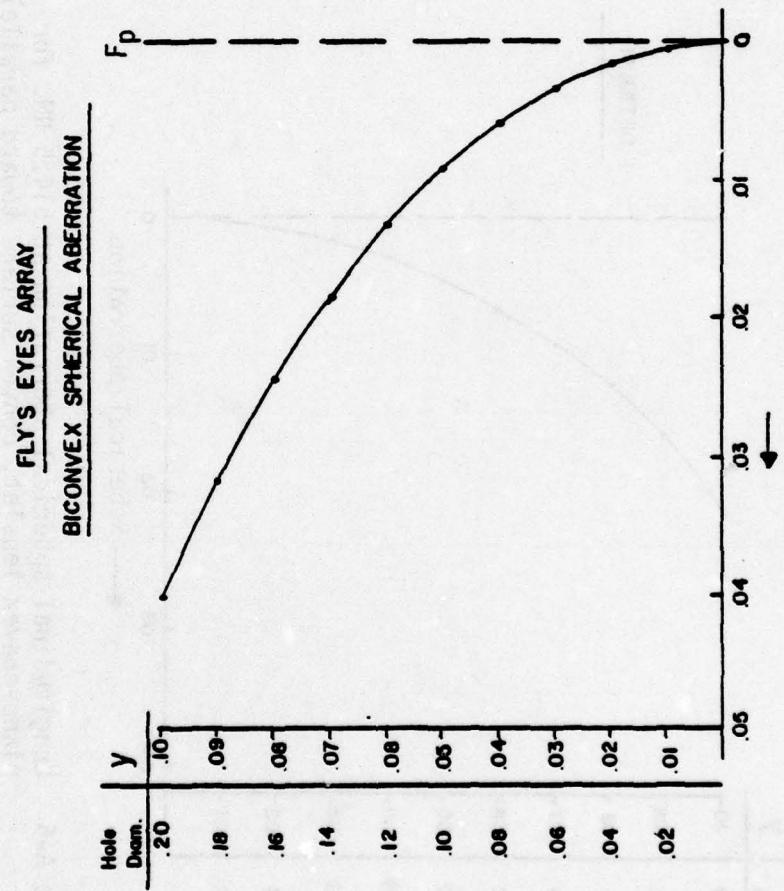
Figure A-5. Longitudinal spherical aberration at 514.5 NM. for bi-
convex lenslet, either side toward parallel light.
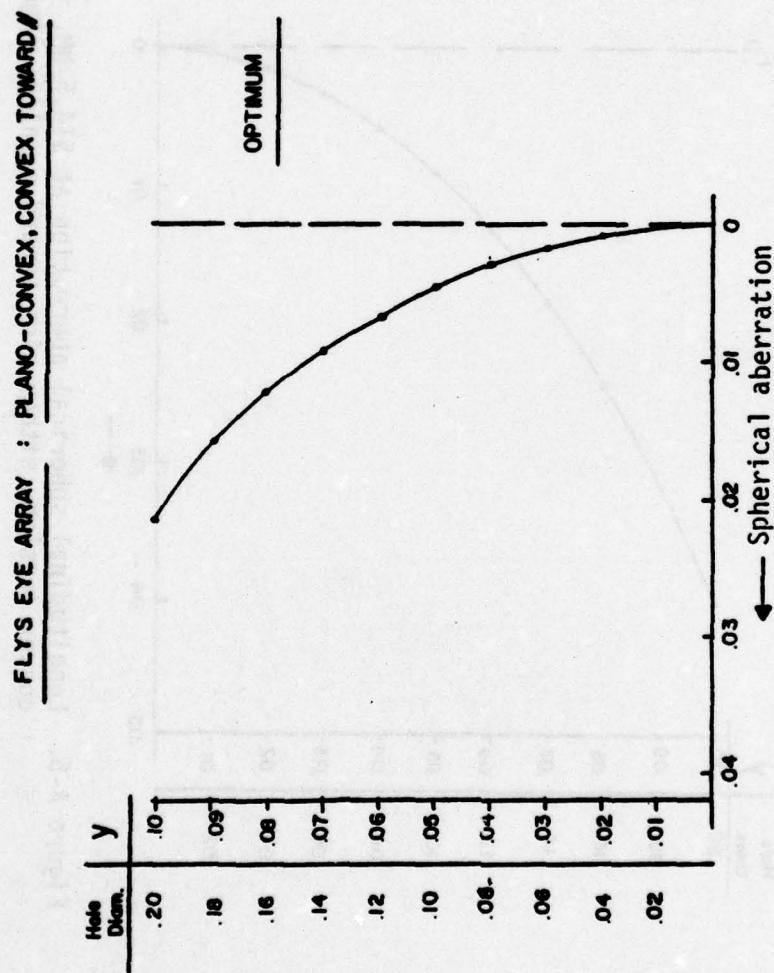
Figure A-6. Longitudinal spherical aberration at 514.5 NM. for plano-convex lenslet, convex surface toward parallel light.

may be seen, this last configuration has the least amount of spherical aberration, thus confirming the results given by the Ronchi test. Comparing Figs. A-4 and A-6 reveals that by merely turning the plano-convex array around we can reduce spherical aberration to less than a fourth of its original value.

With the optimum orientation determined both experimentally and analytically, it remained to calculate the aperture of the stop-down mask holes. From Fig. A-6, we see that a hole diameter of 0.100" gives about .005" of longitudinal aberration, corresponding to an overall blur spot diameter of about 20 μ at focus. The diffraction pattern at this aperture was 6.8 μ in. diameter, or about one-third as large. A smaller hole diameter would produce a smaller blur spot and a larger diffraction pattern, thus improving the lenslet's performance, but would seriously reduce the available illumination to the plate. It was decided to use 7/64", or .109375" holes in the first set of stop-down masks. The 5 x 5 masks were drilled using a milling machine, with the holes on .300" centers, thus skipping every other lenslet. Later in the project, the 10 x 10 stop-down masks were drilled using 3/32" holes located on .150" centers, thus utilizing adjacent lenslets. The smaller holes reduced the available light intensity by 26%, but gave significantly smaller blur spots at focus, the spots now being only about 16 μ in. diameter. The blur spots produced by either set of masks were still of smaller dimensions than the autocorrelation width of the #80 grit ground glass diffuser, estimated at 25-30 μ. Therefore, an insignificant amount of degradation was expected.

An interesting result was observed when spot diagrams of the two lenslet types were generated. These spots appear in Figs. A-7 through A-12. In the generation of spot diagrams, a large number of rays are traced through a lens system using the general skew tracing equations given in either Smith [23, pp. 254-262] or in the Military Handbook of Optical Design MIL-HDBK-141 [24, pp. 5-5 through 5-21]. Rays only need be traced through quadrants I and IV of the system, as the spot is symmetric for quadrants II and III. In this project a computer code was written to trace a total of 117 rays through the right half of a system, the left half of the spot being generated only during plotting. In Figs. A-7, A-8, and A-9, we see the spots produced by the plano-convex lenslet (convex toward parallel light) for 5°, 2.5°, and 0° off-axis, respectively, for an aperture of 7/64". The sizes of these spots may be estimated from the square enclosing them, which is .002", or 50.8 μ, on a side. We see that the spot at 5° off-axis, shown in Fig. A-7, is highly enlarged and elongated when compared to the on-axis spot shown in Fig. A-9. The significance of this behavior is that the plano-convex lenslet array is very sensitive to angular rotation with respect to the optical axis. A small amount of rotation causes the point images to flare considerably.

The spot diagrams for the biconvex lenslets are shown in Figs. A-10, A-11, and A-12. All are generated for the same clear aperture of 7/64". The spots are now enclosed in squares .006", or 152.4 μ, on a side, three times larger than those in Figs. A-7, A-8, and A-9. We see at once that the biconvex lenslets produce immense spots when compared to those produced by the plano-convex lenslets. However, it is apparent from Figs.
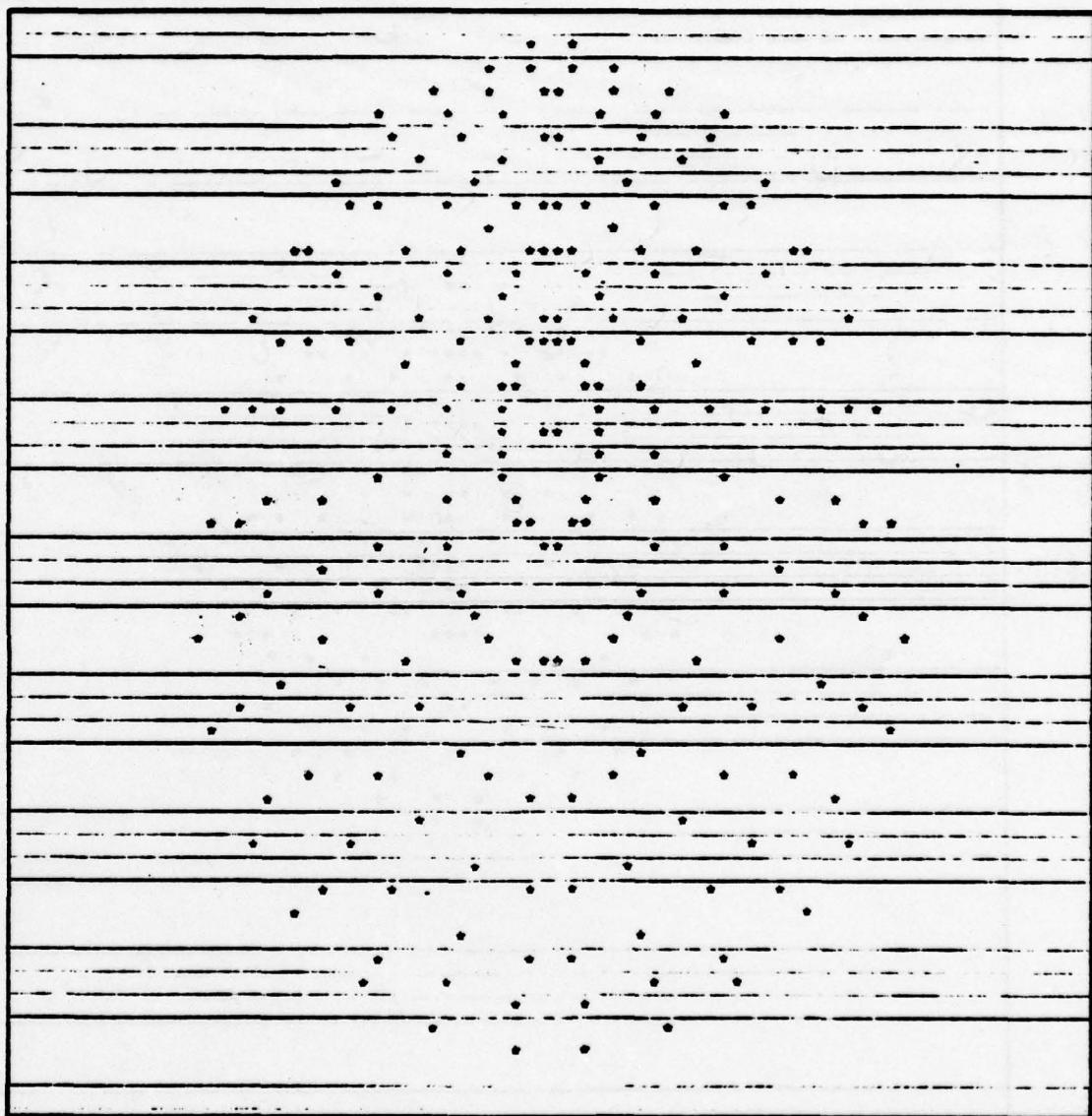
Figure A-7. Spot diagram for plano-convex lenslet, λ = 514.5 NM.,
convex side toward parallel light, 7/64" clear aperture,
5° off axis. The enclosing squares for Figs. A-7, A-8,
and A-9 are .002" on a side. All spots are those below
the optical axis.
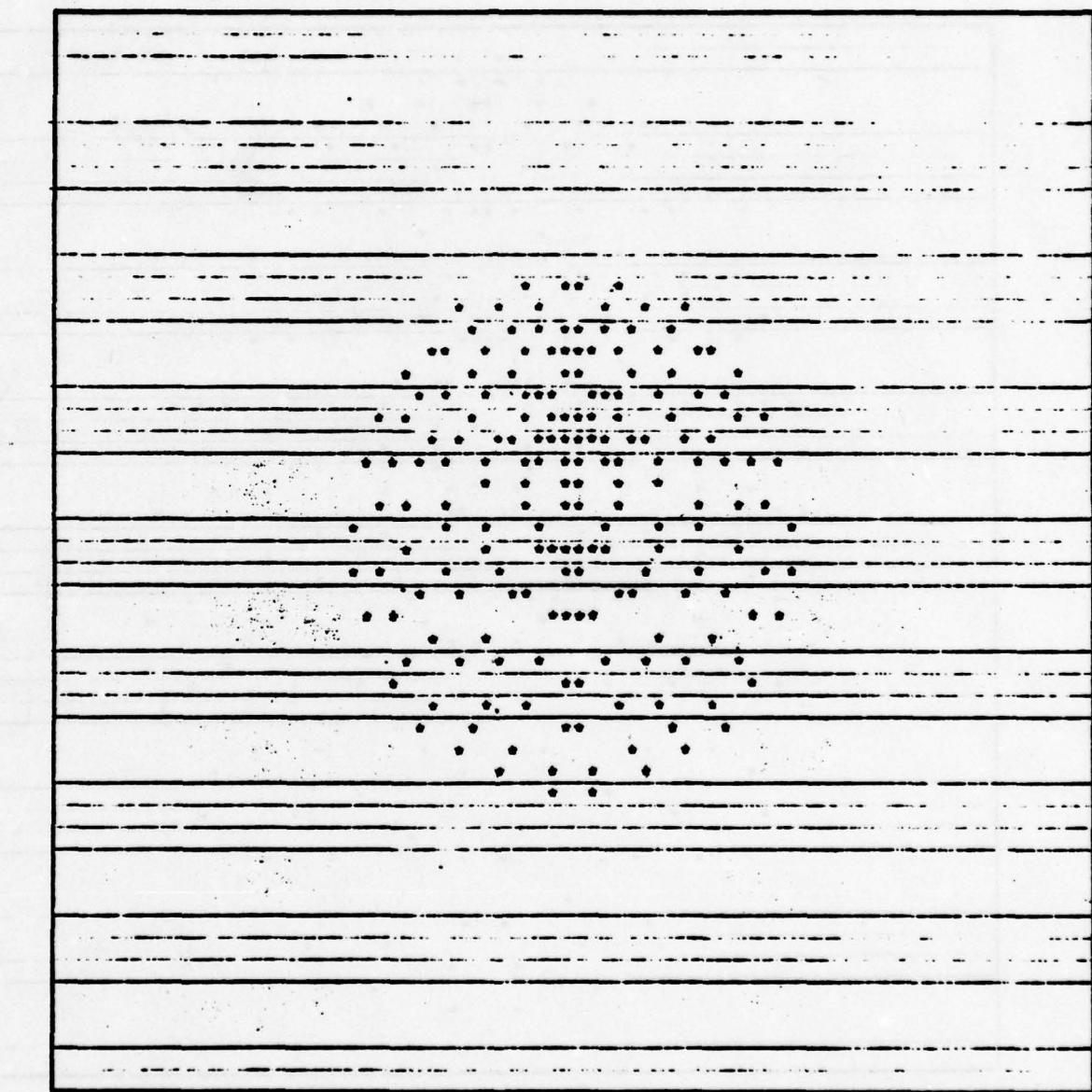
Figure A-8. Spot diagram for plano-convex lenslet, 2.5° off axis.
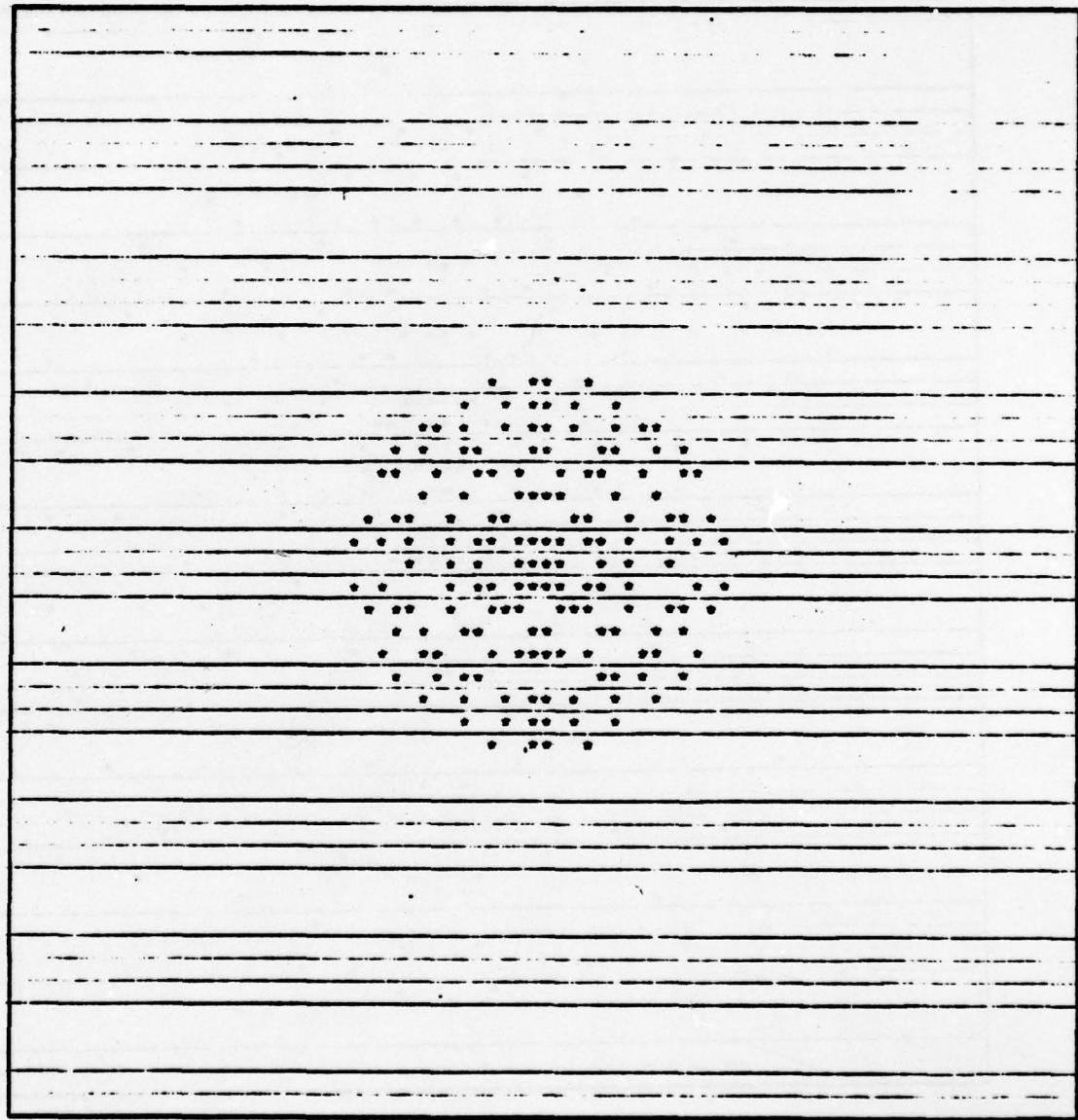
Figure A-9. On-axis spot diagram for plano-convex lenslet, convex side toward parallel light.
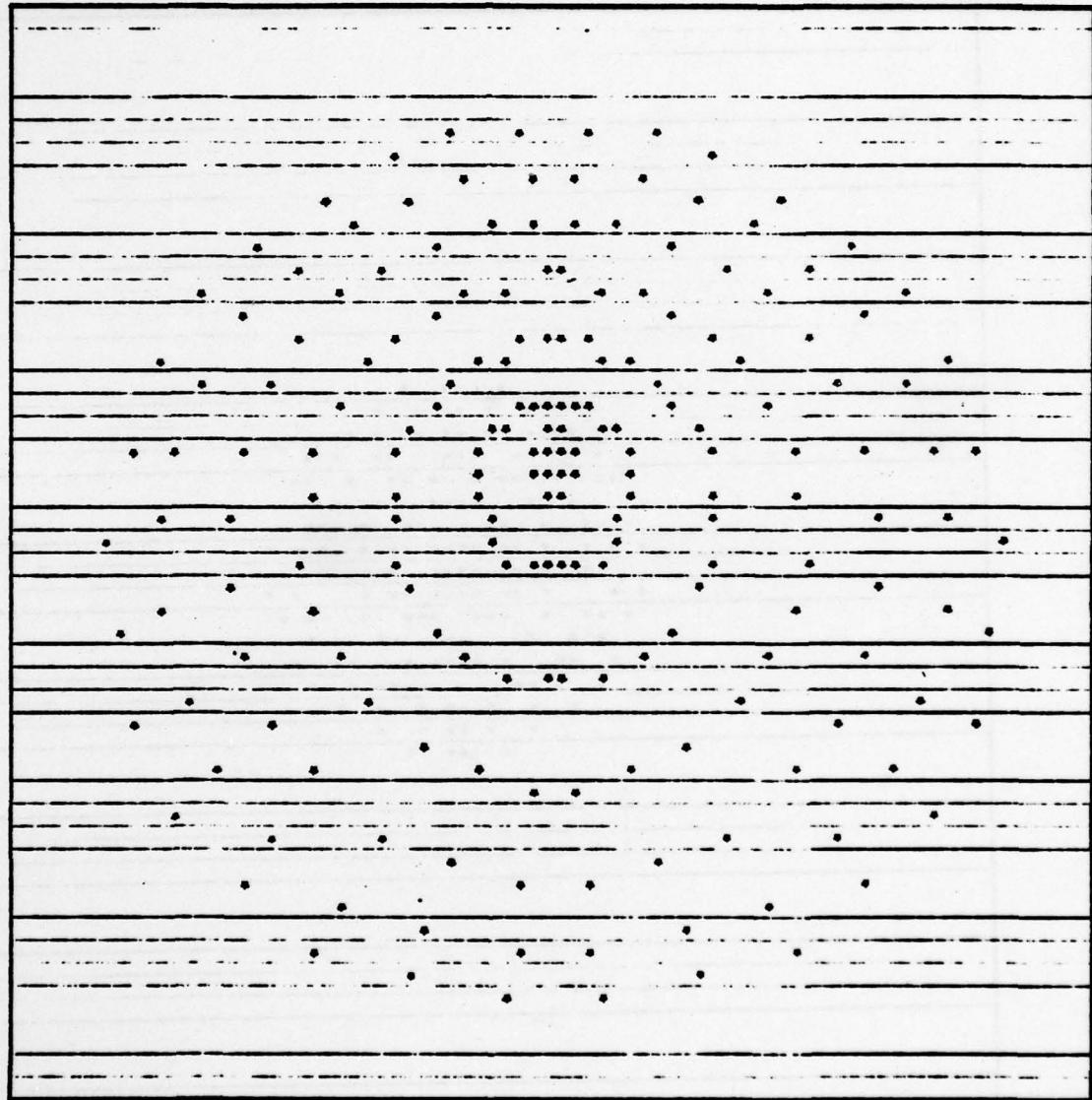
Figure A-10. Spot diagram for biconvex lenslet, λ = 514.5 NM., 7/64" clear aperture, 5° off-axis. The enclosing squares for Figs. A-10, A-11, and A-12 are .006", or 152.4 μ, on a side.
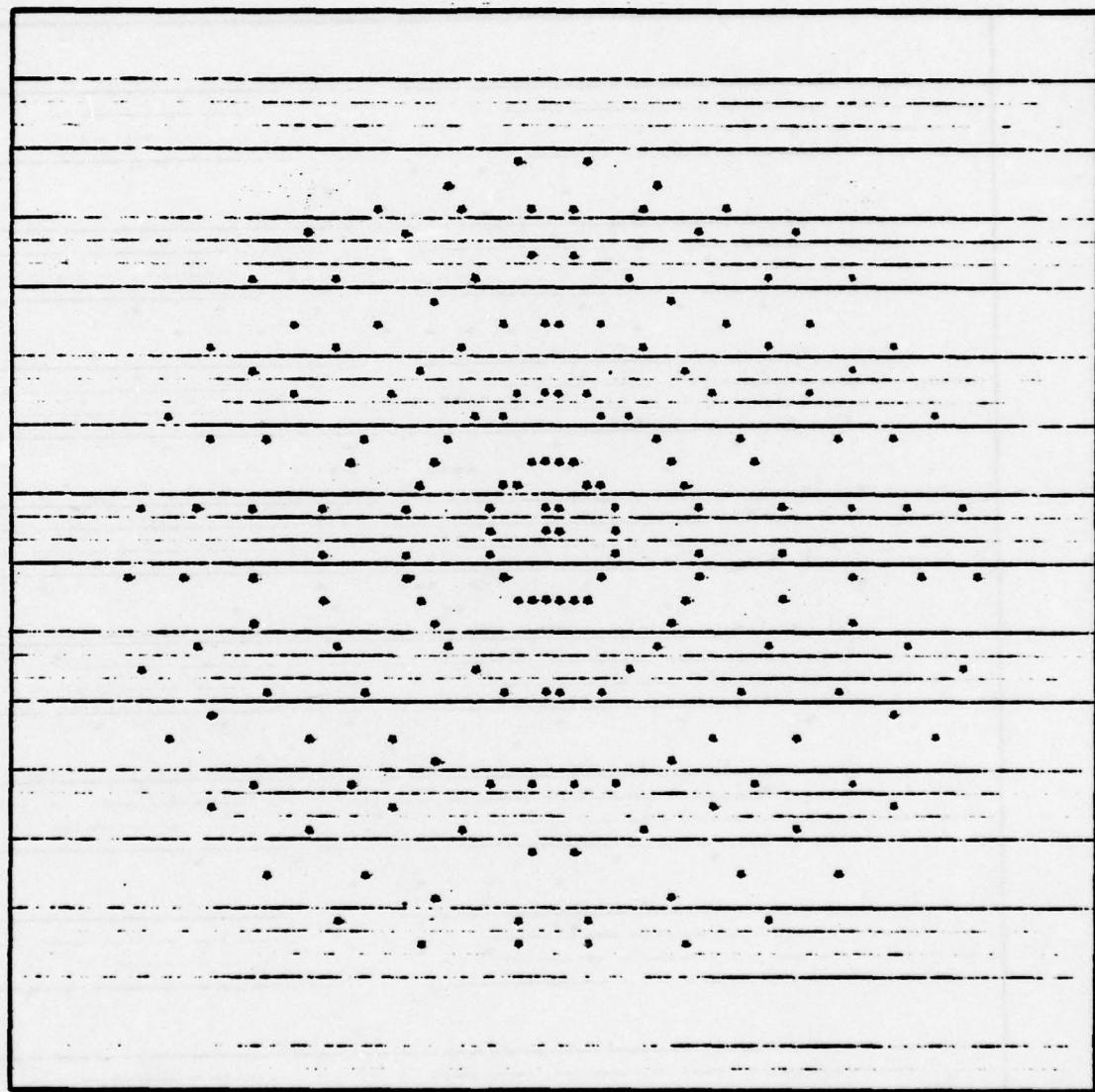
Figure A-11. Spot diagram for biconvex lenslet, 2.5° off axis.
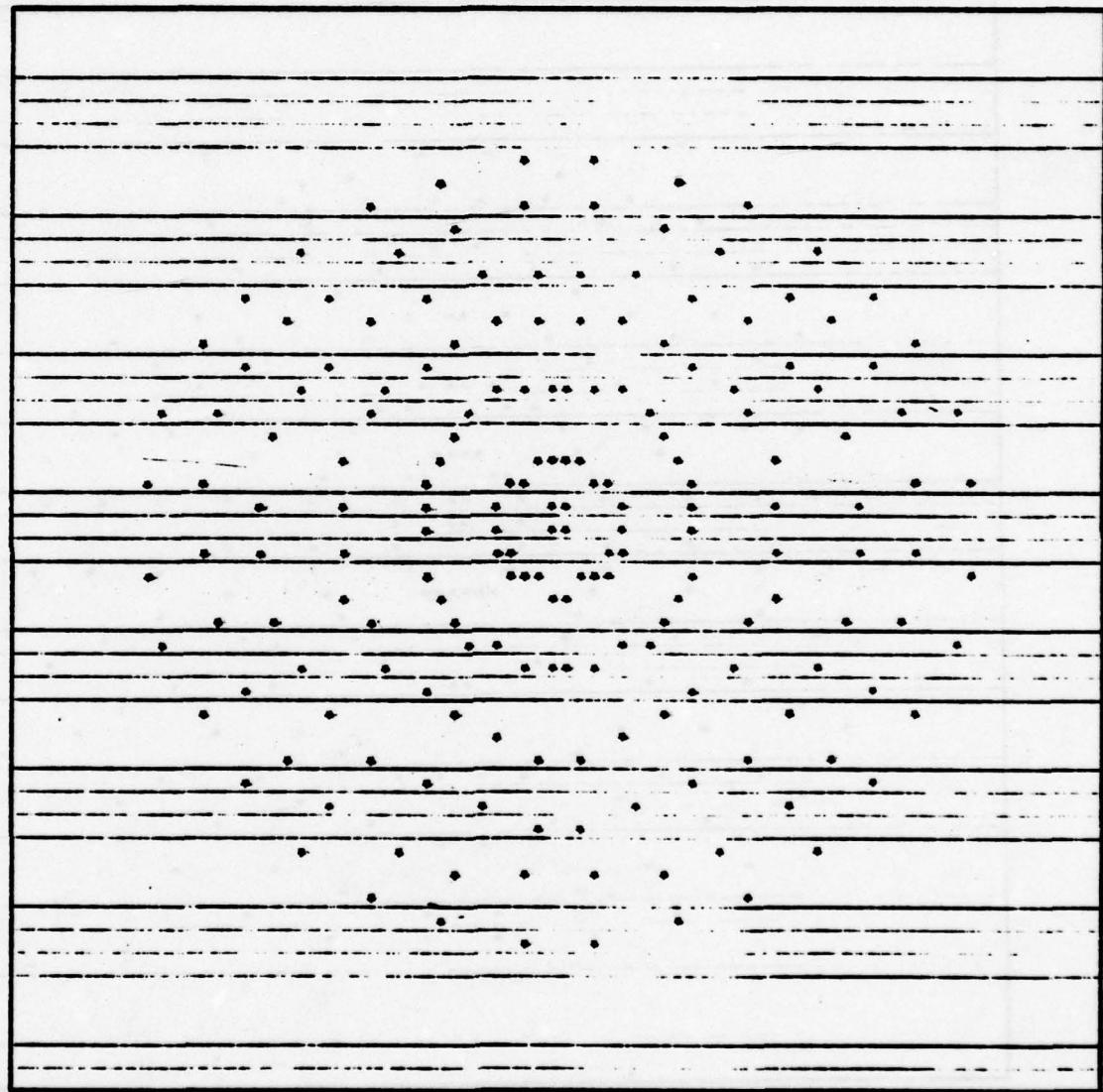
Figure A-12.   On-axis spot diagram for biconvex lenslet.

A-10, A-11, and A-12 that the biconvex array is quite insensitive to angular rotation, as the spots change very little in appearance at all three field angles. The important results from studying these spot diagrams are that:

    (1) The plano-convex lenslet arrays, when used with their convex surfaces toward the collimated light, produce superior point sources, with their stop-down masks in place. They are, however, exceedingly susceptable to image flare, and must be aligned with great care.

    (2) The biconvex lenslet arrays produce relatively poor point sources, even with stop-down masks having reasonably-sized apertures in place, but are much less sensitive to optical misalignment.

It should be noted that when the aberrations of an optical system produce blur spots that are significantly larger than the system's theoretical Airy patterns, the computer-generated spot diagrams provide very good representations of the optical system's point spread functions. The lenslets discussed here all produced spot diagrams much larger than their theoretical Airy patterns. Therefore, from the spot diagrams shown here, we are able to accurately see the light intensity distribution of the point spread functions used in sampling a given optical system for holographic representation in this project.

APPENDIX B

FABRICATION OF GROUND-GLASS DIFFUSER PLATES

The ground-glass diffusers used in this thesis were hand-ground using a simple technique described here. Silicon carbide was used as the grinding compound. This extremely hard material may be purchased in loose particle form, by weight, from many optical and telescope-making supply houses. Silicon carbide is available in the following sizes [17]:

Grit #	Avg. particle size in μ
60	293
80	185
100	148
120	123
180	86
220	73
320	40
400	34
600	25

Finer gradings are available, but it is not advisable to grind plates finer than about #400 grit, as the autocorrelation width, and thus repositioning tolerance, becomes prohibitively small for finer grinds. Aluminum oxide is another abrasive readily available, and is graded the same as silicon carbide. It is not advisable to use aluminum oxide for grinding diffuser plates, however, because it is much softer than silicon carbide and thus requires a larger amount of grinding compound and a longer period of grinding time. The particles of

silicon carbide are sharp and jagged, while aluminum oxide particles are more rounded and smooth. A diffuser ground with silicon carbide will have a rougher, more jagged surface than one ground with aluminum oxide, and will therefore provide better crosstalk dispersion.

In fabricating the ground-glass plates for this thesis, several 4" x 5" scratch-free pieces of 1/8" common window plate glass were first procured. Then, the sharp edges and corners on each piece were beveled under slowly running tap water with a small, flat #220 grit knife-sharpening stove, for safety and to prevent chipping. When beveling, the stone should always be stroked in one direction, away from the faces of each glass plate, to prevent chips from being broken out of the face. All sharp edges and corners were beveled and rounded until smooth to the touch. Care was taken to prevent scratching the faces of the plates during the beveling process.

Then, clean newspaper was spread over a flat, well-lighted work area, and sprinkled with water until moist. A large 12" x 16" piece of 1/4" scrap plate glass was placed on the moist newspaper, and sprinkled thoroughly with water. A spoonful of grit was placed on the plate and smoothed around in the water with the finger. The amount of grit is important; too much results in a thick, pasty mud, in which all grinding action ceases. If too little grit is used the glass scratches rather than grinds. Then, the 4" x 5" plate was placed on the lower plate. Grinding was accomplished by applying moderate to heavy pressure with the palms and stroking the plate back and forth across the lower plate, first in a long sweeping "W"

stroke, and then in a large figure-8 stroke to blend the surfaces and keep the lower plate flat. At the beginning of grinding, a harsh, grating sound is observed, and as the grinding continues, the grit particles break down and the sound changes to a soft, swishing sound. At this point the plates should be separated and rinsed off in a pail of water. Then fresh grit is applied and the cycle repeated. This completes what is commonly termed as one "wet." Depending on grinding pressure used, about ten to fifteen wets should be sufficient to completely frost one side of a 4" x 5" plate. One important note: do not wash the plates in a sink, as grit will plug drainpipes about as well as concrete. All washing should be done in a pan or pail of water that can be dumped and rinsed outdoors.

When grinding the diffuser plates for this thesis, it was noticed that the grinding action was very uneven for the first few wets. Portions of the glass plate were well-frosted while other parts would be nearly clear. Uneven pressure and surface waviness and irregularity were the reasons. As we are not interested in optical flatness, it is entirely acceptable to apply extra pressure to the clear areas. The important thing is that one entire face be evenly and thoroughly frosted, and the other face be as scratch-free as possible. The total time necessary to make a finished 4" x 5" diffuser plate, including beveling time, is about 1½-2 hours.

REFERENCES

1. L. M. Deen, "Holographic Representations of Optical Systems," M.S. Thesis (Department of Electrical Engineering, Texas Tech University, Lubbock, Texas, 1975).

2. L. M. Deen, J. F. Walkup and M. O. Hagler, "Representations of Space-Variant Optical Systems Using Volume Holograms," Appl. Opt. 14, 2438 (1975).

3. R. J. Marks II, "Space-Variant Coherent Optical Processing," Ph.D. Dissertation (Department of Electrical Engineering, Texas Tech University, Lubbock, Texas, 1977).

4. W. D. Redus, "Two-Dimensional Phase Codes for Multiplex Holography," M.S. Thesis (Department of Electrical Engineering, Texas Tech University, Lubbock, Texas, 1978).

5. E. L. Kral, "Correlation Properties of Diffusers for Multiplex Holography," M.S. Thesis (Department of Electrical Engineering, Texas Tech University, Lubbock, Texas, 1979).

6. R. J. Marks II, J. F. Walkup and M. O. Hagler, "A Sampling Theorem for Space-Variant Systems," J. Opt. Soc. Am., Vol. 66, pp. 918-921, 1976.

7. T. F. Krile, R. J. Marks II, J. F. Walkup and M. O. Hagler, "Space-Variant Holographic Optical Systems Using Phase-Coded Reference Beams," Proc. of 1977 International Optical Computing Conf., San Diego, Aug. 1977, SPIE Vol. 118, pp. 6-10.

8. T. F. Krile, R. J. Marks II, J. F. Walkup and M. O. Hagler, "Holographic Representations of Space-Variant Systems Using Phase-Coded Reference Beams," Appl. Opt. 16, pp. 3131-3134, 1977.

9. T. F. Krile, M. O. Hagler, W. D. Redus and J. F. Walkup, "Multiplex Holography with Chirp-Modulated Binary Phase-Coded Reference-Beam Masks," Appl. Opt. 18, pp. 52-56, 1979.

10. Dr. Marion Hagler and Carl Irby, personal communications, 1977-1979.

11. M. I. Jones, M. O. Hagler and J. F. Walkup, "Implementations of Multiplex Holography in 2-D Space-Variant Optical System Representation," 1978 Annual Meeting of the Optical Society of America, San Francisco, November, 1978.

12. M. I. Jones, J. F. Walkup and M. O. Hagler, "Multiplex Holography for Space-Variant Optical Computing," presented at SPIE Technical Symposium-East, Wash. D.C., April, 1979, SPIE Vol. 177-05.

13. R. N. Bracewell, _The Fourier Transform and its Applications_, (McGraw-Hill, New York, 1965).

14. J. W. Goodman, _Introduction to Fourier Optics_, (McGraw-Hill, New York, 1968).

15. J. D. Gaskill, _Linear Systems, Fourier Transforms, and Optics_, (Wiley, New York, 1978).

16. J. T. La Macchia and D. L. White, "Coded Multiple Exposure Holograms," Appl. Opt. _7_, pp. 91-94, 1968.

17. N. E. Howard, _Standard Handbook for Telescope Making_, (Crowell, New York, 1959), p. 41.

18. R. J. Collier and K. S. Pennington, "Multicolor Imaging from Holograms formed on Two-Dimensional Media," Appl. Opt. _6_, pp. 1091-1095, 1968.

19. D. Malacara, _Optical Shop Testing_, (Wiley, New York, 1978).

20. A. R. Kirkham, "The Ronchi Test for Mirrors," in _Amateur Telescope Making-Book One_, A. Ingalls, ed., (Scientific American, New York, 1970), p. 264.

21. J. A. Anderson and R. W. Porter, "Ronchi's Method of Optical Testing," Astrophys. J., _70_, 175 (1929).

22. J. Texereau, _How to Make a Telescope_, (Interscience, New York, 1957).

23. Warren J. Smith, _Modern Optical Engineering_, (McGraw-Hill, New York, 1966).

24. MIL-HDBK-141, _Optical Design_, Defense Supply Agency, 1962.

25. A. E. Conrady, _Applied Optics and Optical Design_, (Dover Publications, New York, 1957).

26. W. T. Welford, _Aberrations of the Symmetrical Optical System_, (Academic Press, New York, 1974).

27. R. Kingslake, _Lens Design Fundamentals_, (Academic Press, New York, 1974).

28. W. G. Driscoll, ed., _Handbook of Optics_, (McGraw-Hill, New York, 1978).

PART II

CORRELATION PROPERTIES OF DIFFUSERS
FOR MULTIPLEX HOLOGRAPHY

by

E. Lee Kral

ABSTRACT -- PART II

A promising method of representing two-dimensional space-variant optical systems is through multiplex holography. The multiplexing operation requires the use of diffusers in the reference beam path to provide a unique code for each object wave. In this report, various types of diffusers are analyzed and compared within the framework of multiplex holography. A simple model is initially developed which can accommodate a wide range of diffuser families, including pure phase, pure amplitude, and combined amplitude and phase diffusers. Cross-correlation and autocorrelation calculations are then presented for both spherical wave (chirp) illumination and plane wave illumination, and a signal-to-noise analysis based on these calculations is included. Finally, the implications of the analysis are thoroughly discussed, and recommendations for further research are given.

i

TABLE OF CONTENTS -- PART II

Table of Contents (continued)

Table of Contents (continued)

LIST OF FIGURES

vii

LIST OF TABLES

CHAPTER 1

INTRODUCTION

1.1. Use of Diffusers in Multiplex Holography

Several holograms can be stored on the same recording medium if
a different reference beam is used to encode each hologram. A single
hologram can then be accessed by illuminating the storage medium with
the appropriate reference beam. There are two principal methods of
storing the holograms so that they can be accessed individually. One
technique involves the use of volume effects to angle multiplex the
various holograms [1-3]. A second method, and the only one considered
in this thesis, is the use of diffusers in the reference beam path to
provide a unique reference code for each hologram [4-8].

On playback, the ideal wavefront corresponding to any one of the
multiplexed holograms is corrupted by noise. This noise, or crosstalk,
is due to the partial playback of holograms not associated with the
illuminating reference beam code. The severity of the crosstalk is
a function of the spatial autocorrelation and crosscorrelation prop-
erties of the diffuser-encoded reference beams, and is therefore highly
dependent on diffuser characteristics. These points are discussed
in more detail in the following section.

1.2. Space-Variant System Representation by Multiplex Holography

A promising application of multiplex holography, and the primary
motivation for the work in this thesis, is the holographic represen-

1

tation of two-dimensional space-variant optical systems [7, 8]. The recording scheme for such a representation is illustrated in Fig. 1-1.

The space-variant system S in Fig. 1-1 is spatially sampled in a sequential manner by the point sources i_1, i_2, ..., i_N. Each point source i_K elicits a corresponding system impulse response h_K. Associated with the Kth input point source is an encoding reference beam r_K. If the recording medium is biased so that the amplitude transmittance of the resulting hologram is proportional to the exposing intensity pattern [9], then the transmittance can be expressed as

$$t = \sum_{i=1}^{N} |H_i + R_i|^2, \qquad (1-1)$$

where H and R are in general complex-valued. The quantities H_i and R_i in Eq. (1-1) are the Fourier transforms of h_i and r_i respectively, and are a consequence of the Fourier transforming properties of lenses L_1 and L_2 in Fig. 1-1.

The playback configuration is shown in Fig. 1-2. The reference beam weighting constants s_1 through s_N are obtained by sampling an input transparency with an array of point sources, as illustrated in Fig. 1-3. These weighted reference beams are Fourier transformed by lens L_2, and simultaneously expose the multiplexed hologram. The field incident on the hologram can therefore be expressed as

$$U_I = \sum_{i=1}^{N} s_i R_i. \qquad (1-2)$$

The field immediately exiting the hologram is equal to the incident field pattern multiplied by the transmittance function of
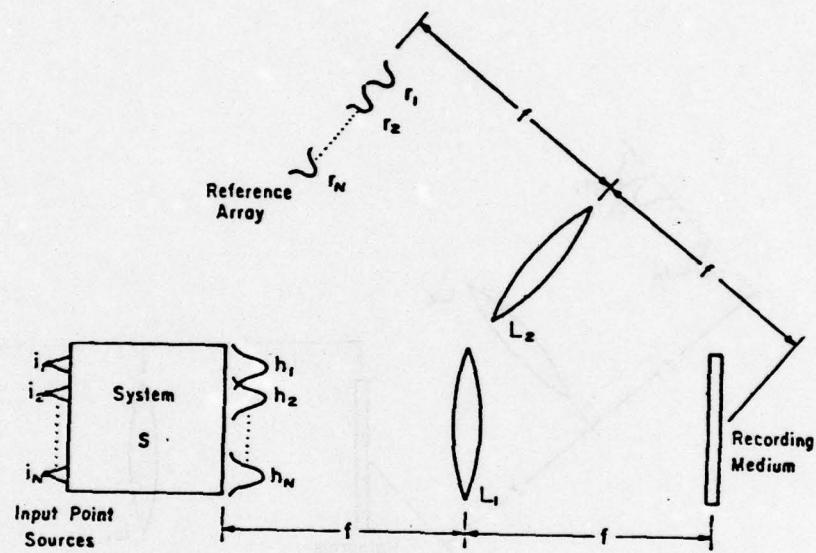
Fig. 1-1 Recording Scheme for the Holographic Representation of a Space-Variant System
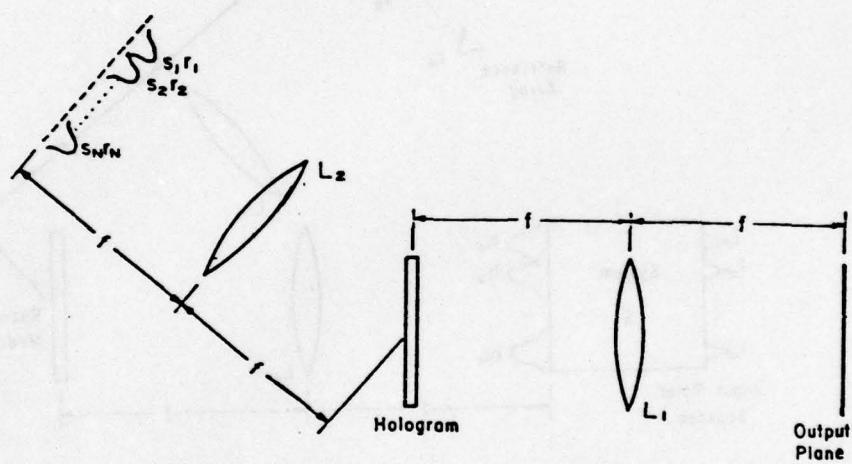
Figure 1-2 Playback Scheme for the Holographic Repre-
sentation of a Space-Variant System
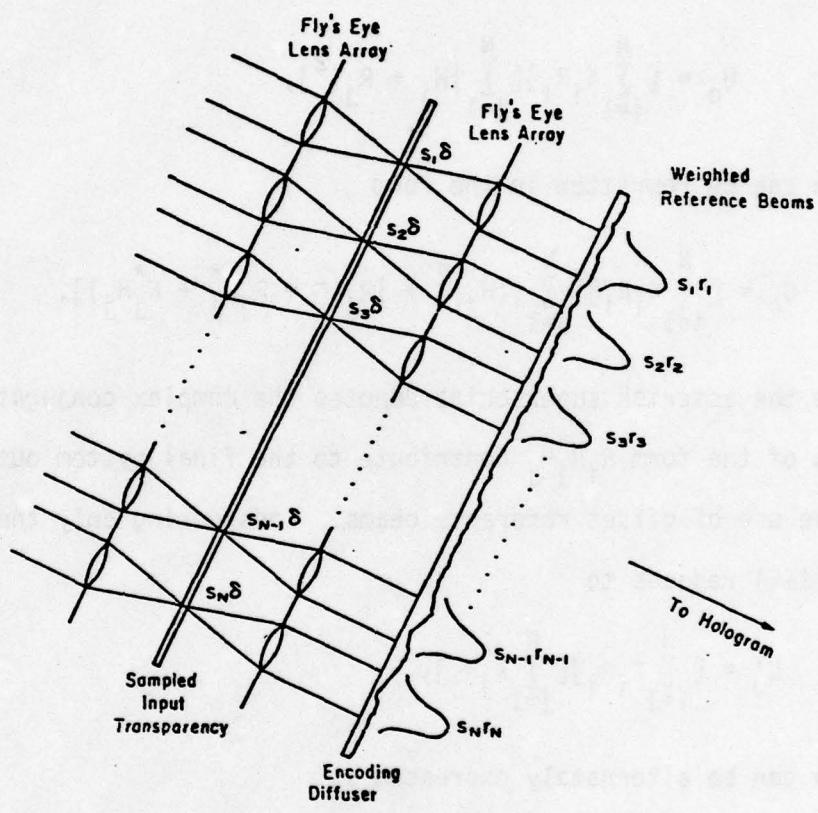
Fig. 1-3 Sampling the System Input

the hologram; that is,

$$U_0 = U_I t \quad . \tag{1-3}$$

Substituting for U_I and t from Eqs. (1-1) and (1-2) gives

$$U_0 = [\sum_{i=1}^{N} s_i R_i][\sum_{j=1}^{N} |H_j + R_j|^2], \tag{1-4}$$

which can be rewritten in the form

$$U_0 = [\sum_{i=1}^{N} s_i R_i][\sum_{j=1}^{N} (|H_j|^2 + |R_j|^2 + R_j H_j^* + R_j^* H_j)], \tag{1-5}$$

where the asterisk superscript denotes the complex conjugate. Only terms of the form $R_i R_j^* H_j$ contribute to the final system output, due to the use of offset reference beams. Considering only these terms, Eq. (1-5) reduces to

$$U_0' = [\sum_{i=1}^{N} s_i R_i][\sum_{j=1}^{N} R_j^* H_j], \tag{1-6}$$

which can be alternately expressed as

$$U_0' = \sum_{i=1}^{N} s_i H_i |R_i|^2 + \sum_{\substack{i \neq j}}^{N} \sum^{N} s_i R_i R_j^* H_j \quad . \tag{1-7}$$

The field U_0' is Fourier transformed by lens L_1 (see Fig. 1-2) to give the output plane field distribution

$$0 = \sum_{i=1}^{N} s_i h_i^* (r_i \otimes r_i) + \sum_{\substack{i \neq j}}^{N} \sum^{N} s_i h_j^* (r_i \otimes r_j), \tag{1-8}$$

where * denotes convolution, $\otimes$ denotes correlation, and the convolu-

tion, correlation, and linearity properties of the Fourier transform are used [10].

The ideal output of the system shown in Fig. 2-1 is

$$O_{ideal} = \sum_{i=1}^{N} s_i h_i. \tag{1-9}$$

From Eqs. (1-8) and (1-9), it is seen that the actual output O reduces to the ideal output O_{ideal} if the reference beam autocorrelations $r_i \circledast r_i$ are Dirac delta functions and the crosscorrelations $r_i \circledast r_j$, $i \neq j$, are zero-valued. Now the reference beams r_1 through r_N are related to the transmittance functions of the encoding diffusers by

$$r_i = u_i t_i, \tag{1-10}$$

where u_i is the field incident on the ith diffuser and t_i is the corresponding diffuser transmittance function. The performance of the system is therefore dictated primarily by the diffuser characteristics (the incident field u_i is also important, but is much more restricted in functional form than t).

1.3. Objectives of the Thesis

As demonstrated in the preceding section, the output of a multiplexed hologram representing an optical system is strongly dependent on the encoding diffuser properties. The principal objective of this thesis is to analyze the effect of salient diffuser parameters (such as resolution cell size, transmittance characteristics, etc.) on system performance. To this end, a simple general model is developed

which can accommodate a wide variety of diffuser families, and calculations are subsequently carried out through which meaningful conclusions can be drawn. A second objective, which is closely related to the diffuser analysis, is to mathematically compare the effects of spherical wave (chirp) illumination and plane wave illumination in terms of crosstalk suppression [8, 11].

1.4. Overview of the Thesis

A general diffuser model based on the random telegraph signal is presented in Chapter 2, along with specific models for pure phase, pure amplitude, and combined amplitude and phase diffusers. The spatial crosscorrelation properties of the various diffuser models are calculated in Chapter 3 for both plane wave and chirp illumination. The diffuser autocorrelation properties are evaluated in Chapter 4, again for both plane wave and chirp illumination. A signal-to-noise ratio performance analysis is presented in Chapter 5, which provides a basis for diffuser comparisons. Finally, in Chapter 6, the results of the previous chapters are summarized and conclusions are drawn.

CHAPTER 2

DIFFUSER MODELS

2.1. Introduction

A diffuser family can be represented mathematically as a two-dimensional random amplitude transmittance $t(x,y)$, where t is in general a complex quantity. Each particular diffuser is a realization or sample value of this random process. For simplicity, the diffuser function is assumed to be separable into a product of two independent one-dimensional random processes; that is, $t(x,y) = t_1(x)t_2(y)$. Under this assumption, the analysis can be carried out in one dimension without sacrificing any generality in the final results.

Careful modeling of the amplitude transmittance representing a diffuser family is an important first step in analyzing and comparing the different classes of diffusers. It is desirable to choose a model which incorporates all the important diffuser characteristics but is free from needless complications. A simple diffuser model which boasts these advantages and is also intuitively appealing is a variation of the so-called random telegraph wave [12] used in modeling communication signals.

2.2. Random Telegraph Wave Description

A typical binary-valued random telegraph signal (temporal) is illustrated in Fig. 2-1. The randomness of the signal is manifested

9
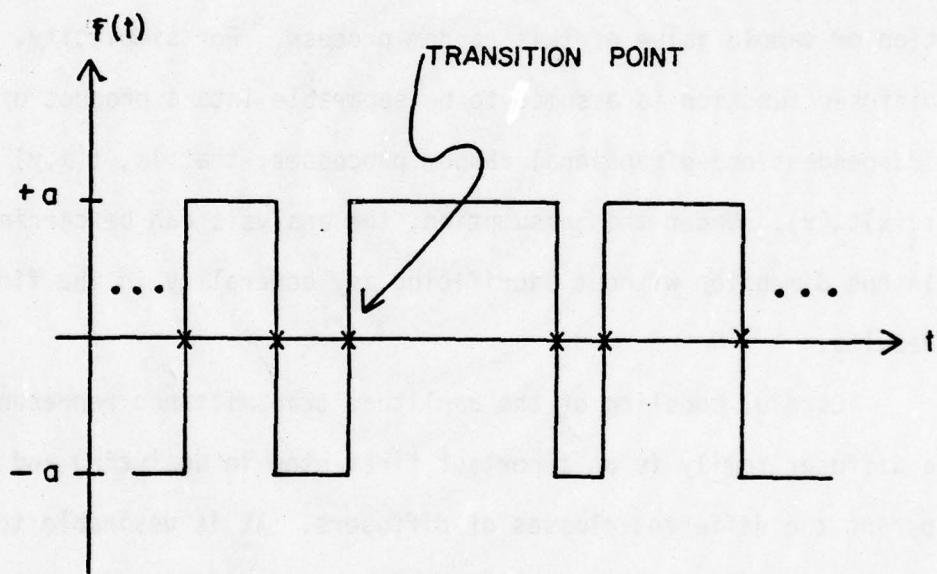
Fig. 2-1 A Typical Random Telegraph Wave

in both the possible amplitude levels and the transition points. The
amplitude is a random variable in that it can assume either of two
possible values governed by some probability law, for example $P(a) =$
$P(-a) = \frac{1}{2}$ (see Fig. 2-1). The spacing between the transition points
is also, in general, a random variable. The transition points of
the signal in Fig. 2-1 are indicated by x's.

2.3. General Diffuser Model Based on the Random Telegraph Wave

The general diffuser model which will now be developed is
based on the random telegraph wave,[#] but differs from the traditional
random telegraph wave in two respects. First, the amplitude in the
diffuser model is a complex amplitude transmittance, which can in
general assume any of a continuous range of values, whereas the
traditional random telegraph signal is restricted to two amplitude
levels. Second, a diffuser represents a random process in space,
whereas the telegraph wave is a random process in time. These dis-
tinctions are illustrated in Fig. 2-2.

All of the diffuser models implemented in this thesis have the
following two properties:

(1) The complex amplitude transmittance between consecu-
tive transitions is a constant.

(2) The amplitude transmittance values in different
diffuser cells are statistically independent.

The term "diffuser cell" is defined in Sec. 2.4.1.2. As an example,
regions 1 and 2 of Fig. 2-2(a) represent different diffuser cells, and
the transmittance levels in these intervals are therefore statistically
independent.

[#]Burckhardt [26] points out this analogy for a binary phase diffuser.
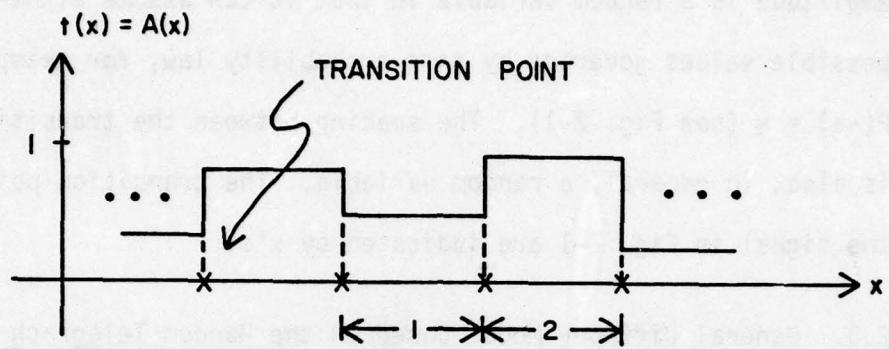
(a) Transmittance function
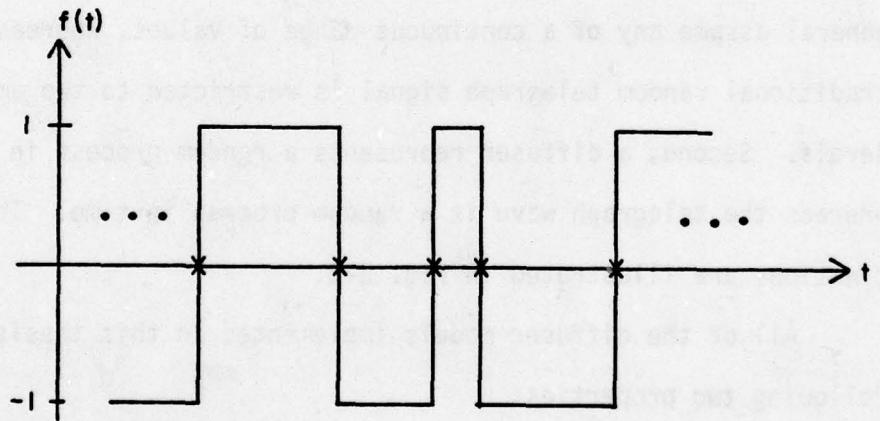
(b) Telegraph wave

Fig. 2-2 Comparison of a Diffuser Transmittance Function
and a Random Telegraph Wave

Property (1) is directly analogous to the random telegraph wave. Property (2) is very important in reducing the complexity of the calculations. These features of the general diffuser model are described more fully in the next section.

2.4. Specific Diffuser Models

The transition characteristics and amplitude transmittance characteristics of the general diffuser model can be tailored to fit various diffuser families. The models used in the analysis and the types of diffusers they represent are listed below.

2.4.1. Diffuser Transition Models

Before defining the two transition models employed in this thesis, it is useful to distinguish between an "actual" transition point and a "potential" transition point. The actual transition points, as marked on Figs. 2-1 and 2-2, are where the function changes value; in other words, a discontinuity in a diffuser function defines the location of an actual transition point. On the other hand, a diffuser function may or may not change value at a potential transition point; the transmittance is not necessarily discontinuous at such a point. This concept finds application in Sec. 2.4.1.2.

2.4.1.1. Poisson Transition Points

A model for ground glass based on the random telegraph wave must incorporate a degree of randomness in the spacing of the complex amplitude transition points. The Poisson model is an obvious choice, and has been used in a somewhat similar context by other authors [13].

The number of (actual) amplitude transitions in a diffuser of
finite width W is modeled as a Poisson-distributed random variable
(the diffuser width W in the one-dimensional analysis corresponds
to diffuser area in a two-dimensional sense). Specifically,

$$P(T) = \begin{cases} \dfrac{e^{-\lambda W}(\lambda W)^T}{T!} & , T = 0, 1, 2, \ldots \\ 0, & \text{otherwise,} \end{cases} \qquad (2-1)$$

where T represents the number of transitions in width W, $P(T)$ is the
associated probability mass function, and λ is the mean number of
transitions per unit length. This Poisson modeling of transitions
is tantamount to modeling the spacing between transitions as a random
variable with a negative exponential distribution [14]. The ground
glass phase function of Fig. 2-3 is an example of a waveform exhibit-
ing a Poisson-like spacing of transition points (the previously dis-
cussed concept of "potential" transition points is not pertinent
for this Poisson model).

2.4.1.2. Evenly Spaced Potential Transition Points

Deterministic diffusers, such as Gold code masks [8, 11],
are usually characterized by a constant spacing between potential
transition points. This transition model is illustrated by the binary
amplitude diffuser function in Fig. 2-4, where the actual and potential
transition points are indicated by x's and o's, respectively. Note
that an actual transition point is necessarily a potential transition
point (but not conversely).
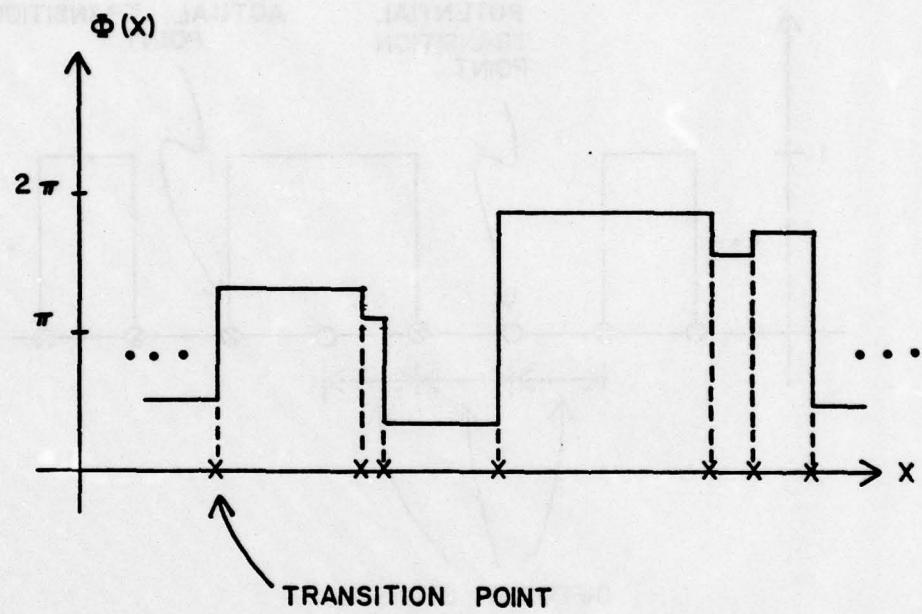
Fig. 2-3 A Ground Glass Phase Function with Poisson
Transitions
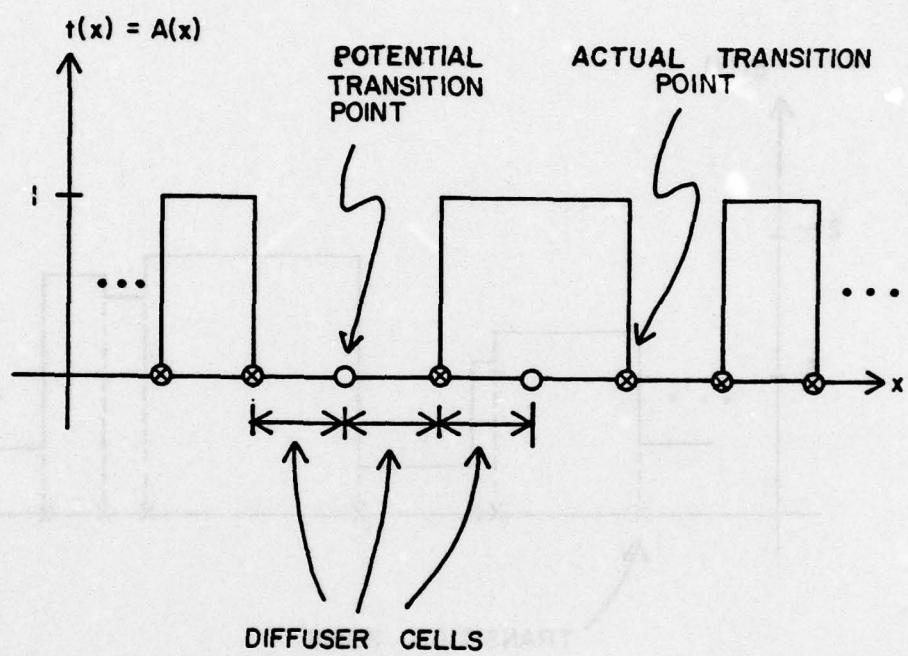
Fig. 2-4 A Binary Amplitude Diffuser Function with
Evenly Spaced Potential Transition Points

The region between adjacent <u>potential</u> transition points will hereafter be referred to as a "diffuser cell." In terms of the Poisson transition model, a diffuser cell is defined as the region between actual transitions, since the concept of potential transitions does not apply to this model (see Sec. 2.4.1.1). From Fig. 2-4, it is evident that the transmittance need not change value from one diffuser cell to the next, due to the statistical independence property of different diffuser cells (see Sec. 2.3).

In addition to deterministic diffusers, many types of random diffusers are characterized by evenly spaced potential transition points. Hence, this model is an exact representation for a wide variety of practical diffusers.

2.4.2. Diffuser Transmittance Models

2.4.2.1. Pure Phase Models

Pure phase diffusers are defined as those diffusers which do not attenuate an incident wavefront but do provide a spatially varying phase shift. The complex amplitude transmittance of these diffusers is mathematically represented as $t(x) = e^{j\phi(x)}$. The randomness in transmittance of a pure phase diffuser is associated entirely with the phase variable $\phi(x)$. Several important phase models are enumerated below.

2.4.2.1.1. Uniformly Distributed Phases

The phase of a ground glass transmittance function can assume any of a continuous range of values. For analytical purposes,

it is modeled as a random variable with a uniform distribution on
the interval $[0, 2\pi]$. Mathematically, this probability density
function (pdf) is expressed as

$$p(\phi) = \begin{cases} \frac{1}{2\pi}, & \phi\epsilon \ [0, 2\pi] \\ \\ 0, & \text{otherwise.} \end{cases} \tag{2-2}$$

The uniform probability density function for the phase distribution
of ground glass has been employed by others [13]. A typical ground
glass model based on both uniformly distributed phase and Poisson
transitions is shown in Fig. 2-3.

2.4.2.1.2. Multilevel (n-level) Phases

A diffuser phase function will be classified as multi-
level if the allowed phases are restricted to a finite number of
discrete values. A probability mass function (pmf) describes this
type of random variable. The following special case of the n-level
model is most commonly encountered, and is the only one considered
in this analysis. The allowed phases are equally spaced over the
entire interval $[0, 2\pi]$, and all phase levels have equal probability
of occurrence. The appropriate probability mass function is

$$P(\phi) = \begin{cases} \frac{1}{n}, & \phi = 0, \frac{2\pi}{n}, \frac{4\pi}{n}, \ldots, \frac{(n-1)(2\pi)}{n} \\ \\ 0, & \text{otherwise.} \end{cases} \tag{2-3}$$

A multilevel model satisfying Eq. (2-3) will hereafter be referred to as a "balanced" phase model. Note that the uniform phase model of Eq. (2-2) is a limiting case of the balanced model as the number of allowed levels n approaches infinity. Phasor representations of a number of multilevel phase models, including both the balanced and unbalanced cases, are shown in Fig. 2-5. The phasor angles of Fig. 2-5 correspond to the allowed phases, and the phasor lengths are proportional to the probability of occurrence.

One characteristic of the balanced model which makes it especially attractive is that the difference $\phi_1 - \phi_2$ of two independent, identically distributed balanced phase variables is also a balanced phase variable (if the phase is considered in a modulo - 2π sense). This property is used extensively in Chapters 3 and 4, and is demonstrated in Appendix A-1.

2.4.2.1.3. Binary Phases

The binary phase model is an important special case of the multilevel model. The binary phase model employed in the calculations is the previously defined balanced model, where

$$P(\phi) = \begin{cases} \frac{1}{2}, & \phi = 0, \pi \\ 0, & \text{otherwise.} \end{cases} \tag{2-4}$$

A sample binary phase diffuser function is shown in Fig. 2-6.

(a) Unbalanced phase models

$n = 4$
$\Phi \in [0, \pi/4, 3\pi/2, 7\pi/4]$
$P(0) = 1/5$
$P(\pi/4) = 2/5$
$P(3\pi/2) = 1/5$
$P(7\pi/4) = 1/5$

$n = 4$
$\Phi \in [0, \pi/2, \pi, 3\pi/2]$
$P(0) = 1/4$
$P(\pi/2) = 1/8$
$P(\pi) = 1/8$
$P(3\pi/4) = 1/2$
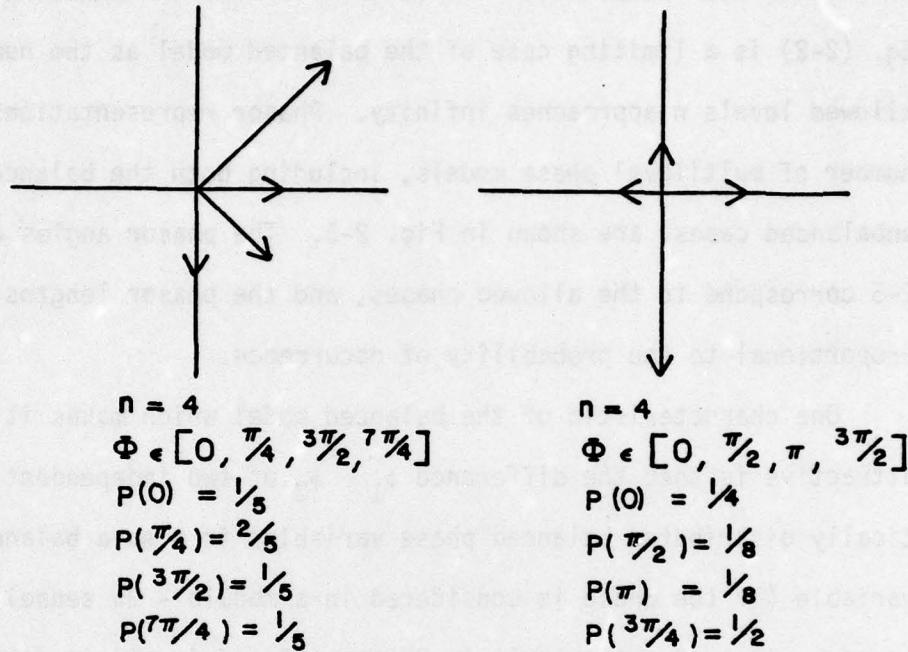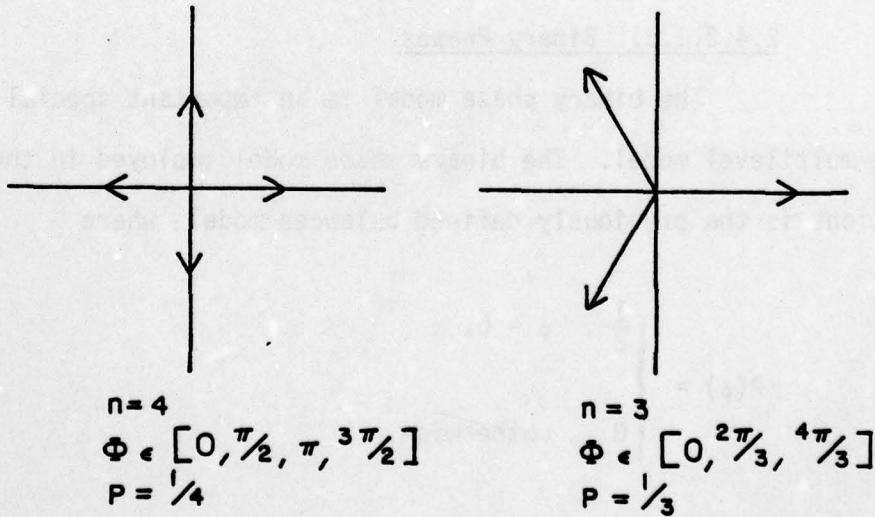
(b) Balanced phase models

$n = 4$
$\Phi \in [0, \pi/2, \pi, 3\pi/2]$
$P = 1/4$

$n = 3$
$\Phi \in [0, 2\pi/3, 4\pi/3]$
$P = 1/3$

Fig. 2-5 Phasor Representation of the Multilevel Phase
         Model
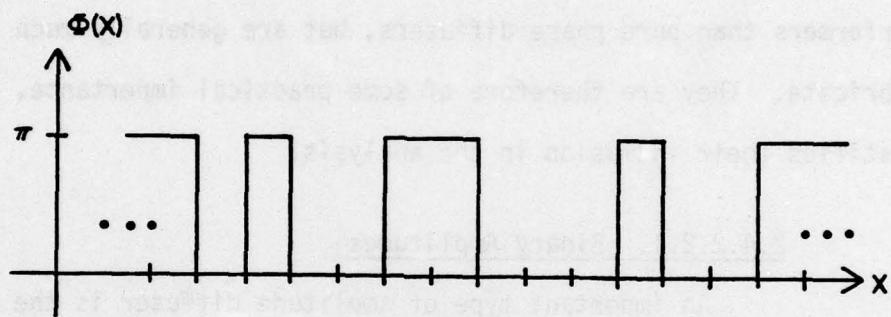
Fig. 2-6 A Binary Phase Diffuser Function

2.4.2.2. Pure Amplitude Models

Pure amplitude diffusers are the class of diffusers which attenuate an incident wavefront in some spatially varying manner, but do not provide a phase shift. Such diffusers are represented mathematically as $t(x) = A(x)$, where $A(x)$ is a real-valued transmittance function. As will be seen, pure amplitude diffusers are poorer performers than pure phase diffusers, but are generally much easier to fabricate. They are therefore of some practical importance, which justifies their inclusion in the analysis.

2.4.2.2.1. Binary Amplitudes

An important type of amplitude diffuser is the binary amplitude diffuser, or random checkerboard, where the pmf is

$$P(A) = \begin{cases} \frac{1}{2}, & A = 0, 1 \\ \\ 0, & \text{otherwise.} \end{cases} \qquad (2\text{-}5)$$

A sample diffuser function of the random checkerboard type is illustrated in Fig. 2-4.

2.4.2.2.2. Uniformly Distributed Amplitudes

The probability density function of the uniform amplitude model is

$$p(A) = \begin{cases} 1, & A \in [0, 1] \\ \\ 0, & \text{otherwise.} \end{cases} \qquad (2\text{-}6)$$

A representative diffuser function based on this model is given in Fig. 2-2(a).

2.4.2.2.3. Multilevel Amplitudes

A multilevel or n-level amplitude model provides for an amplitude which can assume any of n values according to some probability law. An example is the four-level model defined by the pmf

$$P(A) = \begin{cases} \frac{1}{4}, & A = 0, \frac{1}{3}, \frac{2}{3}, 1 \\ \\ 0, & \text{otherwise.} \end{cases} \tag{2-7}$$

This particular model is illustrated in Fig. 2-7. The multilevel and the uniformly distributed amplitude models are not as important as the binary model, but are included for completeness.

2.4.2.3. Combined Amplitude and Phase Models

The most general complex amplitude transmittance model should of course allow for both phase and amplitude variations. Some calculations based on models of this type are included in the following chapters, under the assumption that the amplitude $A(x)$ and the phase $\phi(x)$ of the transmittance function $t(x) = A(x)e^{j\phi(x)}$ are statistically independent random processes.

2.4.3. Diffuser Models Implemented in the Analysis

The transition models and transmittance models described in the preceding sections can be combined in various ways to represent
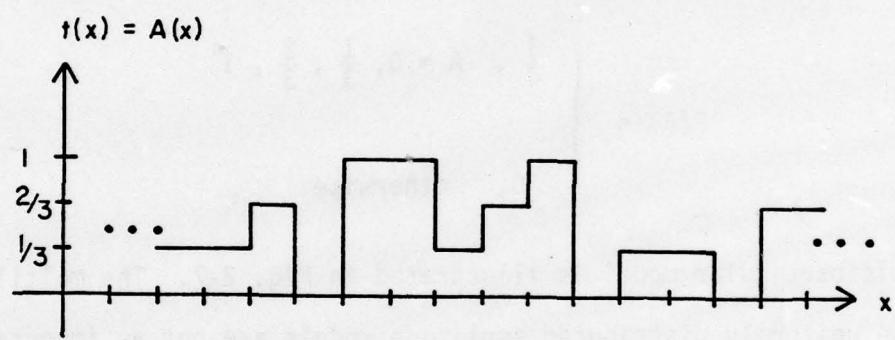
Fig. 2-7 A Four-Level Amplitude Diffuser Function

MICROCOPY RESOLUTION TEST CHART
NATIONAL BUREAU OF STANDARDS
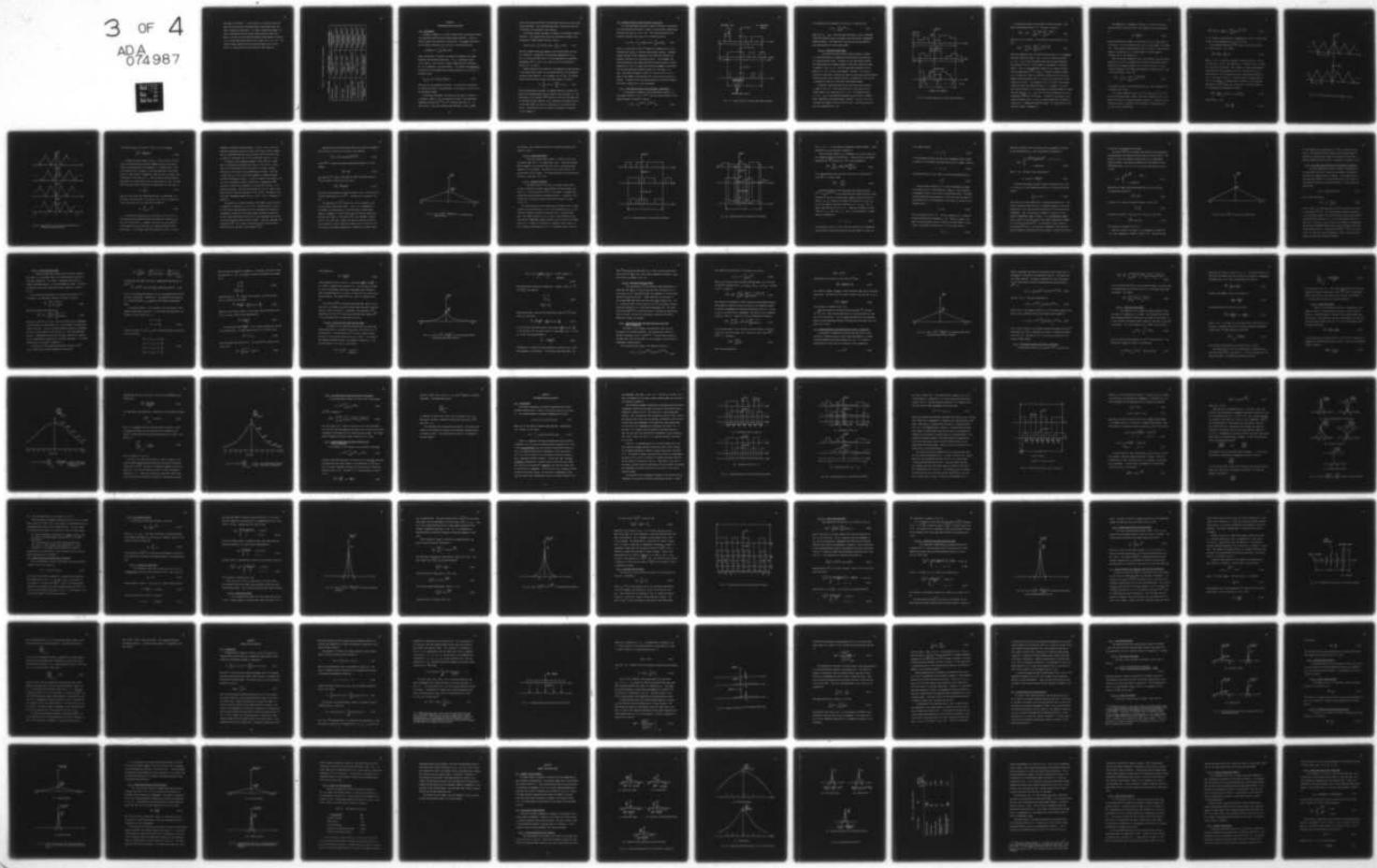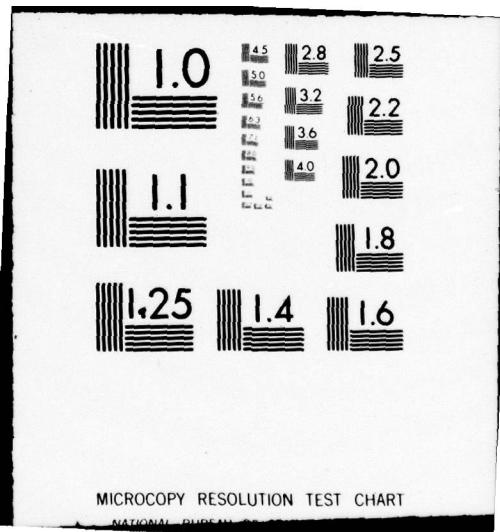
many types of diffusers. In this analysis, the Poisson transition

model and the uniformly distributed phase transmittance model are

used to represent ground glass. All other transmittance models are

used in conjunction with the evenly spaced potential transition

model, since this is the situation frequently encountered in practice

(e.g. the Gold code masks used by Krile, Redus, et al. [8, 11]). The

diffuser models analyzed in the following chapters are listed in

Table 2-1, along with the diffuser families they represent.

TABLE 2-1. Diffuser Models Used in the Analysis

Diffuser Type	Transmittance Model	Transition Model
Ground glass	Uniformly distributed phase on $[0, 2\pi]$	Poisson-distributed transitions
Multilevel phase	Balanced n-level phase	Evenly spaced potential transitions
Binary phase	Balanced 2-level phase (0 and π)	Evenly spaced potential transitions
Binary amplitude	t = 0 or 1 with equal probability	Evenly spaced potential transitions
Uniformly distributed amplitude	t uniformly distributed on $[0, 1]$	Evenly spaced potential transitions
Multilevel amplitude	n-level, real-valued t	Evenly spaced potential transitions
Combination amplitude and phase	Amplitude and phase statistically independent	Evenly spaced potential transitions

CHAPTER 3

CROSSCORRELATION CALCULATIONS

3.1. Introduction

As shown in Chapter 1, an ideal diffuser family would exhibit delta-like autocorrelations and zero-valued crosscorrelations. These are spatial rather than statistical correlations. The <u>spatial</u> correlation of two complex functions $Z_1(x)$ and $Z_2(x)$ is defined to be [15]

$$Z_1(x) \circledast Z_2(x) \triangleq \int_{-\infty}^{\infty} Z_1(\xi) Z_2^*(\xi - x) d\xi, \qquad (3-1)$$

where the asterisk * indicates the complex conjugate and the symbol $\circledast$ denotes the correlation operation. If Z_1 is identically equal to Z_2, then Eq. (3-1) defines a spatial autocorrelation; otherwise, Eq. (3-1) represents a crosscorrelation. In contrast, the <u>statistical</u> correlation of two complex-valued random processes $Z_1(x)$ and $Z_2(x)$ is defined as [16]

$$R_{Z_1 Z_2}(x_1, x_2) \triangleq E[Z_1(x_1) Z_2^*(x_2)], \qquad (3-2)$$

where $E[\cdot]$ is the expectation operator. The statistical correlation of diffuser functions is not pertinent to this analysis, and will not be considered further.

In multiplex holography, the spatial correlation of interest is $r_i(x) \circledast r_j(x)$, where r_i and r_j represent the complex field amplitudes immediately exiting the ith and j^{th} diffusers (see Chap. 1). As shown by Eq. (1-10), the reference beam functions r_i and r_j depend

27

on both the associated diffuser transmittance functions and the illuminating wavefronts. Unit amplitude plane wave illumination and chirp illumination are considered in the analysis.

The diffuser models developed in Chapter 2 are piecewise constant functions. This idealization allows the correlation integral to be replaced by a random complex sum $S(x)$; that is,

$$r_i(x) \circledast r_j(x) \equiv \int_{-\infty}^{\infty} r_i(\xi)r_j^*(\xi-x)d\xi = \sum_{k=1}^{M} z_k = S(x), \qquad (3-3)$$

where the complex-valued z_k's depend on the diffuser model and type of illumination. Henceforth, the functional dependence of S, r_i, and r_j on the correlation shift x will be suppressed for notational convenience; that is, $S(x)$, $r_i(x)$, and $r_j(x)$ will be referred to simply as S, r_i, and r_j.

Roughly speaking, the random sum S corresponds to light amplitude in the system output plane, and the squared modulus $|S|^2$ corresponds to output plane intensity. As an example, for an ideal unit imaging system with point source inputs, the system output is given by

$$0 = \sum_{i=1}^{N} (r_i \circledast r_i) + \sum_{i \neq j}^{N} \sum_{}^{N} (r_i \circledast r_j), \qquad (3-4)$$

which indicates that the output is composed entirely of autocorrelations and crosscorrelations for this special case (see Chap. 5). The mean value of $|S|^2$ (denoted $\overline{|S|^2}$) provides a basis for the comparison of different diffuser families, and is therefore calculated for various diffuser models and types of illumination in the sections that follow. The motivation for this analytical approach is discussed fully in Chapter 5.

3.2. Crosscorrelations with Plane Wave Illumination

If a unit amplitude plane wave is used for diffuser illumination, the field exiting the diffuser is equal to the diffuser transmittance function $t(x)$; that is, $r(x) = t(x)$. The crosscorrelation of two diffuser functions $r_i(x)$ and $r_j(x)$ is therefore given by

$$S = r_i \circledast r_j = \int_{-\infty}^{\infty} t_i(\xi) t_j^*(\xi - x) d\xi = \sum_{k=1}^{M} a_k (t_i t_j^*)_k, \qquad (3-5)$$

where a_k is the width of the kth interval of constant value in the integrand and $(t_i t_j^*)_k$ is the associated complex constant. Constant-valued intervals in the integrand of the correlation integral are hereafter referred to as "correlation cells." As an example, the crosscorrelation of two binary amplitude diffuser functions is shown graphically in Fig. 3-1, where the distinction between a correlation cell and the previously defined diffuser cell (see Chap. 2) is made. Note that the number of terms M in the sum of Eq. (3-5) is equal to the number of correlation cells in the crosscorrelation integrand. Crosscorrelation calculations based on the diffuser models outlined in Chapter 2 will now be presented.

3.2.1. Pure Phase Diffusers with Plane Wave Illumination

As discussed in Chapter 2, the transmittance function of a pure phase diffuser is $t(x) = e^{j\phi(x)}$, and the crosscorrelation of two phase diffusers is therefore given by

$$r_i \circledast r_j = \int_{-\infty}^{\infty} e^{j\phi_i(\xi)} e^{-j\phi_j(\xi - x)} d\xi. \qquad (3-6)$$
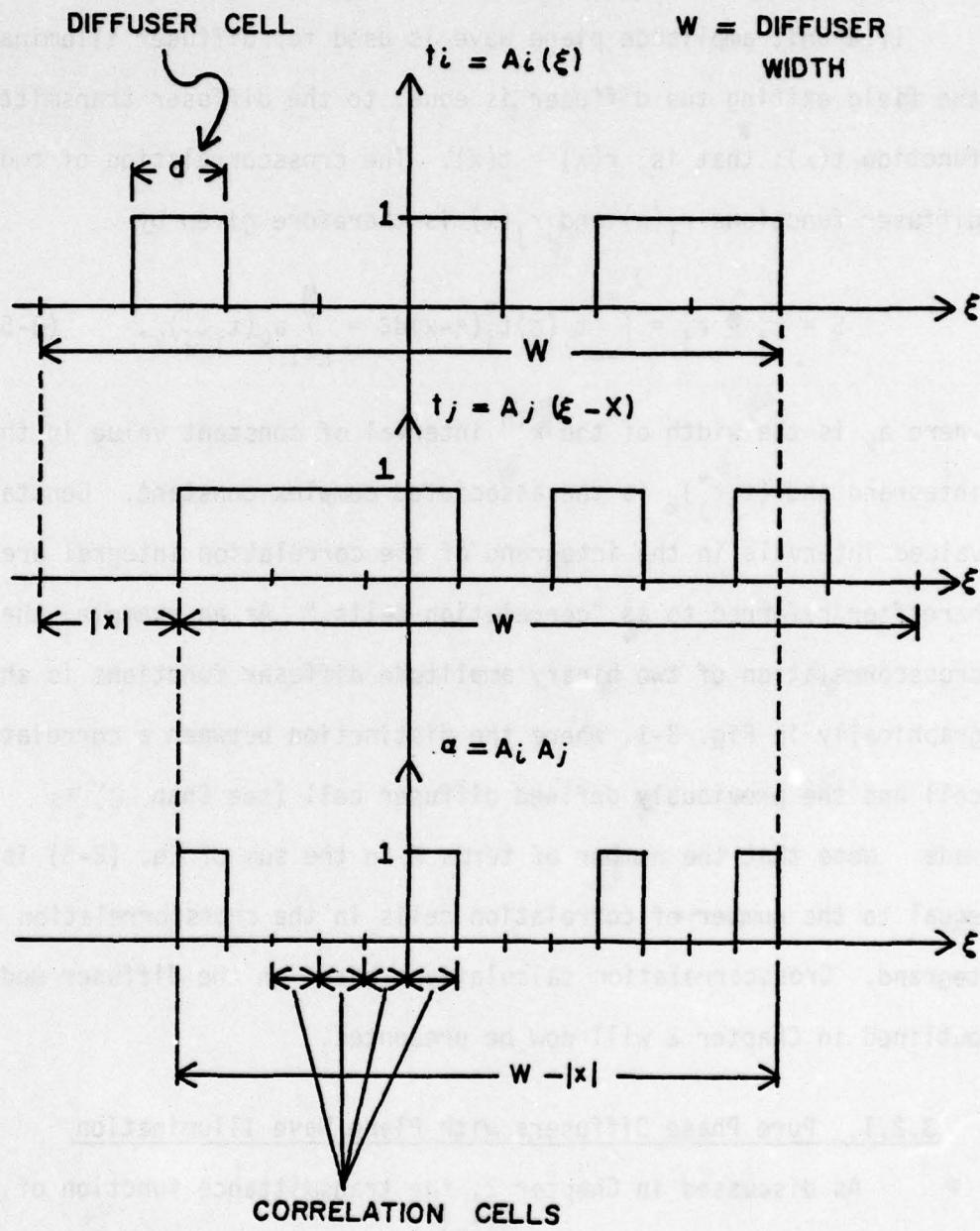
Fig. 3-1 Crosscorrelation of Binary Amplitude Diffusers

This equation can be expressed in the form of a complex sum as

$$r_i \circledcirc r_j = \sum_{k=1}^{M} a_k e^{j\theta_k} \equiv S, \qquad (3\text{-}7)$$

where $\theta_k \triangleq (\phi_i - \phi_j)_k$. Since the phase functions ϕ_i and ϕ_j represent different diffusers, they are assumed to be statistically independent random variables. The statistics of the a_k's and the θ_k's depend on the characteristics of the diffuser model.

3.2.1.1. Multilevel Phase Model

The multilevel phase diffuser model outlined in Chapter 2 is characterized by a transmittance function which can assume any of n possible phase levels. Diffusers of this type usually exhibit the constant spacing d between potential transition points described in Chapter 2, Sec. 2.4.1.2. The Gold code masks employed by Krile, Redus, et al. [8, 11] are a good example. Although it is certainly possible to fabricate a diffuser that does not have evenly spaced potential transition points, only constant spacing is considered in this analysis in conjunction with the n-level phase transmittance model.

A graphical crosscorrelation of two multilevel phase functions is shown in Fig. 3-2. This crosscorrelation is equivalent to the random complex sum S specified in Eq. (3-7). The random variable $\theta_k = (\phi_i - \phi_j)_k$ is the difference between two statistically independent, identically distributed random variables. The a_k's in Eq. (3-7) represent the lengths of the correlation cells. Both the θ_k's and the a_k's are indicated on Fig. 3-2.
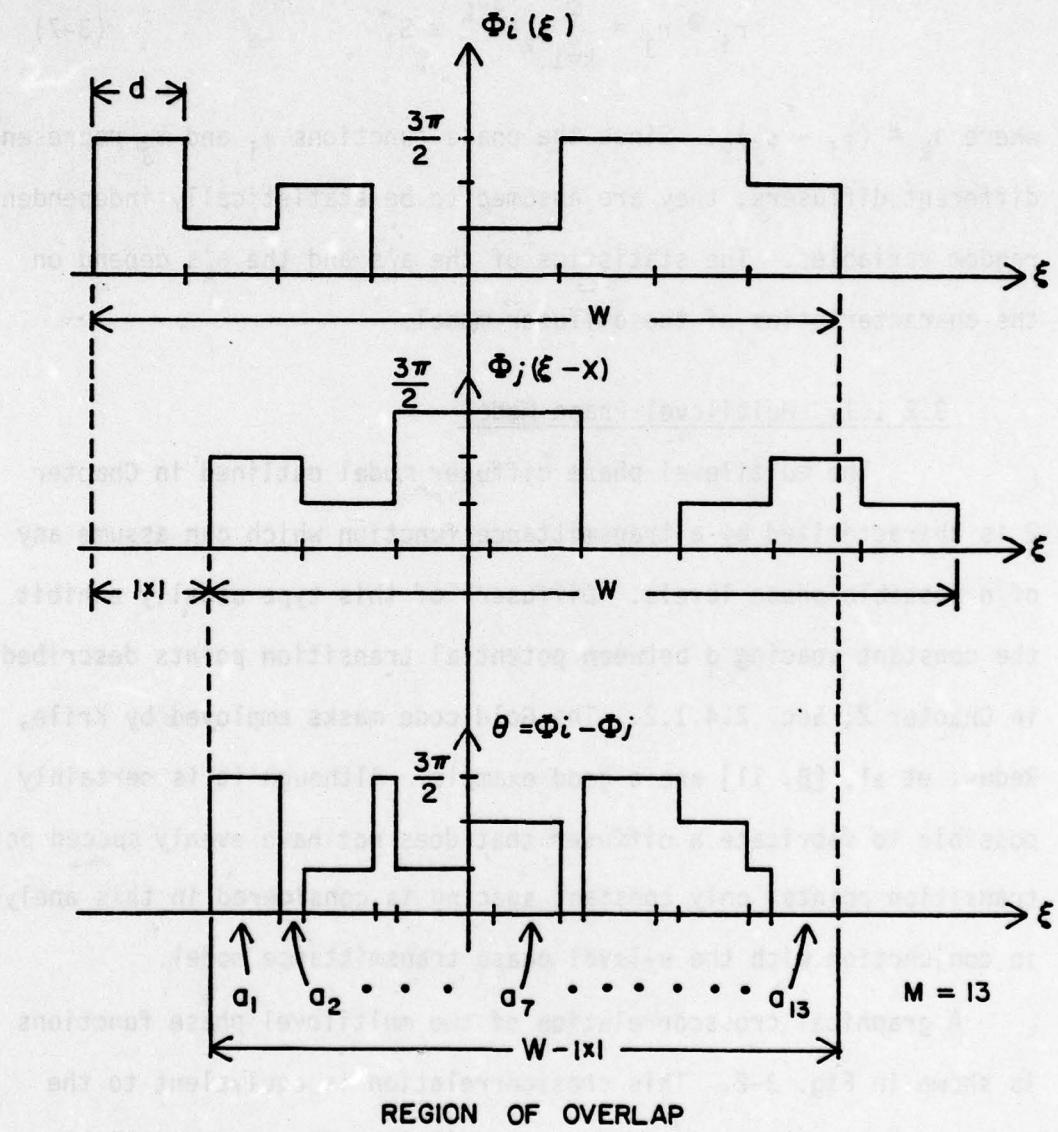
Fig. 3-2 Crosscorrelation of 4-Level Phase Diffusers

As previously stated, the quantity of primary interest is the mean of the squared modulus of S. The mean is given by

$$\overline{|S|^2} = \overline{SS^*} = \overline{\sum_{k=1}^{M} a_k e^{j\theta_k} \sum_{\ell=1}^{M} a_\ell e^{-j\theta_\ell}}, \tag{3-8}$$

where Eq. (3-7) is applied. This equation can be rewritten in the form

$$\overline{|S|^2} = \overline{\sum_{k=1}^{M} a_k^2} + \overline{\sum_{k \neq \ell}^{M} \sum^{M} a_k a_\ell e^{j\theta_k} e^{-j\theta_\ell}}. \tag{3-9}$$

Under the assumption that the diffuser phase function ϕ is a __balanced__ multilevel phase (see Chap. 2, Sec. 2.4.2.1.2), then the function $\theta_k = (\phi_i - \phi_j)_k$ is also a balanced phase with the same probability distribution as the ϕ's (if the phase is considered in a modulo-2π sense). This is a <u>very important</u> property of θ_k, because it means that the expectation $(e^{j\theta_k})$ is zero. An equally important property of θ_k is that the θ values in different correlation cells are independent random variables; that is, θ_k and θ_ℓ are statistically independent for all $k \neq \ell$. This property is also a result of the balanced probability model associated with the ϕ's. In general, if the diffuser phase function ϕ is not described by a balanced probability model, then the phase $\underline{\theta_k} = (\phi_i - \phi_j)_k$ ($i \neq j$) will not be balanced, and so the expectation $(e^{j\theta_k})$ will not be zero. In addition, the phases in different correlation cells, θ_k and θ_ℓ, cannot necessarily be treated as statistically independent random variables. All these points are explained in detail in Appendix A.

The summation S is composed of M terms. For the case of evenly spaced potential transition points, the integer M can be approximated by

$$M \doteq \frac{2(W-|x|)}{d} \quad , \tag{3-10}$$

where M represents the number of correlation cells, W is the width of a diffuser, x is the correlation shift, and d is the width of a diffuser cell. These quantities are marked on Figs. 3-1 and 3-2. Note that the number of correlation cells is approximately twice the number of diffuser cells in the length W-|x|.

Now the diffuser parameters W and d are constants, and M as approximated by Eq. (3-10) is a deterministic function of correlation shift x. Hence, the only random variables in Eq. (3-9) are the θ's. If the linearity property of the expectation operation is applied to Eq. (3-9), it can be rewritten in the form

$$\overline{|S|^2} = \sum_{k=1}^{M} \overline{a_k^2} + \sum_{k \neq \ell}^{M} \sum^{M} \overline{a_k a_\ell e^{j\theta_k} e^{-j\theta_\ell}} \quad . \tag{3-11}$$

A few words are now in order concerning the a_k's, which represent the correlation cell widths.

For a given correlation shift x_0, half of the a_k's in Eq. (3-11) are of a constant length a, where a lies on the interval [0, d]. The other half of the a_k's have the constant length d-a. Figure 3-2 illustrates this point. Since $\frac{M}{2}$ is half the number of correlation cells, Eq. (3-11) can be modified as

$$\overline{|S|^2} = \frac{M}{2}(a^2) + \frac{M}{2}(d-a)^2 + \sum_{\substack{k \neq \ell}}^{M} \sum^{M} \overline{a_k a_\ell} \ \overline{e^{j\theta_k}} \ \overline{e^{-j\theta_\ell}} \ . \tag{3-12}$$

In this equation, the statistical independence of a and θ has been used, as well as the independence of θ_k and θ_ℓ for $k \neq \ell$.

For a balanced phase model, $\overline{e^{j\theta}}$ is zero, so the cross terms in Eq. (3-12) drop out. This leaves

$$\overline{|S|^2} = \frac{M}{2}(a^2) + \frac{M}{2}(d-a)^2 \ , \tag{3-13}$$

where $a \equiv a(x)$ is a periodic function of correlation shift x, and M is given by Eq. (3-10). This periodicity is shown in Fig. 3-3, where $a(x)$ and $d-a(x)$ are plotted. Now in general it seems unreasonable to assume that the value assumed by $a(x)$ for a certain shift x_0 is a known quantity. To illustrate this point, some possible values of a at $x = 0$ are shown in Fig. 3-4. Since the mean or average value of $|S|^2$ is of interest, a credible course of action is to average the expression for $\overline{|S|^2}$ given by Eq. (3-13) over all possible values of a. Evaluating the corresponding integral

$$\overline{|S|^2} = (\frac{M}{2})[\frac{1}{d} \int_0^d [a^2(x) + (d-a(x))^2]dx] \tag{3-14}$$

gives the expression

$$\overline{|S|^2} = \frac{Md^2}{3} \ . \tag{3-15}$$
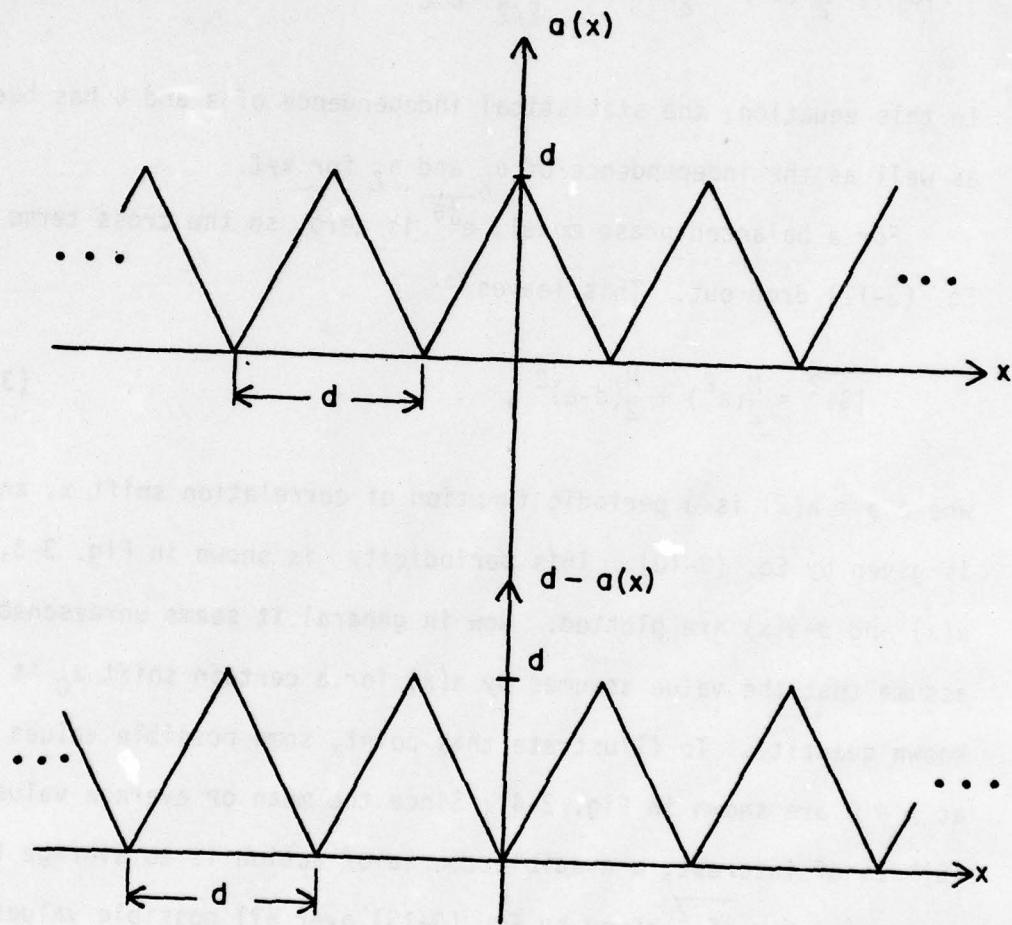
Fig. 3-3 Plots of Correlation Cell Widths a and d-a
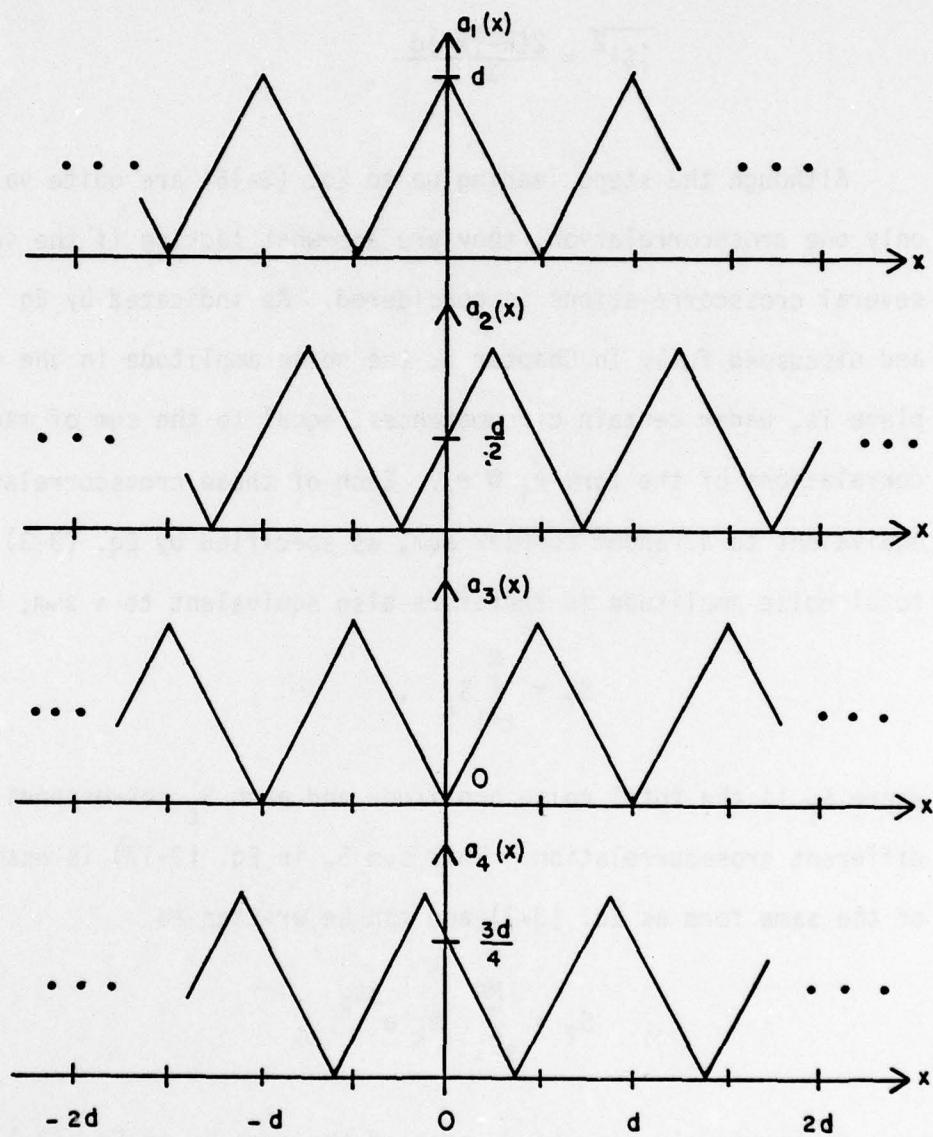
Fig. 3-4   Some Possible Correlation Width Functions for
Different Crosscorrelations

After substituting for M from Eq. (3-10), Eq. (3-15) becomes

$$\overline{|S|^2} = \frac{2(W-|x|)d}{3} .$$

(3-16)

Although the steps leading up to Eq. (3-16) are quite valid for only one crosscorrelation, they are somewhat lacking if the sum of several crosscorrelations is considered. As indicated by Eq. (3-4) and discussed fully in Chapter 5, the noise amplitude in the output plane is, under certain circumstances, equal to the sum of many cross-correlations of the form $r_i \circledast r_j$. Each of these crosscorrelations is equivalent to a random complex sum, as specified by Eq. (3-3), and the total noise amplitude is therefore also equivalent to a sum; that is,

$$S_T = \sum_{\ell=1}^{N} S_\ell ,$$

(3-17)

where S_T is the total noise amplitude and each S_ℓ corresponds to a different crosscorrelation. This sum S_T in Eq. (3-17) is essentially of the same form as Eq. (3-7), and can be written as

$$S_T = \sum_{k=1}^{MN} a_k e^{j\theta_k} .$$

(3-18)

As previously discussed, each of the sums S_ℓ in Eq. (3-17) is characterized by the constant-valued correlation cell widths a_ℓ and $d-a_\ell$ for a given shift x_0. However, the value of a_ℓ at x_0 need not be the same for each S_ℓ, since the S_ℓ's represent different cross-correlations. For instance, each of the functions in Fig. 3-4 could

represent a different crosscorrelation. The a_k's in Eq. (3-18) can therefore assume many different values on the interval $[0,d]$, whereas the a_k's associated with one sum S_ℓ are restricted to the two values a_ℓ and $d-a_\ell$ (once again, this is for a particular value of $x = x_0$).

The thrust of the preceding argument is that there is a great deal of uncertainty associated with the a_k's in Eq. (3-18). Each a_k must lie in the interval $[0,d]$, but there is no reason to expect one value in this interval to be preferred over another. With this in mind, the a_k's in Eq. (3-18) can be modeled as random variables uniformly distributed on $[0,d]$. In order to simplify the analysis, the a_k's will be modeled as mutually statistically independent random variables, although this assumption is not entirely accurate. It is comforting, however, that the uniform model for the a_k's leads to the same solution as derived differently in Eq. (3-16). The nature of the statistical dependence between the a_k's in Eq. (3-18) is discussed in Appendix C.

The quantity of ultimate interest in the signal-to-noise analysis of Chapter 5 is the sum S_T in Eq. (3-17). Anticipating this, the a_k's for the single crosscorrelation sum S will henceforth be treated as independent, identically distributed random variables characterized by the uniform distribution on $[0, d]$, for _all_ subsequent calculations involving the evenly spaced transition model. Using this approach, the expectation $\overline{|S|^2}$ for a single crosscorrelation can later be easily modified to give the total noise intensity $\overline{|S_T|^2}$.

Applying the uniform distribution model and statistical independence of the a_k's to Eq. (3-11) results in the equation

$$\overline{|S|^2} = M \overline{a^2} + M(M-1)\overline{a}^2(\overline{e^{j\theta}})(\overline{e^{-j\theta}}). \tag{3-19}$$

Since $(\overline{e^{j\theta}}) = 0$ under the assumed balanced phase model, Eq. (3-19) becomes

$$\overline{|S|^2} = M\overline{a^2} . \tag{3-20}$$

The quantity $\overline{a^2}$ is easily calculated to be $\frac{d^2}{3}$, and substituting for $\overline{a^2}$ and M (see Eq. (3-10)) gives the result

$$\overline{|S|^2} = \frac{2(W-|x|)d}{3} . \tag{3-21}$$

Note that the two methods of analysis leading to Eqs. (3-16) and (3-21) give the same expression for $\overline{|S|^2}$. The function is plotted in Fig. 3-5.

The expression for $\overline{|S|^2}$ given by Eq. (3-21) and shown in Fig. 3-5 has several interesting facets. First, it is independent of the number of allowed phases n in the multiphase diffuser model. Second, it depends in a linear fashion on both diffuser width W and diffuser cell width d. The function $\overline{|S|^2}$ also decreases linearly with $|x|$ for $|x| \epsilon [0, W]$, because the region of overlap of the diffuser functions r_i and r_j decreases linearly with $|x|$ (see Fig. 3-2). This result can be better understood in comparison with other types
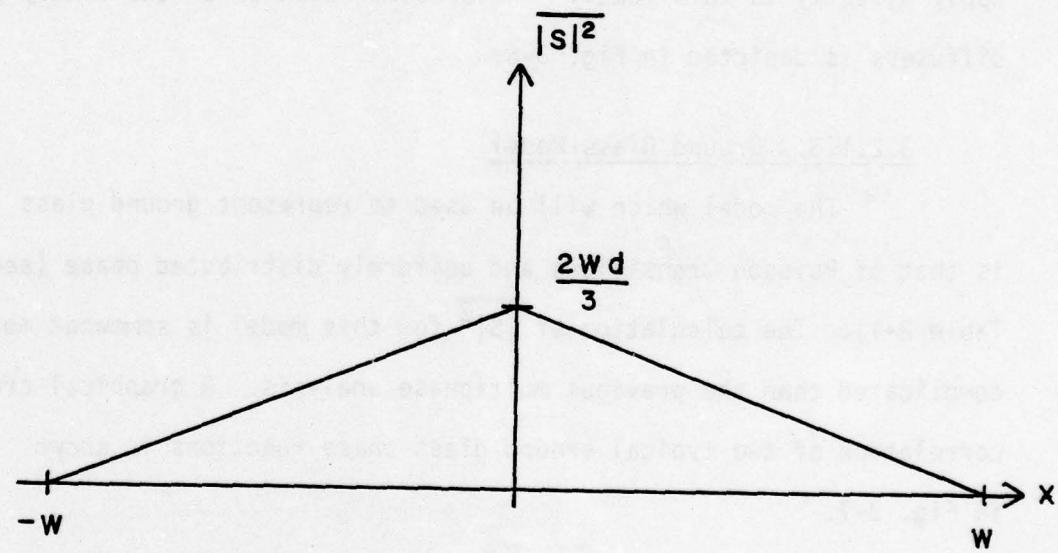
Fig. 3-5 Plot of $\overline{|S|^2} = \dfrac{2(W-|x|)d}{3}$ for the Multilevel Phase Diffuser

of diffusers, and a detailed discussion is therefore postponed until Chapters 5 and 6.

3.2.1.2. Binary Phase Model

The binary phase diffuser model is a special case of the multiphase model with n = 2 allowed phase levels. Under the balanced phase assumption, the allowed levels are 0 and π, each having equal probability of occurrence. The results of Eq. (3-21) and Fig. 3-5 apply directly to this model. The crosscorrelation of two binary phase diffusers is depicted in Fig. 3-6.

3.2.1.3. Ground Glass Model

The model which will be used to represent ground glass is that of Poisson transitions and uniformly distributed phase (see Table 2-1). The calculation of $\overline{|S|}^2$ for this model is somewhat more complicated than the previous multiphase analysis. A graphical cross-correlation of two typical ground glass phase functions is shown in Fig. 3-7.

The crosscorrelation of two ground glass diffusers gives a random complex sum as described by Eq. (3-7), but the quantities θ_k, a_k, and M exhibit different statistical properties than in the multiphase case. The random variable $\theta_k = (\phi_i - \phi_j)_k$ is the difference of two statistically independent random variables, each uniformly distributed on $[0, 2\pi]$. If phase is considered in a modulo-2π sense, then θ_k is also uniformly distributed on $[0, 2\pi]$. Furthermore, each of the θ_k's
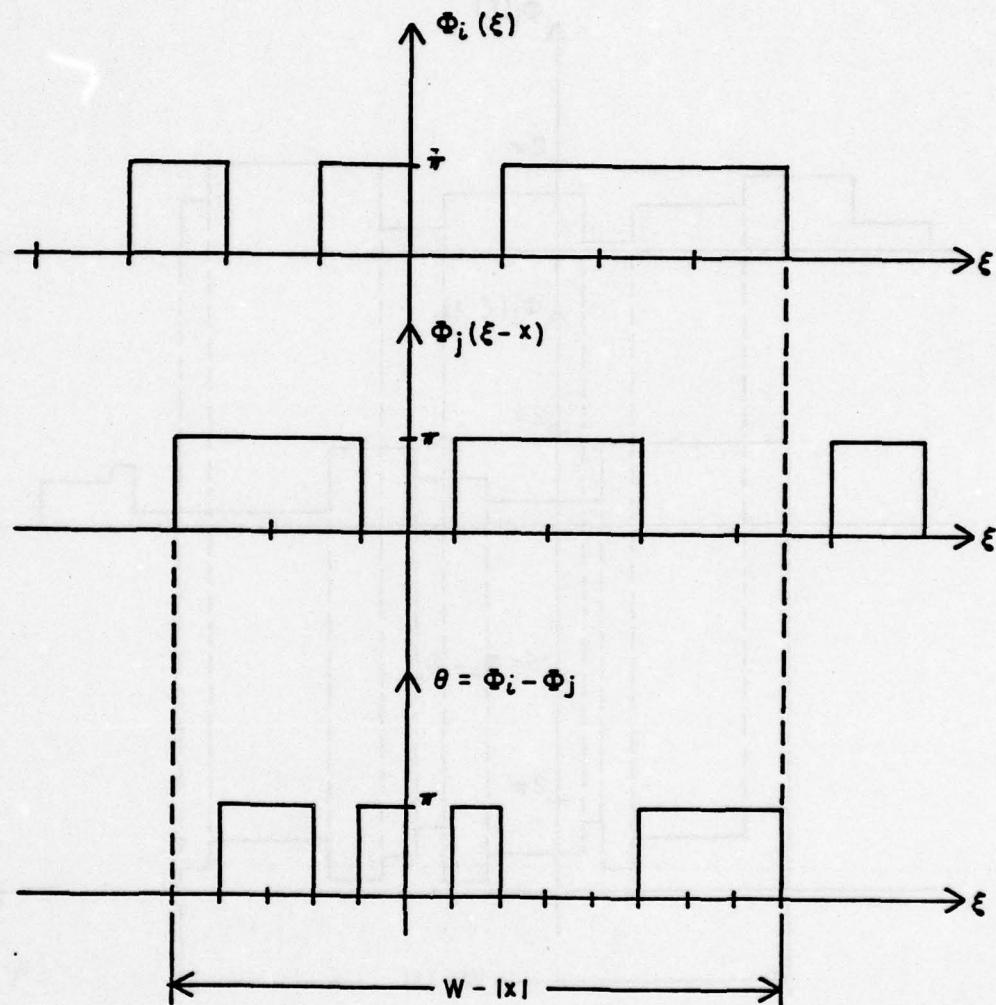
Fig. 3-6 Crosscorrelation of Binary Phase Diffusers
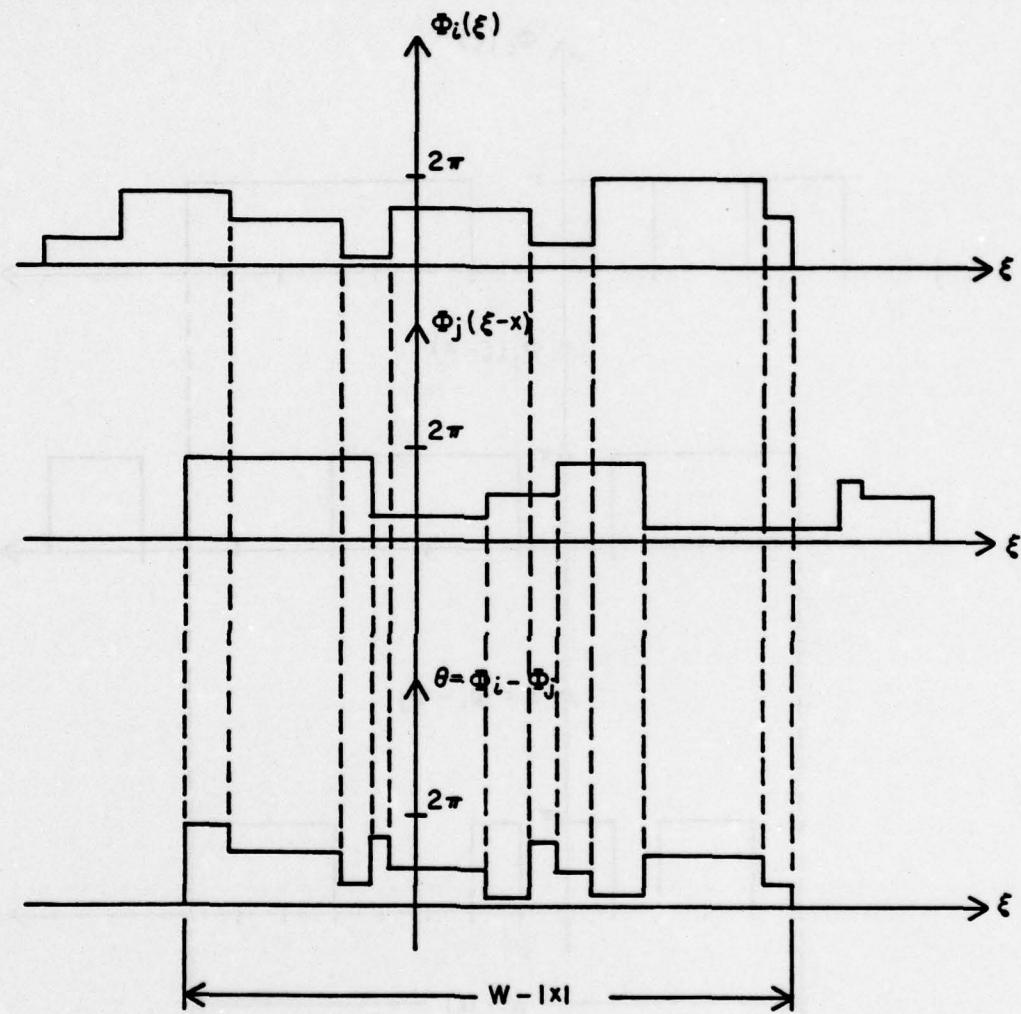
Fig. 3-7 Crosscorrelation of Ground Glass Diffusers

for k = 1, 2, ..., M are mutually independent random variables. These properties of θ_k are derived in Appendix A.

Now the random variable θ_k is independent of a_k and M, which are also random variables for ground glass. Using this fact, the general expression for $\overline{|S|^2}$ given by Eq. (3-9) can be expressed as

$$\overline{|S|^2} = \overline{\sum_{k=1}^{M} a_k^2} + (\overline{e^{j\theta}})(\overline{e^{-j\theta}}) \overline{\sum_{k \neq \ell}^{M} \sum^{M} a_k a_\ell}. \qquad (3-22)$$

As in the multiphase case, the cross terms in Eq. (3-22) drop out, since $(\overline{e^{j\theta}}) = 0$, which leaves

$$\overline{|S|^2} = \overline{\sum_{k=1}^{M} a_k^2}. \qquad (3-23)$$

The multiplication of the two ground glass phase functions $e^{j\phi_i(\xi)}$ and $e^{-j\phi_j(\xi-x)}$ in the crosscorrelation integrand gives a phase function $e^{j\theta}$ that has, on the average, <u>twice</u> as many transitions as either ϕ_i or ϕ_j; in effect, the number of transitions of $\phi_i(\xi)$ and $\phi_j(\xi-x)$ are added to give the transitions of $\theta = (\phi_i - \phi_j)$. This is easily seen with the aid of Fig. 3-7. Denoting the number of transitions for ϕ_i, ϕ_j, and θ by T_i, T_j, and T_θ, the relationship is mathematically expressed as

$$T_\theta = T_i + T_j. \qquad (3-24)$$

The quantities T_i and T_j in Eq. (3-24) are statistically independent, and both have a Poisson distribution with mean number of counts per

unit length given by

$$\lambda_i = \lambda_j = \frac{1}{d} . \tag{3-25}$$

It can be shown [17] that the sum of two independent Poisson random variables is also Poisson, with mean counts per unit length λ given by

$$\lambda = \lambda_i + \lambda_j . \tag{3-26}$$

This implies that T_θ in Eq. (3-24) is Poisson and characterized by

$$\lambda = \frac{2}{d} . \tag{3-27}$$

Now the random variable M in Eq. (3-23) represents the number of correlation cells in the width $W-|x|$, where x is the correlation displacement (see Eq. (3-1)) and W is the diffuser width. The number of phase transitions experienced by θ is one less than the number of correlation cells M if the endpoints of the region of overlap are not counted; that is,

$$T_\theta = M-1 . \tag{3-28}$$

This can be seen from Fig. 3-7. Strictly speaking, M-1 is therefore Poisson distributed with parameter $\lambda = \frac{2}{d}$. Normally, however, the mean of the distribution, which is equal to the mean number of transitions in the region of overlap $W-|x|$, will be large; that is,

$$\overline{T_\theta} \gg 1 . \tag{3-29}$$

Under this condition, the distribution of M is essentially the same as the distribution of T_θ, and can therefore be expressed as

$$P(M) = \begin{cases} \dfrac{e^{-\lambda(W-|x|)}\lambda(W-|x|)^M}{M!} , & M = 0, 1, 2, \ldots \\ 0, \text{ otherwise}, \end{cases} \quad (3\text{-}30)$$

where $\lambda = \dfrac{2}{d}$. The mean of the distribution is

$$\overline{M} = \lambda(W-|x|) = \frac{2(W-|x|)}{d} . \quad (3\text{-}31)$$

Given that the random variable M takes on some particular value $M = m$, the a_k's in the correlation sum of Eq. (3-7) must satisfy the relation

$$\sum_{k=1}^{m} a_k = W-|x| , \quad (3\text{-}32)$$

since the a_k's are the subdivisions of the overlap region $W-|x|$. The range of possible values for the a_k's therefore depends on the value assumed by M. This implies that M and the a_k's are not statistically independent. Also, as explained in Appendix C, the a_k's are not mutually independent random variables. The interdependence between the a_k's and M is involved, and for this reason approximation methods will be used to calculate $\overline{|S|^2}$. The preliminary steps involved in calculating $\overline{|S|^2}$ exactly are outlined in Appendix D, and the mathematical complexity associated with this approach is ample justification

for the use of approximation techniques.

The value of $\overline{|S|^2}$ for the ground glass model can be approximated by assuming that the random variable M takes on its mean value $\overline{M}$. The analysis is also facilitated by treating the a_k's as independent random variables, each negative exponentially distributed with mean value $\frac{d}{2}$ (see Chap. 2, Sec. 2.4.1.1); the associated density function is [18]

$$p(a) = \begin{cases} \frac{2}{d} e^{-(\frac{2}{d})a} & , \quad a\epsilon[0, \infty) \\ \\ 0, \text{ otherwise.} \end{cases} \quad (3-33)$$

Application of these simplifying assumptions to Eq. (3-23) gives the approximate expression

$$\overline{|S|^2} \doteq \overline{M} \; \overline{a^2}. \quad (3-34)$$

The mean of a^2 is easily calculated from Eq. (3-33) to be

$$\overline{a^2} = \frac{d^2}{2}. \quad (3-35)$$

Substituting from Eqs. (3-35) and (3-31) into Eq. (3-34) gives

$$\overline{|S|^2} \doteq (W-|x|)d. \quad (3-36)$$

This equation is graphed in Fig. 3-8.

While Eq. (3-36) is not exact, it is reasonable to assume that it at least represents a "typical" value of $|S|^2$. Note that except
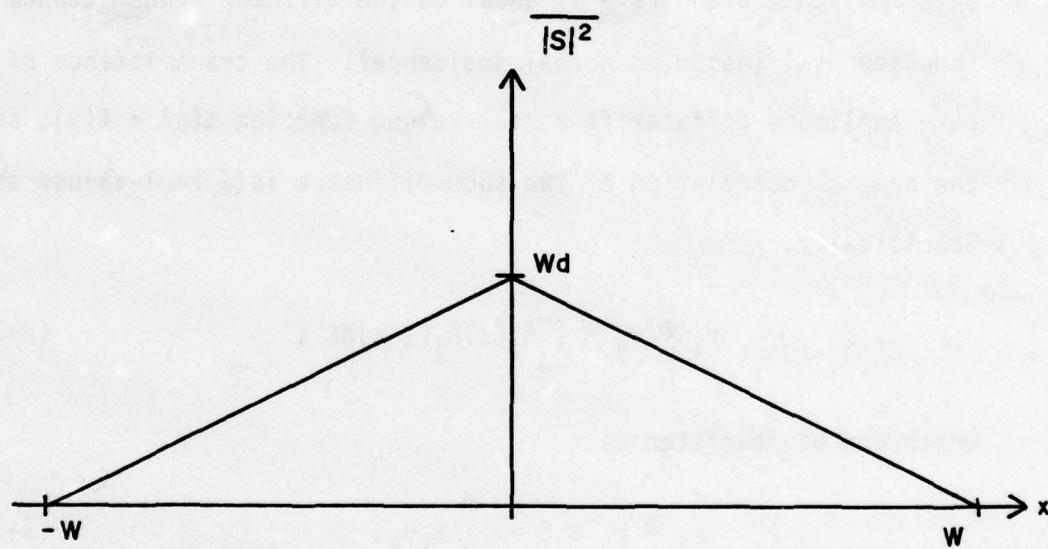
Fig. 3-8 Plot of $\overline{|S|^2}$ = (W-|x|)d for Ground Glass

for the multiplicative constant $\frac{2}{3}$, Eq. (3-36) is identical to Eq. (3-21). Multiphase diffusers evidently share the same essential properties as ground glass, based on the previous calculations. A detailed comparison and discussion is presented in Chapters 5 and 6.

3.2.2. Pure Amplitude Diffusers with Plane Wave Illumination

The field immediately exiting a diffuser illuminated by a unit amplitude plane wave is equal to the diffuser transmittance function $t(x)$ (assuming normal incidence). The transmittance of a pure amplitude diffuser is a real-valued function $t(x) = A(x)$, so the spatial correlation of two such diffusers is a real-valued sum. Specifically,

$$r_i \circledast r_j = \int_{-\infty}^{\infty} A_i(\xi) A_j(\xi - x) d\xi , \qquad (3-37)$$

which can be rewritten as

$$r_i \circledast r_j \equiv S = \sum_{k=1}^{M} a_k \alpha_k . \qquad (3-38)$$

In Eq. (3-38), α_k is the amplitude of the kth correlation cell and a_k is the width of kth cell. All the amplitude diffusers considered in the following analysis are characterized by evenly spaced potential transition points (spacing = d). As in the multiphase analysis of Sec. 3.2.1.1, the a_k's in Eq. (3-38) will be modeled as independent, identically distributed random variables, each uniformly distributed on the interval [0, d]. Calculations of $\overline{S^2}$ ($\overline{S^2} \equiv \overline{|S|^2}$ in this case, since S is real) will now be presented for binary, uniformly distributed, and multilevel amplitude diffusers.

3.2.2.1. Binary Amplitude Model

The binary amplitude diffuser model outlined in Chapter 2 (see Table 2-1) can assume either of the transmittance values 0 or 1 with equal probability. This model is sometimes referred to as a random checkerboard pattern (in the two-dimensional case). The cross-correlation of two binary amplitude diffuser functions is shown in Fig. 3-1.

As in the pure phase analysis, the mean of the quantity $|S|^2$ is of interest. For amplitude diffusers, this mean is given by

$$\overline{S^2} = \overline{\sum_{k=1}^{M} a_k \alpha_k \sum_{\ell=1}^{M} a_\ell \alpha_\ell} \, , \tag{3-39}$$

which can be broken into two terms as

$$|S|^2 = \overline{S^2} = \overline{\sum_{k=1}^{M} a_k^2 \alpha_k^2} + \overline{\sum_{k \neq \ell}^{M} \sum a_k a_\ell \alpha_k \alpha_\ell} \, . \tag{3-40}$$

Now the a_k's and the α_k's in Eq. (3-40) are statistically independent, since the width of a correlation cell is not related to the amplitude value of the cell. The a_k's have been modeled as mutually independent, but this is not necessarily true for the α_k's. While the amplitude values α in nonadjacent correlation cells <u>are</u> statistically independent, the amplitudes in adjacent cells are <u>not</u> independent. This rather peculiar fact is explained in Appendix B.

In the light of the preceding discussion, the mean value $\overline{S^2}$ in Eq. (3-40) can be further decomposed into the terms

$$\overline{s^2} = \overline{\sum_{k=1}^{M} a_k^2 \alpha_k^2} + 2\overline{\sum_{k=1}^{M-1} a_k a_{k+1} \alpha_k \alpha_{k+1}} + \overline{\sum_{|k-\ell|>1}^{M} \sum^{M} a_k a_\ell \alpha_k \alpha_\ell},$$

(3-41)

and employing the proper statistical independence relationships results in

$$\overline{s^2} = M \overline{a^2}\,\overline{\alpha^2} + 2(M-1)\overline{a}^2\,\overline{\alpha_i \alpha_{i+1}} + [M^2 - M - 2(M-1)]\overline{a}^2\,\overline{\alpha}^2. \quad (3-42)$$

Since a is uniformly distributed on [0, d], the expectations $\overline{a}$ and $\overline{a^2}$ are equal to $\frac{d}{2}$ and $\frac{d^2}{3}$, respectively. The probability distributions of α and the product $\alpha_i \alpha_{i+1}$ depend on the diffuser transmittance model.

The random variable α is the product of two statistically independent transmittance functions. For the binary amplitude model, the probability mass function for α is

$$P(\alpha = 0) = \frac{3}{4}$$

$$P(\alpha = 1) = \frac{1}{4}, \quad (3-43)$$

and the joint pmf of α_i and α_{i+1} (which represent adjacent correlation cells) is given by

$$P(\alpha_i = 0, \alpha_{i+1} = 0) = \frac{5}{8}$$

$$P(\alpha_i = 0, \alpha_{i+1} = 1) = \frac{1}{8}$$

$$P(\alpha_i = 1, \alpha_{i+1} = 0) = \frac{1}{8} \quad (3-44)$$

$$P(\alpha_i = 1, \alpha_{i+1} = 1) = \frac{1}{8}.$$

These relations are derived in Appendix B. Using Eqs. (3-43) and (3-44), the quantities $\bar{\alpha}$, $\overline{\alpha^2}$, and $\overline{\alpha_i \alpha_{i+1}}$ are easily calculated to be (Appendix B)

$$\bar{\alpha} = \frac{1}{4}$$
$$\overline{\alpha^2} = \frac{1}{4} \qquad\qquad (3\text{-}45)$$
$$\overline{\alpha_i \alpha_{i+1}} = \frac{1}{8} .$$

Substituting for $\bar{\alpha}$, $\overline{\alpha^2}$, $\overline{\alpha_i \alpha_{i+1}}$, and M from Eqs. (3-10) and (3-45) into Eq. (3-42) gives the result

$$\overline{S^2} = \frac{(W-|x|)^2}{16} + \frac{19}{96}(W-|x|)d - \frac{d^2}{32}. \qquad (3\text{-}46)$$

Generally, the diffuser width W is much larger than the diffuser resolution d, and Eq. (3-46) can be approximated as

$$\overline{S^2} \doteq \frac{(W-|x|)^2}{16} . \qquad (3\text{-}47)$$

The terms other than $\frac{(W-|x|)^2}{16}$ in Eq. (3-46) represent the variance of the random sum S. The mean-squared value of S is given by [19]

$$\overline{S^2} = \bar{S}^2 + \sigma_S^2 , \qquad (3\text{-}48)$$

where σ_S^2 denotes the variance of S. The value of $\bar{S}^2$ is easily calculated to be

$$\bar{S}^2 = \left(\overline{\sum_{k=1}^{M} a_k \alpha_k} \right)^2 = (M \bar{a} \, \bar{\alpha})^2, \qquad (3\text{-}49)$$

which reduces to

$$\overline{S}^2 = \frac{(W-|x|)^2}{16} \tag{3-50}$$

after substituting for M, $\overline{a}$, and $\overline{\alpha}$. The quantity $\frac{19}{96}(W-|x|)d\frac{d^2}{32}$ in Eq. (3-46) is therefore the variance of S. This variance, σ_S^2, goes to zero as the diffuser resolution d approaches zero, indicating that the approximation of Eq. (3-47) is quite valid for finely structured diffusers. The function $\overline{S^2}$ in Eq. (3-47) is plotted in Fig. 3-9.

The mean value $\overline{S^2}$ for the binary amplitude model does not go to zero with d, as opposed to the pure phase models previously analyzed (see Eqs. (3-21) and (3-36)). Furthermore, the magnitude of $\overline{S^2}$ is proportional to $(W-|x|)^2$ in the binary amplitude case, whereas $\overline{|S|^2}$ in the pure phase case is proportional to $(W-|x|)$.

3.2.2.2. Uniformly Distributed Amplitude Model

Diffusers of this type are characterized by an amplitude transmittance which is uniformly distributed on the interval [0, 1] (see Table 2-1). The calculation of $\overline{S^2}$ for such a model proceeds exactly as in the previous analysis up to Eq. (3-42). For uniformly distributed amplitude diffusers, the probability density for α and the joint density of α_i and α_{i+1} are given by

$$p(\alpha) = \begin{cases} \ln\left(\frac{1}{\alpha}\right), & \alpha\epsilon\ [0,\ 1] \\ 0, & \text{otherwise} \end{cases}$$
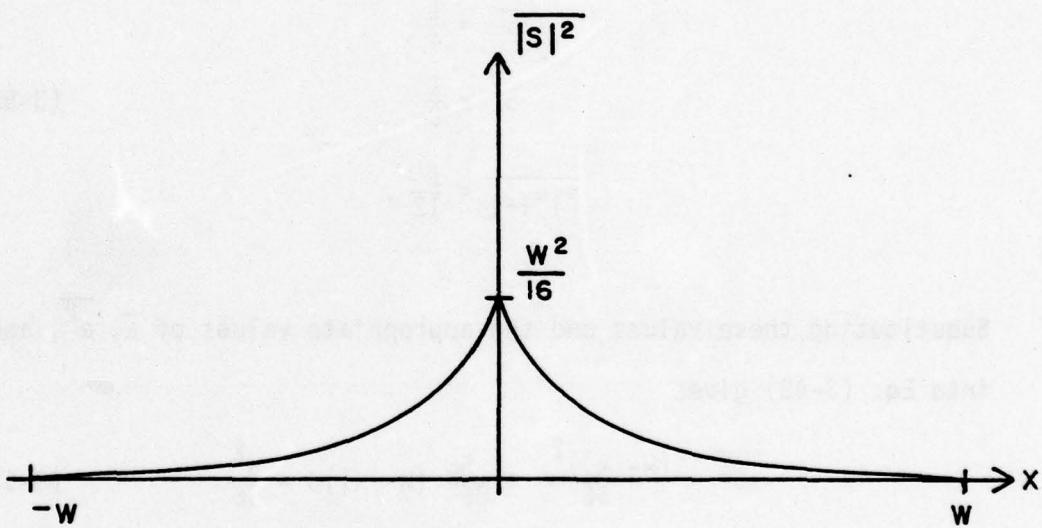
Fig. 3-9 Plot of $\overline{|S|^2} = \dfrac{(W-|x|)^2}{16}$ for Binary and Uniformly Distributed Amplitude Diffusers

$$p(\alpha_i, \alpha_{i+1}) = \begin{cases} \dfrac{1}{\max(\alpha_i, \alpha_{i+1})} - 1, & \alpha_i \text{ and } \alpha_{i+1} \epsilon [0, 1] \\ \\ 0, & \text{otherwise} . \end{cases}$$

$$(3\text{-}51)$$

These densities are derived in Appendix B. From Eq. (3-51), $\overline{\alpha}$, $\overline{\alpha^2}$, and $\overline{\alpha_i \alpha_{i+1}}$ are given by

$$\overline{\alpha} = \frac{1}{4}$$

$$\overline{\alpha^2} = \frac{1}{9}$$

$$(3\text{-}52)$$

$$\overline{\alpha_i \alpha_{i+1}} = \frac{1}{12} .$$

Substituting these values and the appropriate values of $\overline{a}$, $\overline{a^2}$, and M into Eq. (3-42) gives

$$\overline{S^2} = \frac{(W - |x|)^2}{16} + \frac{55}{864} (W - |x|)d - \frac{d^2}{96}. \qquad (3\text{-}53)$$

As in the binary amplitude analysis, the quantity $\frac{55}{864} (W - |x|)d - \frac{d^2}{96}$ is the variance of S, and goes to zero as d approaches zero. For W>>d, Eq. (3-53) can be approximated as

$$\overline{S^2} \doteq \frac{(W - |x|)^2}{16} . \qquad (3\text{-}54)$$

Although this is exactly the same expression as derived in Eq. (3-47), the agreement is coincidental. For different amplitude models, the

mean $\overline{S^2}$ would have the same form as Eq. (3-54), but the factor multiplying $(W-|x|)^2$ ($\frac{1}{16}$ in Eq. (3-54)) would probably be different. Equation (3-54) is plotted in Fig. 3-9.

3.2.2.3. Multilevel Amplitude Model

The calculation of $\overline{S^2}$ for multilevel amplitude models proceeds much the same as in the previous two cases, differing only in the values of $\overline{\alpha}$, $\overline{\alpha^2}$, and $\overline{\alpha_i \alpha_{i+1}}$ (under the assumption of evenly spaced potential transition points).   These quantities are functions of the allowed amplitude levels and their associated probabilities. For $n > 2$ possible levels, the calculation of $\overline{\alpha}$, $\overline{\alpha^2}$, and $\overline{\alpha_i \alpha_{i+1}}$ is complicated only because it is a rather messy bookkeeping job. The crosscorrelation mean $\overline{S^2}$ for a multilevel model is obtained by substituting into Eq. (3-42). No specific calculations involving a multilevel amplitude diffuser are included.

3.2.3. Combined Amplitude and Phase Diffusers with Plane Wave Illumination

Diffusers in this category can attenuate as well as shift the phase of an incident wavefront. The transmittance function is therefore expressed as $t(x) = A(x)e^{j\phi(x)}$. In the following analysis, the amplitude $A(x)$ and the phase $\phi(x)$ are assumed to be statistically independent random processes.

The crosscorrelation integral for combined diffusers is

$$r_i \circledast r_j = \int_{-\infty}^{\infty} A_i(\xi)e^{j\phi_i(\xi)} A_j(\xi-x)e^{-j\phi_j(\xi-x)} \, d\xi. \tag{3-55}$$

This equation can be written in the familiar sum form as

$$r_i \circledast r_j = S = \sum_{k=1}^{M} a_k \alpha_k e^{j\theta_k} , \qquad (3-56)$$

where, as in the pure phase and pure amplitude cases, a_k is the width of the kth correlation cell, $\alpha_k = (A_i A_j)_k$, and $\theta_k = (\phi_i - \phi_j)_k$. The mean of $|S|^2$ is given by

$$\overline{|S|^2} = \overline{SS^*} = \overline{\sum_{k=1}^{M} a_k^2 \alpha_k^2} + \overline{\sum_{k \neq \ell}^{M} \sum^{M} a_k a_\ell \alpha_k \alpha_\ell e^{j\theta_k} e^{-j\theta_\ell}} . \qquad (3-57)$$

The diffusers are assumed to exhibit constant spacing between consecutive potential transition points, and the a_k's are therefore modeled as mutually independent and uniformly distributed on $[0, d]$. For $k \neq \ell$, θ_k and θ_ℓ are statistically independent, and they are also independent of the a_k's and α_k's. Equation (3-57) can therefore be written as

$$\overline{|S|^2} = \overline{\sum_{k=1}^{M} a_k^2 \alpha_k^2} + (\overline{e^{j\theta}})(\overline{e^{-j\theta}}) \overline{\sum_{k \neq \ell}^{M} \sum^{M} a_k a_\ell \alpha_k \alpha_\ell} . \qquad (3-58)$$

For a balanced phase θ (this includes the uniform phase distribution on $[0, 2\pi]$), the cross terms in Eq. (3-58) go to zero, since $(\overline{e^{j\theta}}) = (\overline{e^{-j\theta}}) = 0$. Therefore,

$$\overline{|S|^2} = \overline{\sum_{k=1}^{M} a_k^2 \alpha_k^2} , \qquad (3-59)$$

which can be expressed as

$$\overline{|S|^2} = M \, \overline{a^2} \, \overline{\alpha^2}. \tag{3-60}$$

Substituting for M from Eq. (3-10) and for $\overline{a^2}$ gives

$$\overline{|S|^2} = \frac{2(W-|x|)d}{3} \, (\overline{\alpha^2}) \; . \tag{3-61}$$

As a specific example, consider a binary amplitude model and any balanced phase model. The value of $\overline{\alpha^2}$ for such a diffuser is $\frac{1}{4}$ (see Sec. 3.2.2.1), so

$$\overline{|S|^2} = \frac{(W-|x|)d}{6} \; . \tag{3-62}$$

This function is plotted in Fig. 3-10.

Note that except for the multiplicative constant $\overline{\alpha^2}$, the value of $\overline{|S|^2}$ in Eq. (3-61) has the same form as in the pure phase case (see Eqs. (3-21) and (3-36)). This is because the addition of the balanced phase to a pure amplitude diffuser eliminates the cross terms ($k \neq \ell$) present in Eq. (3-40).

3.3. Crosscorrelations with Spherical Wave (Chirp) Illumination

Illumination of ground glass and Gold code masks with a chirp wavefront (a spherical wave) has been shown experimentally to reduce crosstalk between multiplexed holograms [11, 20]. If a quadratic approximation is used, the chirp wavefront can be expressed as

$$u_i = e^{j\gamma x^2} \; , \tag{3-63}$$

$$\overline{|S|^2}$$

$$\frac{Wd}{6}$$

−W   W   x
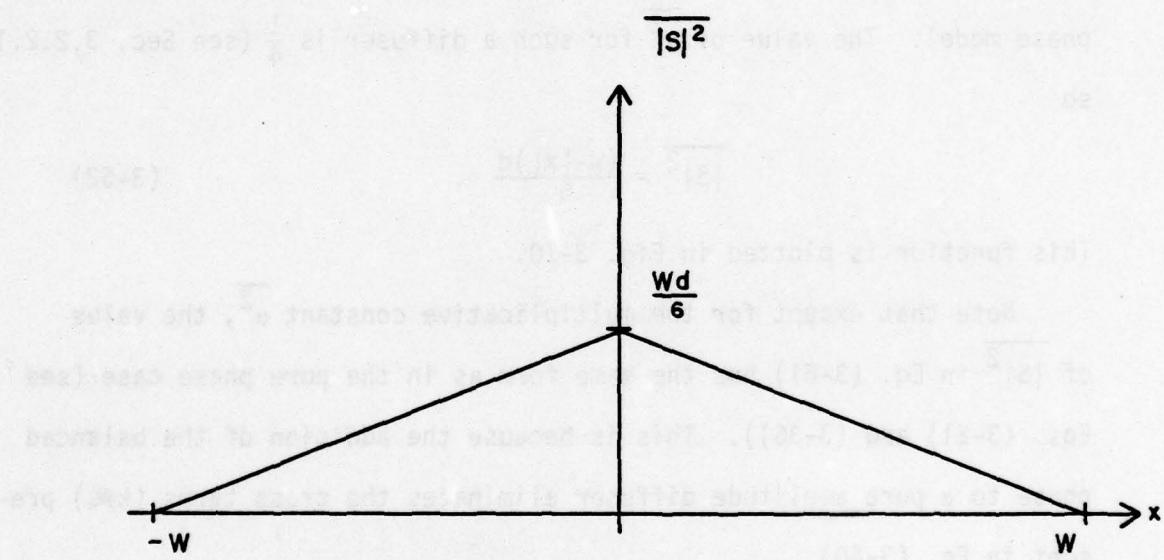
Fig. 3-10 Plot of $\overline{|S|^2} = \dfrac{(W-|x|)d}{6}$ for Combined Binary Amplitude and Balanced Phase Diffusers

where u_i represents the wavefront impinging on the diffuser and γ is the degree of curvature of the wavefront (units of γ are radians per unit length squared). The general expression for the crosscorrelation of two diffuser functions illuminated by the chirp wavefront $e^{j\gamma x^2}$ is

$$r_i \circledast r_j = \int_{-\infty}^{\infty} t_i(\xi) e^{j\gamma\xi^2} t_j^*(\xi-x) e^{-j\gamma(\xi-x)^2} d\xi \qquad (3\text{-}64)$$

(see Eq. (3-1)). This can be rewritten as

$$r_i \circledast r_j = e^{-j\gamma x^2} \int_{-\infty}^{\infty} t_i(\xi) t_j^*(\xi-x) e^{j\beta\xi} d\xi , \qquad (3\text{-}65)$$

where $\beta \triangleq 2\gamma x$. The product $t_i(\xi) t_j^*(\xi-x)$ is a piecewise constant function, so the crosscorrelation can be written as the random sum

$$S \equiv r_i \circledast r_j = e^{-j\gamma x^2} \sum_{k=1}^{M} [(t_i t_j^*)_k \int_{\Delta k} e^{j\beta\xi} d\xi]. \qquad (3\text{-}66)$$

In Eq. (3-66), $(t_i t_j^*)_k$ is the complex constant associated with the kth correlation cell, and Δ_k represents the region of integration spanned by the kth cell. The mean of $|S|^2$ will now be calculated for the various diffuser models.

3.3.1. Pure Phase Diffusers with Chirp Illumination

For pure phase diffusers, the quantity $\overline{|S|^2}$ is specified by

$$\overline{|S|^2} = \overline{SS^*} = \overline{\sum_{k=1}^{M} \sum_{\ell=1}^{M} [e^{j\theta_k} e^{-j\theta_\ell}][(\int_{\Delta_k} e^{j\beta\xi}d\xi)(\int_{\Delta_\ell} e^{j\beta\xi}d\xi)^*]}.$$

(3-67)

As in the plane wave analysis of pure phase diffusers, the cross terms in the double sum of Eq. (3-67) drop out if the diffuser phase model is balanced. This leaves

$$\overline{|S|^2} = \overline{\sum_{k=1}^{M}(\int_{\Delta_k} e^{j\beta\xi}d\xi)(\int_{\Delta_k} e^{j\beta\xi}d\xi)^*}.$$

(3-68)

3.3.1.1. Multilevel Phase Model

The integrals in Eq. (3-68) are random variables in that the region of integration Δ_k is random. For diffusers with constant spacing between potential transitions, the length of the interval Δ_k is the uniformly distributed random variable a_k described in the plane wave analysis. The first integral in Eq. (3-68) can be written as

$$\int_{\Delta_k} e^{j\beta\xi}d\xi = \int_{k_1}^{k_2} e^{j\beta\xi}d\xi ,$$

(3-69)

where k_1 and k_2 are the endpoints of the kth correlation cell. Performing the integration results in the equation

$$(\int_{\Delta_k} e^{j\beta\xi}d\xi)(\int_{\Delta_k} e^{j\beta\xi}d\xi)^* = \frac{2}{\beta^2}[1-\cos\beta a_k] ,$$

(3-70)

where the cell width a_k is equal to $k_2 - k_1$. The random variable a_k is uniformly distributed on $[0, d]$, and the a_k's are mutually independent. The expectation of Eq. (3-68) can therefore be written as

$$\overline{|S|^2} = \frac{2M}{\beta^2} [1-\overline{\cos\beta a}].$$ (3-71)

The mean value $\overline{\cos\beta a}$ is easily calculated to be

$$\overline{\cos\beta a} = \frac{\sin\beta d}{\beta d},$$ (3-72)

and substituting for M from Eq. (3-10) gives

$$\overline{|S|^2} = \frac{4(W-|x|)}{\beta^2 d} [1 - \frac{\sin\beta d}{\beta d}],$$ (3-73)

where $\beta = 2\gamma x$. As a check, it can be shown that in the limit as the curvature γ approaches zero (i.e. as the chirp wavefront approaches a plane wave), the above expression approaches

$$\overline{|S|^2} \Big|_{\gamma=0} = \frac{2(W-|x|)d}{3},$$ (3-74)

which agrees with the plane wave analysis (see Eq. (3-21)).

The nature of Eq. (3-73) can be understood by normalizing the correlation mean $\overline{|S|^2}$ by its value at $\gamma = 0$, which corresponds to the plane wave result. The normalized function is given by

$$\frac{\overline{|S|^2}}{\overline{|S|^2}\Big|_{\gamma=0}} = \frac{6(\beta d - \sin\beta d)}{(\beta d)^3} \, ,$$

(3-75)

and is plotted in Fig. 3-11. This figure demonstrates that the chirp wavefront can greatly reduce the value of $\overline{|S|^2}$ (over the plane wave case) at the tails of the function, while leaving it unaffected at x = 0 (thus helping confine the crosstalk spatially).

3.3.1.2. Ground Glass Model

Here, as in the plane wave analysis of ground glass, the number of terms M in the correlation sum of Eq. (3-66) is approximated as a constant $\overline{M}$ equal to the mean of the Poisson process characterizing M. The ground glass analysis then proceeds as in the previous multiphase analysis up to Eq. (3-71), with the exception that $\overline{M}$ replaces M; that is,

$$\overline{|S|^2} = \frac{2\overline{M}}{\beta^2} [1 - \overline{\cos\beta a}].$$

(3-76)

For ground glass, the random variable a in Eq. (3-76) is negative exponentially distributed with mean $\frac{d}{2}$ (see Eq. (3-33)), and the quantity $\overline{\cos\beta a}$ is therefore

$$\overline{\cos\beta a} = \frac{4}{4 + (\beta d)^2} \, .$$

(3-77)
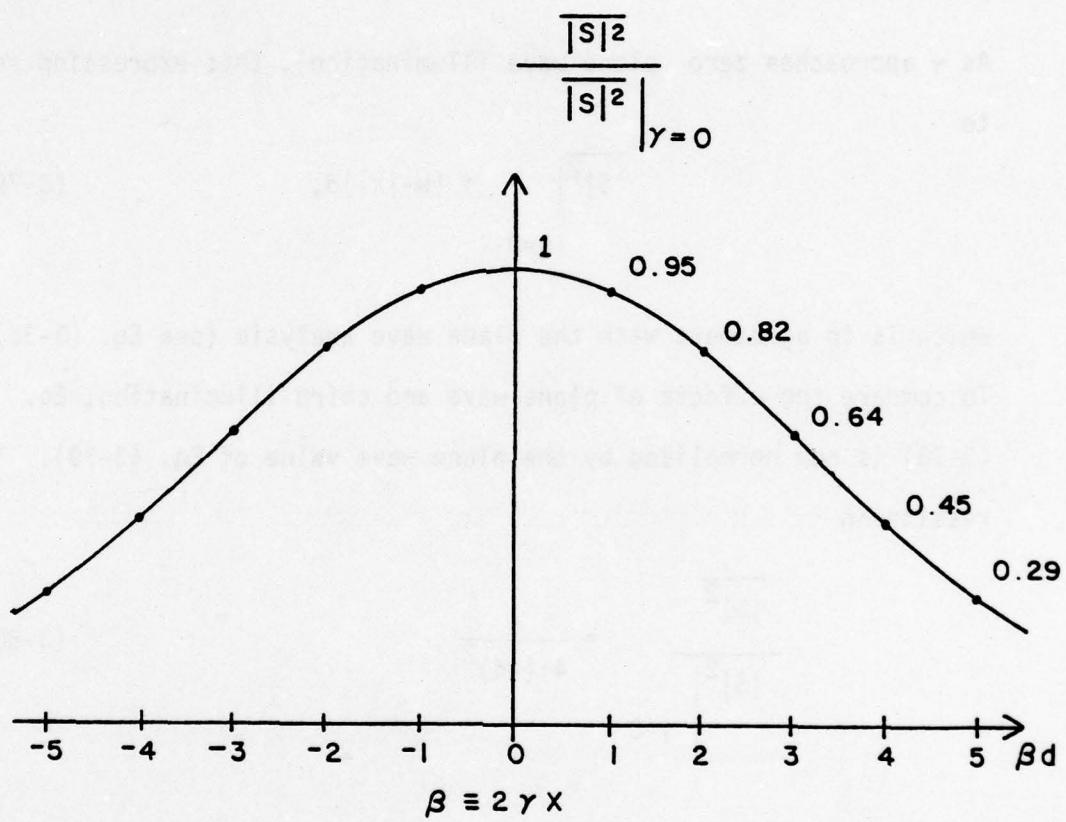
$$\frac{\overline{|S|^2}}{\overline{|S|^2}\Big|_{\gamma=0}}$$

Fig. 3-11 Plot of $\dfrac{\overline{|S|^2}}{\overline{|S|^2}\Big|_{\gamma\approx0}} = \dfrac{6(\beta d - \sin\beta d)}{(\beta d)^3}$ for Multilevel Phase Diffusers with Chirp Illumination

$\beta \equiv 2\gamma X$

Substituting from Eq. (3-77) and Eq. (3-31) for $\overline{M}$ and $\overline{\cos\beta a}$ into Eq. (3-76) gives

$$\overline{|S|^2} = \frac{4(W-|x|)d}{4+(\beta d)^2} \quad .$$

<div align="right">(3-78)</div>

As γ approaches zero (plane wave illumination), this expression reduces to

$$\overline{|S|^2}\bigg|_{\gamma=0} = (W-|x|)d,$$

<div align="right">(3-79)</div>

which is in agreement with the plane wave analysis (see Eq. (3-36)). To compare the effects of plane wave and chirp illumination, Eq. (3-78) is now normalized by the plane wave value of Eq. (3-79). This results in

$$\frac{\overline{|S|^2}}{\overline{|S|^2}\bigg|_{\gamma=0}} = \frac{4}{4+(\beta d)^2} \quad ,$$

<div align="right">(3-80)</div>

which is plotted in Fig. 3-12.

From Fig. 3-12, the chirp wavefront is seen to produce a significantly smaller crosscorrelation mean than plane wave illumination at the tails of $\overline{|S|^2}$. The amount of attenuation depends on the chirp factor $\gamma(\beta = 2\gamma x)$ and the correlation shift x, with no attenuation occurring at x = 0. Note that although the functional forms of Eqs. (3-80) and (3-75) are different, the effect is essentially the same.
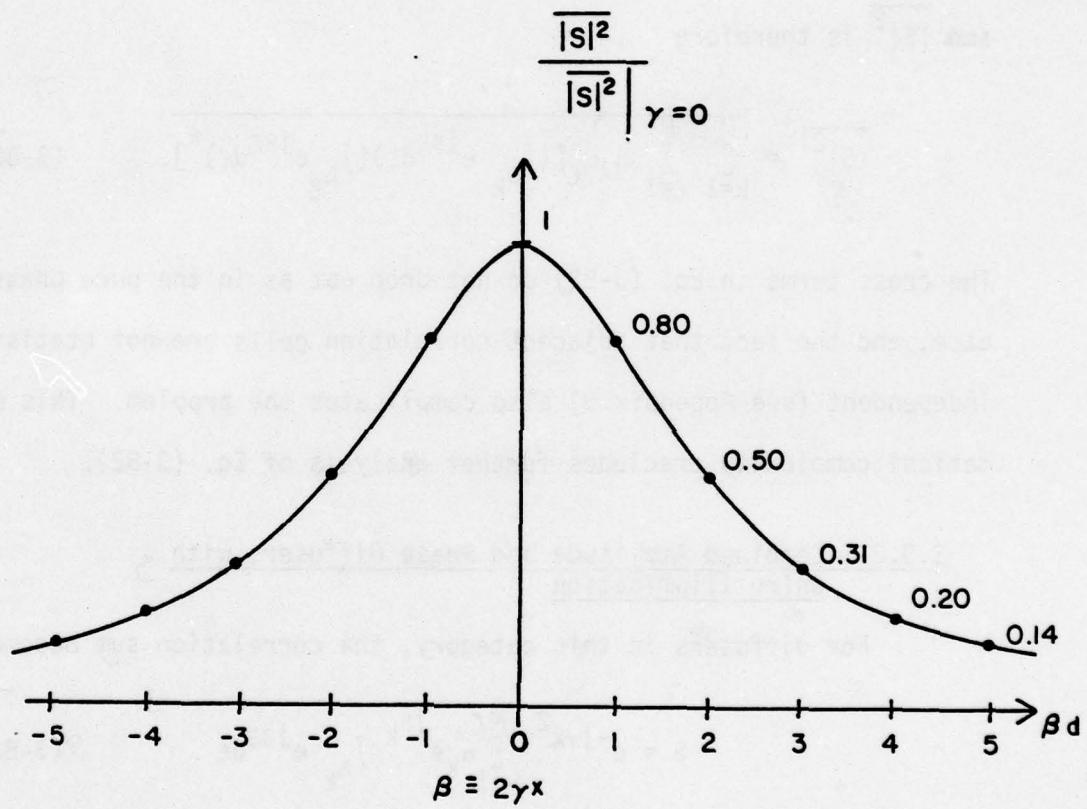
Fig. 3-12 Plot of $\dfrac{\overline{|S|^2}}{\overline{|S|^2}\big|_{\gamma=0}} = \dfrac{4}{4+(\beta d)^2}$ for Ground Glass Diffusers with Chirp Illumination

3.3.2. Pure Amplitude Diffusers with Chirp Illumination

For pure amplitude diffusers, the sum in Eq. (3-66) becomes

$$S = e^{-j\gamma x^2} \sum_{k=1}^{M} \alpha_k \int_{\Delta_k} e^{j\beta\xi} d\xi \ , \tag{3-81}$$

and $\overline{|S|^2}$ is therefore

$$\overline{|S|^2} = \overline{\sum_{k=1}^{M} \sum_{\ell=1}^{M} \alpha_k \alpha_\ell [(\int_{\Delta_k} e^{j\beta\xi} d\xi)(\int_{\Delta_\ell} e^{j\beta\xi} d\xi)^*]} . \tag{3-82}$$

The cross terms in Eq. (3-82) do not drop out as in the pure phase case, and the fact that adjacent correlation cells are not statistically independent (see Appendix B) also complicates the problem. This mathematical complexity precludes further analysis of Eq. (3-82).

3.3.3. Combined Amplitude and Phase Diffusers with Chirp Illumination

For diffusers in this category, the correlation sum becomes

$$S = e^{-j\gamma x^2} \sum_{k=1}^{M} \alpha_k e^{j\theta_k} \int_{\Delta_k} e^{j\beta\xi} d\xi \ . \tag{3-83}$$

Assuming a balanced phase model and statistically independent amplitude and phase, the cross terms present in the expression for $\overline{|S|^2}$ go to zero in a manner completely analogous to the plane wave illumination analysis of Sec. 3.2.3. The mean of $|S|^2$ can be written as (see Eq. (3-71))

$$\overline{|S|^2} = \frac{2M\overline{\alpha^2}}{\beta^2} \ [1 - \frac{\sin\beta d}{\beta d}] \ , \tag{3-84}$$

where M is given by Eq. (3-10), $\beta = 2\gamma x$, and $\overline{\alpha^2}$ depends on the amplitude model. The normalized function

$$\frac{\overline{|S|^2}}{\overline{|S|^2}\Big|_{\gamma=0}}$$

is identical to that of Eq. (3-75), and is plotted in Fig. 3-11. Once again, the chirp illumination helps reduce the value of $\overline{|S|^2}$ away from x = 0.

This concludes the crosscorrelation analysis. The results contained in this chapter are compared and discussed in greater detail in Chapters 5 and 6. The autocorrelation analysis is presented in the next chapter.

CHAPTER 4

AUTOCORRELATION CALCULATIONS

4.1. Introduction

In multiplex holography, the spatial autocorrelation of each encoding reference beam is ideally a Dirac delta function (see Chap. 1). This autocorrelation is expressed mathematically as [15]

$$r(x) \circledast r(x) \triangleq \int_{-\infty}^{\infty} r(\xi)r^*(\xi-x)d\xi , \qquad (4-1)$$

where $r(x)$ is the complex reference beam amplitude. Substituting for r from Eq. (1-10) yields

$$r \circledast r = \int_{-\infty}^{\infty} u(\xi)u^*(\xi-x)t(\xi)t^*(\xi-x)d\xi . \qquad (4-2)$$

There is a fundamental difference between the crosscorrelation integrand of Eq. (3-3) and the autocorrelation integrand of Eq. (4-2). In the <u>crosscorrelation</u> case, the diffuser transmittance functions t_i and t_j are assumed statistically independent in every correlation cell (i.e. for all values of ξ in the region of overlap), because t_i and t_j represent different diffusers. On the other hand, the <u>autocorrelation</u> integrand can in general contain correlation cells where $t(\xi)$ and $t(\xi-x)$ are necessarily <u>identical</u>, and also cells where they are statistically independent. Since $t(\xi)$ and $t(\xi-x)$ represent shifted versions of the same diffuser, the statistical independence arises from the premise that transmittance values in different diffuser cells

70

are independent (see Chap. 2, Sec. 2.3). From now on, the term "perfectly correlated" will be used to denote regions where $t(\xi)$ and $t(\xi-x)$ are necessarily identical.

The distinction between the perfectly correlated and statistically independent correlation cells which can arise in the autocorrelation integrand is shown in Fig. 4-1 for the case of a binary amplitude diffuser. For a correlation shift satisfying $|x|\epsilon[0, d]$ (Fig. 4-1(a)), the functions $t(\xi)$ and $t(\xi-x)$ are perfectly correlated in half the correlation cells and independent in the other half (the regions where $t(\xi)$ and $t(\xi-x)$ are independent are denoted by the letter "I"). If the shift $|x|$ is greater than the potential transition spacing d, then $t(\xi)$ and $t(\xi-x)$ are statistically independent in all correlation cells (Fig. 4-1(b)), and for $|x| = 0$, they are perfectly correlated in all cells.

Figure 4-1 is representative of all diffuser models with a constant spacing d between potential transition points, which includes all the models presented in Chapter 2 except ground glass (see Table 2-1). The regions of perfect correlation and statistical independence are shown in Fig. 4-2 for a portion of a ground glass phase function and two values of correlation shift $|x|$. Note that for any shift in the range $|x|\epsilon(0,W)$, there can conceivably be both perfectly correlated and independent correlation cells due to the nature of the Poisson transition model.

The purpose of this dichotomous treatment of the autocorrelation integrand is to justify dividing the autocorrelation into a "signal"
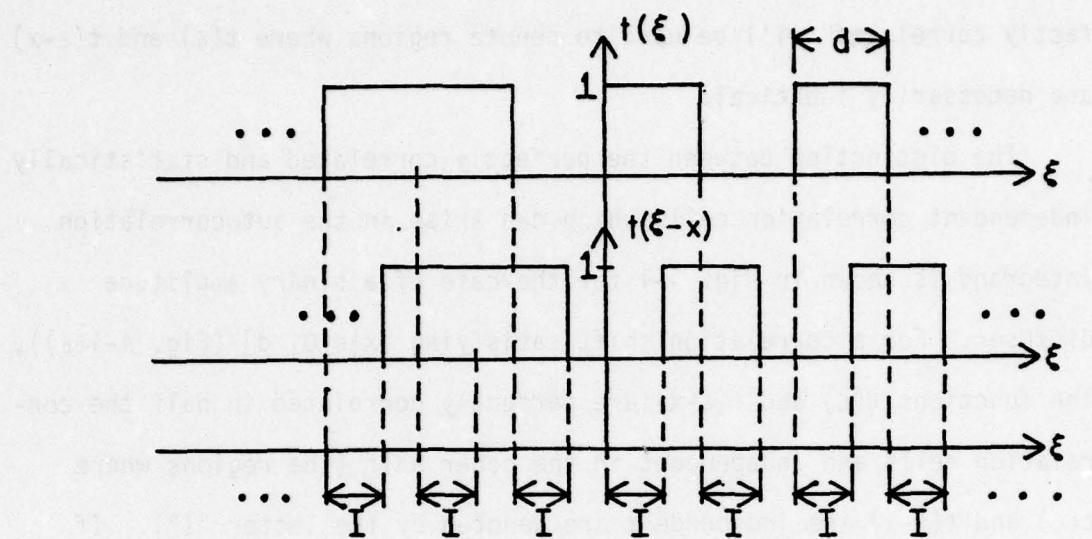
(a) Correlation shift $|x| \epsilon [0, d]$
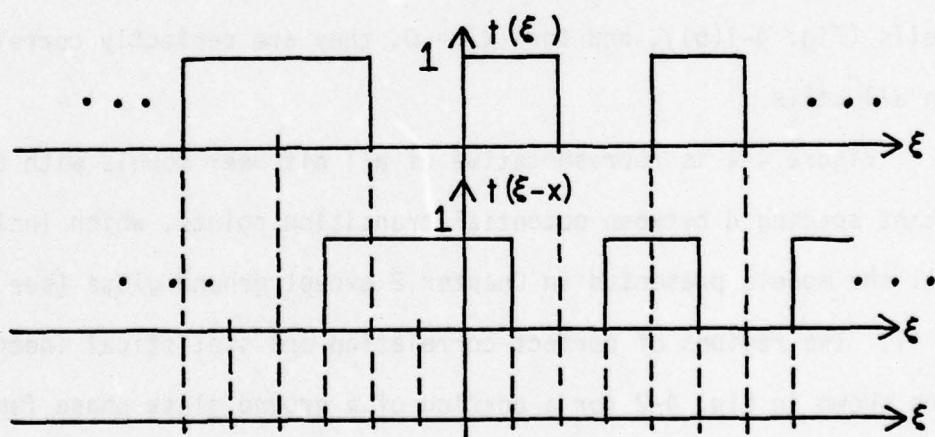
(b) Correlation shift $|x| > d$

Fig. 4-1 Autocorrelation for a Binary Amplitude Diffuser
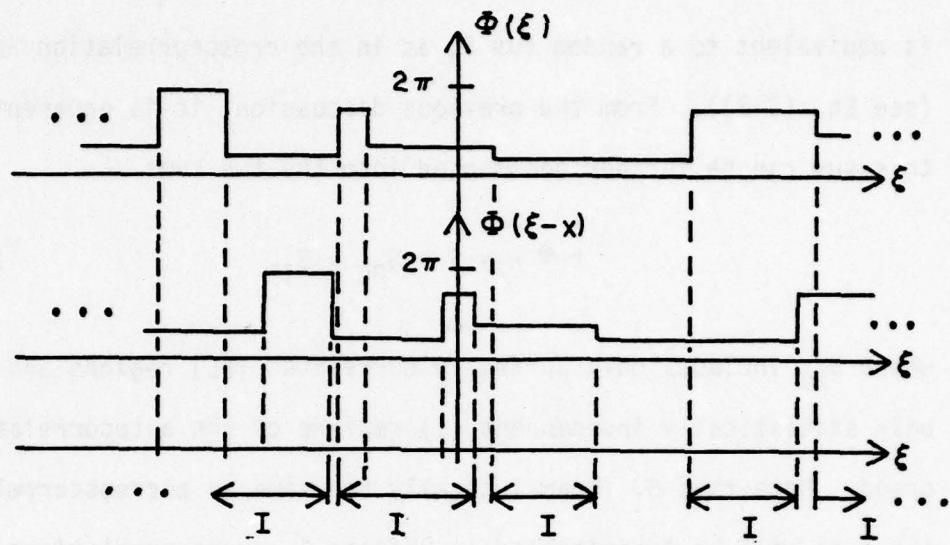
(a) Correlation shift $|x_1|$
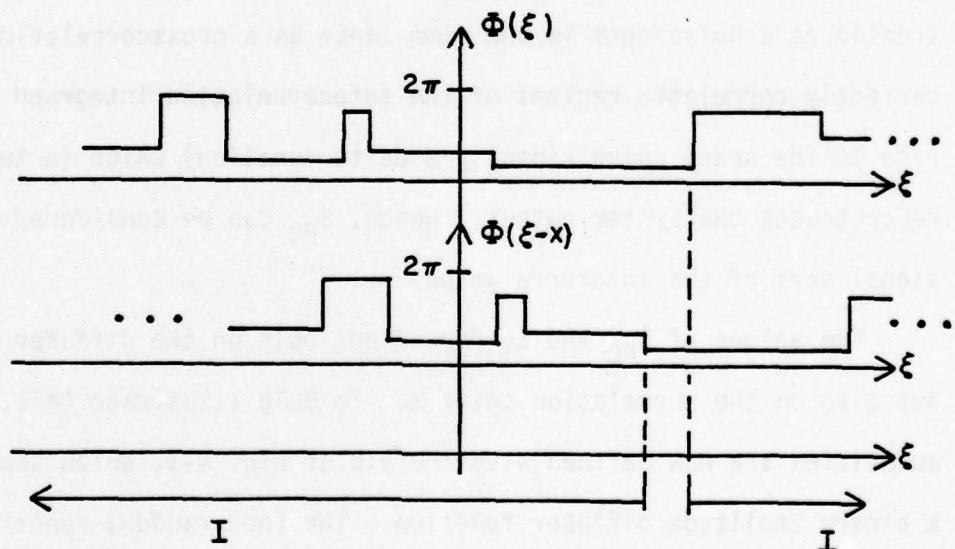
(b) Correlation shift $|x_2| > |x_1|$

Fig. 4-2 Autocorrelation for a Ground Glass Diffuser

part and a "noise" part. The autocorrelation integral of Eq. (4-1)
is equivalent to a random sum S, as in the crosscorrelation analysis
(see Eq. (3-3)). From the previous discussion, it is apparent that
this sum can be further decomposed into the two sums

$$r \circledast r = S = S_{PC} + S_I,$$ (4-3)

where S_{PC} includes only perfectly correlated (PC) regions and S_I includes
only statistically independent (I) regions of the autocorrelation inte-
grand. Note that S_I is analytically the same as a crosscorrelation
sum. As will be demonstrated in Chapter 5, crosscorrelations corres-
pond closely to output plane noise, and the sum S_I can therefore be
treated as a noise term in the same sense as a crosscorrelation. The
perfectly correlated regions of the autocorrelation integrand give
rise to the sharp spike (ideally a delta function) which in turn
reconstructs the system output. Hence, S_{PC} can be considered as the
signal part of the autocorrelation.

The values of S_{PC} and S_I depend not only on the diffuser model,
but also on the correlation shift x. To help illustrate this, several
quantities are now defined with the aid of Fig. 4-3, which shows
a binary amplitude diffuser function. The (non-random) function
$L_T(x)$ denotes the total correlation length or region of overlap of
the transmittances $t(\xi)$ and $t(\xi-x)$. The function $L_{PC}(x)$ is defined
as the portion of $L_T(x)$ over which perfect correlation of $t(\xi)$ and
$t(\xi-x)$ exists; that is, $L_{PC}(x)$ is the sum of the lengths of all
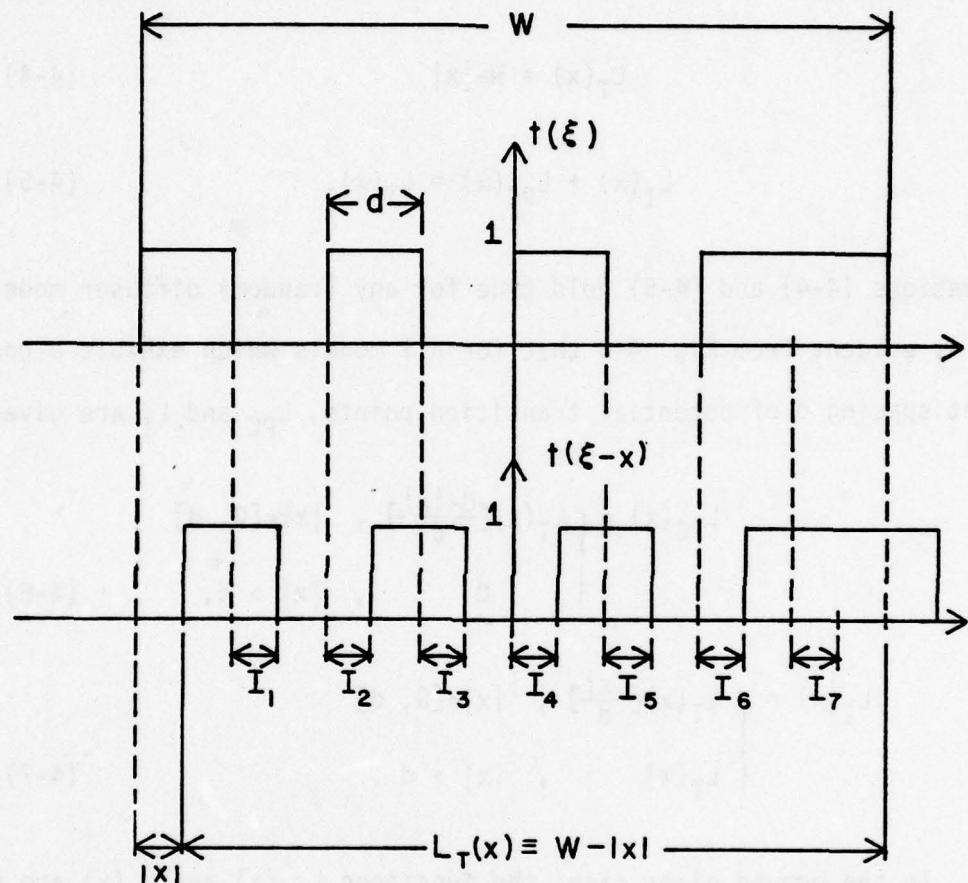
$$L_I(x) = \sum_n I_n$$

$$L_{PC}(x) = L_T(x) - L_I(x)$$

Fig. 4-3 Definition of $L_T(x)$, $L_I(x)$, and $L_{PC}(x)$

regions in $L_T(x)$ with perfect correlation. The portion of $L_T(x)$ where $t(\xi)$ and $t(\xi-x)$ are statistically independent is referred to as $L_I(x)$. These statements can be summarized by the following two equations:

$$L_T(x) = W-|x| \qquad (4-4)$$

$$L_I(x) + L_{PC}(x) = L_T(x). \qquad (4-5)$$

Equations (4-4) and (4-5) hold true for any (random) diffuser model. It is evident from Fig. 4-3 that for all models which exhibit a constant spacing d of potential transition points, L_{PC} and L_I are given by

$$L_{PC}(x) = \begin{cases} L_T(x)[\dfrac{d-|x|}{d}] \, , & |x|\epsilon[0, \, d] \\ 0 \, , & |x| > d, \end{cases} \qquad (4-6)$$

$$L_I(x) = \begin{cases} L_T(x)[\dfrac{|x|}{d}] \, , & |x|\epsilon[0, \, d] \\ L_T(x) \, , & |x| > d \, . \end{cases} \qquad (4-7)$$

In the ground glass case, the functions $L_{PC}(x)$ and $L_I(x)$ are random variables, since the transition spacing is random. Figure 4-2 indicates that as the correlation shift $|x|$ increases, L_{PC} decreases and L_I increases. It can be shown (see Appendix E) that the mean values of L_{PC} and L_I are given by

$$\overline{L_{PC}(x)} = L_T(x)e^{\dfrac{-|x|}{d}} \, , \qquad (4-8)$$

$$\overline{L_I(x)} = L_T(x)[1-e^{\frac{-|x|}{d}}], \qquad (4\text{-}9)$$

where $L_T(x) = W-|x|$.

Note that for a correlation shift $|x| > 3d$ in Eq. (4-9), $t(\xi)$ and $t(\xi-x)$ are statistically independent over better than 95% of $L_T(x)$. For a correlation shift $|x| > d$ in Eq. (4-7), $L_T(x)$ consists <u>entirely</u> of correlation cells where $t(\xi)$ and $t(\xi-x)$ are independent. Usually the diffuser width W is much greater than the spacing constant d. This implies that for a correlation shift greater than some small fraction of the diffuser width W, the autocorrelation integral of Eq. (4-1) is mathematically the same (or nearly the same in the ground glass case) as a crosscorrelation integral. To help illustrate this point, the normalized functions

$$\frac{\overline{L_{PC}(x)}}{L_T(x)} \qquad \text{and} \qquad \frac{\overline{L_I(x)}}{L_T(x)}$$

are plotted in Fig. 4-4 for both transition models. In a true cross-correlation of statistically independent functions, the ratio

$$\frac{\overline{L_I(x)}}{L_T(x)}$$

is unity for <u>all</u> shifts $|x|\epsilon[0, W]$, since there are never any regions where $t_i(\xi)$ and $t_j(\xi-x)$ are perfectly correlated. For comparison purposes, the function

$$\frac{\overline{L_I(x)}}{L_T(x)}$$
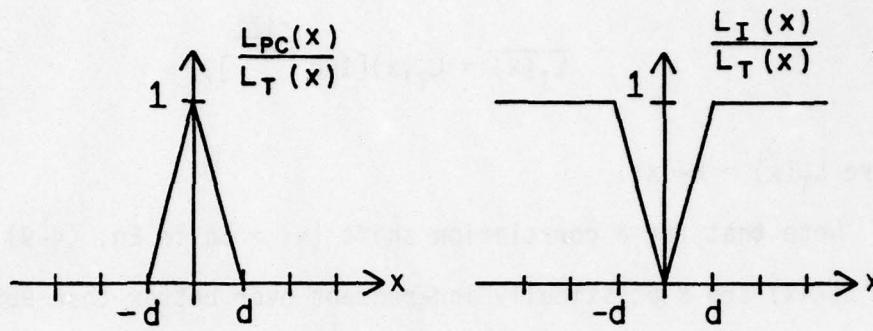
(a) Evenly spaced potential transitions
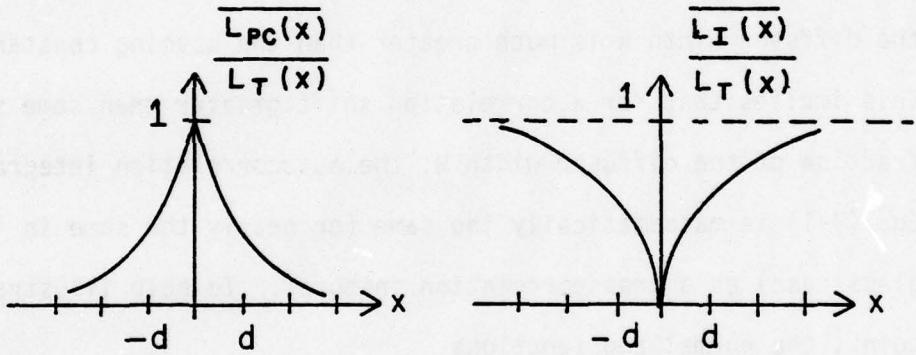
(b) Poisson transitions
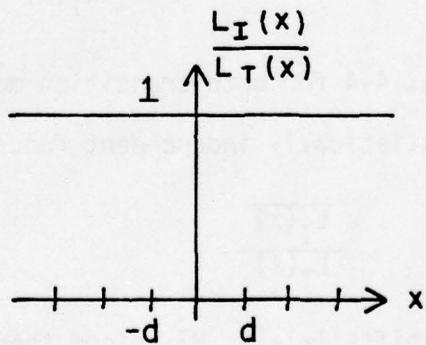
(c) Crosscorrelation case

Fig. 4-4 Plots of $\dfrac{\overline{L_{PC}(x)}}{L_T(x)}$ and $\dfrac{\overline{L_I(x)}}{L_T(x)}$ for Both Transition Models

for a true crosscorrelation is also shown in Fig. 4-4.

From the preceding arguments (specifically Fig. 4-4) it is evident that, except for a small "hole in the middle," one autocorrelation can contribute as much noise as one crosscorrelation. For this reason, the autocorrelation analysis is carried out in the following manner:

(1) Only the perfectly correlated, or "signal," part S_{PC} (see Eq. (4-3)) is considered when calculating $|S|^2$ for an auto-correlation.

(2) The noise part S_I of the total autocorrelation sum S (Eq. (4-3)) is later counted as the equivalent of a cross-correlation in the signal-to-noise analysis of Chapter 5.

Autocorrelation calculations will now be presented for the diffuser models analyzed earlier in Chapter 3.

4.2. Autocorrelations with Plane Wave Illumination

For unit amplitude plane wave illumination, the autocorrelation integral of Eq. (4-2) reduces to

$$r \circledast r = \int_{-\infty}^{\infty} t(\xi)t^*(\xi-x)d\xi , \qquad (4-10)$$

which can be equivalently expressed as a complex-valued random sum. For reasons given in Sec. 4.1, only the sum S_{PC} is considered in this analysis. The mean value $\overline{|S_{PC}|^2}$, which is related to signal intensity in the same way that the crosscorrelation mean $\overline{|S|^2}$ is related to noise intensity (see Chaps. 3 and 4), is calculated for various diffuser models in the following sections.

4.2.1. Pure Phase Diffusers

The sum S_{PC} for pure phase diffusers is given by

$$S_{PC} = \sum_{k=1}^{M} a_k \, e^{j\theta_k} \, , \tag{4-11}$$

where $\theta_k = (\phi_i - \phi_j)_k$. Since only the perfectly correlated regions are included, the phases $(\phi_i)_k$ and $(\phi_j)_k$ are identical, and Eq. (4-11) reduces to the real-valued sum

$$S_{PC} = \sum_{k=1}^{M'} a_k . \tag{4-12}$$

The calculation of $\overline{|S_{PC}|^2}$ is relatively straightforward in the multi-level phase case, but requires some approximations in the ground glass case.

4.2.1.1. Multilevel Phase Model

For diffusers of this type, the sum S_{PC} of Eq. (4-12) is a __deterministic__ function of the correlation shift x, and is given by

$$S_{PC} = M'a. \tag{4-13}$$

Now the number of terms M' in the sum is an integer approximated by

$$M' \doteq \frac{W - |x|}{d} \, , \quad |x| \epsilon [0,d], \tag{4-14}$$

and the correlation cell width a is given by

$$a = d - |x| \, , \qquad |x| \epsilon [0,d]. \tag{4-15}$$

Note that the number of perfectly correlated cells M' is only half the total number of correlation cells, as demonstrated by Fig. 4-1(a) (see Eq. (3-10)). Substituting for a and M' gives

$$S_{PC} = \begin{cases} \dfrac{(W-|x|)(d-|x|)}{d} & , \quad |x|\epsilon[0 \ d] \\ \\ 0 & , \quad |x| > d. \end{cases} \quad (4\text{-}16)$$

Since the diffuser width W is generally many times larger than the transition spacing d, Eq. (4-16) can be approximated as

$$S_{PC} \doteq \begin{cases} \dfrac{W(d-|x|)}{d} & , \quad |x|\epsilon \ [0, \ d] \\ \\ 0 & , \quad |x| > d \ . \end{cases} \quad (4\text{-}17)$$

The mean value of a deterministic function is the function itself, so

$$|\overline{S_{PC}}|^2 = S_{PC}^{\ 2} = \begin{cases} \dfrac{W^2(d-|x|)^2}{d^2} & , \quad |x|\epsilon[0 \ d] \\ \\ 0 & , \quad |x| > d. \end{cases} \quad (4\text{-}18)$$

This function is plotted in Fig. 4-5.

The result of Eq. (4-18) is applicable to any type of multi-level phase diffuser with evenly spaced potential transitions and a balanced phase model. This of course includes binary phase diffusers.

4.2.1.2. Ground Glass Model

For the ground glass model, the real-valued sum S_{PC} of Eq. (4-12) is random, whereas in the multilevel phase case (Sec. 4.2.1.1)
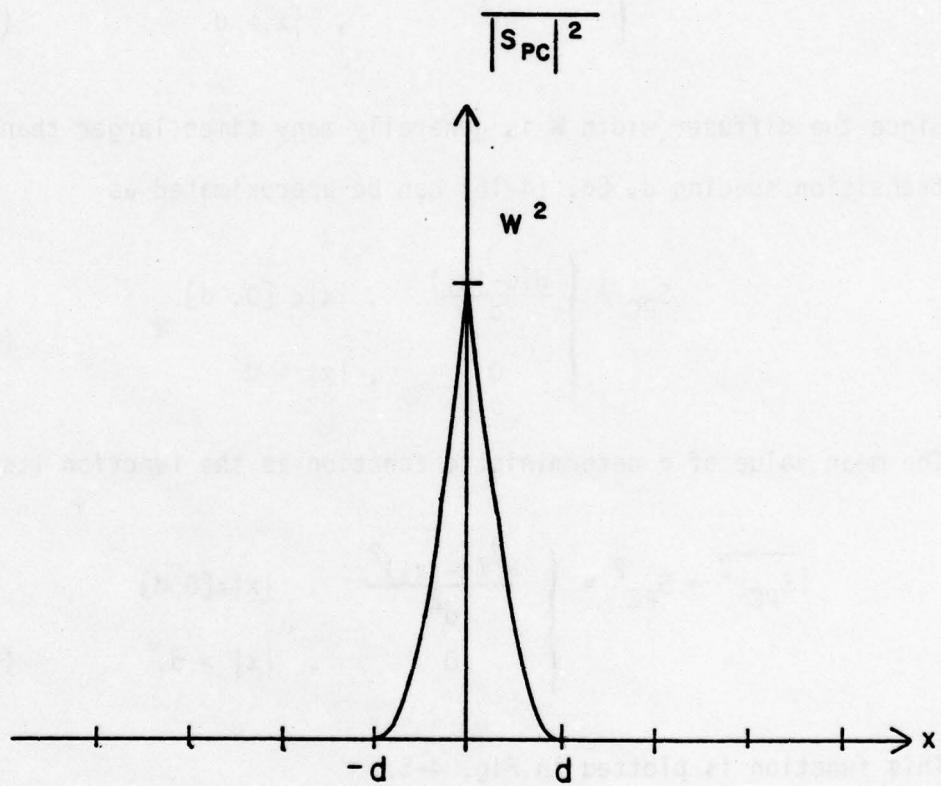
Fig. 4-5 Plot of $\overline{|S_{PC}|^2} = \dfrac{W^2(d-|x|)^2}{d^2}$ for Multilevel Phase Diffusers

S_{PC} is deterministic. The exact determination of $\overline{|S_{PC}|^2}$ for the ground glass model requires knowledge of the joint density $p(M', a_1, a_2, ...,a_k)$. As in the crosscorrelation analysis, these random variables are not mutually independent (see Chap. 3, Sec. 3.2.1.3, and Appendix C). Approximations are therefore necessary to keep the mathematics tractable.

While the mean of $|S_{PC}|^2$ is difficult to compute exactly, the mean of S_{PC} can be easily calculated as

$$\overline{S_{PC}} = \overline{\sum_{k=1}^{M'} a_k} = (W-|x|)e^{\frac{-|x|}{d}} . \tag{4-19}$$

Note that $\overline{S_{PC}}$ is exactly the same quantity as $\overline{L_{PC}}$ in Eq. (4-8). The mean square value $\overline{|S_{PC}|^2}$ can be approximated by

$$\overline{|S_{PC}|^2} \doteq (\overline{S_{PC}})^2, \tag{4-20}$$

and substituting for $\overline{S_{PC}}$ from Eq. (4-19) gives

$$\overline{|S_{PC}|^2} \doteq (W-|x|)^2 e^{\frac{-2|x|}{d}} . \tag{4-21}$$

This can be further approximated, since $W \gg d$, as

$$\overline{|S_{PC}|^2} \doteq W^2 e^{\frac{-2|x|}{d}} . \tag{4-22}$$

Equation (4-22) is plotted in Fig. 4-6.
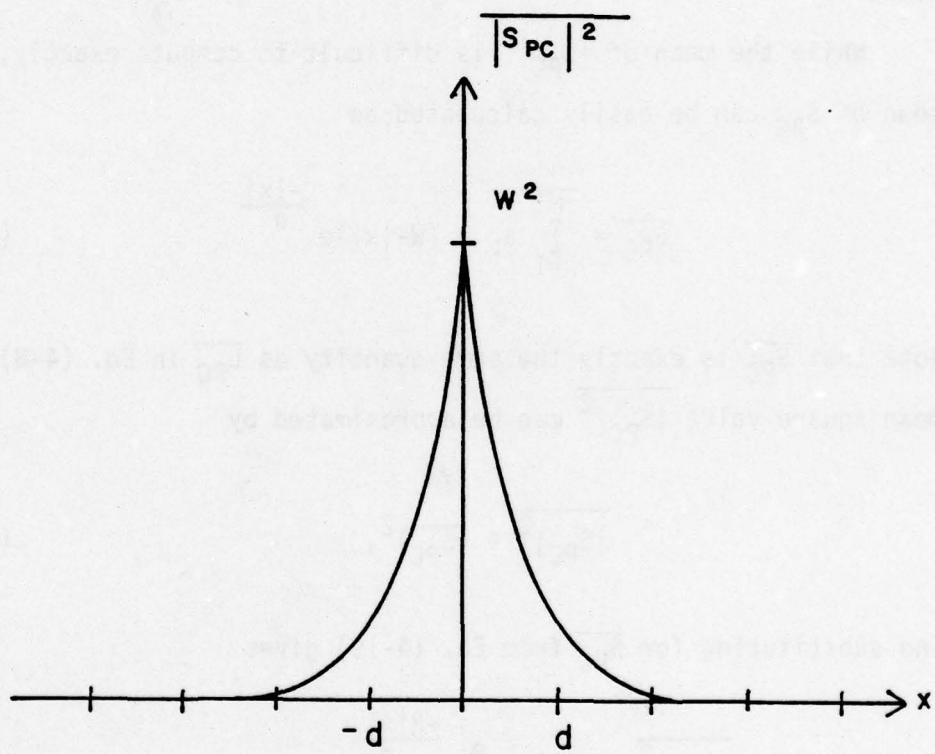
Fig. 4-6 Plot of $\overline{|S_{PC}|^2} = W^2 e^{\frac{-2|x|}{d}}$ for Ground Glass Diffusers

The true value of $\overline{|S_{PC}|^2}$ is given by [19]

$$\overline{|S_{PC}|^2} = (\overline{S_{PC}})^2 + \sigma_{PC}^2 , \qquad (4\text{-}23)$$

where σ_{PC}^2 is the variance of S_{PC}. For a variance σ_{PC}^2 that is much smaller than $\overline{S_{PC}}$, Eq. (4-22) represents a very good approximation; however, the variance of S_{PC} is unknown, so the accuracy of Eq. (4-22) is also unknown. The approximation is justified for several reasons. First, it avoids a great deal of mathematical complexity. Second, it represents a lower bound for the possible values of $\overline{|S_{PC}|^2}$, and is therefore a conservative estimate of signal strength. Finally, the approximation of Eq. (4-22) is <u>exact</u> at x = 0; that is, at x = 0 S_{PC} is equal to the constant W, so $\overline{|S_{PC}|^2} = W^2$. The signal-to-noise analysis in Chapter 5 utilizes only the value of $\overline{|S_{PC}|^2}$ at x=0, where Eq. (4-22) is completely accurate.

4.2.2. Pure Amplitude Diffusers

The sum S_{PC} for pure amplitude diffusers is real-valued and random, and is expressed as

$$S_{PC} = \sum_{k=1}^{M'} a_k \alpha_k, \qquad (4\text{-}24)$$

where $\alpha_k = (t^2)_k$ is the squared value of the amplitude transmittance in the kth perfectly correlated cell, and a_k is the width of this cell. These quantities are indicated in Fig. 4-7, where the product $t(\xi)t(\xi-x)$ is shown for a typical binary amplitude diffuser. The mean of $|S_{PC}|^2$ is now calculated for some specific amplitude models.
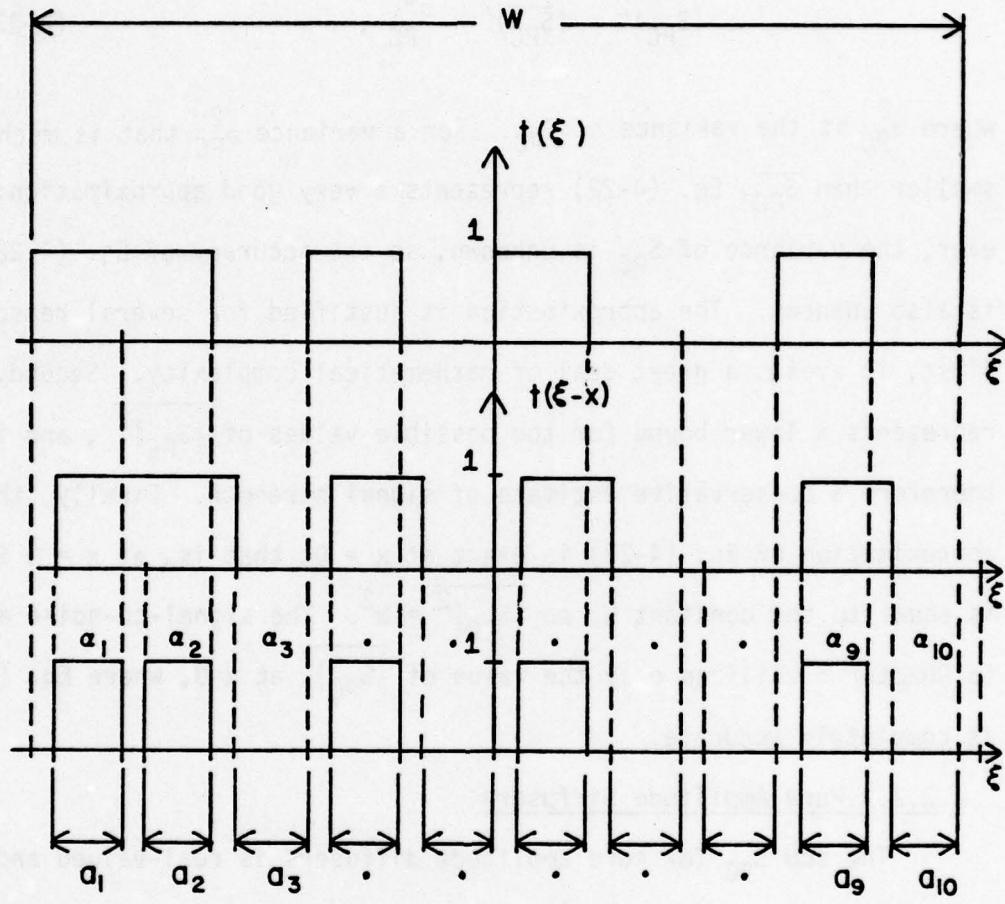
Fig. 4-7 Autocorrelation of Binary Amplitude Diffusers

4.2.2.1. Binary Amplitude Model

The squared value of the sum in Eq. (4-24) is given by

$$|S_{PC}|^2 = \sum_{k=1}^{M'} a_k^2 \alpha_k^2 + \sum_{k \neq \ell}^{M'} \sum^{M'} a_k a_\ell \alpha_k \alpha_\ell \ ,$$
(4-25)

where M' and the a_k's are the deterministic functions specified in
Eqs. (4-14) and (4-15). The α_k's represent the only randomness in
S_{PC}, and are statistically independent and identically distributed.
Note that the statistical dependence of adjacent α values encountered
in the crosscorrelation analysis (see Appendix B) does not apply here,
since all α values are taken from non-adjacent correlation cells (see
Fig. 4-7). The expectation can therefore be written as

$$\overline{|S_{PC}|^2} = M'a^2\overline{\alpha^2} + M'(M'-1)a^2\overline{\alpha}^2 \ .$$
(4-26)

Substituting for $\overline{\alpha^2}$, $\overline{\alpha}$, a, and M' from Eqs. (3-45), (4-14), and (4-15)
gives the result

$$\overline{|S_{PC}|^2} = \begin{cases} \dfrac{(W-|x|)(d-|x|)^2}{16d}[3 + \dfrac{(W-|x|)}{d}] & , \ |x|\epsilon[0, \ d], \\ \\ \qquad\qquad 0, \qquad |x| > d. \end{cases}$$
(4-27)

Noting that $W \gg d$ and $\dfrac{W}{d} \gg 3$, Eq. (4-27) can be approximated by

$$\overline{|S_{PC}|^2} \doteq \begin{cases} \dfrac{W^2(d-|x|)^2}{16d^2} & , \ |x|\epsilon[0, \ d] \\ \\ \qquad 0 & , \ |x| > d \ . \end{cases}$$
(4-28)

This expression is graphed in Fig. 4-8.

It is interesting to note that the peak value of $\overline{|S_{PC}|^2}$ (attained at $|x| = 0$) is $\frac{W^2}{16}$, whereas the peak of $\overline{|S_{PC}|^2}$ in the pure phase case is W^2. The reason for this difference is that the pure phase diffusers do not attenuate, while pure amplitude diffusers can attenuate quite a lot.

4.2.2.2. Uniformly Distributed Amplitude Model

If the amplitude transmittance is assumed uniformly distributed on [0, 1], then the means $\overline{\alpha}$ and $\overline{\alpha^2}$ are given by Eq. (3-52). Substituting these values and the appropriate values for M' and a into Eq. (4-26) gives

$$\overline{|S_{PC}|^2} = \begin{cases} \dfrac{(W-|x|)(d-|x|)^2}{16d}\left[\dfrac{7}{9} + \dfrac{W-|x|}{d}\right], & |x|\epsilon[0, d] \\\\ 0, & |x| > d. \end{cases} \quad (4\text{-}29)$$

Since $W \gg d$ and $\frac{W}{d} \gg \frac{7}{9}$, Eq. (4-29) can be simplified as

$$\overline{|S_{PC}|^2} \doteq \begin{cases} \dfrac{W^2(d-|x|)^2}{16d^2}, & |x|\epsilon[0, d] \\\\ 0, & |x| > d. \end{cases} \quad (4\text{-}30)$$

This function is the same as given by Eq. (4-28), and is shown in Fig. 4-8.

The mean square value $\overline{|S_{PC}|^2}$ can be easily calculated for any other amplitude diffuser type with evenly spaced potential transition
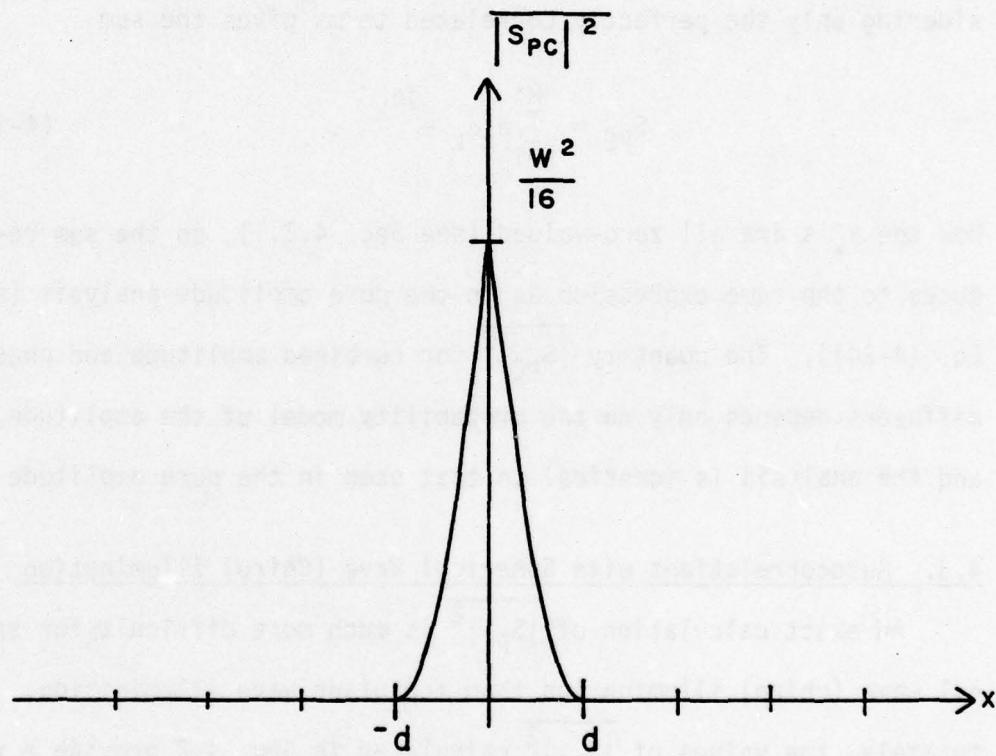
Fig. 4-8 Plot of $\overline{|S_{PC}|^2} = \dfrac{W^2(d-|x|)^2}{16d^2}$ for Binary and Uniformly Distributed Amplitude Diffusers

points. The means $\bar{\alpha}$ and $\overline{\alpha^2}$ are computed according to the appropriate probability model and then substituted into Eq. (4-26).

4.2.3. Combined Amplitude and Phase Diffusers

As in the crosscorrelation analysis (Chap. 3, Sec. 3.2.3), constant spacing between potential transition points is assumed. Considering only the perfectly correlated terms gives the sum

$$S_{PC} = \sum_{k=1}^{M'} a_k \alpha_k \, e^{j\theta_k} \quad . \tag{4-31}$$

Now the θ_k's are all zero-valued (see Sec. 4.2.1), so the sum reduces to the same expression as in the pure amplitude analysis (see Eq. (4-24)). The quantity $\overline{|S_{PC}|^2}$ for combined amplitude and phase diffusers depends only on the probability model of the amplitude, and the analysis is identical to that used in the pure amplitude case.

4.3. Autocorrelations with Spherical Wave (Chirp) Illumination

An exact calculation of $\overline{|S_{PC}|^2}$ is much more difficult for spherical wave (chirp) illumination than for plane wave illumination. Fortunately, the values of $\overline{|S_{PC}|^2}$ calculated in Sec. 4.2 provide a very reasonable approximation for the chirp autocorrelations. This approximation is justified for the following reasons. First, the peak value of $\overline{|S_{PC}|^2}$ (attained at x = 0) is the same for both chirp ($e^{j\gamma x^2}$) and unit amplitude plane wave illumination. Since the signal-to-noise analysis of Chapter 5 uses only the peak value, the approximation is exact in this regard. Second, the chirp illumination does not signifi-

cantly affect the correlation value for a small neighborhood of correlation shifts centered at x = 0 [8], which implies that the autocorrelation sum S_{PC} is relatively unaffected by the presence of the chirp wavefront. This idea is perhaps best illustrated with the aid of an example.

Consider the case of a random binary phase diffuser with width W = 3.8 mm and 128 diffuser cells, corresponding to a cell width d ≐ 0.03 mm. Assume further that the diffuser is illuminated by a spherical wavefront emanating from a point source a distance f = 10 mm away. This example corresponds closely to a computer simulation done by Redus [11] and experimental work done by Jones [20]. The problem setup is illustrated in Fig. 4-9.

A quadratic approximation to the spherical wave generated by a point source at a distance f from the source is given by [21]

$$chirp = e^{j\frac{k}{2f}x^2} = e^{j\gamma x^2} , \qquad (4-32)$$

where k is the wave number. The chirp factor γ is therefore

$$\gamma = \frac{k}{2f} = \frac{\pi}{\lambda f} . \qquad (4-33)$$

The wavelength used in the experimental work [20] was 5145 angstroms (Argon laser), and substituting for f and λ gives

$$\gamma \doteq 611 \frac{rad}{(mm)^2} . \qquad (4-34)$$
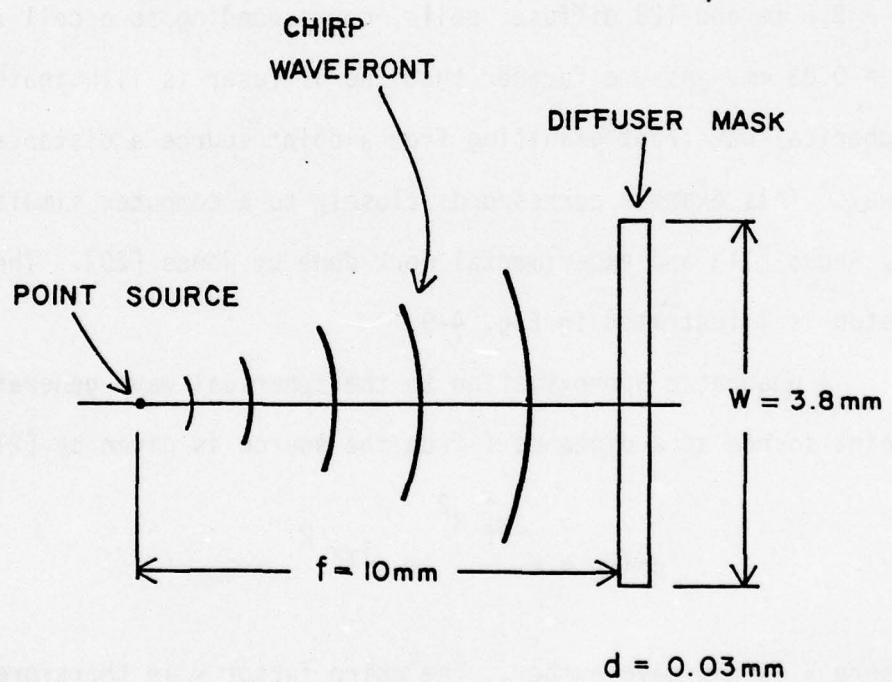
Fig. 4-9 Problem Setup for the Chirp Illumination Example

For a correlation shift $|x| = d$, the autocorrelation integral is entirely equivalent to a crosscorrelation. The normalized function

$$\frac{\overline{|S|^2}}{\overline{|S|^2}\Big|_{\gamma = 0}}$$

of Eq. (3-75) can therefore serve as a comparison of autocorrelation values for chirp and plane wave illumination, as long as the correlation shift x satisfies $|x| \geq d$. Substituting the values $\gamma = 611$ and $|x| = d = 0.03$ mm into Eq. (3-75) gives

$$\frac{\overline{|S|^2}}{\overline{|S|^2}\Big|_{\gamma = 0}} = 0.94. \tag{4-35}$$

From Eq. (4-35), the chirp wavefront is seen to have only a minor effect on the mean square value of the autocorrelation integral at $|x| = d$, and should have even less effect for $|x| < d$. Since only correlation shifts $|x| \leq d$ are significant in calculating $\overline{|S_{PC}|^2}$ for any diffuser model with evenly spaced potential transitions (see Fig. 4-5), it is reasonable to ignore the effect of chirp illumination on this "signal" part of the autocorrelation. The "noise" part S_I (see Eq. (4-3)) is of course reduced in magnitude at the autocorrelation tails in the same way as a crosscorrelation (see Fig. 3-11).

In light of the preceding arguments, the quantity $\overline{|S_{PC}|^2}$ for chirp illumination will be approximated by the values calculated in Sec. 4.2 for plane wave illumination. These values are given in

Eqs. (4-18), (4-22), (4-28), and (4-30). This concludes the auto-
correlation analysis. A signal-to-noise analysis is presented in the
next chapter.

CHAPTER 5

SIGNAL-TO-NOISE ANALYSIS

5.1. Introduction

As demonstrated in Chapter 1 (see Eq. (1-8)), the output of a linear optical system (which can in general be space-variant) represented by a multiplexed hologram is expressed as

$$0 = \sum_{i=1}^{N} s_i h_i * (r_i \circledast r_i) + \sum_{i \neq j}^{N} \sum_{}^{N} s_i h_j * (r_i \circledast r_j), \qquad (5\text{-}1)$$

where the h's are the sampled impulse responses, the s's are complex constants associated with the system input, and the r's represent the multiplexing reference beams. The ideal output of such a multiplexed hologram is given by

$$0_{ideal} = \sum_{i=1}^{N} s_i h_i, \qquad (5\text{-}2)$$

which indicates that the autocorrelation terms $r_i \circledast r_i$ are ideally Dirac delta functions, and the crosscorrelation terms $r_i \circledast r_j$ ($i \neq j$) are ideally zero. These correlations are of course not ideal in practice, and the fidelity of the output suffers as a result. The extent of the degradation is difficult to determine in a quantitative sense without knowing the exact nature of both the system and the input. For this reason, the following analysis is based on an ideal imaging system having unit magnification, with point sources of unit strength serving as the system input. Although the selection of this

95

particular (space-invariant) system may seem somewhat arbitrary, it provides the framework for a simple and meaningful comparison of different diffuser families.

The response of an ideal unit imaging system to a point source input is given by the Dirac delta function as

$$h_i(x) \equiv S[\delta(x-x_i)] = \delta(x-x_i), \qquad (5\text{-}3)$$

where the one-dimensional case is considered for simplicity. The input is assumed to consist entirely of unit strength point sources, so the sampling constants are given by

$$s_i = 1, \quad i = 1, 2, \ldots, N. \qquad (5\text{-}4)$$

Substituting these values for h_i and s_i into the general expression of Eq. (5-1) yields

$$0 = \sum_{i=1}^{N} \delta(x-x_i)*(r_i \circledast r_i) + \sum_{i \neq j}^{N} \sum^{N} \delta(x-x_j)*(r_i \circledast r_j). \quad (5\text{-}5)$$

The portion of the system output 0 which is accessed by the kth reference beam r_k is given by

$$0_k = \delta(x-x_k)*(r_k \circledast r_k) + \sum_{\substack{j=1 \\ j \neq k}}^{N} \delta(x-x_j)*(r_k \circledast r_j) . \qquad (5\text{-}6)$$

Now if the ith reference beam r_i is centered at the coordinate x_i, then the term $\delta(x-x_j)*(r_k \circledast r_\ell)$ is centered at $x = x_j + x_k - x_\ell$, due to the

properties of convolution and correlation [15]. For the purposes of this analysis, both the reference beams and the input point sources are assumed to be equally spaced. This situation is illustrated in Fig. 5-1. As a consequence, the first term in Eq. (5-6) is centered at the point $x = x_k + x_k - x_k = x_k$, and the terms in the summation are centered at $x = x_j + x_k - x_j = x_k$, so $\underline{\text{all}}$ the terms in Eq. (5-6) are centered at $x = x_k$. Using the convolution property of the Dirac delta function in Eq. (5-6) gives

$$O_k = [(r_k \circledast r_k) + \sum_{\substack{j=1 \\ j \neq k}}^{N} (r_k \circledast r_j)]_{\substack{\text{centered} \\ \text{at } x_k}} . \qquad (5\text{-}7)$$

The first term $r_k \circledast r_k$ in Eq. (5-7) is an autocorrelation, and can be decomposed into a signal part and a noise part (see Chap. 4, Sec. 4.1). The cross terms $r_k \circledast r_j$ are the crosscorrelations analyzed in Chapter 3. Designating the signal part of the autocorrelation by $(AC)_s$, the noise part by $(AC)_n$, and the crosscorrelations by $(CC)^\#$, Eq. (5-7) can be rewritten as

$$O_k = (AC)_s + (AC)_n + \sum_{\substack{j=1 \\ j \neq k}}^{N} (CC)_j, \qquad (5\text{-}8)$$

—————

#The quantities $(AC)_s$, $(AC)_n$, and (CC) are exactly the same terms previously denoted by S_{pc}, S_I^n, and S, respectively (see Eqs. (4-3) and (3-3)). The reason for changing notation here is that the new designations are more suggestive, and will hopefully minimize confusion and aid in keeping track of the various correlations through the remainder of the signal-to-noise analysis.

Fig. 5-1 Reference Beam and Input Point Source Spacing

where O_k is centered at $x = x_k$. As demonstrated in Chapter 4, Sec. 4.1, the noise part of the autocorrelation is approximately the same in overall effect as a crosscorrelation; that is,

$$(AC)_n \triangleq (CC) \qquad (5-9)$$

(see Fig. 4-4). Equation (5-8) can therefore be modified and expressed as

$$O_k = (AC)_s + \sum_{j=1}^{N} (CC)_j . \qquad (5-10)$$

As Eq. (5-10) indicates, the system output O_k at each point x_k, $k = 1, 2, \ldots, N$, consists of both an autocorrelation signal term and N crosscorrelation noise terms, all centered at x_k. The output O_k can be described as a sharp spike surrounded by a "cloud" of diffuse noise, as illustrated in Fig. 5-2. The total output O is an array of these spikes, with (potentially) overlapping noise clouds.

A signal-to-noise ratio will now be defined based on the output O_k, which results from the referencing of a single hologram. The definition also holds for simultaneous as well as single point playback, as long as the (spatially displaced) noise clouds associated with each hologram (see Fig. 5-2) do not overlap. The SNR is specified in terms of Eq. (5-10) as

$$SNR \triangleq \left. \frac{\overline{|(AC)_s|^2}}{\overline{|\sum_{j=1}^{N} (CC)_j|^2}} \right|_{x = x_k} . \qquad (5-11)$$
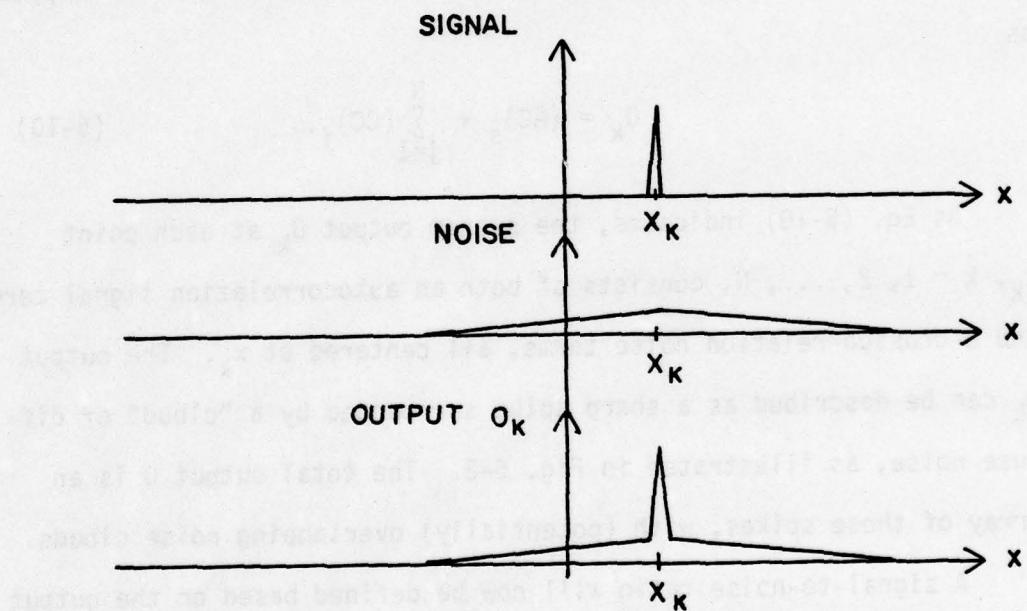
Fig. 5-2 Output Accessed by the kth Reference Beam (O_k)

Since both the numerator and denominator of Eq. (5-11) attain their peak values at x_k (see Fig. 5-2), the SNR can be equivalently defined as

$$SNR \triangleq \frac{\overline{|(AC)_s|^2}_{peak}}{\overline{|\sum\limits_{j=1}^{N} (CC)_j|^2}_{peak}} . \qquad (5-12)$$

The denominator of the SNR is the mean value of the squared modulus of N crosscorrelations added on an amplitude basis. The results in Chapter 3 are based on only one crosscorrelation, but can be easily modified to accommodate the sum of several crosscorrelations. Note that the previous analysis was carried out with this in mind (see Eqs. (3-17) and (3-18)). The sum in the denominator of Eq. (5-12) can be expressed as

$$\sum_{j=1}^{N} (CC)_j = \sum_{j=1}^{N} S_j , \qquad (5-13)$$

and substituting for S_j from Eq. (3-3) gives

$$\sum_{j=1}^{N} (CC)_j = \sum_{j=1}^{N} (\sum_{k=1}^{M} z_k)_j . \qquad (5-14)$$

Since each of the N sums in Eq. (5-14) represents a different cross-correlation, they are statistically independent. The double sum in Eq. (5-14) is therefore equivalent (in a probabilistic sense) to the following:

$$\sum_{j=1}^{N} (CC)_j = \sum_{k=1}^{MN} z_k \qquad (5\text{-}15)$$

(see also Chap. 3, Sec. 3.2.1.1). The implication of Eq. (5-15) is that the mean of $|\sum_{j=1}^{N} (CC)_j|^2$ can be calculated in a manner completely analogous to the calculations of $\overline{|S|^2}$ included in Chapter 3, the only difference being the number of terms in the sum. If the quantity MN is substituted for M in the crosscorrelation analysis, the results of Chapter 3 can be directly applied.

Before proceeding with the analysis, the SNR definition of Eq. (5-12) will be examined from a qualitative viewpoint. This particular definition has several attractive qualities. First of all, it is a function only of the reference beam statistics, and is therefore a very direct basis for diffuser comparisons. Second, it is intuitively appealing, because it reflects the dependence of output fidelity on both the autocorrelation and crossocrrelation characteristics of the reference beams. This SNR is basically the same definition used by La Macchia and White [6], and Leger and Lee [22].

A disadvantage of the SNR definition is that it does not show the dependence of the system resolution capability on the width of the autocorrelation function [5]. It also does not reflect the previously demonstrated benefits of chirp diffuser illumination, since chirping has a negligible effect for small correlation shifts (see Chap. 3, Sec. 3.3, and Chap. 4, Sec. 4.3). Finally, this SNR does

not take into account the finite apertures encountered in the optical system (except for the diffuser); that is, it does not include diffraction effects at these apertures (for a more detailed discussion in this regard, see Ref. [6]). These are all relatively minor points, especially in comparing different diffuser types (rather than types of diffuser illumination). Another characteristic of the definition of Eq. (5-12) (although not necessarily a disadvantage) is that it is based essentially on a single point playback; that is, the effect of other "noise clouds" is not considered (see Fig. 5-2).

It should be emphasized that the SNR defined in Eq. (5-12) is for comparative purposes only, and is not intended to be an absolute measure of system performance. Signal-to-noise calculations are now included for the various diffuser families analyzed in Chapters 3 and 4.

5.2. Signal-to-Noise Ratio Calculations

As stated in the preceding section, the SNR definition of Eq. (5-12) does not distinguish between plane wave and chirp illumination, so the SNR's calculated in the following sections apply to both cases. The effect of increasing the number of terms in the crosscorrelation sum from M to MN (see Eq. (5-15)), where N is the number of exposures, can in all cases be accounted for by substituting $N(W-|x|)$ for the quantity $(W-|x|)$ in the final results of Chapter 3. This can easily be verified by proceeding through each analysis of Chapter 3 after substituting MN for M.

5.2.1. Pure Phase Diffusers

The autocorrelation and crosscorrelation results of Chapters 3 and 4 for both multilevel balanced phase diffusers and ground glass are summarized in Fig. 5-3, where the effect of N exposures is included.

5.2.1.1. Multilevel Phase Model

From Fig. 5-3(a), the SNR for diffusers of this class is given by

$$SNR \triangleq \frac{\text{Peak of autocorrelation expression}}{\text{Peak of crosscorrelation expression}} = \frac{3}{2}(\frac{W}{Nd}).$$

(5-16)

Note that the SNR is directly proportional to diffuser width W (in two dimensions, this would be area) and inversely proportional to both diffuser cell width d and number of exposures N. The factor $\frac{W}{d}$ corresponds to a space-bandwidth product, which is in agreement with the analysis of Leger and Lee [22].[#]

5.2.1.2. Ground Glass Model

In the case of ground glass, the SNR is seen from Fig.

[#]A function that is both space-limited and (approximately) band-limited can be sufficiently specified by approximately XB numbers, where X is the spatial extent of the function and B is the bandwidth (see Gaskill [23]). In the case of diffusers, these are complex numbers. If the diffuser "bandwidth" is approximated as $B \doteq \frac{1}{d}$ (a common approximation in communication theory), then according to the previous comments, a diffuser can be specified by $W(\frac{1}{d})$ complex numbers. These numbers would, of course, correspond to the transmittance values in the $\frac{W}{d}$ cells comprising the diffuser.
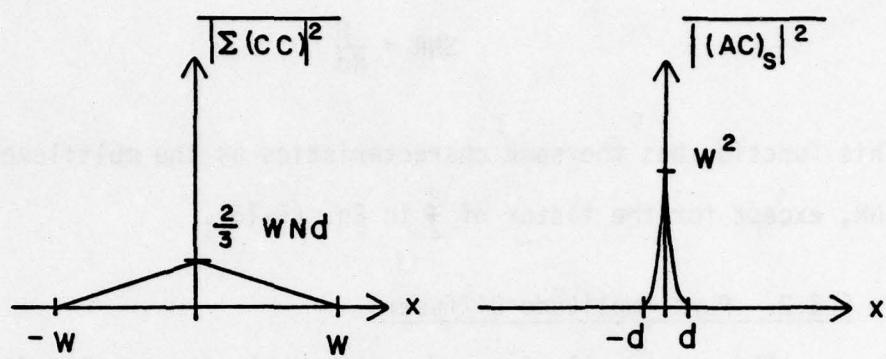
(a) Multilevel phase
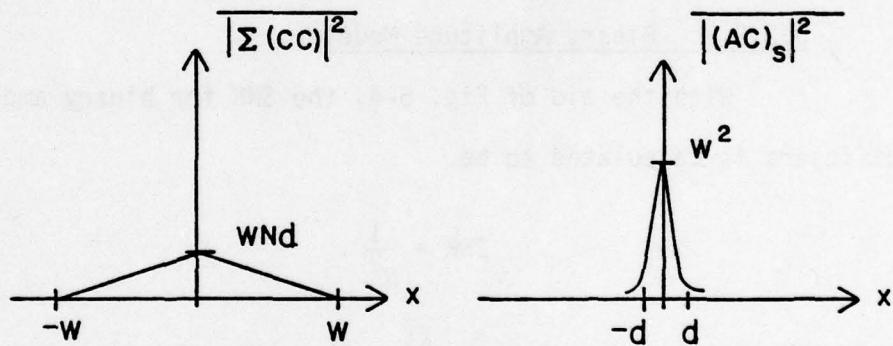
(b) Ground glass

Fig. 5-3 Autocorrelations and Total Crosscorrelations for
Pure Phase Diffusers

5-3(b) to be

$$SNR = \frac{W}{Nd} .$$ (5-17)

This function has the same characteristics as the multilevel phase SNR, except for the factor of $\frac{3}{2}$ in Eq. (5-16).

5.2.2. Pure Amplitude Diffusers

The autocorrelation and crosscorrelation results for both binary and uniformly distributed amplitude diffusers are repeated in Fig. 5-4, where the exposure number N is incorporated in the crosscorrelation result.

5.2.2.1. Binary Amplitude Model

With the aid of Fig. 5-4, the SNR for binary amplitude diffusers is calculated to be

$$SNR = \frac{1}{N^2} .$$ (5-18)

This SNR will in general be much smaller than the pure phase SNR's of Eqs. (5-16) and (5-17). Note the inverse dependence on N^2 rather than N.

5.2.2.2. Uniformly Distributed Amplitude Model

From Fig. 5-4, the SNR for uniformly distributed amplitude diffusers is also given by

$$SNR = \frac{1}{N^2} .$$ (5-19)

$$\overline{\left|\Sigma(CC)\right|^2}$$

$$\frac{W^2N^2}{16}$$

$$-W \qquad W \qquad X$$

(a) Crosscorrelation

$$\overline{\left|(AC)_S\right|^2}$$

$$\frac{W^2}{16}$$

$$-d \qquad d \qquad X$$
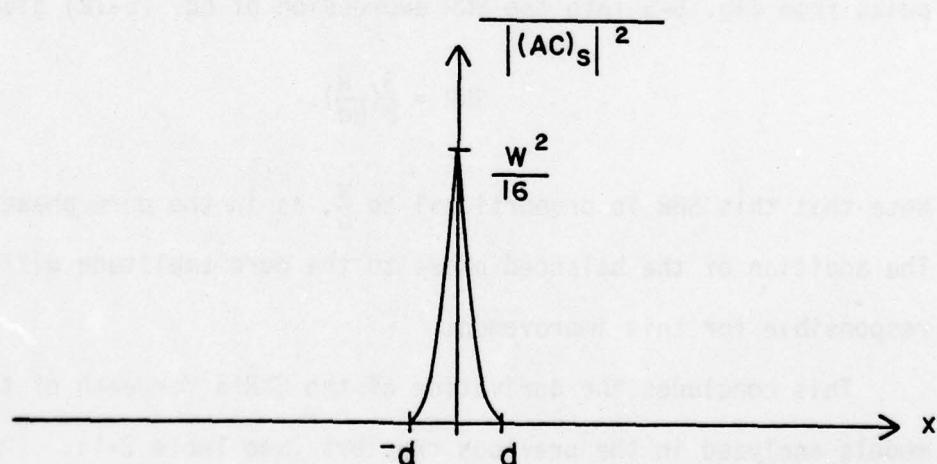
(b) Autocorrelation

Fig. 5-4 Autocorrelation and Total Crosscorrelation for
Binary and Uniformly Distributed Amplitude Dif-
fusers

It is interesting to note that neither the diffuser cell width d or the total width W appears in Eqs. (5-18) and (5-19), as opposed to the pure phase case (see Eqs. (5-16) and (5-17)). Since the number of exposures N would probably be large in practice, it is evident that the pure phase diffusers are in general much better performers than the pure amplitude diffusers.

5.2.3. Combined Amplitude and Phase Diffusers

As in the previous analysis of combined amplitude and phase diffusers (see Chap. 3, Sec. 3.2.3), the phase and amplitude are considered to be statistically independent. The results of Chapters 3 and 4 for a binary amplitude, balanced phase diffuser are summarized in Fig. 5-5. Substituting the autocorrelation and crosscorrelation peaks from Fig. 5-5 into the SNR expression of Eq. (5-12) gives

$$SNR = \frac{3}{8}\left(\frac{W}{Nd}\right). \tag{5-20}$$

Note that this SNR is proportional to $\frac{W}{d}$, as in the pure phase case. The addition of the balanced phase to the pure amplitude diffuser is responsible for this improvement.

This concludes the derivation of the SNR's for each of the diffuser models analyzed in the previous chapters (see Table 2-1). The results are applicable for both plane wave and chirp illumination, since the chirp illumination does not significantly affect the crosscorrelation noise (as defined here) for small correlation shifts $|x|$. This does not imply that chirp illumination is no better than plane wave illumi-
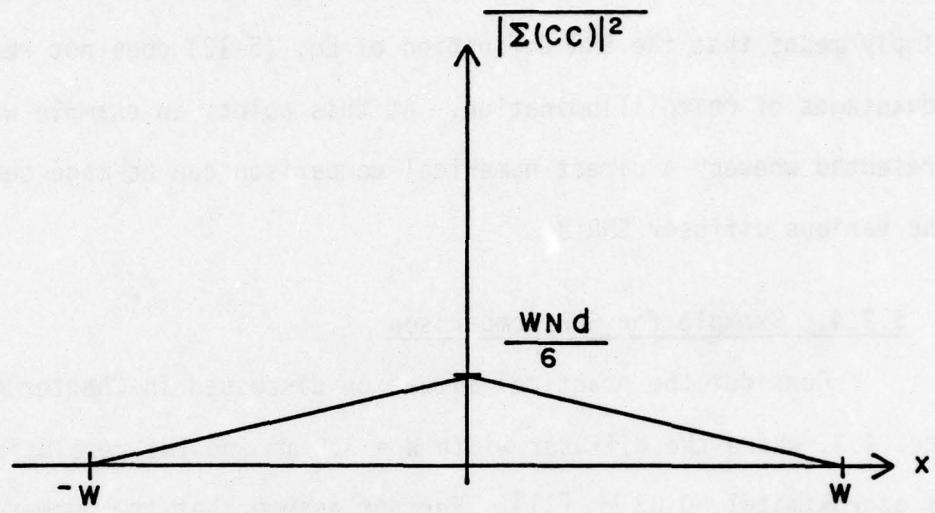
(a) Crosscorrelation
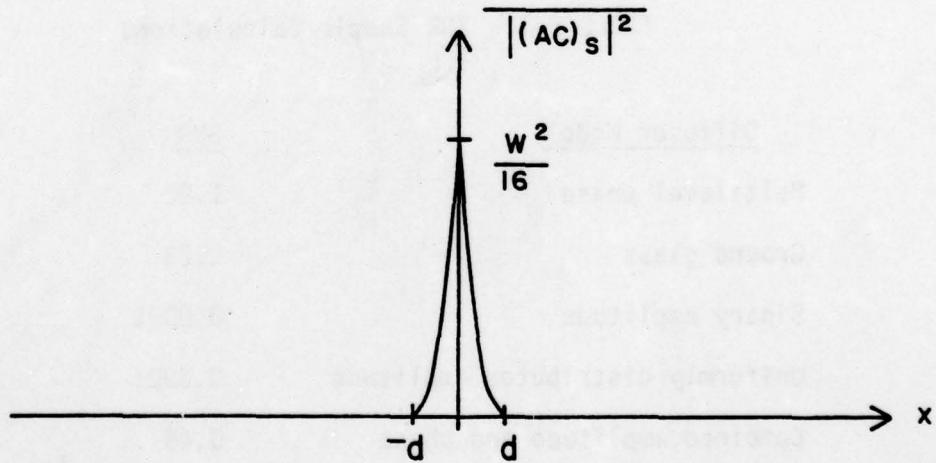
(b) Autocorrelation

Fig. 5-5 Autocorrelation and Total Crosscorrelation for a
Combined Binary Amplitude and Balanced Phase
Diffuser

nation, because chirping can reduce the crosscorrelation noise substantially at the tails of the function (see Chap. 3, Sec. 3.3). It simply means that the SNR definition of Eq. (5-12) does not reflect the advantages of chirp illumination. At this point, an example will be presented whereby a direct numerical comparison can be made between the various diffuser SNR's.

5.2.4. Example for SNR Comparison

Consider the practical situation discussed in Chapter 4, Sec. 4.3, where the diffuser width W = 3.8 mm and the resolution d is approximately 0.03 mm [11]. Further assume that the number of exposures N is 100. Substituting these values into Eqs. (5-16), (5-17), (5-18), (5-19), and (5-20) yields the SNR's of Table 5-1.

TABLE 5-1. SNR Sample Calculations

Diffuser Model	SNR
Multilevel phase	1.92
Ground glass	1.28
Binary amplitude	0.0001
Uniformly distributed amplitude	0.0001
Combined amplitude and phase	0.48 .

From this analysis, based closely on an experimental situation [11, 20], the multilevel phase and ground glass diffuser models are seen to be the best performers. The SNR's would also seem to indicate that for a given (average) diffuser cell width d, multiphase diffusers

outperform ground glass; however, recalling the approximate nature of
the ground glass analysis (see Chap. 3, Sec. 3.2.1.3), a more reason-
able conclusion is that a multiphase diffuser (including binary phase)
can perform as well as ground glass, if the spatial "fineness" of
the diffusers are the same. Both amplitude models exhibit an ex-
tremely low SNR, which indicates that pure amplitude diffusers would
probably perform poorly for any reasonable number of exposures N. The
addition of the balanced phase to the amplitude model greatly improves
the SNR over the pure amplitude case.

The results of this chapter, and also Chapters 3 and 4, are sum-
marized and discussed further in the next chapter.

CHAPTER 6

SUMMARY AND CONCLUSIONS

6.1. Summary of Major Results

The major results of Chapters 2 through 5 are now summarized for easy reference and comparison. The diffuser models used in the analysis are listed in Table 2-1. The crosscorrelation results with plane wave illumination are repeated in Fig. 6-1, and the crosscorrelations with spherical wave (chirp) illumination are included in Fig. 6-2. Figure 6-3 shows the major autocorrelation results of Chapter 4, and the signal-to-noise ratios calculated in Chapter 5 are listed in Table 6-1. The significance of these results is discussed in the following section.

6.2. Discussion of Major Results

There are four basic parameters introduced in the analysis which affect system performance. These are the diffuser cell width d (which is directly related to the transition model), the total diffuser width W, the transmittance model t, and the type of illumination. The influence of each of these parameters will now be discussed.

6.2.1. Diffuser Resolution (Cell Width) d

The significance of the diffuser cell width d can be seen with the aid of Figs. 6-1 and 6-3. Note that for both pure phase and combination amplitude and phase diffusers, the peak crosscorrelation noise is

112

$$\frac{2Wd}{3}$$

$$\overline{|S|^2} = \frac{2}{3}(W-|x|)d$$

(a) Multilevel phase

$$Wd$$

$$\overline{|S|^2} = (W-|x|)d$$

(b) Ground glass

$$\frac{W^2}{16}$$

$$\overline{|S|^2} = \frac{(W-|x|)^2}{16}$$

(c) Binary amplitude

$$\frac{W^2}{16}$$

$$\overline{|S|^2} = \frac{(W-|x|)^2}{16}$$

(d) Uniformly distributed amplitude

$$\frac{Wd}{6}$$

$$\overline{|S|^2} = \frac{(W-|x|)d}{6}$$

(e) Combined binary amplitude and balanced phase
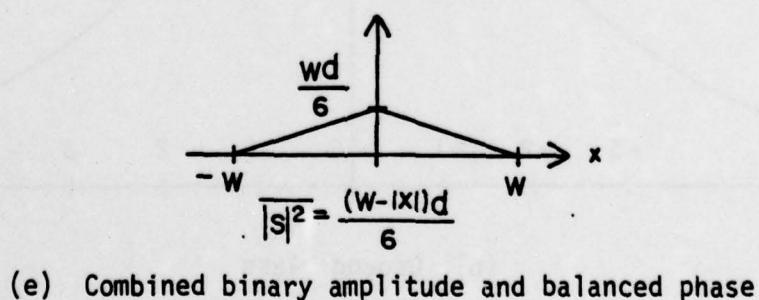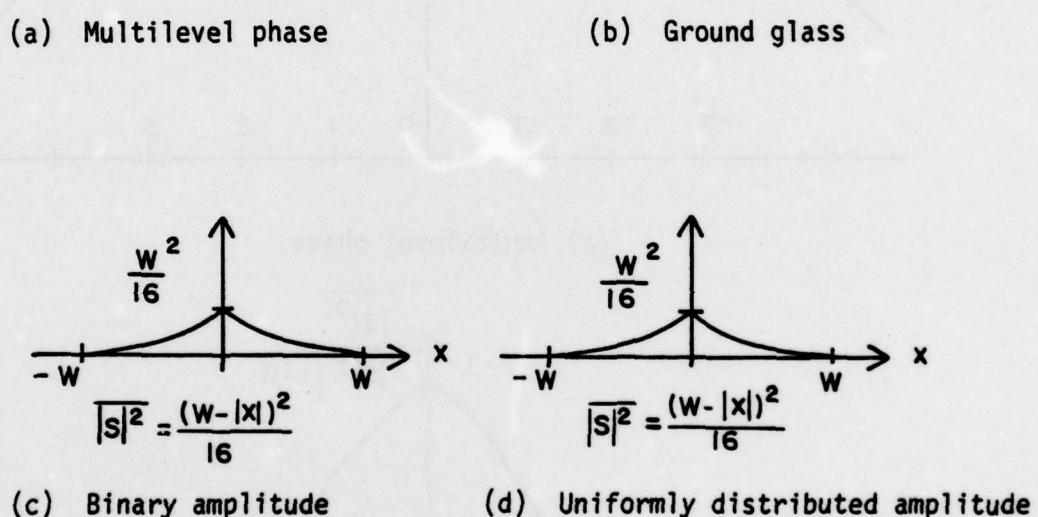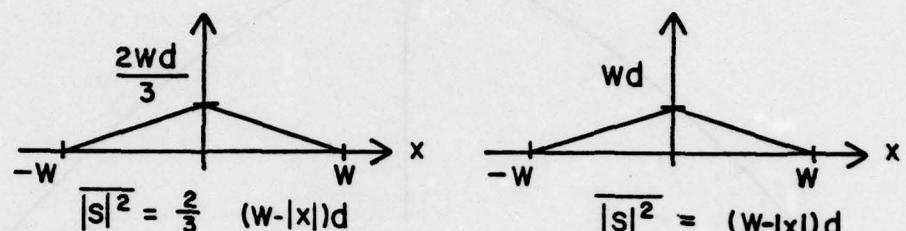
Fig. 6-1 Crosscorrelation Results for Plane Wave Illumination
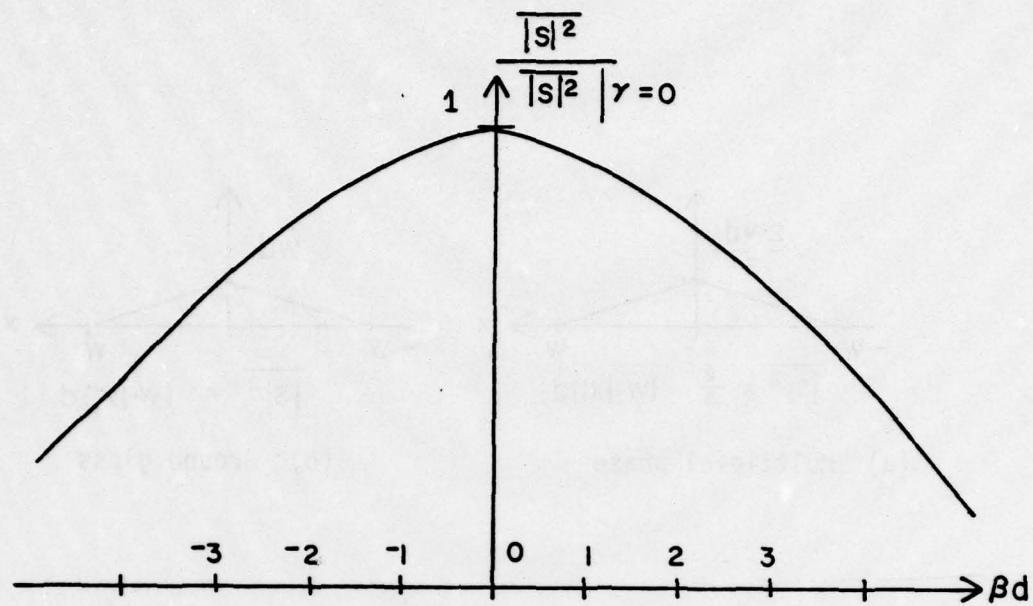
(a) Multilevel phase
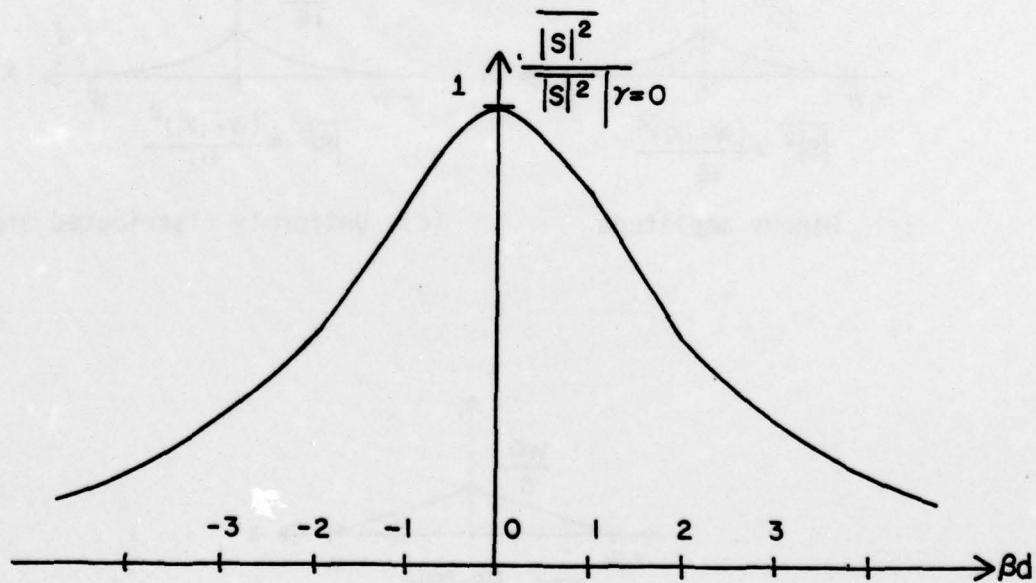
(b) Ground glass

Fig. 6-2 Normalized Crosscorrelations for Chirp Illumination

$$\overline{|S_{PC}|^2} = \frac{W^2}{d^2}(d-|x|)^2$$

(a) Multilevel phase

$$\overline{|S_{PC}|^2} = (W-|x|)^2 e^{-2|x|/d}$$

(b) Ground glass

$$\overline{|S_{PC}|^2} = \frac{W^2(d-|x|)^2}{16d^2}$$

(c) Binary and uniformly distributed amplitude
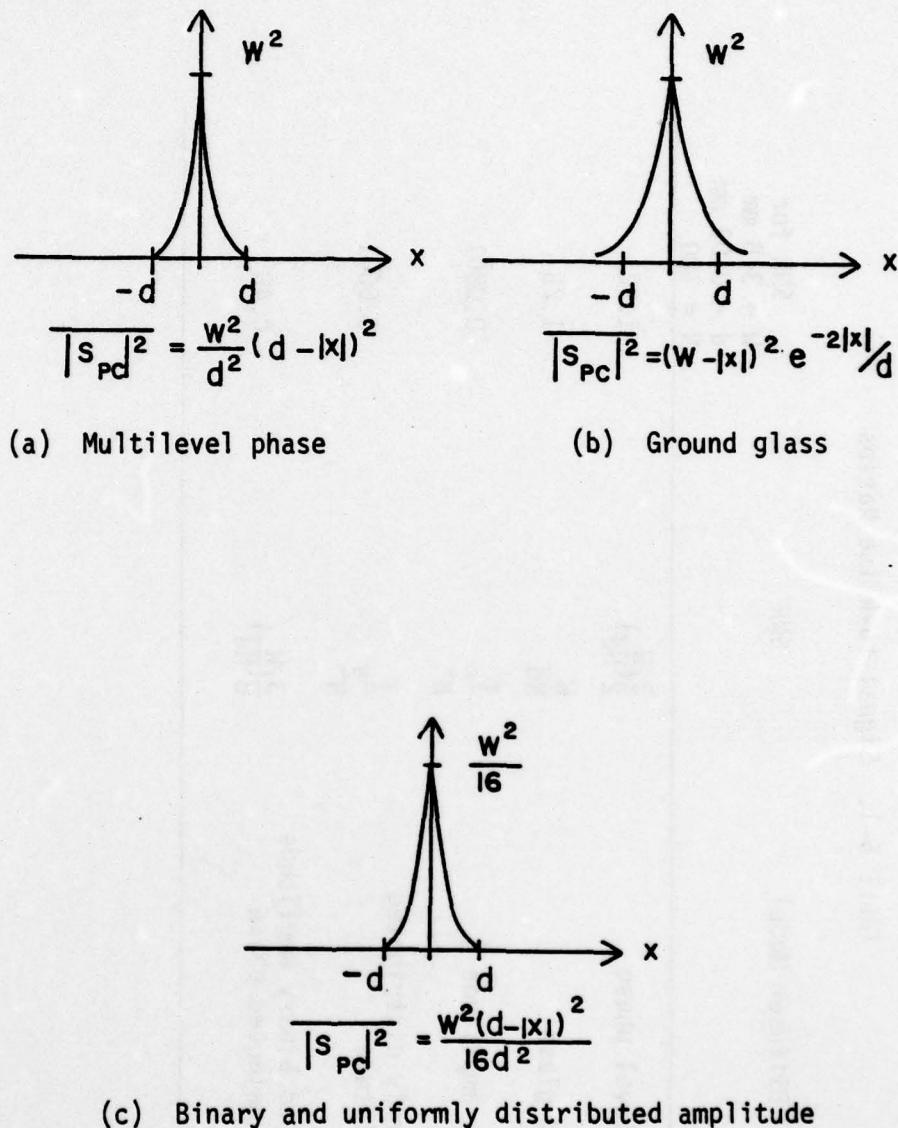
Fig. 6-3 Autocorrelation Results

TABLE 6-1. Signal-to-Noise Ratios

Diffuser Model	SNR	SNR for W = 3.8 mm d = 0.03 mm N = 100
Multilevel phase	$\frac{3}{2}\left(\frac{W}{Nd}\right)$	1.92
Ground glass	$\frac{W}{Nd}$	1.28
Binary amplitude	$\frac{1}{N^2}$	0.0001
Uniformly distributed amplitude	$\frac{1}{N^2}$	0.0001
Combined binary amplitude and balanced phase	$\frac{3}{8}\left(\frac{W}{Nd}\right)$	0.48

directly proportional to d (see Fig. 6-1). This is not an unexpected result, since a finer structure would seem to decrease the chance that any two diffusers in a family are significantly correlated. In the pure amplitude case, however, the peak crosscorrelation value is not a function of d if the diffuser width W satisfies W >> d (see Eqs. (3-46) and (3-47)). This is basically because the individual "phasor" elements which make up the random crosscorrelation sum S are all real-valued in the pure amplitude case, and must therefore add in phase no matter how finely each diffuser is subdivided.

As indicated by Fig. 6-3, the diffuser cell width d determines the width of the perfectly correlated part $\overline{|S_{PC}|^2}$ of the autocorrelation function, which reconstructs the system output through a convolution operation (see Eq. (1-8)). The cell width d therefore limits the resolution of the output [5]. In all cases, the autocorrelation peak value is independent of d, and depends only on the diffuser width W and the transmittance model.

From these results, the general conclusion can be drawn that a finer diffuser structure (i.e. a smaller cell size d) implies better system performance, except for pure amplitude diffusers.[#] This is indicated by the SNR expressions of Table 6-1. There are practical

---

[#]If W and d do not satisfy W >> d, then the value of $\overline{|S|^2}$ for a pure amplitude crosscorrelation is a function of d (see Eqs. (3-46) and (3-53)). In such a case, decreasing the cell width d does help decrease the value of $|S|^2$, but not nearly as much as for pure phase diffusers.

limitations involved here, however, because a finer diffuser means
smaller positioning tolerances in playback [6, 20], as well as greater
difficulties in mask fabrication. Note that both the multiphase model
(evenly spaced potential transitions) and the ground glass model (Poisson
transitions) perform about equally well, as long as the mean diffuser
cell width for ground glass is equal to the (constant) cell width in
the multiphase case. In fact, the SNR is slightly larger for the multi-
phase model, which is much less random in transition spacing than ground
glass.

6.2.2. Total Diffuser Width W

As illustrated in Fig. 6-1, the peak crosscorrelation values
for both pure phase and combination diffusers increase linearly with
diffuser width W. The autocorrelation peaks of Fig. 6-3 increase as
W^2. Consequently, the signal-to-noise ratio defined in Eq. (5-12) is
proportional to W for all models exhibiting a random phase (see Table
6-1). This result, coupled with the increase in SNR with decreasing
cell width d, indicates that the SNR is proportional to the number
of resolution cells $\frac{W}{d}$, which is in agreement with the work of La Macchia
and White [6], and Leger and Lee [22].

In the pure amplitude case, both the autocorrelation and cross-
correlation peaks are proportional to W^2. The SNR for these diffusers
is therefore not a function of W. A comparison of the SNR's for the
phase diffuser models and the pure amplitude models (Table 6-1) shows

that the diffuser width W (for a given cell width d) is much more signifi-
cant for the phase models than for the pure amplitude models.

6.2.3. Diffuser Transmittance Model t

As indicated by Table 6-1, the SNR is very much dependent on
the transmittance properties of the encoding diffusers. In the sample
SNR calculations, the pure amplitude models make a much poorer showing
than the pure phase and combined phase and amplitude diffusers. Also,
the SNR of the combination diffuser is significantly lower than the
SNR's of the pure phase diffusers. The conclusion is that phase dif-
fusers are generally far superior to amplitude diffusers in terms
of system performance.

Perhaps the most interesting analytical result concerning the
various transmittance models arises in the pure phase case, where the
number of allowed phase levels (assumed balanced) does not affect the
SNR. This implies that a binary phase diffuser can work just as well
as a diffuser incorporating far more phase levels, which is attractive
from a practical standpoint.

6.2.4. Diffuser Illumination

Although the SNR definition of Eq. (5-12) does not reflect the
difference between chirp and plane wave illumination (see Chap. 5), the
advantages of chirp illumination can be seen in Fig. 6-2. In both the
ground glass and multilevel phase cases, the chirp illumination sig-
nificantly reduces the crosscorrelation values away from the origin.

The plots of Fig. 6-2 are in good agreement with the experimental work of Krile, Redus, Jones, et al. [8, 11, 20].

6.2.5. Comparison with the Gold Code Bound

Krile, Hagler, et al. [8, 11, 20] have done some work involving the use of binary phase diffuser masks in which the phase levels are determined by separable Gold code sequences [24]. These are an adaptation of the codes commonly used in spread spectrum communication systems. The crosscorrelation of two Gold code sequences is defined as

$$C_{GC} = \text{\#agreements} - \text{\#disagreements} \qquad (6\text{-}1)$$

over one period of the code, and the crosscorrelation of two codes with a period of $2^n - 1$ bits is upper bounded by

$$|C_{GC}| \le \begin{cases} 2^{(\frac{n+1}{2})} & , \ n \text{ odd} \\ 2^{(\frac{n+2}{2})} & , \ n \text{ even.} \end{cases} \qquad (6\text{-}2)$$

Now consider a random binary phase diffuser of the type previously analyzed. The number of cells, or bits, in such a diffuser is just $\frac{W}{d}$, where W is the total diffuser width and d is the cell width. This is analogous to a Gold code diffuser which satisfies

$$\frac{W}{d} = 2^n - 1 \ . \qquad (6\text{-}3)$$

Assuming that W >> d, n can be expressed as

$$n = \log_2(\frac{W}{d}) \quad . \qquad (6\text{-}4)$$

END
DATE
FILMED

11 –79

DDC

MICROCOPY RESOLUTION TEST CHART
NATIONAL BUREAU OF STANDARDS
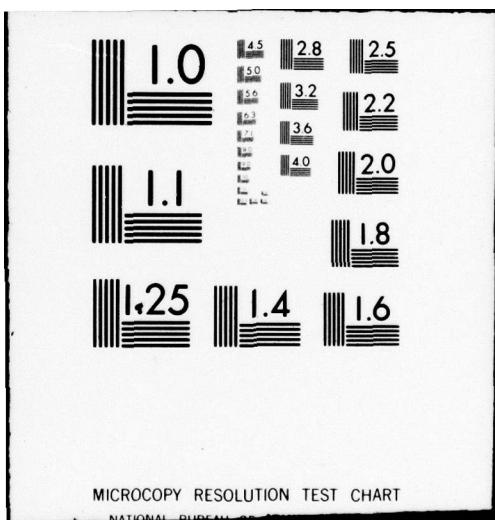
Substituting into Eq. (6-2), and using the approximation n >> 1, the upper bound can be rewritten as

$$|C_{GC}| \leq 2^{\frac{\log_2(\frac{W}{d})}{2}} = (\frac{W}{d})^{\frac{1}{2}} \ . \qquad (6-5)$$

Realizing that, in the sense of a spatial crosscorrelation, each bit in the code has width d, the spatial crosscorrelation can be expressed as

$$|CC| = |C_{GC}|d \leq (Wd)^{\frac{1}{2}} \ . \qquad (6-6)$$

The squared modulus of the crosscorrelation of two Gold code masks is therefore upper bounded by

$$|CC|^2 \leq Wd \ , \qquad (6-7)$$

and the mean square (peak) value for the random binary phase model is given by (see Fig. 6-1)

$$\overline{|S|^2} = \frac{2Wd}{3} \ . \qquad (6-8)$$

Equations (6-7) and (6-8) compare quite favorably. The value of $\overline{|S|^2}$ is smaller than the upper Gold code bound $\overline{|CC|^2}$, which is reasonable.

6.2.6. Extension to Two Dimensions

Although the entire analysis has been carried out in one dimension, the results are directly applicable to two-dimensional diffusers as long as the transmittance function t(x, y) is separable into the

factors $t(x)t(y)$, where $t(x)$ and $t(y)$ are statistically independent. In such a case, the parameter W would correspond to the total diffuser area in a 2-D sense, and the cell width d would also correspond to an area. The peak values of the crosscorrelations and autocorrelations shown in Figs. 6-1 and 6-3 (and therefore the SNR expressions of Table 6-1) can be modified to accommodate a 2-D separable diffuser function by simply replacing W by the total diffuser area and d by the area (or mean area) of a resolution cell. The quantities plotted in Figs. 6-1 and 6-3 would fall to zero in a fashion determined by the shape of the 2-D diffuser (e.g. circular, square, etc.), because the area of overlap for a given correlation shift (x_0, y_0) depends on the diffuser shape.[#] Note that in the pure phase and combined amplitude and phase cases, the SNR values of Table 6-1 would still be proportional to the total number of resolution cells in the diffuser, and in the pure amplitude cases, the SNR's would remain equal to $\frac{1}{N^2}$.

For a non-separable diffuser transmittance function, the analysis would probably be much more complicated (depending of course on the nature of the function). However, the qualitative aspects of the 1-D treatment should also hold for non-separable transmittances.

_____

[#]This situation is somewhat analogous to the dependence of an imaging system's optical transfer function on the shape of the exit pupil [25].

6.2.7. Synopsis

The important conclusions of the previous sections are listed below.

(1) In terms of the SNR definition of Eq. (5-12), the pure phase diffuser models are much better performers than the pure amplitude diffusers, and are also significantly better than combined amplitude and phase diffusers. However, there may certainly be circumstances where pure amplitude diffusers are adequate.

(2) A larger number of diffuser resolution cells (number of resolution cells $= \frac{W}{d}$) implies better system performance. This improvement is much more pronounced for phase diffusers than for amplitude diffusers.

(3) The number of allowed phase levels for multilevel balanced-phase diffusers does not affect the SNR as defined in Eq. (5-12). This means that a binary phase diffuser, such as a Gold code mask, can perform as well as ground glass or other types of multiphase diffusers (for a given mean cell width d), with the additional advantage that Gold code families are computer-generatable. For amplitude diffusers, the nature of the transmittance model (e.g. binary, uniformly distributed on [0, 1], etc.) also has little effect on the SNR.

(4) The type of spatial transition model (e.g. Poisson and evenly spaced potential transitions) appears to have a relatively minor effect on the SNR, even though there is a great deal more randomness associated with the Poisson ground glass model than the evenly spaced potential transition model. The average diffuser cell width, or "fineness," is much more important than the actual transition model (see [2] above).

(5) Chirp illumination improves system performance by decreasing the crosscorrelation magnitude at the tails of the crosscorrelation function (see Fig. 6-2).

6.3. Contributions of the Thesis

The principal contributions of this thesis are enumerated below.

(1) A simple framework for diffuser modeling has been provided which can accommodate a wide range of diffuser families.

(2) The performance characteristics of several important diffuser families have been thoroughly analyzed in the context of multiplex holography. Most diffuser research published prior to this analysis was aimed at providing uniform illumination for exposing a single hologram [26-29].

(3) The analysis provides insight into the effect of salient diffuser parameters on system performance.

(4) The experimental results of Krile, Jones, et al. [8, 11, 20] indicating the benefits of chirp illumination have been mathematically corroborated.

6.4. Suggestions for Further Research

Since the analysis has been carried out in one dimension exclusively, the results are not directly applicable to non-separable two-dimensional diffuser models. Due to the nature of the random telegraph-based diffuser model, the results cannot be directly related to continuous diffuser functions, either. However, if the random telegraph model does in reality embody the most important characteristics of a diffuser, then the qualitative aspects of the analysis should still apply. Some additional research directed into these areas should be fruitful.

The signal-to-noise ratio defined in Eq. (5-12) is excellent for diffuser comparisons, but it is based on only one system; a unit magnifier with unit strength point source inputs. A more detailed SNR analysis based on a general space-variant system would be useful.

Another significant area not covered in this work is diffuser fabrication. Techniques which would enable easy manufacture and duplication of high resolution phase diffusers have yet to be perfected.

Finally, and most importantly, new holographic storage mediums are needed which can maintain a linear response over a very wide dynamic range. This would allow high-quality multiplexing of the large number of holograms required to accurately represent most space-variant systems.

APPENDIX A

CHARACTERISTICS OF THE BALANCED PHASE PROBABILITY MODEL

A.1. Distribution of $\theta = (\phi_i - \phi_j)$ (Chap. 2, Sec. 2.4.2.1.2)

As indicated in Chapter 2, the difference between independent, identically distributed balanced phases (interpreted modulo-2π) is a balanced phase with the same probability distribution. The general n-level balanced phase probability model is given in Eq. (2-3). A phase which is uniformly distributed on $[0, 2\pi]$ is also in effect a balanced phase.

Assume that the n-level balanced phase ϕ_i takes on the value $\phi_i = n_0(\frac{2\pi}{n})$, where n_0 is one of the integers $0, 1, 2, \ldots, (n-1)$. Then the possible values of $\theta = (\phi_i - \phi_j)$ are seen from Eq. (2-3) to be

$$(\phi_i - \phi_j) = [n_0(\frac{2\pi}{n}) - \phi_j] \epsilon \{[n_0(\frac{2\pi}{n})], [n_0(\frac{2\pi}{n}) - \frac{2\pi}{n}],$$

$$[n_0(\frac{2\pi}{n}) - \frac{4\pi}{n}], \ldots, [n_0(\frac{2\pi}{n}) - (n-1)(\frac{2\pi}{n})] \}. \qquad \text{(A-1)}$$

Only the modulo-2π phase is of interest; that is, phases in Eq. (A-1) which do not lie in $[0, 2\pi]$ can be converted to an equivalent phase in this interval by adding an appropriate integral multiple of 2π. For $\phi_i = n_0(\frac{2\pi}{n})$, the last $n-n_0-1$ phases in Eq. (A-1) are negative-valued and therefore lie outside $[0, 2\pi]$. Adding 2π to these phases results in

$$(\phi_i - \phi_j) \epsilon \{[n_0(\frac{2\pi}{n})], \ldots, [0], [(n_0+1)(\frac{2\pi}{n})], [(n_0+2)(\frac{2\pi}{n})],$$

$$\ldots, [(n-1)(\frac{2\pi}{n})] \} \qquad . \qquad \text{(A-2)}$$

126

Although the phases in Eq. (A-2) are not ordered from smallest to largest, they include all the possible values of the n-level phases ϕ_i and ϕ_j. Since ϕ_i and ϕ_j are statistically independent, there is no reason for any phase in Eq. (A-2) to be preferred over another. Hence, $\theta = (\phi_i - \phi_j)$ has the same balanced probability distribution as ϕ_i and ϕ_j.

A.2. Calculation of $\overline{(e^{j\theta})}$ (Chap. 3, Sec. 3.2.1.1)

Under the balanced phase condition, every allowed phase level has equal probability of occurrence. Furthermore, the allowed phases are scattered evenly over the interval $[0, 2\pi]$ (see Eq. (2-3)). For an n-level phase (balanced or not), the expectation $\overline{e^{j\theta}}$ is given by

$$\overline{e^{j\theta}} = \sum_{k=1}^{n} e^{j\theta_k} P(\theta_k), \qquad (A-3)$$

where $P(\theta)$ is the corresponding probability mass function. This expectation is effectively the sum of n phasors in the complex plane, with the kth phasor having length $P(\theta_k)$ and phase angle θ_k. From Fig. 2-5, it is obvious that $\overline{e^{j\theta}} = 0$ for a balanced phase model.

A.3. Statistical Independence of θ_k and θ_ℓ for $k \neq \ell$ (Chap. 3, Sec. 3.2.1.1)

Consider the portion of two crosscorrelated balanced binary phase functions shown in Fig. A-1. The phases in the nonadjacent correlation cells e and g are given by $\theta_e = \phi_1 - \phi_3$ and $\theta_g = \phi_2 - \phi_4$. Since ϕ_1, ϕ_2, ϕ_3, and ϕ_4 are mutually independent, θ_e and θ_g are statistically independent; that is, θ_e and θ_g do not share any common phases ϕ,
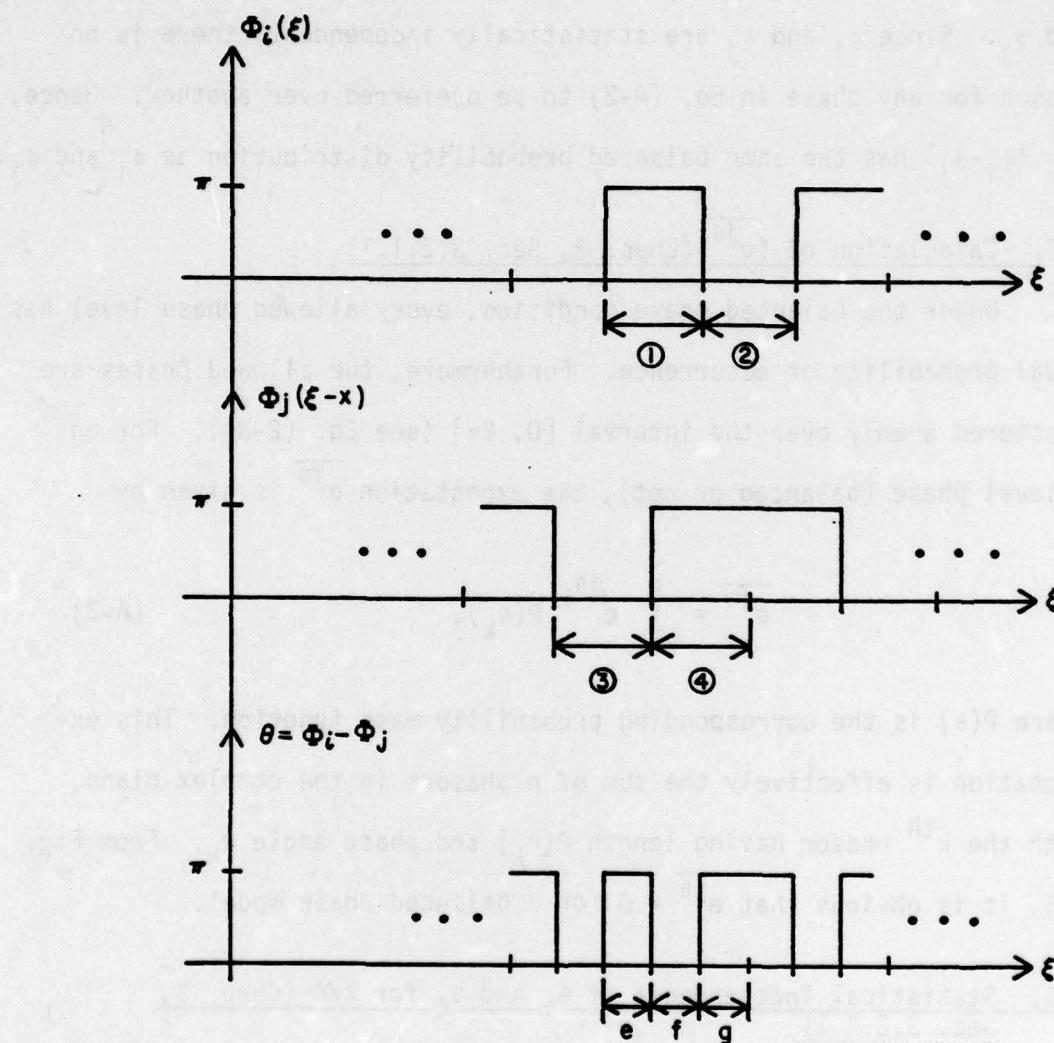
Fig. A-1 Statistical Independence of Correlation Cell Phases

and are therefore independent. This is of course true for all non-adjacent correlation cells. It is not so obvious, however, that the adjacent phases θ_e and θ_f are statistically independent (in the amplitude diffuser case considered in Appendix B, the amplitude values in adjacent correlation cells are <u>not</u> independent).

The phases θ_e and θ_f in Fig. A-1 involve the common phase ϕ_1; that is, $\theta_e = \phi_1 - \phi_3$ and $\theta_f = \phi_1 - \phi_4$. Any two adjacent correlation cells will share a common diffuser phase in this fashion. It would therefore seem that since both θ_e and θ_f depend on the random variable ϕ_1, they must be statistically dependent. This is true in general, but for the special case of the balanced phase model, θ_e and θ_f may assume every possible combination of allowed phases with equal probability. In other words, θ_e can assume any of its n allowed phase levels with equal probability, regardless of the value of θ_f (and vice-versa). The adjacent correlation cell phases θ_e and θ_f are therefore statistically independent.

APPENDIX B

CHARACTERISTICS OF THE PURE AMPLITUDE DIFFUSER MODEL

B.1. Statistical Dependence of Adjacent Correlation Cells (Chap. 3, Sec. 3.2.2.1)

Consider the binary amplitude diffuser functions shown in Fig. B-1. The values of α in the nonadjacent correlation cells e and g are given by $\alpha_e = t_1 t_3$ and $\alpha_g = t_2 t_4$. Since t_1, t_2, t_3, and t_4 are mutually independent random variables, α_e and α_g are statistically independent. The adjacent correlation cells e and f have amplitudes $\alpha_e = t_1 t_3$ and $\alpha_f = t_1 t_4$. Since both α_e and α_f depend on the random variable t_1, they are not independent (all adjacent correlation cells share a common diffuser cell). The statistical dependence can be demonstrated by showing that the conditional probability mass function (pmf) $P(\alpha_e | \alpha_f)$ is not identical to the unconditional pmf $P(\alpha_e)$ [30]. It suffices to show that these functions are not identical at any one mass point.

By Bayes' rule [31], the conditional pmf $P(\alpha_e | \alpha_f)$ is given by

$$P(\alpha_e | \alpha_f) = \frac{P(\alpha_e, \alpha_f)}{P(\alpha_f)} \quad . \tag{B-1}$$

Consider the special case $\alpha_e = 0$ and $\alpha_f = 0$. From Fig. B-1, the joint probability $P(\alpha_e = 0, \alpha_f = 0)$ is seen to be

$$P(\alpha_e = 0, \alpha_f = 0) = P(t_1 = 0) + P(t_1 = 1, t_3 = 0,$$

$$t_4 = 0). \tag{B-2}$$

130
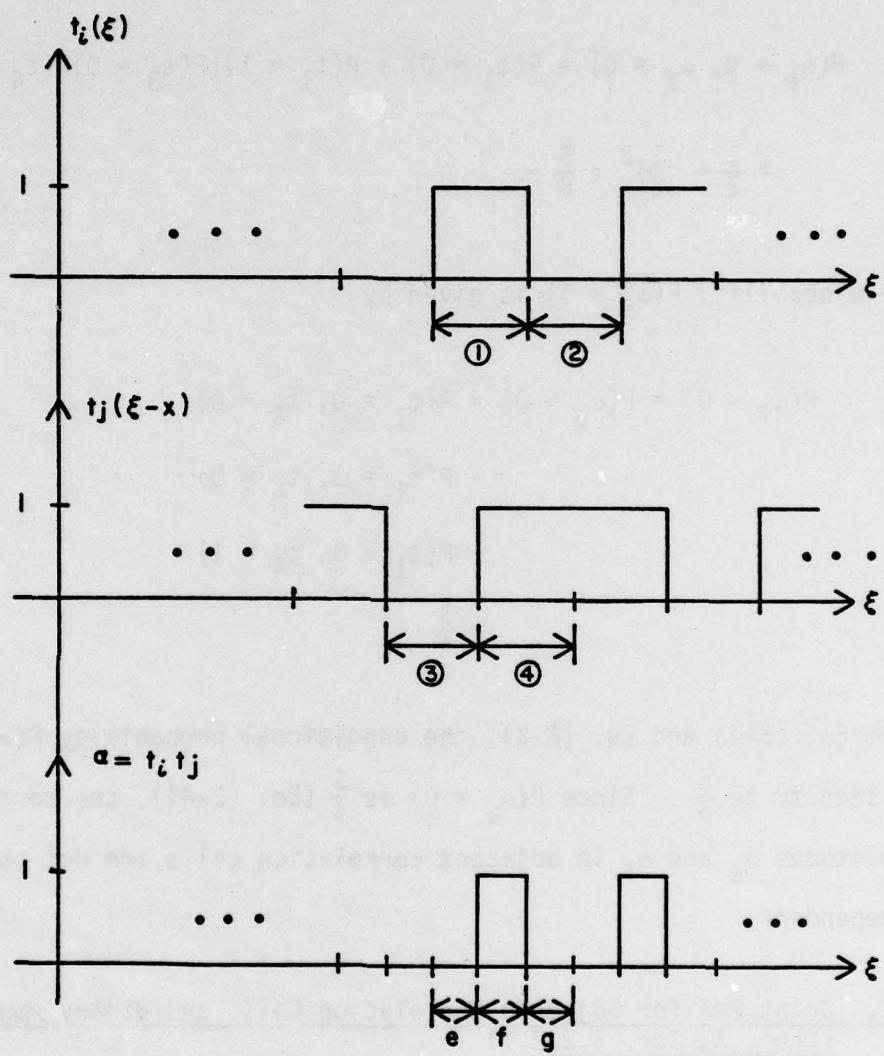
Fig. B-1 Statistical Dependence of Adjacent
Correlation Cell Amplitudes

Using the independence of t_1, t_3, and t_4, this can be expressed as

$$P(\alpha_e = 0, \alpha_f = 0) = P(t_1 = 0) + P(t_1 = 1)(P(t_3 = 0)P(t_4 = 0)$$

$$= \frac{1}{2} + (\frac{1}{2})^3 = \frac{5}{8} \quad . \tag{B-3}$$

The probability $P(\alpha_f = 0)$ is given by

$$
\begin{aligned}
P(\alpha_f = 0) = P(\alpha_e = 0) &= P(t_1 = 0, t_4 = 0) \\
&+ P(t_1 = 1, t_4 = 0) \\
&+ P(t_1 = 0, t_4 = 1) \\
&= \frac{3}{4} \quad .
\end{aligned}
\tag{B-4}
$$

From Eq. (B-4) and Eq. (B-3), the conditional probability $P(\alpha_e = 0 | \alpha_f = 0)$ is seen to be $\frac{5}{6}$. Since $P(\alpha_e = 0)$ is $\frac{3}{4}$ (Eq. (B-4)), the correlation amplitudes α_e and α_f in adjacent correlation cells are not statistically independent.

B.2. Joint PMF for Adjacent Correlation Cells and Binary Amplitude (Chap. 3, Sec. 3.2.2.1)

As shown in the previous section, the α values in adjacent correlation cells are not statistically independent. With the aid of Fig. B-1, the joint pmf for adjacent cells (denoted α_e and α_f in this discussion to correspond to Fig. B-1) can be calculated as

$$P(\alpha_e = 0, \alpha_f = 0) = P(t_1 = 0) + P(t_1 = 1, t_3 = 0, t_4 = 0) = \frac{5}{8}$$

$$P(\alpha_e = 0, \alpha_f = 1) = P(t_1 = 1, t_3 = 0, t_4 = 1) = \frac{1}{8}$$

$$P(\alpha_e = 1, \alpha_f = 0) = P(t_1 = 1, t_3 = 1, t_4 = 0) = \frac{1}{8}$$

$$P(\alpha_e = 1, \alpha_f = 1) = P(t_1 = 1, t_3 = 1, t_4 = 1) = \frac{1}{8} . \qquad \text{(B-5)}$$

B.3. Joint PDF for Adajcent Correlation Cells and Uniformly Distributed Amplitude (Chap. 3, Sec. 3.2.2.2)

The joint probability density function for the α values in adjacent correlation cells can be calculated with the aid of Fig. B-1. Although this figure shows two binary amplitude functions, the characteristics which affect the following derivation apply equally well to uniformly distributed amplitudes. The joint density $p(\alpha_e, \alpha_f)$ will be calculated by first deriving the density $p(\alpha_e, \alpha_f, t_1)$, and then integrating over all t_1 to get $p(\alpha_e, \alpha_f)$.

Now $p(\alpha_e, \alpha_f, t_1)$ can be expressed as the product of densities [31]

$$p(\alpha_e, \alpha_f, t_1) = p(\alpha_e | \alpha_f, t_1) p(\alpha_f | t_1) p(t_1). \qquad \text{(B-6)}$$

The pdf $p(t_1)$ is given by

$$p(t_1) = I_{[0,1]}(t_1), \qquad \text{(B-7)}$$

where the indicator function I [32] specifies the range of allowed values of t_1; I is defined by

$$I_{[a, b]}(x) = \begin{cases} 1, & x \epsilon [a,b] \\ 0, & x \notin [a,b] . \end{cases} \qquad \text{(B-8)}$$

For a given value of t_1, the value of $\alpha_e = t_1 t_3$ depends only on the value of t_3. Since t_3 is uniformly distributed on $[0, 1]$, the conditional density $p(\alpha_f | t_1)$ is also uniformly distributed as

$$p(\alpha_f | t_1) = \frac{1}{t_1} I_{[0, t_1]}(\alpha_f). \tag{B-9}$$

The conditional pdf $p(\alpha_e | \alpha_f, t_1)$ depends on α_f and t_1, but conditioning on both α_f and t_1 is redundant. This pdf can be equivalently expressed as

$$p(\alpha_e | \alpha_f, t_1) = p(\alpha_e | t_1), \tag{B-10}$$

so that (see Eq. (B-9))

$$p(\alpha_e | \alpha_f, t_1) = \frac{1}{t_1} I_{[0, t_1]}(\alpha_e). \tag{B-11}$$

Substituting from Eqs. (B-7), (B-9), and (B-11) into Eq. (B-6) and integrating the resulting joint pdf over t_1 gives

$$p(\alpha_e, \alpha_f) = \int_{-\infty}^{\infty} \frac{1}{t_1^2} I_{[0, 1]}(t_1) I_{[0, t_1]}(\alpha_e) I_{[0, t_1]}(\alpha_f) dt_1. \tag{B-12}$$

This can be alternately expressed as

$$p(\alpha_e, \alpha_f) = \int_0^1 \frac{1}{t_1^2} I_{[0, t_1]}(\alpha_e) I_{[0, t_1]}(\alpha_f) dt_1, \tag{B-13}$$

where the properties of the indicator function are applied. Note that the integrand of Eq. (B-13) is equal to zero for $t_1 \epsilon [0, \max(\alpha_e, \alpha_f)]$.

The lower limit of the integral can therefore be changed, which gives

$$p(\alpha_e, \alpha_f) = \int_{\max(\alpha_e, \alpha_f)}^{1} \frac{1}{t_1^2} dt_1. \qquad \text{(B-14)}$$

Performing the integration, the joint density is seen to be

$$p(\alpha_e, \alpha_f) = \begin{cases} \dfrac{1}{\max(\alpha_e, \alpha_f)} - 1, & \alpha_e \text{ and } \alpha_f \epsilon [0, 1] \\ \\ 0, & \text{otherwise.} \end{cases} \qquad \text{(B-15)}$$

This density can be used to calculate the expectation $\overline{\alpha_i \alpha_{i+1}}$ in Eq. (3-52).

B.4. PMF of α for Binary Amplitude (Chap. 3, Sec. 3.2.2.1)

For a binary amplitude model which can assume either of the values 0 or 1 with equal probability, the pmf of $\alpha = t_i t_j$ is given by

$$\begin{aligned} P(\alpha = 1) &= P(t_i = 1, t_j = 1) \\ &= P(t_i = 1)P(t_j = 1) = \frac{1}{4} \\ P(\alpha = 0) &= 1 - P(\alpha = 1) = \frac{3}{4} . \end{aligned} \qquad \text{(B-16)}$$

B.5. PDF of α for Uniformly Distributed Amplitude (Chap. 3, Sec. 3.2.2.2)

The pdf for the random variable $\alpha = t_i t_j$ can be calculated by first deriving the cumulative distribution function (cdf) and then differentiating to get the density function. The cdf of α is defined as

$$F(\alpha_0) \triangleq P(\alpha \leq \alpha_0) = P(t_i t_j \leq \alpha_0). \qquad \text{(B-17)}$$

Both t_i and t_j are uniformly distributed on [0, 1], and they are statistically independent. The joint pdf for t_i and t_j is therefore given by

$$p(t_i, t_j) = p(t_i)p(t_j) = \begin{cases} 1, & t_i \text{ and } t_j \epsilon [0, 1] \\ \\ 0, & \text{otherwise.} \end{cases} \qquad (B-18)$$

Integrating this joint density over the region $t_i t_j \leq \alpha_0$ gives the cdf $F(\alpha_0)$. From Fig. B-2, the cdf is seen to be

$$F(\alpha_0) = P(t_i t_j \leq \alpha_0) = \alpha_0 + \int_{\alpha_0}^{1} \frac{\alpha_0}{t_i} \, dt_i \ , \qquad (B-19)$$

which reduces to

$$F(\alpha_0) = \alpha_0 (1 - \ln \alpha_0) \ . \qquad (B-20)$$

Differentiating with respect to α_0 gives the pdf

$$p(\alpha = \alpha_0) = \frac{dF(\alpha_0)}{d\alpha_0} = \begin{cases} \ln(\frac{1}{\alpha_0}) \ , & \alpha_0 \epsilon [0, 1] \\ \\ 0 \ , & \text{otherwise.} \end{cases} \qquad (B-21)$$

As a check on both Eqs. (B-21) and (B-15), $p(\alpha)$ can also be calculated from the joint density of Eq. (B-15) by integrating over one of the variables. Carrying out this integration verifies Eq. (B-21).
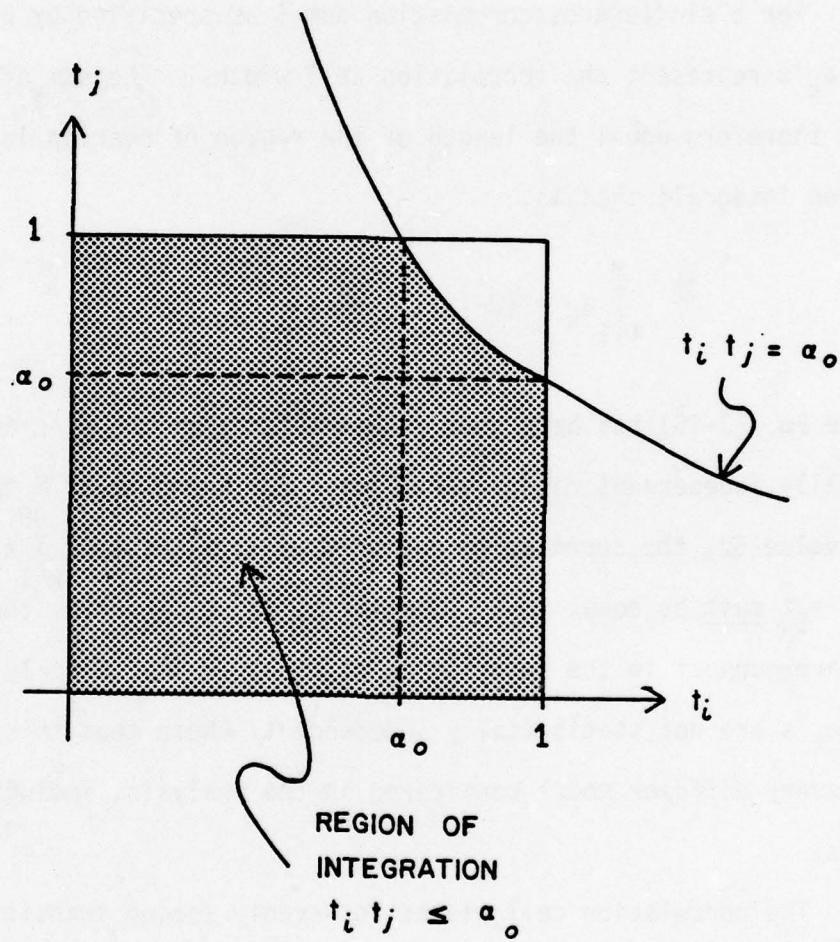
Fig. B-2 Region of Integration for $F(\alpha_0)$

APPENDIX C

STATISTICAL DEPENDENCE OF CORRELATION CELL WIDTHS

Chap. 3, Sec. 3.2.1.1

For a single crosscorrelation sum S as specified by Eq. (3-5), the a_k's represent the correlation cell widths. The sum of the a_k's must therefore equal the length of the region of overlap in the correlation integral; that is,

$$\sum_{k=1}^{M} a_k = (W - |x|) \doteq \frac{Md}{2} , \qquad (C-1)$$

where Eq. (3-10) has been used. This means that the a_k's are not mutually independent random variables. For example, if M takes on the value 50, the correlation region $W - |x| = 100$, and $\sum_{k=1}^{49} a_k = 95$, then a_{50} <u>must</u> be equal to 5. Similarly, if $\sum_{k=1}^{48} a_k = 90$, then a_{49} and a_{50} are subject to the restriction $a_{49} + a_{50} = 10$. Clearly then, the a_k's are not statistically independent. Note that this is true for every diffuser model considered in the analysis, including ground glass.

The correlation cell widths for evenly spaced transitions have been treated as mutually independent random variables uniformly distributed on [0, d], where d is the diffuser cell width. With this model, the mean value of $\sum_{k=1}^{M} a_k$ is given by

$$\overline{\sum_{k=1}^{M} a_k} = M\overline{a} = \frac{Md}{2} , \qquad (C-2)$$

138

so this statistical model for the a_k's has a mean sum which equals the constant value the sum must take on (see Eq. (C-1)). The a_k's for the ground glass model have been treated as statistically independent, negative exponentially distributed random variables with mean value $\overline{a_k} = \frac{d}{2}$ (see Eq. (3-33)). Also, the number of terms M in the complex sum of Eq. (3-7) is treated as the deterministic function

$$\overline{M} = \frac{2(W-|x|)}{d} \tag{C-3}$$

(see Eq. (3-31)). Under these conditions, the sum of the a_k's has a mean value given by

$$\overline{\sum_{k=1}^{M} a_k} = \overline{M}\,\overline{a} = (W-|x|), \tag{C-4}$$

which fits Eq. (C-1).

APPENDIX D

EXACT APPROACH TO THE GROUND GLASS CROSSCORRELATION CALCULATION

Chap. 3, Sec. 3.2.1.3

As noted in Chapter 3, the random variables M, a_1, a_2, ..., a_M in the correlation sum of Eq. (3-7) are not mutually independent. The statistical dependence of the a_k's is demonstrated in Appendix C, where the sum $\sum\limits_{k=1}^{M} a_k$ is shown to take on the value $W - |x|$ (Eq. (C-1)). The actual statistics of the a_k's must therefore depend on the value assumed by the random variable M.

From the law of total probabilities [33], the general expression for $\overline{|S|^2}$ is given by

$$\overline{|S|^2} = \sum_{m=0}^{\infty} E[\sum_{k=1}^{M} a_k^2 | M=m]P(M=m), \qquad (D-1)$$

where $E[\cdot]$ is the expectation operator. This equation can be rewritten as

$$\overline{|S|^2} = \sum_{m=0}^{\infty} E[\sum_{k=1}^{m} a_k^2]P(M=m). \qquad (D-2)$$

Now the expectation $E[\cdot]$ in Eq. (D-2) can be expressed as

$$E[\sum_{k=1}^{m} a_k^2] = \iint\limits_{-\infty}^{\infty}\ldots\int(\sum_{k=1}^{m} a_k^2)p(a_1, a_2, \ldots, a_m)\cdot da_1 da_2 \ldots da_m, \qquad (D-3)$$

where $p(a_1, a_2, \ldots, a_m)$ is the joint density function characterizing a_1 through a_m. This joint density can be expressed as a product of conditional densities:

140

$$p(a_1, a_2, \ldots, a_m) = p(a_m|a_{m-1}, \ldots a_1)p(a_{m-1}|a_{m-2}, \ldots, a_1)$$

$$\cdot p(a_{m-2}|a_{m-3}, \ldots, a_1) \ldots p(a_2|a_1)p(a_1).$$

$$(D-4)$$

Consider the marginal probability density $p(a_1)$ in Eq. (D-3). The random variable a_1 could conceivably take on any value in the interval $[0, W-|x|]$ (a_1 cannot be greater than $W-|x|$ due to the restriction of Eq. (C-1)). A reasonable statistical model for a_1 would be a truncated exponential density. For m terms in the sum, the mean value of a_1 is

$$\overline{a_1} = \frac{W_1}{m}, \tag{D-5}$$

where $W_1 \triangleq W-|x|$. The corresponding density for a_1 is defined as

$$p(a_1) = \frac{\lambda_1 e^{-\lambda_1 a_1}}{1-e^{-\lambda_1 W_1}} \; I_{[0, \, W_1]}(a_1) , \tag{D-6}$$

where $I_{[0, \, W_1]}(a_1)$ is the indicator function [32] defined by

$$I_{[0, \, W_1]}(a_1) = \begin{cases} 1 , & a_1 \epsilon [0, \, W_1] \\ \\ 0, & \text{otherwise} . \end{cases} \tag{D-7}$$

The parameter λ_1 in Eq. (D-6) is specified so that Eq. (D-5) is satisfied. Solving for $\overline{a_1}$ gives

$$\overline{a_1} = \frac{1}{\lambda_1} - \frac{W_1}{e^{\lambda_1 W_1} - 1} , \tag{D-8}$$

and substituting for $\overline{a_1}$ from Eq. (D-5) results in

$$\frac{W_1}{m} = \frac{1}{\lambda_1} - \frac{W_1}{e^{\lambda_1 W_1} - 1} \quad . \tag{D-9}$$

This equation must be solved for λ_1 (in terms of W_1 and m) to completely specify the density $p(a_1)$ of Eq. (D-6). Note that for large W_1 or λ_1, $e^{\lambda_1 W_1} \gg W_1$, and Eq. (D-9) is approximately

$$\frac{W_1}{m} = \overline{a_1} \triangleq \frac{1}{\lambda_1} \quad . \tag{D-10}$$

This implies that the mean of the truncated density is approximately the same as the nontruncated density; i.e. the portion of the original exponential density function that gets "chopped off" to form the truncated density has a negligible effect.

Now the conditional pdf $p(a_2|a_1)$ can be developed in a similar fashion to $p(a_1)$. For a given value of a_1, the random variable a_2 is restricted to the interval $a_2 \epsilon [0, W-|x|-a_1]$. The truncated density for a_2 conditioned on a_1 is given by

$$p(a_2|a_1) = \frac{\lambda_2 e^{-\lambda_2 a_2}}{1-e^{-\lambda_2 W_2}} \, I_{[0, W_2]}(a_2), \tag{D-11}$$

where $W_2 \triangleq W-|x|-a_1$, and λ_2 satisfies the equation

$$E[a_2|a_1] = \frac{W_2}{m-1} = \frac{1}{\lambda_2} - \frac{W_2}{e^{\lambda_2 W_2}-1} \quad . \tag{D-12}$$

In general, the conditional density $p(a_k|a_{k=1}, \ldots, a_1)$ is specified by

$$p(a_k | a_{k-1}, \ldots, a_1) = \frac{\lambda_k e^{-\lambda_k a_k}}{1-e^{-\lambda_k W_k}} \ I_{[0, W_k]}(a_k), \qquad \text{(D-13)}$$

where $W_k \triangleq W - |x| - \sum\limits_{\ell=1}^{k-1} a_\ell$, and λ_k is the solution of the equation

$$E[a_k | a_{k-1}, \ldots, a_1] = \frac{W_k}{m-k+1} = \frac{1}{\lambda_k} - \frac{W_k}{e^{\lambda_k W_k} - 1} \ . \qquad \text{(D-14)}$$

The joint density function $p(a_1, a_2, \ldots, a_m)$ is the product of these conditional densities, and substituting from Eq. (D-13) into Eq. (D-4) gives

$$p(a_1, a_2, \ldots, a_m) = \frac{(\prod\limits_{k=1}^{m} \lambda_k) e^{-(\sum\limits_{k=1}^{M} \lambda_k a_k)}}{\prod\limits_{k=1}^{m} (1-e^{-\lambda_k W_k})} \ \prod\limits_{k=0}^{m} I_{[0, W_k]}(a_k).$$

$$\text{(D-15)}$$

Substituting this joint density into Eq. (D-3) gives $E[\sum\limits_{k=1}^{m} a_k^2]$. The quantity M has been modeled as a Poisson random variable with a probability mass function given by Eq. (3-30). If Eq. (3-30) and Eq. (D-15) are applied to Eqs. (D-3) and (D-2), a very accurate mathematical representation for $\overline{|S|}^2$ is obtained. It would be very difficult, however, to solve analytically for $\overline{|S|}^2$ from such an involved expression. The obvious complexity of this more exact approach is plenty of justification for the approximations made in Chapter 3.

APPENDIX E

PERFECTLY CORRELATED AND STATISTICALLY INDEPENDENT CORRELATION LENGTHS IN THE GROUND GLASS AUTOCORRELATION INTEGRAND

Chap. 4, Sec. 4.1

Consider the shifted Poisson transition models of Fig. E-1, which represent the autocorrelation of two ground glass diffuser functions (the phase values are not shown). The transmittance values are perfectly correlated in regions of the ξ axis where identically numbered diffuser cells overlap. At any point ξ_0, the probability that ξ_0 will lie in a region of perfect correlation is equal to the probability that the Poisson process <u>does</u> <u>not</u> make a transition within the length of the correlation shift $|x|$. As shown by Fig. E-1, this means that all dif-fuser cell widths greater than $|x|$ will contribute a region of perfect correlation, and all cell widths less than $|x|$ will lie in regions where the transmittance values are statistically independent.

The probability that the Poisson process which describes the transition model does not have a transition within length $|x|$ is given by

$$P[0 \text{ transitions}] = \left. \frac{e^{-\lambda|x|}(\lambda|x|)^T}{T!} \right|_{T=0} = e^{-\lambda|x|} , \qquad (E-1)$$

where λ is the mean number of transitions per unit length (see Eq. (2-1)). Substituting the value $\lambda = \frac{1}{d}$ into Eq. (E-1) gives

144
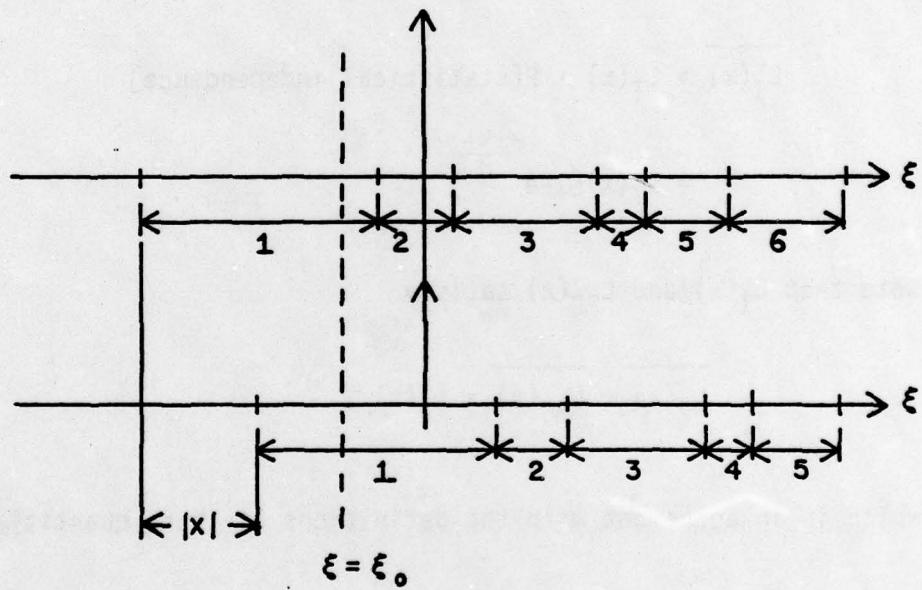
Fig. E-1 Transitions for the Autocorrelation of a
Ground Glass Diffuser

$$P[\text{0 transitions}] \equiv P[\text{perfect correlation}] = e^{-\frac{|x|}{d}} . \qquad (E-2)$$

The mean value of L_{PC}, as defined in Chapter 4, Sec. 4.1, is given by

$$\overline{L_{PC}(x)} = L_T(x) \cdot P[\text{perfect correlation}]$$
$$= L_T(x)e^{-\frac{|x|}{d}} . \qquad (E-3)$$

Similarly, the mean of $L_I(x)$ is given by

$$\overline{L_I(x)} = L_T(x) \cdot P[\text{statistical independence}]$$
$$= L_T(x)[1-e^{-\frac{|x|}{d}}] . \qquad (E-4)$$

Note that $L_I(x)$ and $L_{PC}(x)$ satisfy

$$\overline{L_I(x)} + \overline{L_{PC}(x)} = L_T(x) , \qquad (E-5)$$

which is in agreement with the definitions of these quantities.

SYMBOLS

a: correlation cell width

A: real-valued amplitude transmittance

α: the product $t_i t_j$ of two amplitude diffuser functions

AC: autocorrelation

$(AC)_n$: the noise part of the autocorrelation integral

$(AC)_s$: the signal part of the autocorrelation integral

$(\cdot)*(\cdot)$: the convolution operation

$(\cdot)^*$: complex conjugate

$(\cdot) \circledast (\cdot)$: the correlation operation

$|\cdot|$: absolute value or modulus

β: defined as $\beta \triangleq 2\gamma x$

CC: crosscorrelation

C_{GC}: the crosscorrelation of Gold code functions over one period of the code

cdf: cumulative distribution function

d: diffuser cell width

$\overline{(\cdot)}$: the expectation or mean value of a random quantity

γ: degree of chirp, measured in $\dfrac{rad}{(length)^2}$

h: optical impulse response

H: Fourier transform of the optical impulse response

I: statistically independent

λ: the mean number of counts per unit length in a Poisson process

L_I: sum of the widths of all regions of statistical independence in the autocorrelation integrand

L_{PC}: sum of the widths of all regions of perfect correlation in the autocorrelation integrand

L_T: total width of the region of overlap of two correlated diffuser functions $(=W-|x|)$

147

M: *number of terms in the crosscorrelation sum, or equivalently the number of correlation cells in the crosscorrelation integrand*

M': number of perfectly correlated or statistically independent terms in the autocorrelation sum for evenly spaced potential transitions and $|x| \epsilon [0, d]$

N: number of exposures or multiplexed holograms

O: system output with simultaneous playback

O_{ideal}: ideal output for zero-valued crosscorrelations and delta-like autocorrelations

O_k: system output for single point playback

ϕ: phase function for a pure phase diffuser

ξ: variable of integration in the correlation integral

p(·): a probability density function

P(·): a probability mass function

PC: perfectly correlated

pdf: probability density function

pmf: probability mass function

r: reference beam amplitude immediately exiting the encoding diffuser

R: Fourier transform of r

s: sampled value of the transparency input to the optical system

S: correlation sum equivalent to the correlation integral

S_I: the portion of the autocorrelation sum including only regions of statistical independence

S_{PC}: the portion of the autocorrelation sum including only regions of perfect correlation

SNR: signal-to-noise ratio

t: transmittance

T: number of transitions

149

θ: correlation cell phases in the correlation of phase diffusers

u: wavefront illuminating a diffuser

U_I: field illuminating the developed multiplex hologram during simultaneous playback

U_O: field immediately exiting the multiplex hologram during simultaneous playback

W: total diffuser width

x: correlation shift in the correlation integral, or the output plane coordinate

REFERENCES

1. L. M. Deen, J. F. Walkup, and M. O. Hagler, "Representations of Space-Variant Optical Systems Using Volume Holograms," _Applied Optics_, Vol. 14, October 1975, pp. 2438-2446.

2. J. F. Walkup and M. O. Hagler, "Volume Hologram Representations of Space-Variant Optical Systems," in _Proceedings 1975 Electro-Optical Systems Design Conference_ (Industrial and Scientific Conference Management, Inc., Chicago, 1975), pp. 31-37.

3. R. J. Marks II and T. F. Krile, "Holographic Representations of Space-Variant Systems: System Theory," _Applied Optics_, Vol. 15, September 1976, pp. 2241-2245.

4. R. J. Collier, C. B. Burckhardt, and L. H. Lin, _Optical Holography_ (Academic, New York, 1971), Chap. 17.

5. R. J. Collier and K. S. Pennington, "Multicolor Imaging from Holograms Formed on Two-Dimensional Media," _Applied Optics_, Vol. 6, June 1967, pp. 1091-1095.

6. J. T. La Macchia and D. L. White, "Coded Multiple Exposure Holograms," _Applied Optics_, Vol. 7, January 1968, pp. 91-94.

7. T. F. Krile, R. J. Marks II, J. F. Walkup, and M. O. Hagler, "Holographic Representations of Space-Variant Systems Using Phase-Coded Reference Beams," _Applied Optics_, Vol. 16, December 1977, pp. 3131-3135.

8. T. F. Krile, M. O. Hagler, W. D. Redus, and J. F. Walkup, "Multiplex Holography with Chirp-Modulated Binary Phase-Coded Reference Beam Masks," _Applied Optics_, Vol. 18, January 1979, pp. 52-56.

9. J. W. Goodman, _Introduction to Fourier Optics_ (McGraw-Hill, New York, 1968), p. 201.

10. R. Bracewell, _The Fourier Transform and its Applications_ (McGraw-Hill, New York, 1965), p. 122.

11. W. D. Redus, "Two-Dimensional Phase Codes for Multiplex Holography," M.S. Thesis, Dept. of Electrical Engineering, Texas Tech University, Lubbock, Texas (May 1978).

12. A. Papoulis, _Probability, Random Variables, and Stochastic Processes_ (McGraw-Hill, New York, 1965), pp. 288-290.

13. L. N. Enloe, "Noise-Like Structure in the Image of Diffusely Reflecting Objects in Coherent Illumination," _Bell System Technical Journal_, September 1967, pp. 1479-1489.

14. A. M. Mood, F. A. Graybill, and D. C. Boes, <u>Introduction to the Theory</u> <u>of Statistics</u> (McGraw-Hill, New York, 1974), pp. 113-114.

15. Bracewell, pp. 41, 46.

16. W. B. Davenport and W. L. Root, <u>An Introduction to the Theory of Ran-</u> <u>dom Signals and Noise</u> (McGraw-Hill, New York, 1958), p. 60.

17. Mood, Graybill, and Boes, p. 193.

18. Mood, Graybill, and Boes, p. 540.

19. Mood, Graybill, and Boes, p. 70.

20. M. I. Jones, "Multiplex Holography for Space-Variant Optical Pro-
cessing," M.S. Thesis, Dept. of Electrical Engineering, Texas Tech
University, Lubbock, Texas (August 1979).

21. Goodman, p. 80.

22. J. R. Leger and S. H. Lee, "Coherent Optical Implementation of
Generalized Two-Dimensional Transforms," in <u>Proceedings of the</u>
<u>Society of Photo-Optical Instrumentation Engineers</u>, Vol. 154, Au-
gust 1978, pp. 210-218.

23. J. D. Gaskill, <u>Linear Systems, Fourier Transforms, and Optics</u> (Wiley
and Sons, New York, 1978), pp. 272-273.

24. R. Gold, "Maximal Recursive Sequences with 3-Valued Recursive Cross-
correlation Functions," <u>IEEE Transactions on Information Theory</u>,
January 1968, pp. 154-156.

25. Goodman, p. 114.

26. C. B. Burckhardt, "Use of a Random Phase Mask for the Recording of
Fourier Transform Holograms of Data Masks," <u>Applied Optics</u>, Vol.
9, March 1970, pp. 695-700.

27. H. Akahori, "Comparison of Deterministic Phase Coding with Random
Phase Coding in Terms of Dynamic Range," <u>Applied Optics</u>, Vol. 12,
October 1973, pp. 2336-2343.

28. K. Sato and T. Shimizu, "Characteristics of Deterministic Phase Codes
for Holography," <u>Applied Optics</u>, Vol. 14, January 1975, pp. 102-104.

29. W. J. Dallas, "Deterministic Diffusers for Holography," <u>Applied Optics</u>,
Vol. 12, June 1973, pp. 1179-1187.

30. Mood, Graybill, and Boes, p. 150-151,

31. Mood, Graybill, and Boes, p. 36.

32. Mood, Graybill, and Boes, p. 20.

33. Mood, Graybill, and Boes, p. 35.